CPPM-T-2015-06

Aix-Marseille Université
Faculté des Sciences
Université de Science et Technologie Chinoise
Faculté des Sciences

Thèse de doctorat

Discipline : *Physique et Sciences de la Matière*
Spécialité : *Physique des Particules et Astroparticules*

Mesure de la section efficace de production WW dans les collisions proton-proton a $\sqrt{s} = 8$ TeV avec le détecteur ATLAS

présentée by

Jun Gao

en vue d'obtenir le grade de docteur de l'Université d'Aix-Marseille

Soutenue le 30 Octobre 2015 devant le jury composé de :

Dr Shenjian CHEN	Examinateur	NJU
Dr Eric KAJFASZ	Examinateur	CPPM
Dr Jan KRETZSCHMAR	Examinateur	LIV
Dr Yanwen LIU	Directeur de thèse	USTC
Dr Emmanuel MONNIER	Directeur de thèse	CPPM
Dr Yajun MAO	Rapporteur	PKU
Dr Emmanuel SAUVAN	Rapporteur	LAPP
Dr Zhengguo ZHAO	Examinateur	USTC

CPPM-T-2015-06

University of Aix-Marseille
Faculty of Science

University of Science and Technology of China
Faculty of Science

PhD THESIS

Domain : *Physics and Matter Sciences*
Specialty : *Particle Physics and Astroparticles*

Measurement of the WW production cross-section in Proton-Proton Collisions at $\sqrt{s} = 8$ TeV with the ATLAS Detector

presented by

Jun Gao

To obtain the degree of Doctor of Aix Marseille University

Sustained on 30th October 2015, in front of a jury composed of :

Dr Shenjian CHEN	Examiner	NJU
Dr Eric KAJFASZ	Examiner	CPPM
Dr Jan KRETZSCHMAR	Examiner	LIV
Dr Yanwen LIU	Thesis supervisor	USTC
Dr Emmanuel MONNIER	Thesis supervisor	CPPM
Dr Yajun MAO	Reviewer	PKU
Dr Emmanuel SAUVAN	Reviewer	LAPP
Dr Zhengguo ZHAO	Examiner	USTC

中国科学技术大学

博士学位论文

ATLAS 探测器上利用 8TeV 质子对撞数据对 W^+W^- 到双轻子道的产生截面的测量

作者姓名：高 军

学科专业：粒子物理与核物理专业

导师姓名：刘衍文 教授

Emmanuel Monnier 研究员

完成时间：二〇一五年十月

University of Science and Technology of China

A dissertation for doctor's degree

Measurement of the WW production cross-section in Proton-Proton Collisions at $\sqrt{s} = 8$ TeV with the ATLAS Detector

Author : Jun Gao

Speciality : Particle Physics and Nuclear Physics

Supervisor : Emmanuel Monnier

Yanwen Liu

Finished Time : October, 2015

中国科学技术大学学位论文原创性声明

本人声明所呈交的学位论文, 是本人在导师指导下进行研究工作所取得的成果。除已特别加以标注和致谢的地方外，论文中不包含任何他人已经发表或撰写过的研究成果。与我一同工作的同志对本研究所做的贡献均已在论文中作了明确的说明。

作者签名：_____ 签字日期：_____

中国科学技术大学学位论文授权使用声明

作为申请学位的条件之一，学位论文著作权拥有者授权中国科学技术大学拥有学位论文的部分使用权，即：学校有权按有关规定向国家有关部门或机构送交论文的复印件和电子版，允许论文被查阅和借阅，可以将学位论文编入《中国学位论文全文数据库》等有关数据库进行检索，可以采用影印、缩印或扫描等复制手段保存、汇编学位论文。本人提交的电子文档的内容和纸质论文的内容相一致。

保密的学位论文在解密后也遵守此规定。

□公开 □保密 _____ 年

作者签名：_____ 导师签名：_____

签字日期：_____ 签字日期：_____

Contents

Chapter 1 Introduction

1.1 Particles and forces

There are basic quantities known as distance, mass and time. The universe, as far as we know, consists of matter and energy.

The Standard Model (SM), which is formulated in the 1970s, is now a fundamental theory in particle physics. It gives the description of our universe. The SM has been already tested and validated by experiments all over the world and is considered as the most successful model for particle physics. In the SM, fundamental particles consist of quarks, leptons, force-carrying particles and the Higgs (see Figure 1.1). Particles like protons and neutrons are composites of quarks. The anti particles can exist, e.g. the electron's anti-particle is called the positron (anti-electron). The particles can be categorized as follows:

- **Hadrons**
  Composites made of quarks or anti-quarks. Hadrons are held together by gluons which participate in the strong interactions. Reflected in their spin, the hadrons can be categorized to two types: baryons (fermions with odd half-integer spins) and mesons (bosons with integer spins).
- **Leptons**
  Leptons participate in the electro-magnetic and weak interactions. There are three generations of leptons: e, μ, τ and corresponding neutrinos.

There are 4 known forces in nature: gravity, weak, electro-magnetic and strong. All but the gravity are described in the SM. In the Standard Model, a force is described as an exchange of bosons between the objects affected, such as a photon for the electro-magnetic force and a gluon for the strong interaction. Those particles are called force carriers. An detailed description is given below:

- **Electro-magnetic force**
  Mediated by the massless photon. It acts over an infinite range. All charged particles are sensitive to the Electro-Magnetic force.
- **Weak force**
  Mediated by the massive W and Z bosons. It acts over a short range. It may change the types of quarks or leptons, or the so-called flavors.
- **Strong force**
  Mediated by the massless gluon. It can hold quarks together and then form protons and neutrons, which further form the nucleus. The force is stronger than the electro-magnetic force which repels protons. We cannot directly detect

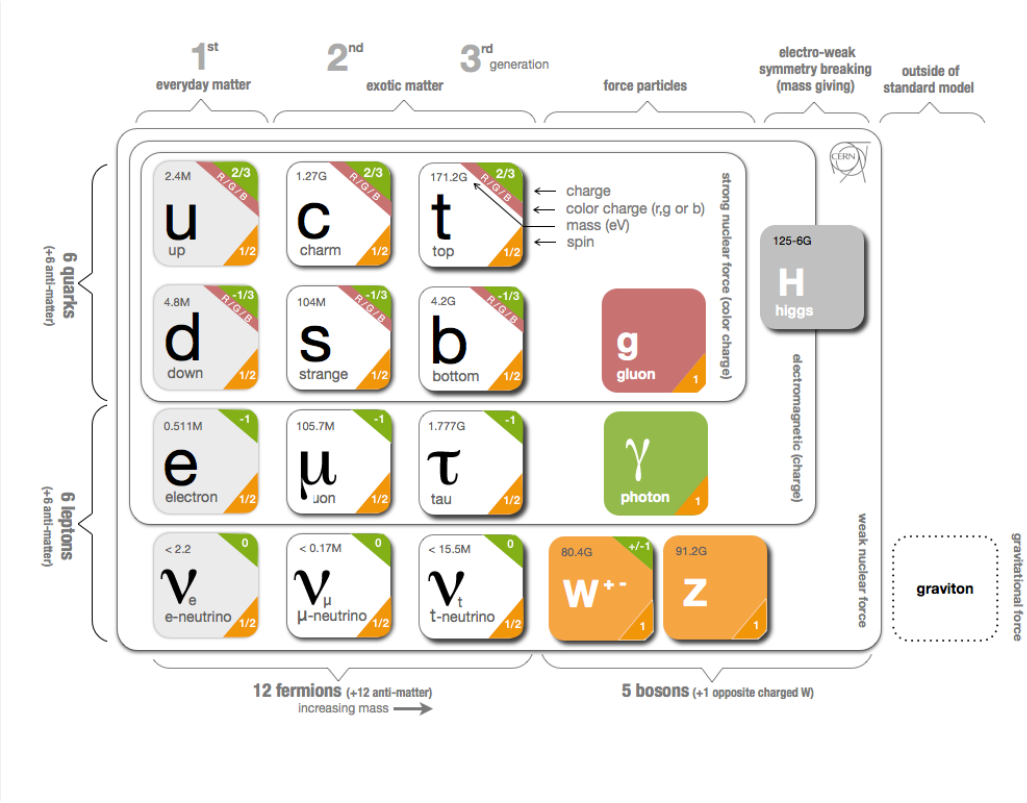

Figure 1.1 Fundamental particles and forces.

a bare quark.

– **Gravity**

Not described in the SM.

The uncertainty relation $\Delta E \Delta t > \frac{\hbar}{2}$ implies that energy does not have to be conserved if the time interval over which it is not conserved is small enough. When the interaction is short enough, two particles can exchange particles and transfer energies. The SM gives us the detailed explanation of the forces. We will go into the details in the following paragraph.

1.2 QCD and strong nuclear force

The special unitary group with degree n ($SU(n)$), is the group of $n \times n$ unitary matrices whose determinant equals to 1. It is a subgroup of the unitary group U(n) which consists of all $n \times n$ unitary matrices. The SU(n) groups find wide applications in the Standard Model of particle physics, e.g. $SU(3)$ in Quantum ChromoDynamics (QCD), which is a theory to describe the strong interactions.

From the Dirac field, we introduce the gauge field G_μ and the interaction between the gauge field and Dirac fermion, then the Lagrangian density can be expressed as the

sum of the free term $\mathcal{L}_0$, the G_μ gauge term $\mathcal{L}_g$, and the interaction term $\mathcal{L}_I$:

$$\begin{aligned}\mathcal{L} &= \mathcal{L}_0 + \mathcal{L}_g + \mathcal{L}_I \\ \mathcal{L}_0 &= \bar{\Psi}(i\gamma^\mu \partial_\mu - M)\Psi \\ \mathcal{L}_g &= -\frac{1}{4} G^A_{\mu\nu} G^{A,\mu\nu} \\ \mathcal{L}_I &= -g J^{A,\mu} G^A_\mu\end{aligned} \tag{1.1}$$

where the g is the $SU(3)$ coupling constant. Let T_i (i=1,2,3...N) be generators of the group with the dimension N.Then the commutation relations are satisfied:

$$[T_A, T_B] = i f^{ABC} T_C$$

where f^{ABC} is the structure constant in the $SU(3)$ group which is anti-symmetric under interchange of any pair of indices. The gauge invariant current:

$$J^{A,\mu} = \bar{\Psi}\gamma^\mu T^A \Psi$$

The tensor fields:

$$G^A_{\mu\nu} = \partial_\mu G^A_\nu - \partial_\nu G^A_\mu - g f^{ABC} G^B_\mu G^C_\nu$$

In this way, the requirement of the local gauge invariance is satisfied. The $SU(3)$ gauge theory is successful in describing the QCD. The quarks are categorized by three colors: red (R), green (G) and blue (B), then the vector field Ψ is three-dimensional. The anti-quarks are assigned to have the complementary colors ($\bar{R}$, $\bar{G}$, $\bar{B}$). We have a set of ways to obtain colorless combinations by mixing colors (quarks) and complementary colors (anti-quarks), e.g. RGB, $\bar{R}\bar{G}\bar{B}$, and $R\bar{R}$.

If Q^2 represents the momenta transferred in the reaction, quarks interact weakly at $Q^2 \to \infty$, allowing perturbative calculations of cross sections in deep inelastic processes of particle physics (It is the so-called asymptotic freedom); and strongly at $Q^2 \to 0$, preventing the unbinding of baryons or mesons, the composite particles of nuclear matter. Although at high energy the quarks are bare and the sum of their masses will be much smaller than the mass of nucleus, we still cannot detect the bare quarks experimentally. Color charged particles cannot be observed directly. They are always bound together to form colorless states. This is called color confinement.

So far we have discussed the QCD and strong interactions. Next we will discuss the electro-weak model.

1.3 Electro-weak model and the Higgs mechanism

1.3.1 $SU(2)_L \times U(1)_Y$ gauge theory

The weak nuclear force exchange particles like W^+, W^- and Z bosons. W^+ is the anti-particle of the W^-, while the Z boson is electrically neutral, and can be considered

itself as its own anti-particle.

The generic field can be divided into left-handed field and right-handed field:

$$\begin{aligned} \Psi &= \Psi_L + \Psi_R = P_L\Psi + P_R\Psi \\ P_L &= \frac{1-\gamma_5}{2} \\ P_R &= \frac{1+\gamma_5}{2} \end{aligned} \tag{1.2}$$

where γ_5 is the chiral operator and the P_L and P_R are projector operators for the left-handed and the right-handed respectively.

Only left-handed current participates in the weak interactions. For left-handed state we can introduce $SU(2)_L$, with which the conserved quantum number is T_3 which is the third component of the isospin T. For both left-handed and right-handed state we introduce $U(1)_Y$, where the conserved quantum number is the weak hyper-charge Y. The introduction of the $U(1)_Y$ symmetry is done to absorb the charge Q so that the weak and electro-weak interactions can be unified, which will be seen later.

The electro-weak model in the SM is based on $SU(2) \times U(1)$. Initially the Lagrangian contains three massless bosons W^i (i=1,2,3) associated with $SU(2)$ group, and the massless boson B associated with $U(1)$ group. Denote the $SU(2)$ gauge coupling as g_W and the coupling of the $U(1)$ group as g'_W. The Lagrangian of the gauge bosons is written as:

$$\mathcal{L} = -\frac{1}{4}W^{i,\mu\nu}W^i_{\mu\nu} - \frac{1}{4}B^{\mu\nu}B_{\mu\nu} \tag{1.3}$$

where the field strength tensors of the $U(1)$ gauge field B and the $SU(2)$ gauge fields W^i are defined as:

$$\begin{aligned} W^i_{\mu\nu} &= \partial_\mu W^i_\nu - \partial_\nu W^i_\mu - g_W\epsilon^{ijk}W^j_\mu W^k_\nu \\ B_{\mu\nu} &= \partial_\mu B_\nu - \partial_\nu B_\mu \end{aligned} \tag{1.4}$$

where ϵ^{ijk} is the tensor. The coupling of the gauge fields to fermionic matter fields is implemented using the covariant derivative:

$$D^\mu = \delta_{ij}\partial^\mu + ig_W(T\cdot W^\mu)_{ij} + iY\delta_{ij}g'_W B^\mu \tag{1.5}$$

Define

$$\begin{aligned} T^\pm &= \frac{1}{\sqrt{2}}[T^1 \pm iT^2] \\ W^\pm_\mu &= \frac{1}{\sqrt{2}}[W^1_\mu \mp W^2_\mu] \end{aligned} \tag{1.6}$$

Then from the terms quadratic in the vector boson fields, we therefore derive the gauge fields W and B which are expressed in terms of the observable vector bosons W, Z and A

$$
\begin{aligned}
W_\mu^1 &= \frac{1}{\sqrt{2}}(W_\mu^+ + W_\mu^-) \\
W_\mu^2 &= \frac{i}{\sqrt{2}}(W_\mu^+ - W_\mu^-) \\
W_\mu^3 &= cos\theta_w Z_\mu + sin\theta_w A_\mu \\
B_\mu &= -sin\theta_w Z_\mu + cos\theta_w A_\mu
\end{aligned}
\tag{1.7}
$$

where θ_w is the Weinberg mixing angles.

Then from the following relations:

$$
\begin{aligned}
g_W &= \frac{e}{sin\theta_w} \\
g'_W &= \frac{e}{cos\theta_w}
\end{aligned}
\tag{1.8}
$$

The left-handed fermion fields of the i^{th} fermion family transform as doublets:

$$
\psi_i = \begin{pmatrix} \nu_i \\ l_i^- \end{pmatrix} \text{ and } \begin{pmatrix} u_i \\ d'_i \end{pmatrix}
$$

under $SU(2)$, where $d'_i = \sum_j V_{ij} d_j$ and V is the mixing matrix which will be talked about later. The lagrangian for the fermions Ψ_i is

$$
\begin{aligned}
\mathcal{L}_F = &\sum_i \bar{\Psi}_i (i\partial\!\!\!/ - m_i - \frac{m_i H}{v})\Psi_i - e\sum_i Q_i \bar{\Psi}_i \gamma^\mu \Psi_i A_\mu \\
&- \frac{g_W}{2cos\theta_W} \sum_i \bar{\Psi}_i \gamma^\mu (g_V^i - g_A^i \gamma^5)\Psi_i Z_\mu \\
&- \frac{g_W}{2\sqrt{2}} \sum_i \bar{\psi}_i \gamma^\mu (1-\gamma^5)(T^+ W_\mu^+ + T^- W_\mu^-)\psi_i
\end{aligned}
\tag{1.9}
$$

Where $g_V^i = T_3^i - 2Q_i sin^2\theta_W$ and $g_A^i = T_3^i$. H is the Higgs scalar which will be discussed in the next section.

Through the above relations, we can see that the model introduces the photon field A and fields of the gauge bosons W and Z. It describes the interaction between these bosons and the matter field. The W and Z bosons are the elementary particles that mediate the weak interaction. They are regarded as the intermediate vector bosons. The W bosons have a positive and negative electric charge of 1 respectively and are each other's antiparticles. The Z boson is electrically neutral and is its own antiparticle. The three particles have a spin of 1. All three of these particles are very short-lived with a half-life of about 3×10^{-25} s. By now we have a good description of these fields.

But there is more to be discussed. The mass terms of gauge bosons W and Z are not given. What's more, the renormalization of the theory is not guaranteed. We have to find a way to answer these questions without breaking the gauge symmetry of the Lagrangian.

1.3.2 The Higgs mechanism

Despite the fermion field Ψ, we can introduce a boson field Φ. From this spin-0 complex field, together with the gauge field B_μ and the covariant derivative D_μ, the Lagrangian has the following form

$$\mathcal{L} = (D^\mu \Phi^\dagger)(D_\mu \Phi) - \mu^2 \Phi^\dagger \Phi - \lambda(\Phi^\dagger \Phi)^2 \tag{1.10}$$

In order to satisfy the $SU(2)_L \times U(1)_Y$ spontaneous symmetry breaking, we need to introduce scalar fields. Since we desire to end up with three heavy vector bosons associated with the weak interactions and a massless vector boson (photon), so we require four independent scalar fields. The simplest choice is a doublet of complex scale fields with one charged and one neutral.

$$\Phi = \begin{pmatrix} \phi^+ \\ \phi^0 \end{pmatrix} = \begin{pmatrix} \phi_1^+ + i\phi_2^+ \\ \phi_1^0 + i\phi_2^0 \end{pmatrix} \tag{1.11}$$

For the vacuum state, we can specify a direction.

$$\Phi^0 = \begin{pmatrix} 0 \\ \frac{v}{\sqrt{2}} \end{pmatrix}, \qquad v = \sqrt{\frac{-\mu^2}{\lambda}} \tag{1.12}$$

and the fields can be re-expressed as

$$\begin{aligned} \Phi &= \begin{pmatrix} 0 \\ \frac{v+H(x)}{\sqrt{2}} \end{pmatrix} \\ D_\mu \Phi &= \frac{1}{\sqrt{2}} \begin{pmatrix} \frac{ig}{\sqrt{2}} W_\mu^+ (v+H) \\ \partial_\mu H - \frac{ig}{\sqrt{2}} Z_\mu (v+H) \end{pmatrix} \end{aligned} \tag{1.13}$$

apply it in the Lagrangian, then we get the mass terms for the bosons:

$$m_W = \frac{gv}{2}, \qquad m_Z = \frac{m_W}{cos\theta_W}, \qquad m_H = \sqrt{-2\mu^2} \tag{1.14}$$

The Higgs mechanism indicates that, the vacuum is filled with the Higgs field. Bosons and fermions couple with Higgs field and obtain masses. The photon and gluon fields are not coupling with the Higgs field, so they are still massless. The Higgs field is a scalar field. The Higgs boson has no spin and acts as its own antiparticle. It is CP-even, and has zero electric and colour charge.

Furthermore, the leptons and quarks can acquire their masses from the Higgs mechanism by Yukawa Couplings. For example, for the first generation leptons, we can add an interaction term into the Lagrangian:

$$\mathcal{L}_e = -G_e(\bar{e}_R \Phi^\dagger l_L + \bar{l}_L \Phi e_R) \quad l_L = \begin{pmatrix} \nu_e \\ e \end{pmatrix}_L \tag{1.15}$$

where $G_e = 2.9 \times 10^{-6}$ represents the coupling constant between the electron field and the Higgs field. And the electron mass

$$m_e = \frac{G_e v}{\sqrt{2}}$$

Similarly, for the second and third generation we introduce the coupling constants G_μ and G_τ, then μ and τ can acquire masses. In the SM, neutrinos are considered to be massless, and right-handed neutrinos do not exist.

Returning now to the weak interactions, we generalize the Cabibbo schema by assuming that the eigen states of the weak interactions are a mixture of mass eigen states for the down-type quarks.

$$\begin{pmatrix} d' \\ s' \\ b' \end{pmatrix}_L = V \begin{pmatrix} d \\ s \\ b \end{pmatrix}_L \qquad (1.16)$$

$$V = \begin{pmatrix} V_{ud} & V_{us} & V_{ub} \\ V_{cd} & V_{cs} & V_{cb} \\ V_{td} & V_{ts} & V_{tb} \end{pmatrix}$$

where V is the Cabbibo-Kobaiashy-Maskawa (CKM) matrix. The elements of the matrix are complex. Experimentally the diagonal elements V_{ud}, V_{cs} and V_{tb} are clearly dominant while the rest are small. This implies, for example, that the charm particles preferentially decay into strange particles. Now we have a complete description of the quark mixing.

1.3.3 Vector boson pair production

A W boson can decay into a lepton and a neutrino. It can also decay to an up-type quark and a down-type quark. The decay width of the W boson to a pair of quark and anti-quark is proportional to the corresponding squared CKM matrix element and the number of quark colours, $N_C = 3$. The unitarity of the CKM matrix implies that:

$$|V_{ud}|^2 + |V_{us}|^2 + |V_{ub}|^2 = |V_{cd}|^2 + |V_{cs}|^2 + |V_{cb}|^2 = 1.$$

Therefore the leptonic branching ratios of the W boson are approximately $Br(e^+\nu_e) = Br(\mu^+\nu_\mu) = Br(\tau^+\nu_\tau) = \frac{1}{9}$. The hadronic branching ratio is dominated by the CKM-favored $u\bar{d}$ and $c\bar{s}$ final states. The sum of the hadronic branching ratios has been measured experimentally to be $67.60 \pm 0.27\%$, and the branching ratios of leptonic decays are measured to be $Br(l\nu_l) = 10.80 \pm 0.09\%$ [1].

Vector boson pair production is one of the most important electroweak processes. Among the massive vector boson pair production reactions, W^+W^- has larger cross section than WZ and ZZ production. The SM description of electroweak and strong interactions can be tested through precision measurements of the W^+W^- production cross section at hadron colliders.

At the collider experiment the W boson pairs can be produced in two different processes, via quark-quark annihilation and gluon-gluon fusion. The Standard Model with its gauge symmetry in the electro-weak sector makes precise predictions for the $WW\gamma$ and WWZ couplings. So the measurement of the WW cross section can offer a good test of the Standard Model. Any deviation from SM expectations in the measured production rates and possible changes in certain kinematic distributions of vector boson pairs or their decay products could provide first evidence for effects from physics beyond the SM at high-energy scales. New physics processes that alter the W^+W^- production at high mass scales can be described by operators with mass dimension higher than four in an effective field theory (EFT) framework. In addition the pair production of W bosons is one of the most important background processes for the study of the Higgs boson and the search for the new physics beyond the SM, such as the search for super-symmetric particles.

The W bosons can not be observed directly with the detector, since they will decay into other particles very soon. A W boson can decay into two quarks which is reconstructed as jets in the detector, and it may also decay into a lepton plus a neutrino. Other particles produced in pp collisions can lead to similar final states as the W boson pair production. In normal cases, the final states will consist of quarks and since the direct production of quarks happens more than one million times more often than the pair production of W bosons, it is uneasy to distinguish the W bosons which decay into quarks from direct quark production. After all, the final states with di-electron, di-muons or an electron and a muon, are the ideal choice to analyze the WW production. The details will be stated later.

In ATLAS, Four separate analyses of leptonic WW decay modes have been published so far. First analysis on the 2010 dataset at 7 TeV (first LHC data) is published as a paper with very limited statistics (34 pb^{-1}) [2]. In the following year two analyses have been published, with one on 1.02 fb^{-1} [3] and the other on the full 2011 data 4.64 fb^{-1} [4], which gives measured cross section 51.9 ± 2.0(stat)± 3.9(syst)± 2.0(lumi) compared with the SM prediction $44.7^{+2.1}_{-1.9}$ pb. WW cross section is also measured by the CDF and D0 experiments at the Tevatron collider at 1.96 TeV and compared to the SM prediction 12.0 ± 0.7 pb. CDF shows the measured cross section 12.1 ± 0.9 (stat) $^{+1.6}_{-0.4}$(syst) pb [5]. DO shows the measured cross section 11.5 ± 2.1 (stat+syst) ± 0.7

(lumi) pb [6].

1.4 From SM to the accelerator physics

The $SU(2)_L \times U(1)_Y$ gauge theory model and the spontaneous symmetry breaking combine the electro-magnetic interactions and explain the weak interactions mediated by massive $W^{\pm}$ and Z bosons. Nevertheless, the SM still have problems. We list some problems as follows.

- The SM does not explain why Higgs mass is so much smaller than the Planck mass. It is called the hierarchy problem.
- Gravity is not included in the SM. Unlike the strong or electro-weak interactions which have been described by the SM, it is not described in the SM.
- Neutrinos are massless in the SM, which is not consistent with experimental results.
- The SM cannot explain the observed cold dark matter or dark energy. So as to the universe, the SM is not providing a well-described theory to explain the mass or the energy of the universe.

These unanswered questions motivate studies of the physics beyond the standard model (BSM). This is one of the most important motivations why we design collider experiments. About 100 years ago, Ernest Rutherford used nucleus of helium to hit the target nucleus, and found out that the atom's mass is concentrated in a region about 1/100,000 of the atom's radius. Now we have accelerators to produce particle beams with high energy. One of the most important accelerators and colliders, the Large Hadron Collider (LHC), will offer us a chance to test our understanding of the SM and search for the physics beyond the SM.

The theoretical calculations of the physics processes in hadron colliders are sophisticated due to the complicated structure of the colliding hadrons. In 1969 Richard Feynman proposed the parton model to analyze the high energy hadron collisions. He suggested that a hadron is composed of a number of point-like constituents called partons. The QCD factorization theorem states that the cross sections for high energy hadronic reactions with a large momentum transfer scale Q^2 can be factorized into a parton-level hard scattering convoluted with the Parton Distribution Functions (PDFs). The PDF acts as a connection between the partons and the original hadrons. For example, the PDF $f_{(a/A)}(x_a, Q^2)$ express the probability density that a parton a with energy fraction x_a is extracted from the original incoming hadron A. Then for the scattering of two hadrons A and B which produce a final state X, the cross-section can be written as

$$\sigma_{AB} = \sum_{a,b} \int_0^1 dx_a \int_0^1 dx_b f_{(a/A)}(x_a, Q^2) f_{(b/A)}(x_b, Q^2) \sigma(ab \to X) \tag{1.17}$$

The typical Q^2 in the hard scattering process is much larger than QCD scale $\Lambda^2_{QCD} \approx 200$ (MeV/c)^2. The parton-level hard scattering cross-section can be calculated perturbatively in QCD to $O(\alpha_s^n)$, while the parton distribution functions parameterize the non-perturbative aspect. Denote μ_F as the factorization scale which separates hard and soft physics and μ_R as the renormalization scale which is associated with the running coupling. Normally the values of μ_F and μ_R are chosen to be the order of the typical momentum scales of the hard scattering processes. For example, for Drell-Yan process ($f\bar{f} \to Z/\gamma^* \to l^+l^-$), the standard choice is $\mu_F = \mu_R = m_{l^+l^-}$.

Experimentalists usually rely on phenomenological models (parton shower and hadronisation models) to describe the radiation of the outgoing partons and their hadronisation into final state particles, on a statistical basis (Monte Carlo techniques). Parton showers refer to cascades of radiation produced from QCD processes and interactions. in order to calibrate and interpret (and thus understand) processes in collider experiments, they are simulated extensively in Monte Carlo event generators. The Monte Carlo method is fundamentally a technique for numerical integration using random numbers, or, in practice, numbers from a pseudorandom number generator. To predict the scattering cross section for a collider process, one must integrate the probability density, given by a quantum mechanical matrix element-squared, over the phase space of the process. With these methods, physics events can be described in a fully exclusive way in terms of a complete set of final state particles, which is particularly useful since they can be used directly as inputs to the detector simulation, where every single particle should be traced through the detector.

At a collider, the event rate R is the product of the interaction cross-section σ and the instantaneous Luminosity $\mathcal{L}$:

$$R = \sigma \times \mathcal{L} \tag{1.18}$$

For two high energy colliding beams with a simplified situation, with frequency f and n_1, n_2 particles for each beam, we can write the instantaneous Luminosity as:

$$\mathcal{L} = f \frac{n_1 n_2}{4\pi \sigma_x \sigma_y} \tag{1.19}$$

where the cross section σ_x and σ_y characterize the transverse beam profiles in the horizontal and vertical directions. The beam size is given by $\sigma_{x,y} = \sqrt{\beta_{x,y} \cdot \epsilon_{x,y}}$, with $\epsilon_{x,y}$ the transverse emittance which describes the quality of the injected beam and is normally constant along the beam trajectory and β the amplitude function (beta-function) which is the envelope of the motion of the particles. [1]

Then we integral the instantaneous Luminosity and then the all number of events can be written as:

$$N = \sigma \int \mathcal{L} dt \tag{1.20}$$

The Large Hadron Collider (LHC) provides proton-proton collisions at a designed luminosity of 10^{34} cm^{-2}s^{-1}, which is mostly a proton-proton collider. One of the most important goals of LHC is to search for the new physics beyond the SM using proton collisions and heavy ion collisions. The details will be introduced in the next chapter. LHC and other experiments have produced fruitful results in the past years. One example it the production cross sections of main SM processes in pp or $p\bar{p}$ collisions. The SM proton-(anti)proton cross sections as a function of collider energy is shown in Figure 1.2. The cross-sections are calculated with Next-Leading-Order (NLO) or Next-to-Next-Leading-Order (NNLO) [7].

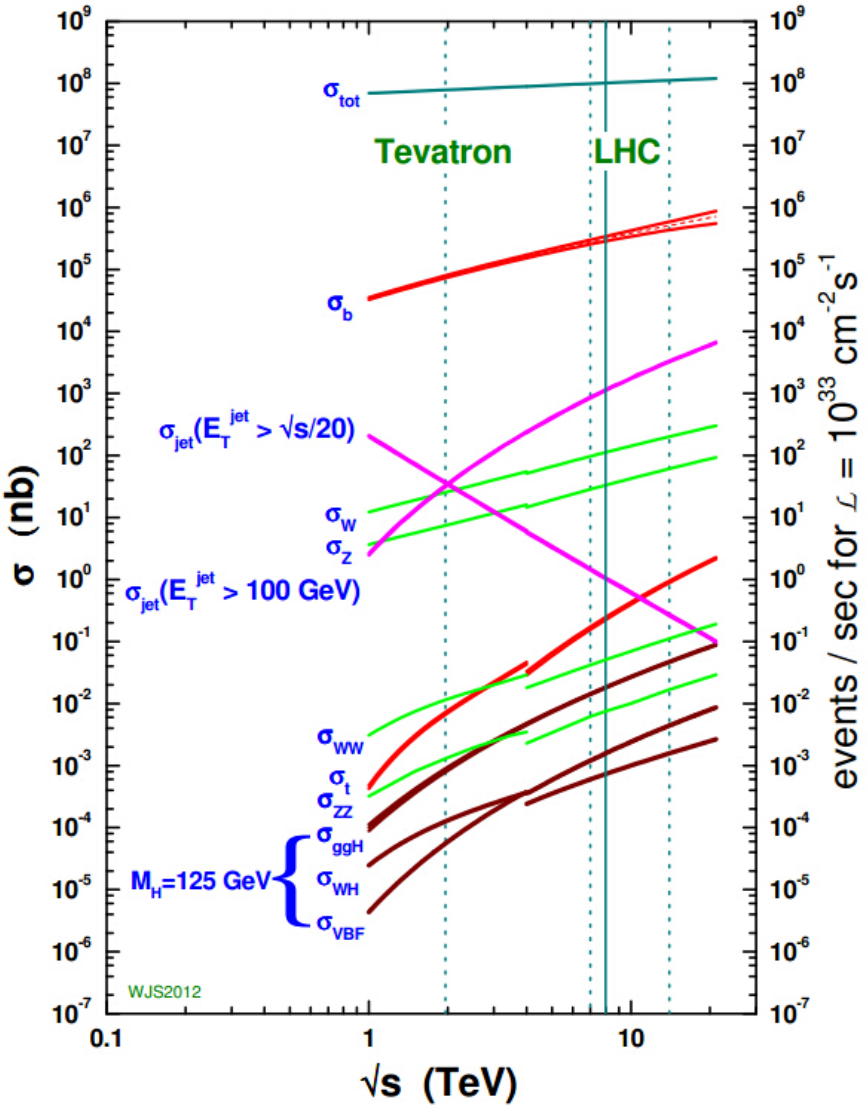

Figure 1.2 The SM proton-(anti)proton cross sections for LHC and Tevatron experiment as a function of collider energy.

Chapter 2 The framework of LHC and ATLAS experiment

2.1 LHC and ATLAS overview

The LHC is located at the boarder of France and Switzerland. It is currently the world's largest two-ring hadron collider built up by CERN. The project for LHC was approved in December 1994. The important history of the LHC can be summarized as follows.

- **Late 2008-2009**
  Startup of LHC and first collisions at center of mass energy of 0.9 TeV and later at 2.36 TeV.
- **March 2010, Run 1**
  First collisions at center of mass energy of 7 TeV.
- **March 2012, Run 1**
  First collisions at center of mass energy of 8 TeV.
- **April 2015, Run 2**
  First collisions at center of mass energy of 13 TeV.
- **Next 15-20 years**
  Continue data taking.

The accelerator is installed underground. It is in the tunnel which is as long as 27 km. Four experiments sit on separate points around the underground accelerator ring (see Figure 2.1). Particles will be accelerated before entering the large ring at LHC. At first the particles are accelerated to 50 MeV at Linac2 machine, and then the proton synchrotron booster (PSB) will accelerate to 1.40 GeV. The chain continues with the proton synchrotron (PS) accelerating to 26 GeV. Finally the super proton synchrotron (SPS) will accelerate up to 450 GeV and particles enter into the LHC ring. There are 2 general-purpose detectors at the LHC, ATLAS and CMS, and 2 dedicated detectors, ALICE for studying heavy ion collisions and LHCb for studying the flavor physics. The LHC was designed with the latest technology and engineering process. One important goal is to probe the physics beyond the SM using proton collisions and heavy ion collisions.

Two beams circulating in opposite directions collide at the geometrical center of the detectors. Practically the bunch collisions will occur every 50 ns (and will be in a near future at 25 ns), which is a challenge for detectors to record this intensive collision. The luminosity is a key feature for colliders, which is a function of the geometrical characteristics of the colliding bunches and of the machine parameters. The luminosity

of the ATLAS detector can be written as: [8]

$$L = \frac{\gamma_r f_{rev} k_b n_1 n_2}{4\pi\epsilon^*\beta^*} F(\theta_c, \sigma_z, \sigma^*) \tag{2.1}$$

where γ_r is the relativistic γ-factor, f_{rev} is the revolution frequency, k_b is the number of colliding bunches, n_i is the number of particles per bunch in each colliding beam, ϵ^* is the root-mean-square normalized transverse emittance ϵ , β^* is the value of the beta-function β at the collision point, and F is the geometrical luminosity reduction factor due to the crossing angle at the interaction point, which is the function of the crossing angle θ_c, the transverse and longitudinal root-mean-square dimensions of the colliding bunches σ^* and σ^z:

$$F(\theta_c, \sigma_z, \sigma^*) = \frac{1}{\sqrt{1 + (\frac{\theta_c \sigma_z}{2\sigma^*})^2}} \tag{2.2}$$

In 2012, the nominal luminosity is at the level of 10^{34} cm^{-2} s^{-1}. With the high center-of-mass energy and high luminosity as described above, approximately 600 million times per second particles collide in LHC. Each collision generates particles that often decay in complex ways into even more particles. Physicists need to deal with this huge amount of data to find out interesting results. The Worldwide LHC Computing Grid (WLCG) is a global computing infrastructure aiming to support people with computing resources. It is very helpful for analyzers to store and analyse the data recorded by LHC. Wherever the analyzers are, they can get access to the data. WLCG is coordinated by CERN and functioning well in the LHC experiments.

ATLAS is one of the four experiments at LHC. It is as long as 45 m and as high as 25 m. The total weight is about 7000 tons. It is designed for the physics processes at high energy, which are less likely to be produced by previous accelerators with lower center-of-mass energy. This experiment is also designed to look for interesting facts beyond the SM. It is now attracting physicists and engineers from more than 30 countries to work together.

The ATLAS experiment adopts a right-handed Cartesian coordinate system. The z-axis is defined using the beam direction, and the positive z-axis is defined counter-clockwise on the LHC ring. Starting from the interaction point, the positive x-axis is defined as pointing to the center of the LHC ring. The positive y-axis is the upward direction. The angle with respect to the beam axis is the polar angle θ. And in most cases this angle is expressed by the other term, which is called pseudo-rapidity $\eta = -\ln\tan(\frac{\theta}{2})$. And $\Delta R = \sqrt{\Delta\eta^2 + \Delta\phi^2}$ is defined to describe the distance between two directions in $\eta - \phi$ plane.

In the Run 1, the luminosity is measured with forward detectors and calibrated with Van De Meer scans [9] [10], during the data-taking, the peak luminosity can reach

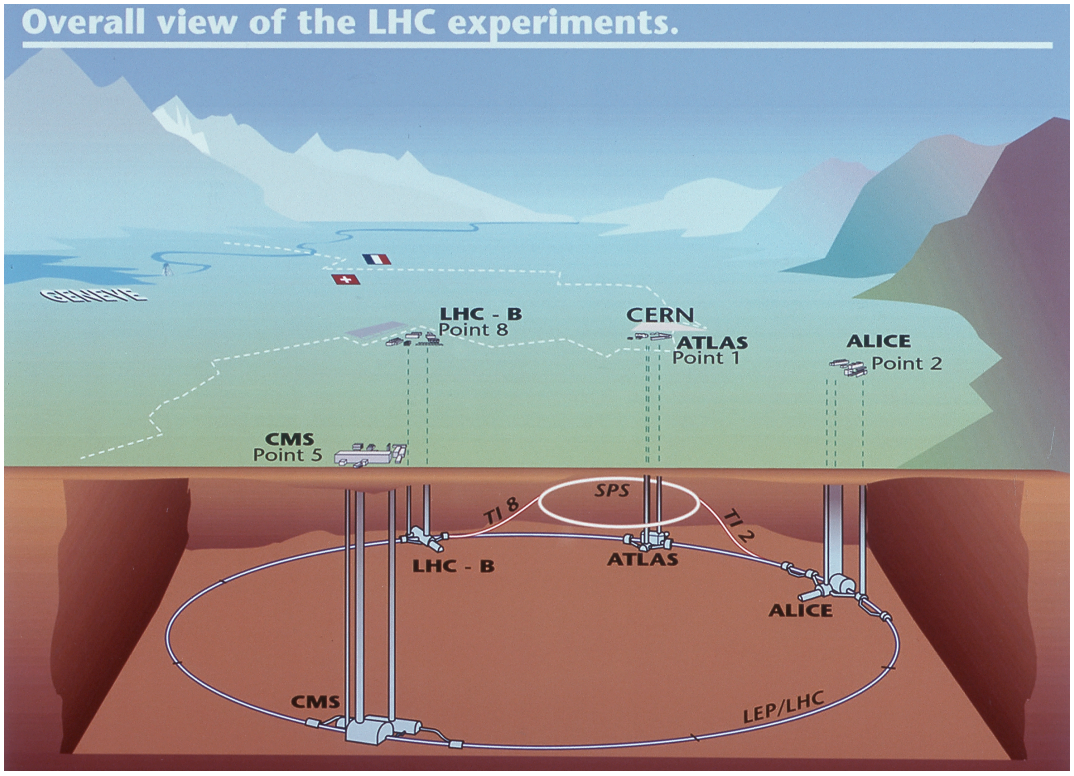

Figure 2.1 LHC experiments.

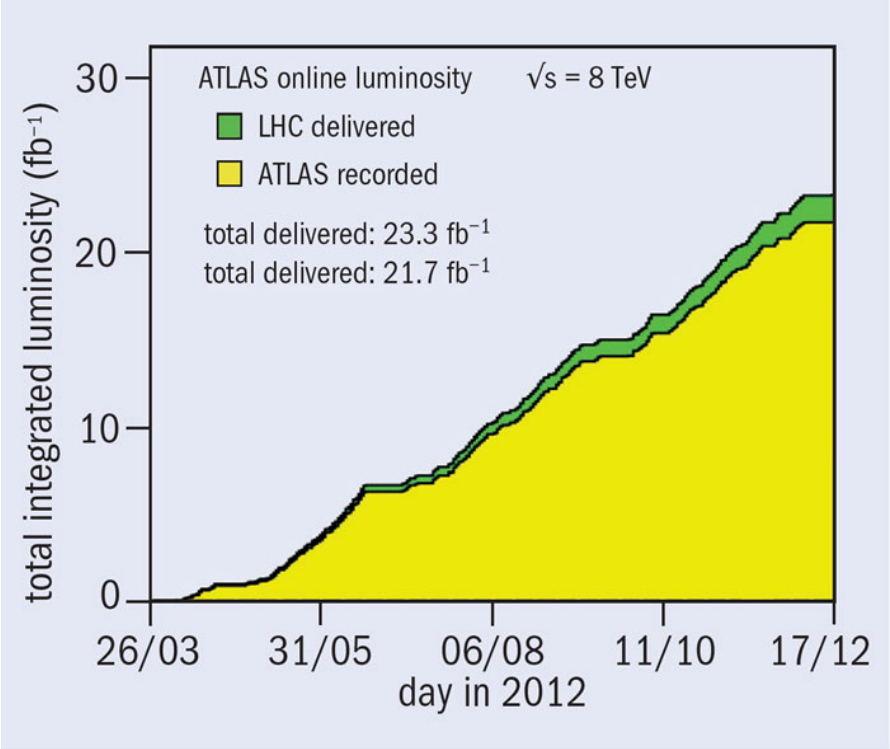

Figure 2.2 Integrated Luminosity of ATLAS in 2012.

7.7×10^{33} cm^{-2} s^{-1}. Figure 2.2 shows the integrated luminosity in 2012. The ATLAS data-taking efficiency for 2011(2012) is 93.0%(93.1%). The fraction of data with good enough quality for physics studies is 90.0%(95.8%). High data quality was partially due to the efficiency recovery from data processing. Given the high data quality efficiency, we use a common set of Good Quality Data across the analyses. Overall 88% of delivered luminosity is used for ATLAS physics analysis. With such a high luminosity, 2012 data-taking is in a high pileup environment (about factor 2 higher than in 2011) with sizable impacts on physics, such as jets, missing transverse energy and tau reconstruction, as well as on trigger rates and computing. The pileup affects the physics object reconstruction and degrades the performance. ATLAS optimized the reconstruction in 2012 to reduce the dependence versus the number of interactions per bunch crossing. The performance for the objects is also outstanding. For leptons, the energy resolution is obtained from $Z \rightarrow ll$ lineshape fit. Electron energy resolution is typically 2% for $p_{\mathrm{T}} > 25$ GeV. Muon momentum resolution is typically 3% in most of the p_{T} spectrum and up to 10% for 1 TeV [11]. Jet energy calibration is based on the studies of the di-jet, γ+jet, Z+jet, and multi-jet. Precise knowledge of the Jet Energy Scale (JES) and Jet Energy Resolution (JER) and its uncertainties has been achieved, which are used in the physics analysis. The detector provided performance characteristics very close to its design values.

The overall ATLAS detector is shown in the Figure 2.3. The sub-detector which is closest to the interaction point is the inner detector, which is immersed in a 2 T solenoidal field. There are also toroid fields, 0.5 T in the barrel and 1 T in the end-cap. The inner detector can cover up to $|\eta| \leq 2.5$. Outside the inner detector, the electro-magnetic calorimeter covers $|\eta| \leq 3.2$ and is based on the Liquid argon (LAr) technology. Behind it, the hadronic calorimeter in $|\eta| \leq 1.7$ is based on the scintillator-tile technology, while in the end-caps $|\eta| \geq 1.5$ it is also using LAr technology. The LAr forward calorimeters provide both electro-magnetic and hadronic energy measurements and extend the coverage to $|\eta| \leq 4.9$. The outmost sub-detector, muon spectrometer, surrounds the calorimeter and has three layers of high precision tracking chambers covering $|\eta| \leq 2.7$. The different components of the ATLAS detector allows us to measure the characteristics of the particles out of the collisions, as shown in the Figure 2.4 and as developed in the following sections.

2.2 Inner detector

The inner detector combines high-resolution sub-detectors from small radius to large radius, as shown in the Figure 2.5 and Figure 2.6. The pixel detectors cover 50.5 mm $-$ 149.6 mm with highest granularity, the silicon microstrip layers (SCT) covers

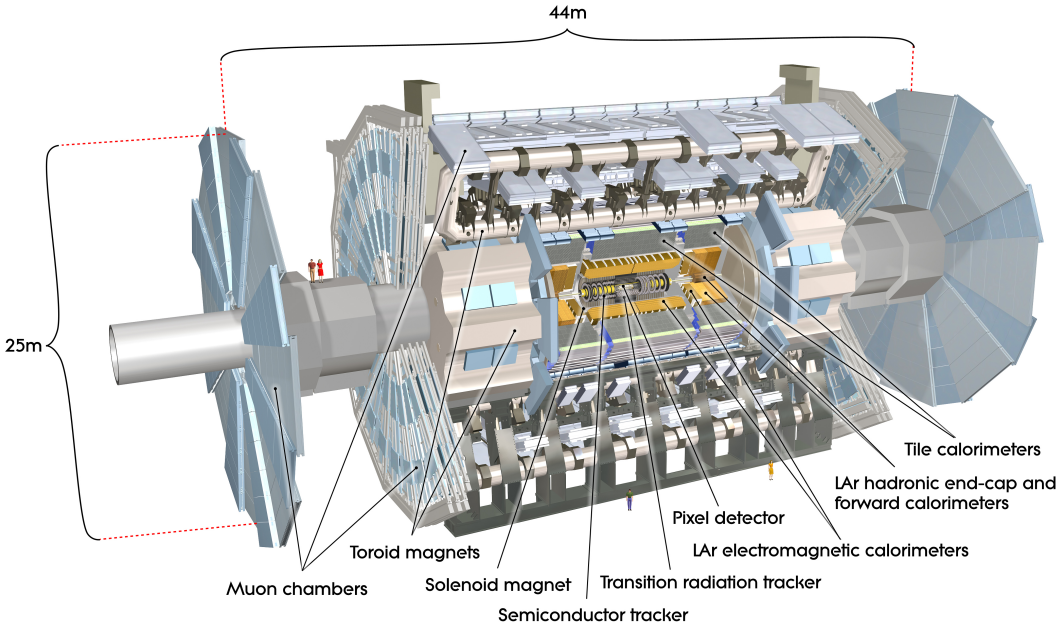

Figure 2.3 Overview of the ATLAS detector. [12]

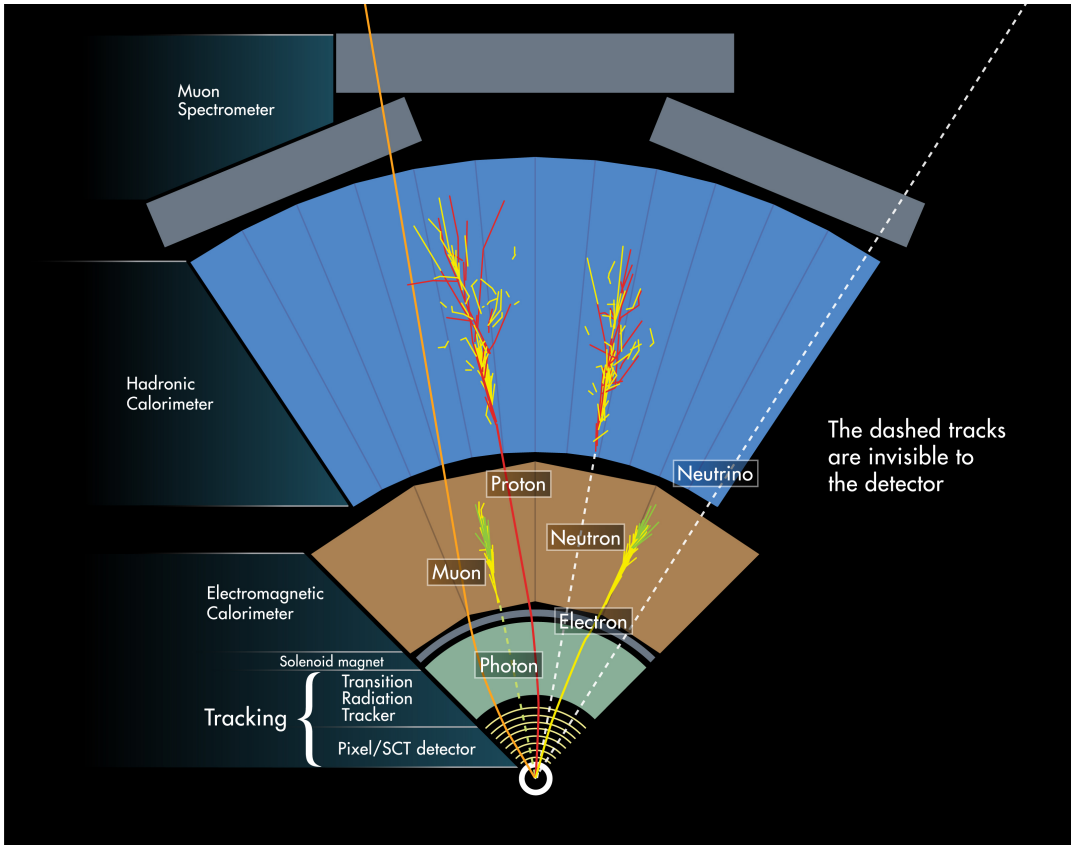

Figure 2.4 Wedge view of the ATLAS detector.

299 mm − 560 mm, and the transition radiation tracker (TRT) covers 563 mm − 1066 mm. The precision tracking detectors (pixel and microstrip) cover $|\eta| \leq 2.5$, which are divided into barrel ($|\eta| \leq 1.4$) and end-caps ($1.4 \leq |\eta| \leq 2.5$). Track reconstruction has been demonstrated to be down to a p_{T} near 100 MeV and insensitive to pile-up [13].

The high-radiation environment imposes stringent requirements on the inner detector sensors, detector electronics, mechanical structure and services. Since the detectors are designed for the lifetime of over ten years, the quality of each component must be satisfied. The pixel inner vertex layer must be replaced after approximately three years of operation at design luminosity. The other pixel layers and the pixel disks must withstand about 1 MeV neutron equivalent fluence F_{neq} of up to 8×10^{14} cm^{-2}. And F_{neq} is obtained by convoluting the various particle energy spectra and fluences with silicon displacement damage functions, normalised using the non-ionising energy loss cross-sections to the expected damage of 1 MeV neutrons. The innermost parts of SCT must withstand F_{neq} of up to 8×2^{14} cm^{-2}. To maintain the adequate noise performance after radiation damage, the silicon sensors are kept at low temperature. In contrast, the TRT is designed to be operated at room temperature.

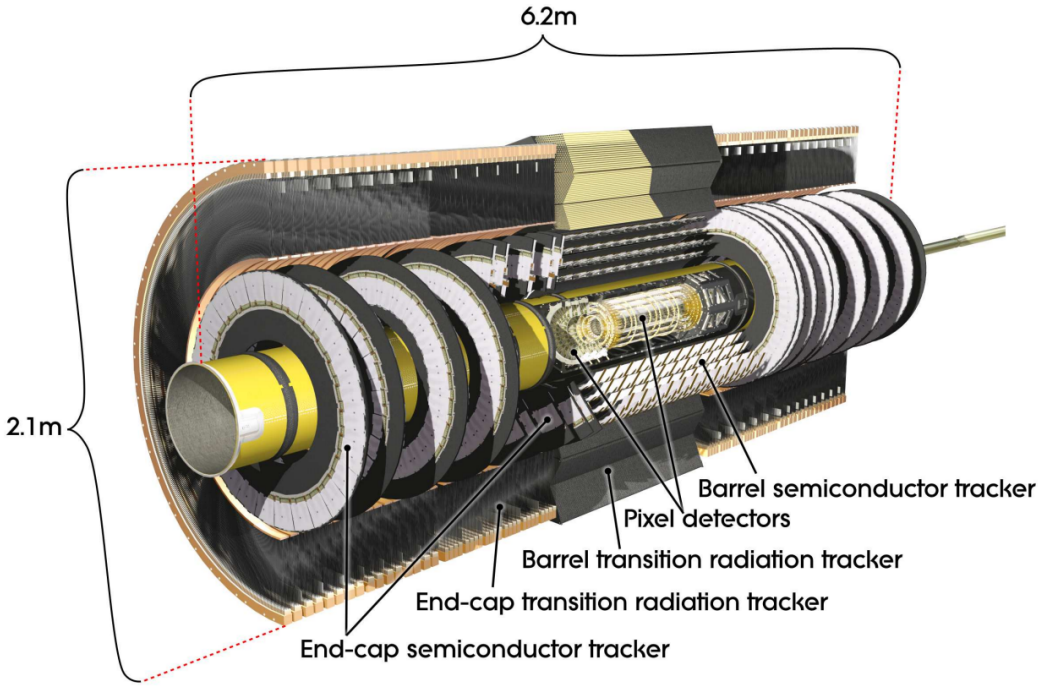

Figure 2.5 Cut-away view of of the ATLAS inner detector. [12]

2.2.1 Solenoid magnet

A hollow cylindrical coil is built up for a large electrical current, which can provide a 2 T magnetic field parallel to the beam axis. The central solenoid is as long as 5.3 m

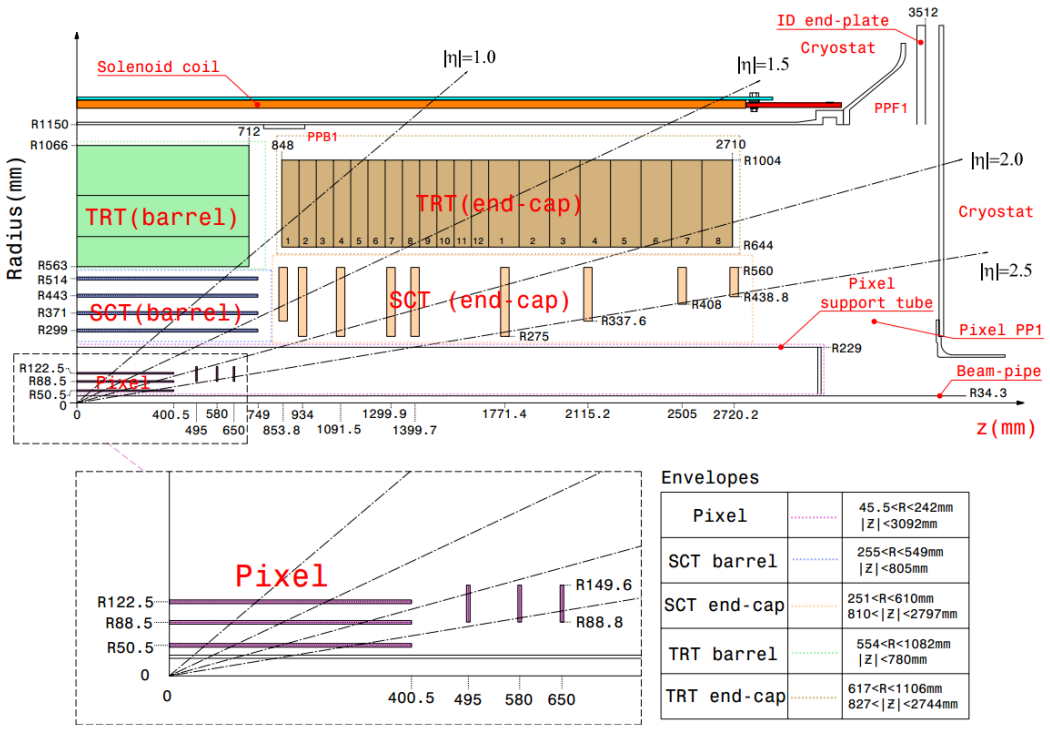

Figure 2.6 Detailed information of the ATLAS inner detector. [12]

and its diameter is 2.4 m. The magnetic field deflects the charged particles. If a particle has small transverse momentum, it will be captured inside the detector, while a particle with a large transverse momentum is able to go outside the inner detector unless they are absorbed or deflected.

2.2.2 Pixel detectors

The sensors closest to the beam pipe are the pixel detectors. There are several layers of rectangular silicon (pixels), which are placed cylindrically. The innermost layer is called the B-layer. A signal will come out that identifies certain pixel has been traversed, as long as a charged particle goes through a layer. Therefore, a precise position can be derived. The system has 1744 modules. Each module is 62.4 mm long and 21.4 mm wide with 46080 pixel elements read out by 16 chips, each serving an array of 18 $\times$ 160 pixels. The modules are overlapped for hermetic measurement, and the pixels are able to cover an area of 1.7 m^2.

During the entire LHC Run 1, the pixel detector has shown a data taking efficiency of 99.9% (Figure 2.7) [13] and radiation effects were found to be within expectations. In Run 1, 5% of pixel modules have been progressively disabled; their failures were found to be highly correlated to thermal cycling.

The definition is impact parameters Z_0 and d_0 is useful for describing tracks and

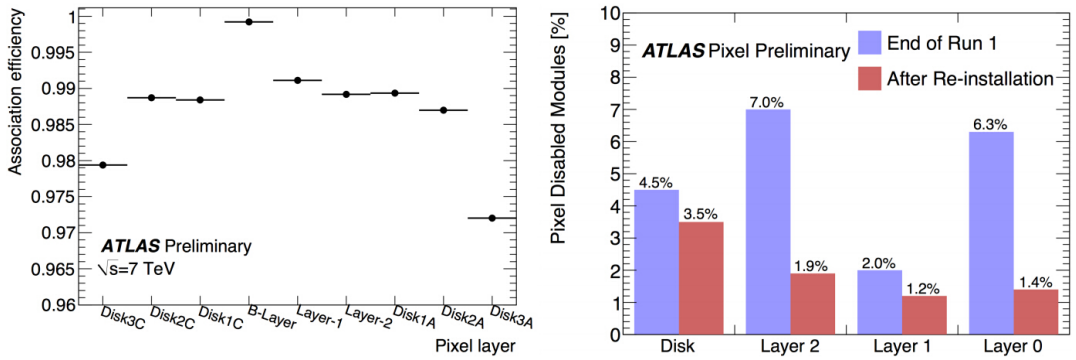

Figure 2.7 Left: efficiency for a track to have a hit associated when crossing a Pixel Detector layer. The full efficiency of B-Layer is due to the track selection, the lower efficiency for the most external disks is mainly due to inefficient regions on some modules. Right: percentage of disabled modules at the end of Run 1 and after the re-insertion of Pixel Detector into the ATLAS Experiment for disk and three layers.

vertices. Considering a track and its point of closest approach to the beam line, the transverse impact parameter d_0 is the radial coordinate of this point, while the longitudinal impact parameter z_0 is the z-coordinate of this point. In practical, the $z_0 \times sin\theta$ is more often used than z_0 in analysis since the z-resolution if the inner detector is approximately proportional to $sin\theta$. The primary vertices are reconstructed using an iterative vertex finding algorithm [13]. Vertex seeds are obtained from the z position of the tracks which is defined as the closest approach between the track and the beam line. An iterative fit is made using the seed and nearby tracks. Depending on the quality of the fit, each track will carry a weight which reflects its compatibility with the vertex seed. During the reconstruction vertices are required to contain at least two tracks, or in some occasions at least three tracks for robustness. Tracks are reconstructed in the pixel detectors based on clusters of pixels. Different techniques for determining the position of the clusters have been implemented. A connected component analysis (CCA) was used until middle 2011 as a default to find groups of neighbouring pixels [14]. During 2001 a new Neural Network (NN) based reconstruction technique became the default approach [15]. This was motivated by the need of taking into account the occurrence of clusters merging in presence of signatures with many collimated particles like in the core of very energetic jets or in the decays of boosted τ leptons into multiple hadrons. In order to establish confidence in tracking quantities obtained from simulated samples, it has been essential to verify that data and simulation agree very closely. Quantities like the track transverse impact parameter with respect to the primary vertex (Figure 2.8) have showed an excellent agreement between data and MC [13].

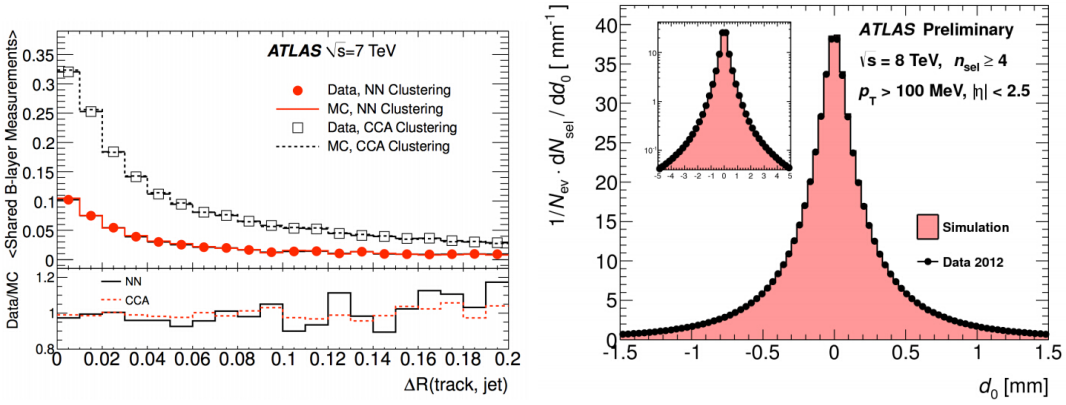

Figure 2.8 Left: The average number of shared measurements in the B-layer on tracks associated to jets for data and simulation, reconstructed with the CCA and NN clustering algorithms, as a function of the distance of the track from the centre of the jet. Right: Comparison between data and MC simulation for the track transverse impact parameter with respect to the primary vertex. A minimum number of four selected tracks is required.

2.2.3 Silicon microstrip detector

The strips can provide us additional information about the trajectories of charged particles. Like the pixel detectors, precise 3-dimensional position measurement can be derived by the SCT. The SCT is outside the pixel detector and help to measure particle momentum, impact parameter and vertex position. In the barrel, there are 8 layers which help to provide 8 precision measurement per track. Every silicon detector is 6.40 cm long and 6.36 cm wide, with 780 readout strips. The total number of readout channels is about 6.3 million.

2.2.4 Transition radiation tracker

In the larger radius, these are collections of gas-wire drift detectors that consist of 4 mm-diameter straws and 30 μm-diameter wires running through the straw centers. Straws are filled with Xenon gas and high voltage is maintained between center wires and the straw surface. When a particle traverses a straw, we can determine which straw was traversed and how far from the wire the particle passed. Transition radiation is a form of electromagnetic radiation emitted when a charged particle crosses boundary of different dielectric constants. Fields must reorganize and some can be shaken off as transition radiation. The probability intensity of producing transition radiation photons is depending on the gamma factor $\frac{E}{m}$ of the particle. The effect starts at the gamma factor above 1000, thus essentially only for electrons in the typical energy range, and it is thus mostly used for identifying electrons. In the TRT, transition radiation photons created between the straws are detected by absorption of the photons in the chamber

gas (Xenon mixture, short absorption length for photons) leading to high electronic pluses. There are about 50000 straws in the barrel and 320000 in the end-caps. Readout channels are set up at both ends for barrel and at the outer radius for end-caps. A total number of 420000 readout channels, each with two independent thresholds, give us drift time measurement with a space resolution 170 μm per straw. The beam-test result shows that transition radiation tracker performance meets with the requirements. A drift-time resolution of about 130 μm with an efficiency of 87% is feasible. For an electron efficiency of 90%, the measured pion efficiency is about 1.2%. [16]

2.2.5 Tracking performance

The track reconstruction efficiency, ϵ_{trk}, is determined from MC and parameterised in bins of p_{T} and η of the generated particle. It is defined as the ratio of reconstructed tracks matched to generated charged primary particles to the number of all generated charged primary particles.

$$\epsilon_{trk}(p_{\mathrm{T}}, \eta) = \frac{N_{rec}^{matched}(p_{\mathrm{T}}, \eta)}{N_{gen}(p_{\mathrm{T}}, \eta)} \tag{2.3}$$

The η distribution of the tracking efficiency for tracks with $p_{\mathrm{T}} > 500$ MeV is shown in Figure 2.9 [13]. The shape of the distribution corresponds to the amount of ID material traversed by charged particles. The systematic uncertainties are dominated by the material uncertainty and are determined using a detector model with $+10\%$ additional material in the whole ID.

The resolution of a track parameter X, can be expressed as a function of p_{T} as [12]:

$$\sigma_X = \sigma_X(\mathrm{inf})(1 \oplus \frac{p_X}{p_T}) \tag{2.4}$$

where $\sigma_X(\mathrm{inf})$ represents the resolution when the momentum is infinite and the constant p_X is the constant representing the value of p_{T}, for which the intrinsic and multiple-scattering terms are equal for the parameter X under consideration. The detailed studies have been performed for the expected track-parameter resolutions of the electrons and muons as a function of p_{T} and η. For example, in the barrel region if the p_{T} of the muons is infinite, the resolution for $\frac{1}{p_{\mathrm{T}}}$ is expected to be 0.34 TeV^{-1}. Table 2.1 shows the detailed values of $\sigma_X(\mathrm{inf})$ and p_X.

The charge of the electrons and muons is measured in the inner detector over the complete η acceptance up to 1 TeV. The mis-charge rate depends on p_{T} and η, which is typically at the level of a few percent. For the barrel region, muons with $p_{\mathrm{T}} \geq 1$GeV can be identified with efficiencies over 98%. This will rise to $\geq 99.5\%$ across the whole acceptance for high p_{T} muons. Electrons suffer from material effects; for tracks around 5 GeV, they are reconstructed with efficiencies between 70% and 95% [12].

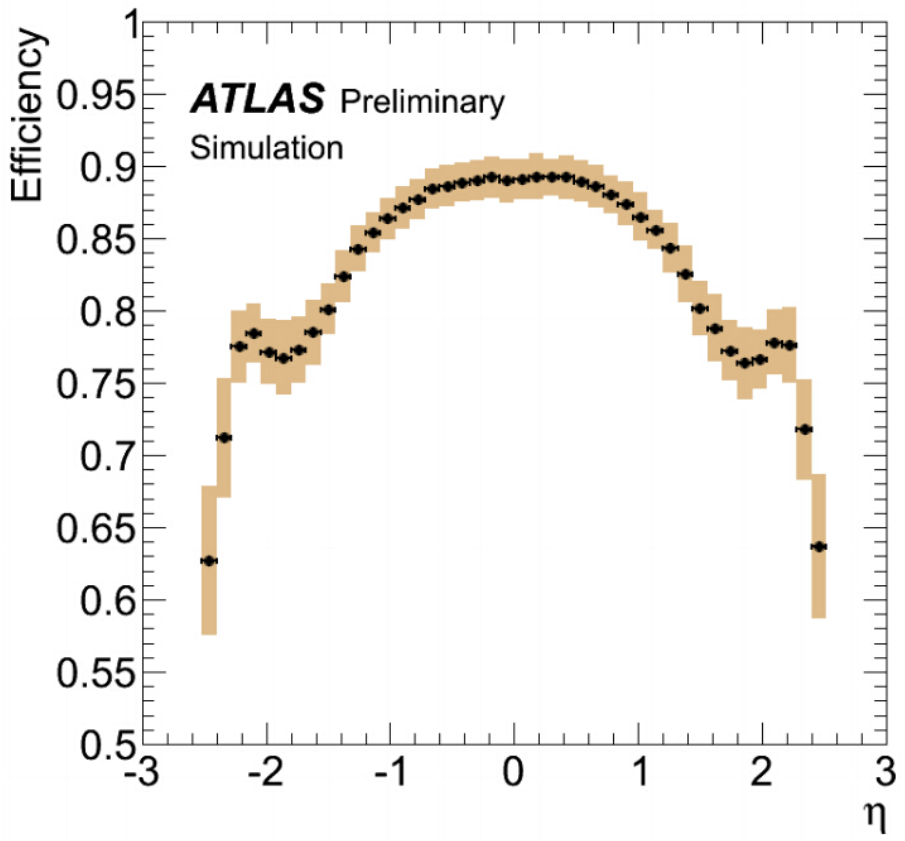

Figure 2.9 Track reconstruction efficiency as a function of η, obtained for tracks with $p_{\mathrm{T}} > 500$ MeV produced in min-bias events.

Track parameter	0.25<$\|\eta\|$<0.50		1.50<$\|\eta\|$<1.75	
	$\sigma_X(\mathrm{inf})$	p_X(GeV)	$\sigma_X(\mathrm{inf})$	p_X(GeV)
Inverse transverse momentum ($\frac{1}{p_{\mathrm{T}}}$)	0.34 TeV^{-1}	44	0.41 TeV^{-1}	80
Azimuthal angle (ϕ)	70 μrad	39	92 μrad	49
Polar angle (cot θ)	0.7×10^{-3}	5.0	1.2×10^{-3}	10
Transverse impact parameter (d_0)	10 μm	14	12 μm	20
Longitudinal impact parameter ($z_0 \times sin\theta$)	91 μm	2.3	71 μm	3.7

Table 2.1 Expected track parameter resolutions at infinite transverse momentum $\sigma_X(\mathrm{inf})$, and transverse momentum p_X. The momentum and angular resolutions are shown for muons, whereas the impact-parameter resolutions are shown for pions. [12].

Since there are significant materials in the inner detector, the electrons will suffer from bremsstrahlung. Algorithms have been developed to improve the reconstruction of electrons, reducing the bias on the measured momentum. While reasonable electron reconstruction is possible in barrel region of the inner detector, it is quite difficult in the end-caps because of the increased amount of bremsstrahlung. So the use of the electromagnetic calorimeter will be essential, as described below.

2.3 Calorimeter

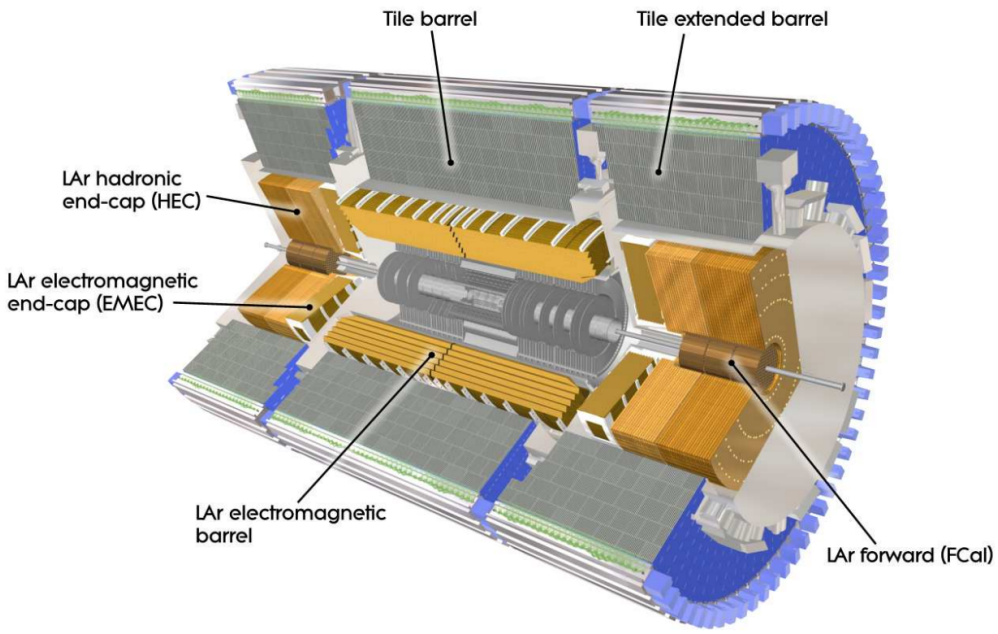

Figure 2.10 Cut-away view of of the ATLAS calorimeter system. [12]

In the ATLAS detector the calorimeter is an important component. In order to achieve a good resolution for measuring the missing transverse momentum it's designed to be hermetic. It can cover up to $|\eta| = 4.9$. For the different region, the calorimeter consists of different sub-detector, which is shown in Figure 2.10. It can measure the electro-magnetic and hadronic showers of particles with energy around TeV scale.

2.3.1 Electromagnetic calorimeter

The electromagnetic calorimeter is designed to measure the energy of electrons and photons. It is divided into a barrel part as well as two end-caps and is designed as a sampling calorimeter with lead as the absorber and liquid argon as the active material. The lead, or any material with high atomic number, will help to produce electron shower if high energy electrons or photons go into it. The initial energies of electrons or photons will be partially transformed into multiple positrons and electrons with a bit lower energy. The number of this kind of positrons/electrons is generally proportional to the initial energy. The lead plates, together with the sensing system, will measure the energies. The lead plates are immersed in the liquid argon, where a large electric field is supplied. When positrons/electrons enter the liquid argon, the electron-ion pairs are produced, after which the drift of the electrons will cause the current on the readout

electrodes. The more the initial incident energy, the more electrons/positrons there are, and the more current we will observe.

The electromagnetic calorimeter was designed to cover $|\eta| \leq 3.2$. The electromagnetic calorimeter is designed be inside three cryostats. Barrel electromagnetic calorimeter is made up with two parts, both of which are covering over the beam pipe as long as 3.2 m (One part is $0 \leq \eta \leq 1.475$ and the other part is $-1.475 \leq \eta \leq 0$). For the end-cap electro-magnetic calorimeter, it covers $1.375 \leq |\eta| \leq 3.2$. In order to correct the loss of energy from the electrons and photons, the pre-sampler is installed which covers $|\eta| \leq 1.8$. It is made up of LAr layer as thick as 1.1 cm (barrel) and 0.5 cm (end-cap).

If the effect of the noise is not considered, the experimental performance can be expressed in the following equation [12] [17]

$$\frac{\sigma(E)}{E} = \frac{a}{\sqrt{E(GeV)}} \oplus b \tag{2.5}$$

where a is the stochastic term and b is the constant term which presents local non-uniformities of the calorimeter response. For the barrel, the test beam data is used to estimate the resolution, which is $\frac{\sigma(E)}{E} = \frac{10\%}{\sqrt{E(GeV)}} \oplus 0.17\%$. The energy response is also found to be linear with respect to the beam energy within $\pm 0.1\%$. For the end-cap, similar conclusion can be drawn [12].

The electromagnetic calorimeter's accordion structure provides complete ϕ symmetry without azimuthal cracks. In the following text, radiation length is denoted as X_0 and interaction length is denoted as λ. The calorimeter is thicker than 22 X_0 for the barrel and 24 X_0 for the end-cap. This is approximately 9.7 λ for the barrel and 10 λ for the end-cap, which ensures good resolution for the jets with high energies. Combined with the large η coverage, this thickness can provide an excellent measurement for the missing transverse energy, which is important for many physics analysis process.

The calorimeter is divided into three layers. The ϕ and η size of cells and relative position of the layers are shown in the Figure 2.11. When the correction is derived, these regions are treated separately. For electrons, in the barrel electromagnetic calorimeter the energy is summed by an area of 3×7 cells in the middle layer, which is $\Delta\eta \times \Delta\phi = 0.075 \times 0.175$. For the converted photons, they are considered in the the way as electrons, while for the unconverted photons, this area is limited to 3×5 cells. As the $|\eta|$ increases, the width of the cluster also increases. So for the end-cap calorimeter, an area of 5×5 cells in the middle layer is used for both electrons and photons.

Most of the energy of an electromagnetically interacting particle is deposited in the sensitive volume of the calorimeter, including the lead absorbers and the liquid-argon gaps. A small fraction is deposited in non-instrumented material in the inner

detector, the cryostats, the solenoid, and the cables between the pre-sampler and the first electromagnetic calorimeter layer. Energy also escapes from the back of the calorimeter. The cluster energy is calculated as a linearly weighted sum of the energy in each of the three calorimeter layers plus the pre-sampler. The factors applied to the four energies are called longitudinal weights [18] and their purpose is to correct for the energy losses, providing optimum linearity and resolution.

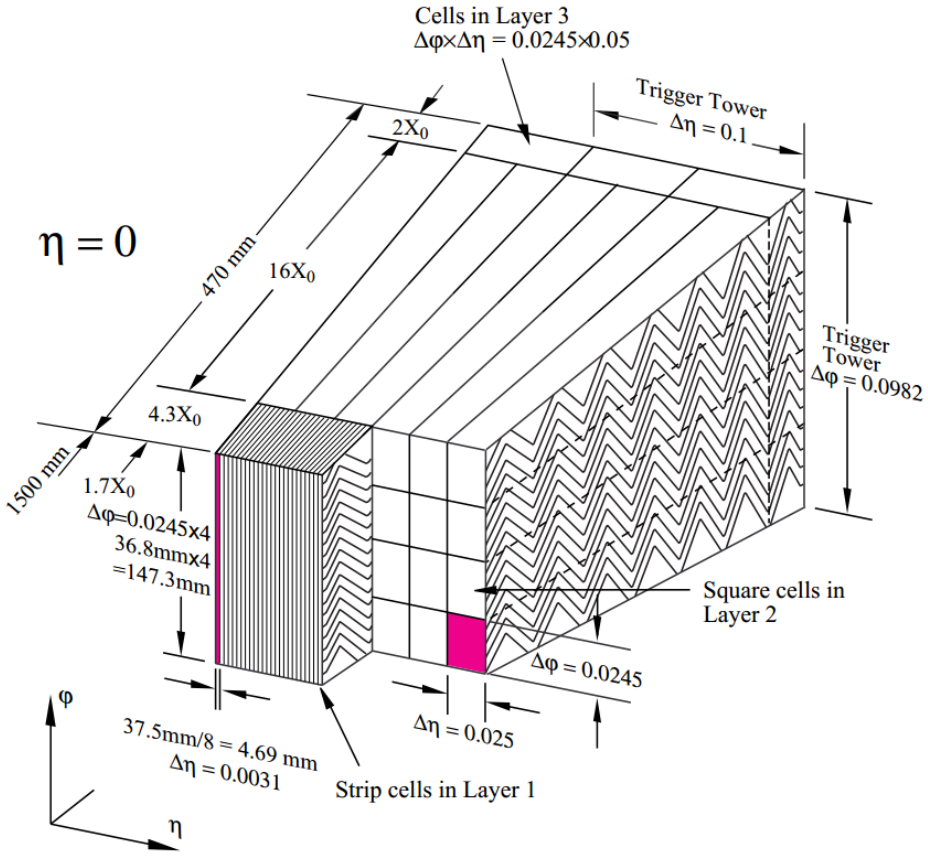

Figure 2.11 Sketch of a barrel module where the different layers are clearly visible with the ganging of electrodes in ϕ. The granularity in η and ϕ of the cells of each of the three layers and of the trigger towers is also shown. [12]

In the ATLAS LAr calorimeter, the calibration of the energy depositions of electrons, photons and consists of six different steps which are based either on simulation or on real data. The calibration proceeds as shown in the Figure 2.12 [19]. Firstly, the electromagnetic cluster properties, including its longitudinal development, and additional information from the ATLAS inner tracking system, are calibrated to the original electron and photon energy in simulated MC samples, optimised by calibration-hits-based method or a multivariate algorithm (MVA) [20]. Secondly, since the electromagnetic calorimeter is longitudinally segmented, the scales of the different longitudinal layers have to be equalised in data with respect to simulation, prior to the determination of

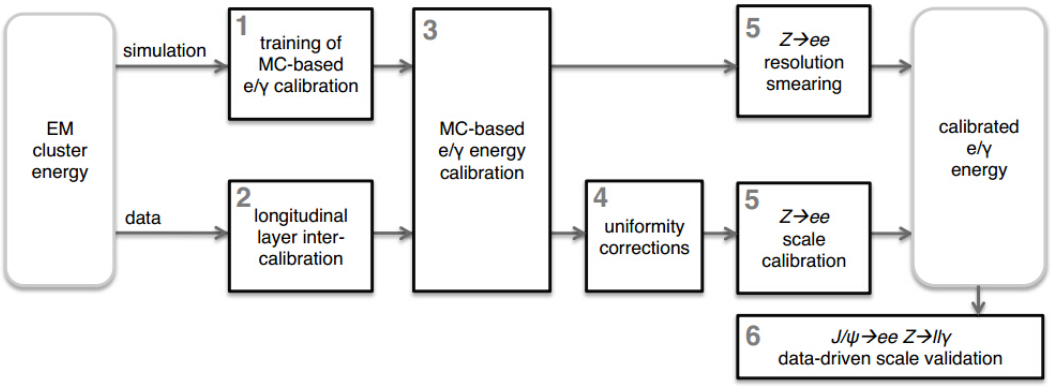

Figure 2.12 Schematic overview of the procedure used to calibrate the energy response of electrons and photons in ATLAS.

the overall energy scale. Thirdly, the electron/photon response calibration is applied to cluster energies both from collision data and MC simulated samples. Step four consists of a set of corrections for uniformity, e.g. the geometric intermodule widening. In the fifth step, the $Z \rightarrow ee$ events are studied to derive the scale for the the absolute energy in data. This is also used to estimate the resolution in data, after which we can do the smearing of the MC resolution to be in agreement with data. The sixth step is the validation step, $J/\Psi \rightarrow ee$ and $Z \rightarrow ll\gamma$ events are used to do the cross check.

Figure 2.13 shows the invariant mass distribution for $Z \rightarrow ee$ process. For the data, it is corrected with the energy scale factors. For the MC the corrected and uncorrected resolution are both shown. What is more, the ratio of the data with correction and MC distributions without correction to the MC distribution with correction are shown with the uncertainty of calibration. After corrections, for the mass interval $85 < m_{ee} < 95$ GeV, the mass distribution of di-electron in data and MC is in good agreement at the level of around 1%. This will go up to around 2% in the low mass region. This slight excess implies that the MC simulation is not well modelled for the low mass region, although we have done the calibration and designed geometry of the detector to improve it. But we should point out that this disagreement is already lying in the uncertainty band.

2.3.2 Hadronic calorimeter

The hadronic calorimeter surrounds the electromagnetic calorimeters. It is designed to measure the energy of hadrons (typically protons, neutrons, pions and kaons). When high energy hadrons traverse the absorbing materials, they produce a hadronic shower in which the initial particle energy is partially transformed into the rest masses of lower energy hadrons and partially used to knock out protons and neutrons from the

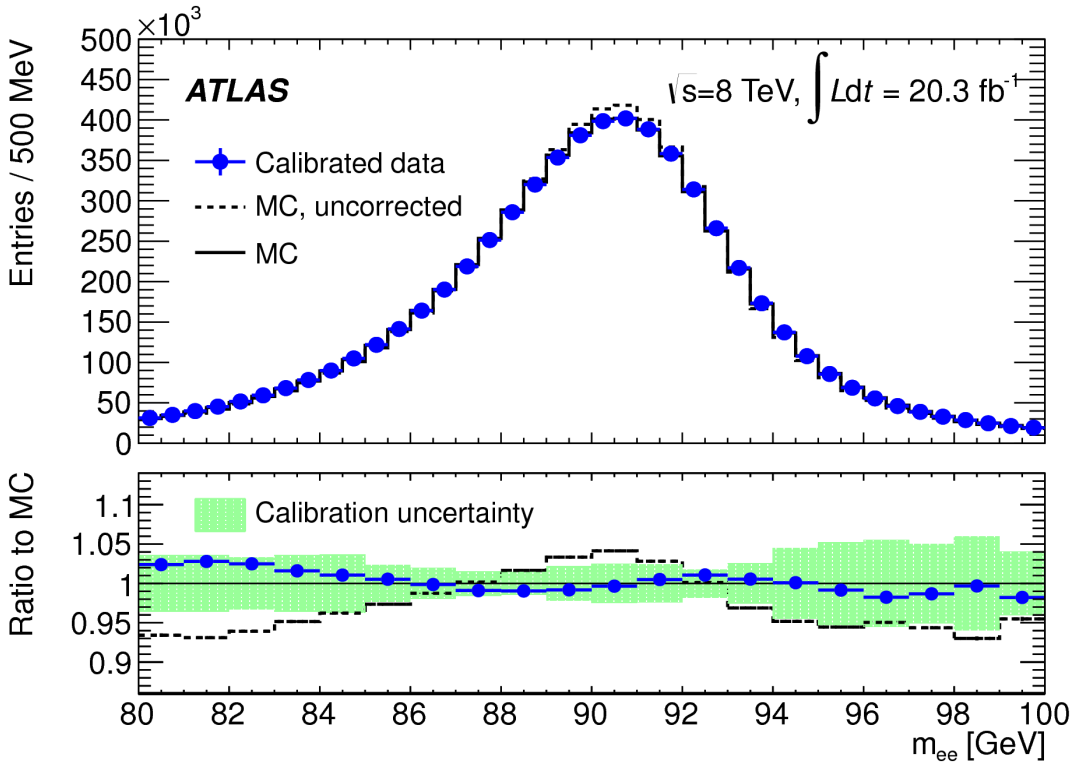

Figure 2.13 Top: electron pair invariant mass distribution for $Z \rightarrow ee$ decays in data and improved simulation. Energy scale corrections are applied to the data. The improved simulation is shown before and after energy resolution corrections, and is normalised to the number of events in data. Bottom: ratio of the data and uncorrected MC distributions to the corrected MC distribution with the calibration uncertainty band.

nuclei of some of the atoms of the absorber material, which will be detected by in the active material readout by sensing devices.

The hadronic calorimeter is based of three parts as follows. For small angle relative to the beam pipe or high η, $3.1 < |\eta| < 4.9$, jets are detected by the Forward Calorimeter (FCAL) made of copper/tungsten for the absorber part and LAr for the active material. For angles between 5 and 25 degrees or $|\eta| = 1.5$ up to $|\eta| = 3.1$, the detector is the Liquid Argon Hadronic end-cap Calorimeter (HEC) made of copper plates for the absorbers and LAr for the active material. For angles greater than 25 degrees, or $|\eta| < 1.7$, jets are detected in the Tile Calorimeter placed around the LAr electromagnetic calorimeter.

The hadronic calorimeter provides accurate hadronic energy measurements. It measure the energies and directions of jets, which correspond to the energy and direction of a quark or a gluon produced in the proton-proton collision. For neutrinos, which are weakly interacting with matters and thus not directly detectable, it participates to their energy measurements. Using the principle of conservation of the transverse components of momentum, it contributes to the measurement of the total missing transverse

energy as well as the sum of energy. Before colliding was provided, the energy response to isolated charged pions of the combined LAr and tile calorimeter system was first tested with test beam data and measured to be $\frac{\sigma(E)}{E} = \frac{52\%}{\sqrt{E(GeV)}} \oplus 3\%$, which is very close to design specifications [12].

Figure 2.14 shows the calorimeter response characterised by energy over momentum E/p for isolated tracks, as measured with the Tile Calorimeter, using proton-proton collision data from 2012 [21]. In order to reconstruct the energy of the isolated hadron, the information is taken from nearby clusters in a cone of $\Delta R < 0.2$. Selected tracks pass minimum quality criteria (at least one pixel hit; two, four or six hits in the SCT for tracks according to their p_{T}), have $p_{\mathrm{T}} > 2$ GeV and deposit less than 1 GeV in the electromagnetic calorimeter. Differences from MC predictions are within a few percent.

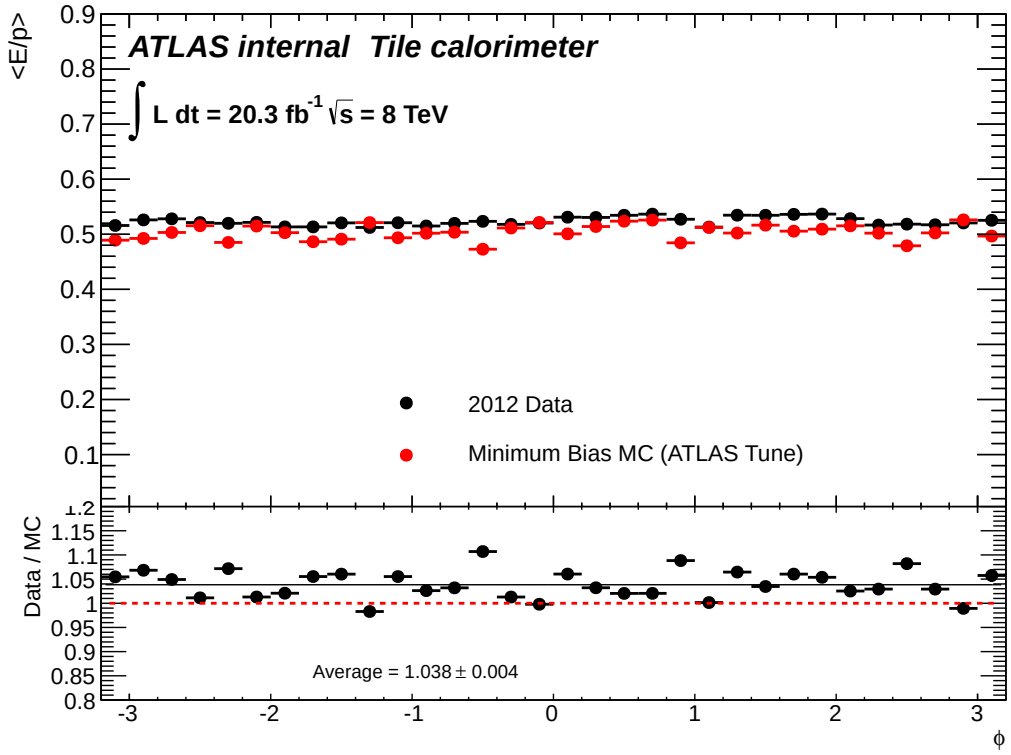

Figure 2.14 Mean E/p as a function of η for 2012 data.

2.4 Muon spectrometer

Most of the charged particles cannot go through all of the calorimeters, except for muons. The muon spectrometer allows us to determine the momenta with good precision. Since a muon is much heavier than an electron, it will not be that much affected by the material they encounter. Therefore, we do not expect the large amount of the electro-magnetic shower, but deposition of minimum amount of energy in the

calorimeter through ionizing.

The muon system is designed to tolerate the radiation levels in the experimental hall. All components were therefore tested to withstand at least five times the radiation levels predicted by the simulation studies.

The muon spectrometer is shown as Figure 2.15. The super-conducting toroidal coils can provide magnetic field, in which sensors are placed.

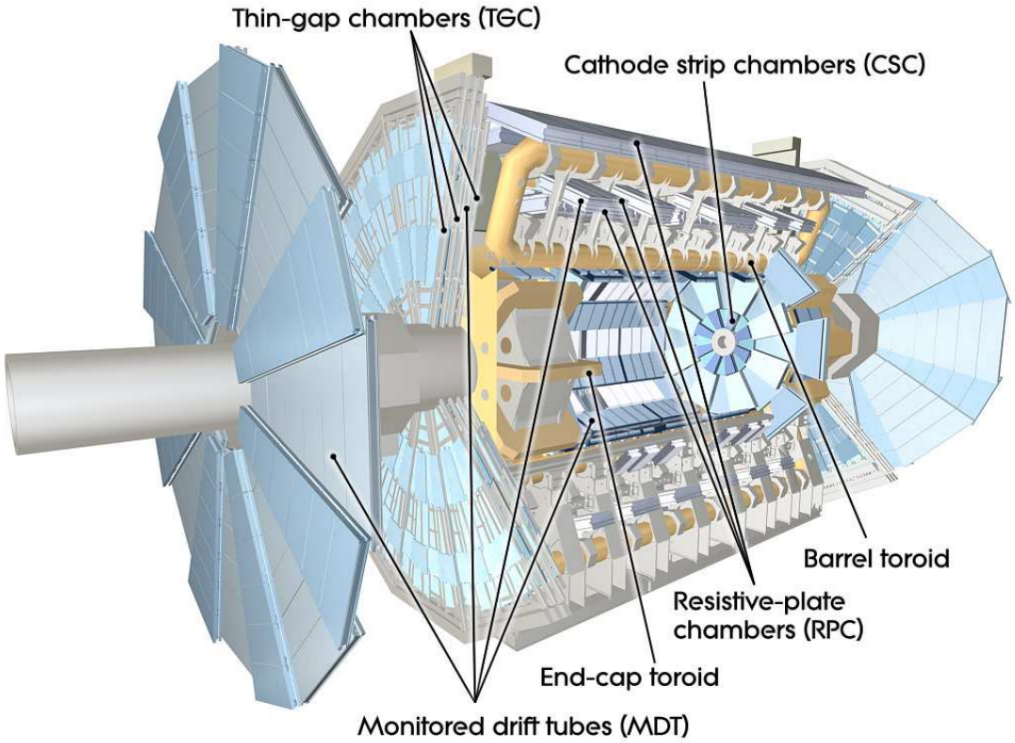

Figure 2.15 The ATLAS muon spectrometer. [12]

2.4.1 Monitored drift tubes

They cover the region up to $|\eta| \leq 2.7$ and provide precision momentum measurement. The metal tubes, 1.5 cm in radius and filled with gas, make up the muon sensors. The high voltage is supplied between the wire and the tube wall. Muons traversing the tubes produce electrical pulses which, with careful timing, determine muon positions to 0.1 mm. The muon path, reconstructed from several such position measurements, determines momentum and sign of charge.

2.4.2 Cathode strip chambers

They cover the region $2.0 \leq |\eta| \leq 2.7$. Due to the large background, drift tubes are not suitable here. Cathode strip chambers, consisting of arrays of closely spaced

parallel wires in a narrow gas enclosure with metal walls arranged in the form of strips, are better to handle the high backgrounds. High voltage is supplied between wires and wall strips. Its precision for the position measurement is at the level of 0.1 mm.

2.4.3 Resistive plate chambers and thin gap chambers

The fast trigger chambers, which are able to deliver the track information with a few tens of nanoseconds after the passage of the particle, are needed for precision track measurement. So Resistive Plate Chambers (RPC) and Thin Gap Chambers (TGC) are designed for this. RPC covers the barrel region $|\eta| \leq 1.05$ and TGC covers the end-cap region $1.05 \leq |\eta| \leq 2.7$. The intrinsic time resolution is 1.5 ns for RPC and 4 ns for TGC, which permits us to identify the bunch crossing with an efficiency as high as 99%.

2.5 Reconstruction of electrons, muons, jets and missing transverse momentum

The signature of an electron in ATLAS is a reconstructed track in the inner detector, associated to a narrow, localized cluster of energy in the electromagnetic calorimeter. In ATLAS, there are two reconstruction algorithms which are built up in the off-line software system. The first algorithm, which is seeded on calorimeter for reconstruction, starts from clusters reconstructed in the calorimeter and then builds the identification variables based on information from the inner detector and the electromagnetic calorimeter. The second one, which is seeded on track information, selects good-quality tracks matching a relatively isolated deposition of energy in the electromagnetic calorimeter.

The first algorithm is the standard algorithm. It initiates with the reconstructed cluster in the electromagnetic calorimeter. When an electron interacts with the calorimeter, its energy is deposited in many different calorimeter cells. A clustering algorithm is used to group individual cells into clusters, which are associated to the particles. In the next step, the seed cluster are associated to tracks reconstructed in the inner detector. Tracks are extrapolated from the end of the inner detector to the middle layer of the calorimeter. To form an electron candidate, at least one track is required to fall with $\Delta\eta < 0.05$ and $\Delta\phi < 0.1(0.5)$ of the reconstructed seed cluster. After the track matching, the seed clusters of the electron candidates are rebuilt, and the electron energy is derived. Electron candidates at this stage of the reconstruction are considered as "reconstructed electrons".

Electron efficiency is divided into three different components that correspond to

the individual steps of triggering, identification and reconstructing the object. The full efficiency of an electron is given as the product of these three components. The reconstruction efficiency is measured using a tag-and-probe method using Z events. The identification efficiency is determined with respect to the reconstructed electrons. Trigger efficiencies are derived by studying the number of electrons passing specific identification criteria. The overall selection efficiency ranges from $70-90\%$ in the central region ($|\eta| < 1.37$) and $5-10\%$ less in the forward region at 8 TeV. The details are given in the [22].

For muons, ATLAS employs a variety of strategies for reconstruction. The direct approach is to reconstruct StandAlone (SA) muons by finding tracks in the muon spectrometer and then extrapolating these to the beam line. Combined (CB) muons are found by matching SA muons to nearby inner detector tracks and then combining the measurements from the two systems. Segment-Tagged (ST) muons are found by extrapolating inner detector tracks to the spectrometer detectors and searching for nearby hits. Calorimeter tagging algorithms are also developed to tag inner detector tracks using the presence of a minimum ionizing signal in calorimeter cells. The last type of muons are the Calorimeter-Tagged (CaloTag) muons . These are formed by ID tracks that are associated to an energy deposit in the calorimeter compatible with a minimum ionizing particle.

The performance of the ATLAS muon reconstruction during 2011−2012 on data is studied based on large reference samples of $J/\Psi \to \mu\mu$, $Z/\gamma^* \to \mu\mu$ decays, compared to Monte Carlo simulations. These studies have been used to correct the MC simulation to improve the agreement between data and MC and to minimize the uncertainties in physics analyses. Figure 2.16 shows the muon reconstruction efficiency as a function of η measured in $Z/\gamma^* \to \mu\mu$ events for different reconstruction algorithms. Over most of the covered phase space (muon $|\eta| < 2.7$ and $5 \leq p_{\mathrm{T}} \leq 100$ GeV), the efficiency is above 99% and is measured with a precision of per mille level [11].

The ID muon reconstruction efficiency as a function of p_{T} is shown in Figure 2.17. The efficiency is greater that 99% in the whole p_{T} range and modelled accurately by the MC. The efficiency for CB+ST muons as a function of p_{T} is also shown. The drop in efficiency observed using the J/Ψ for $p_{\mathrm{T}} > 15$ GeV is due to the inefficiency of the MS to reconstruct muon pairs with small angular separation coming from highly boosted J/Ψ decays. The reconstruction efficiency is also shown as a function of the mean number of interactions per bunch crossing. The efficiency is on average above 99%.

Figure 2.18 shows the comparison of mass resolution from J/Ψ, Υ and Z di-muon

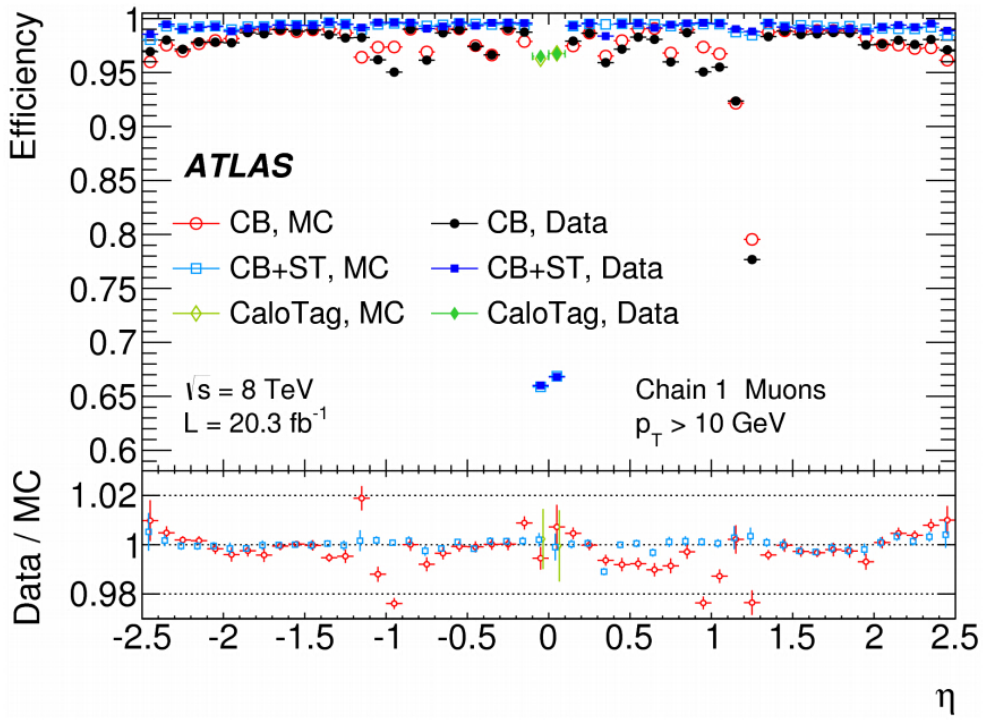

Figure 2.16 Muon reconstruction efficiency as a function of η measured in $Z/\gamma^* \rightarrow \mu\mu$ events for different muon reconstruction types. [12]

decays. In the barrel region the resolution increases from 1.2% for low p_{T} muons to 2% for $p_{\mathrm{T}} = 100$ GeV. For the $|\eta| > 1$ the mass resolution increases from 2% to 3%. Then we can estimate the momentum resolution, which ranges from 1.7% at central rapidity and for p_{T} around 10 GeV, to 4% at large rapidity and p_{T} around 100 GeV. The momentum scale is known with an uncertainty of 0.05% to 0.2% depending on rapidity [11].

For many physics processes, the missing transverse energy E_T^{miss} is acting as an important signature. It is an event-level quantity calculated based on momentum conservation in the transverse plane. The missing transverse energy E_T^{miss} is determined by the energy collected by the electromagnetic and hadronic calorimeters and by the muons measured by the muon spectrometer (will be discussed in the Section 2.4) and inner detector. The E_T^{miss} attributed to the calorimeters is the sum of the transverse energy of calibrated topological clusters which is stored in the METRefFinal term. The E_T^{miss} calculated by the METRefFinal algorithm uses calorimeter energy deposits accociated with high p_{T} objects such as e, μ, γ and jets. The transverse energy of the objects is then used as a replacement for the original cell energy, since the objects have a more acccurate calibration than the bare calorimeter cell calibration. The precise measurement of the missing transverse energy is fundamental in WW analysis.

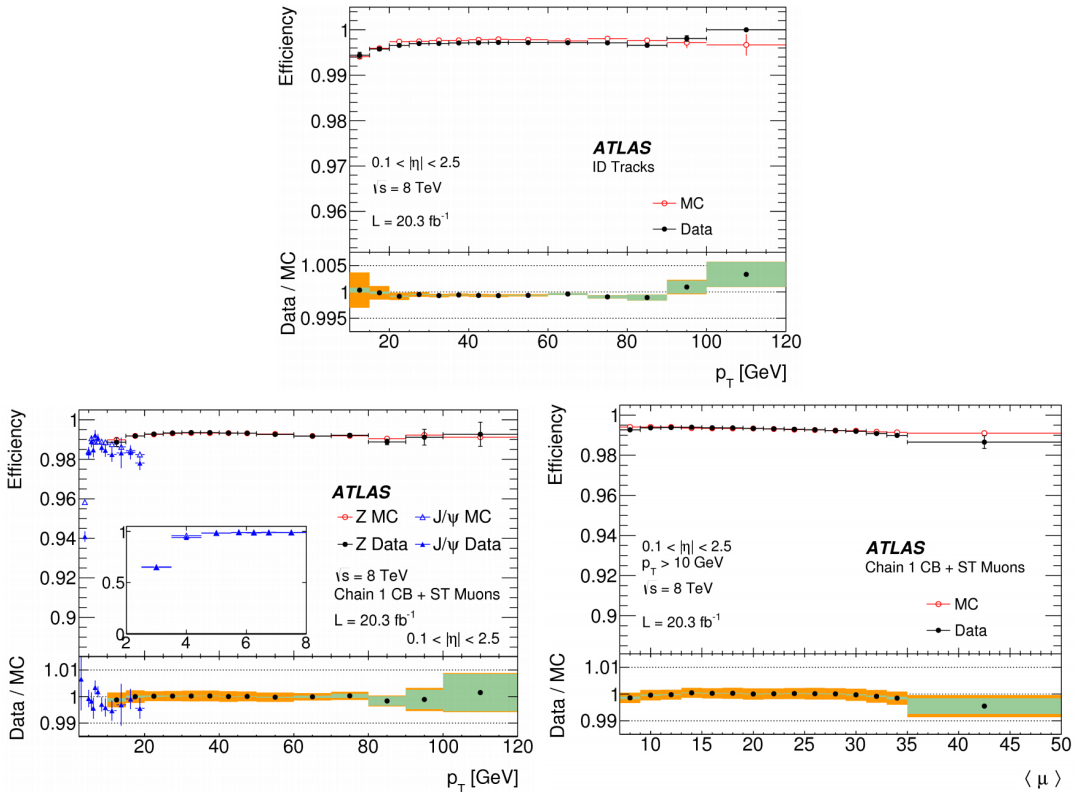

Figure 2.17 Top: ID muon reconstruction efficiency as a function of p_{T} measured in $Z \to \mu\mu$ events. Bottom left: Reconstruction efficiency for CB+ST muons as a function of the muon p_{T}. The insert shows the detail of the efficiency in the low p_{T} region. Bottom right: Measured CB+ST muon reconstruction efficiency as a function of the average number of interactions per bunch crossing.

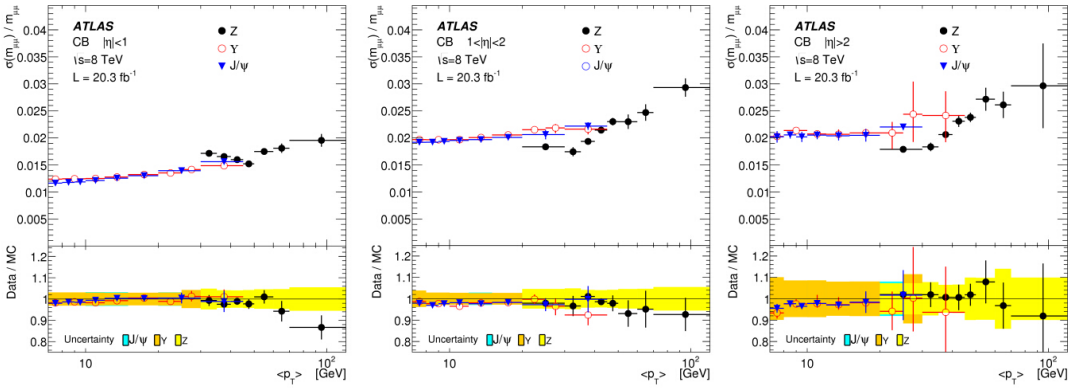

Figure 2.18 Di-muon invariant mass resolution for combined muons measured from J/Ψ, Υ and Z events as a function of the average transverse momentum of two muons $< p_{\mathrm{T}} >$ in three $|\eta|$ ranges. Both muons are required to be in the same $|\eta|$ range.

The pile-up has large effect on the performance of the E_T^{miss} reconstruction. There are several pile-up correction methods for E_T^{miss}. All methods corrects the E_T^{miss} Soft Term [23]. An important method is based on the Soft Term Vertex Fraction (STVF). It scales the E_T^{miss} soft term by a factor constructed from all tracks in the event. The factor is the fraction of the momentum of tracks which match the hard scatter vertex. Further possibilities are to use jet-area-based methods as described above. Figure 2.19 shows the pile-up dependence of reconstructed E_T^{miss} for several pile-up correction methods. The E_T^{miss} with STVF method gives the smallest bias [24] [23].

In WW analysis we carefully choose the best modeled missing transverse energy. More details about the missing transverse momentum used in WW analysis will be discussed later in the Section 3.4.1.

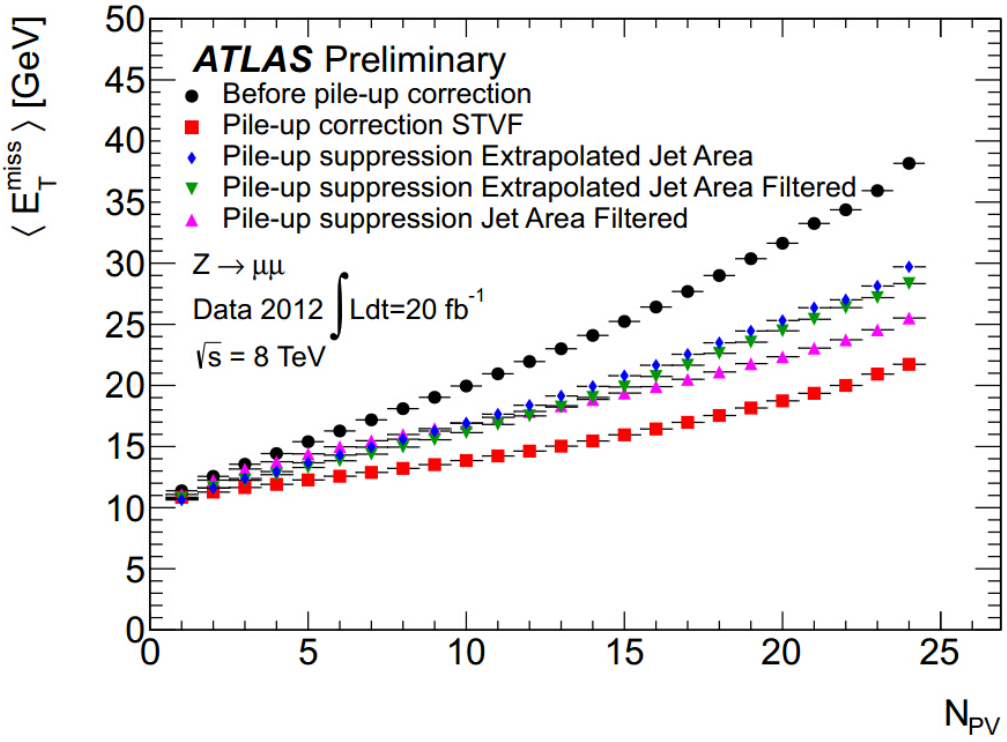

Figure 2.19 The reconstructed E_T^{miss} as a function of N_{PV} for the inclusive $Z \to \mu\mu$ data sample for several pile-up correction methods.

The ATLAS has achieved a very high precision on jet performance. Tracking information is being combined with calorimeter to further improve the jet and missing transverse energy performance. The standard algorithm for the jets in ATLAS is the anti-kT clustering algorithm [25] [26]. The topo-cluster finding is optimized to noise and pile-up suppression. For the data taken in the 2011, the offset correction was performed in order to correct the jet p_{T}. The offset was determined from MC simulations

as a function of the number of primary vertices (N_{PV}) and the instantaneous luminosity in the given event. For 2012 data, jet-area-based correction [27] was used followed by residual offset correction [28]. The "jet-area-based" correction deals with the p_{T} of jets event by event and jet by jet. It is based on the relation [24]:

$$p_T^{corr} = p_T - AD \tag{2.6}$$

in which A is the jet area and D is the density for the pile up. The Figure 2.20 shows the performance of the pile-up correction for 2012 MC simulation. The jet-area-based correction highly reduces the jet p_{T} dependence on the pile-up which is entirely removed after residual offset correction for all jet η.

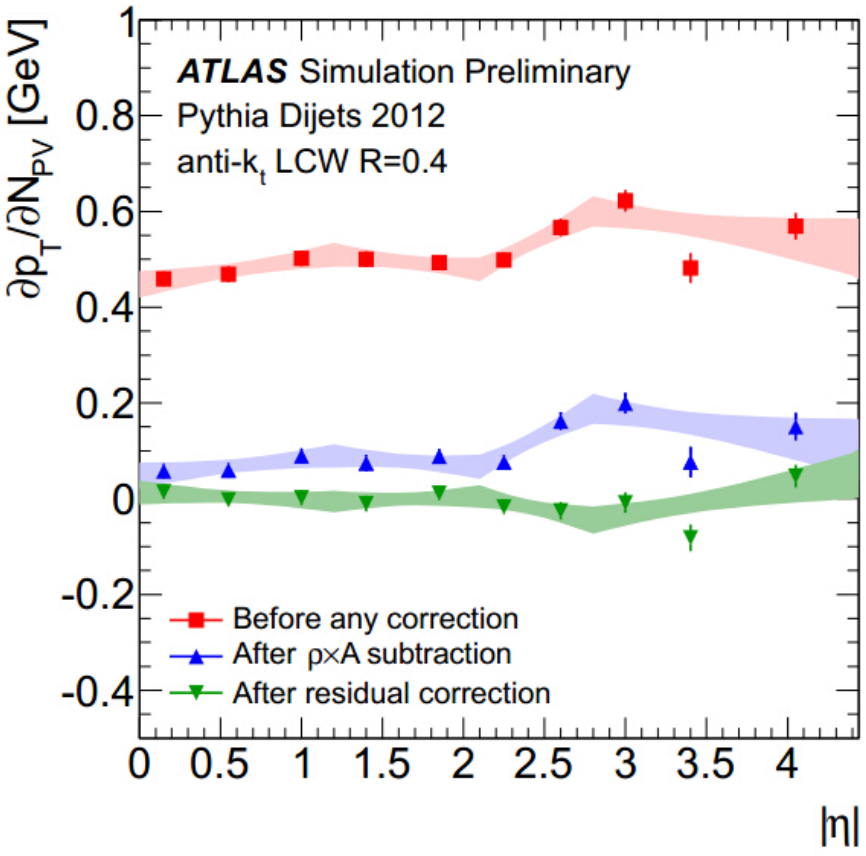

Figure 2.20 The slope of the jet p_{T} dependence on N_{PV} as a function of jet η before any correction, after jet-area-based cor-rection, and after residual offset correction in simulated di-jets events.

2.6 Trigger and data acquisition system

ATLAS is using a three-level trigger system, which is to select events to be recorded on permanent storage. The trigger menu is built for a given target luminosity and then prescales are adjusted during the data-taking, as the luminosity decreases.

2.6.1 Level 1 trigger

The Level 1 Trigger (LV1) searches for the high p_{T} muons, electrons/photons, jets and large $E_{\mathrm{T}}^{\mathrm{miss}}$. Thus the LV1 trigger select the bunch crossing with the interesting signatures. The LV1 trigger is based on the hardware. The rate will be reduce to the level of 100 kHz from 40 MHz.

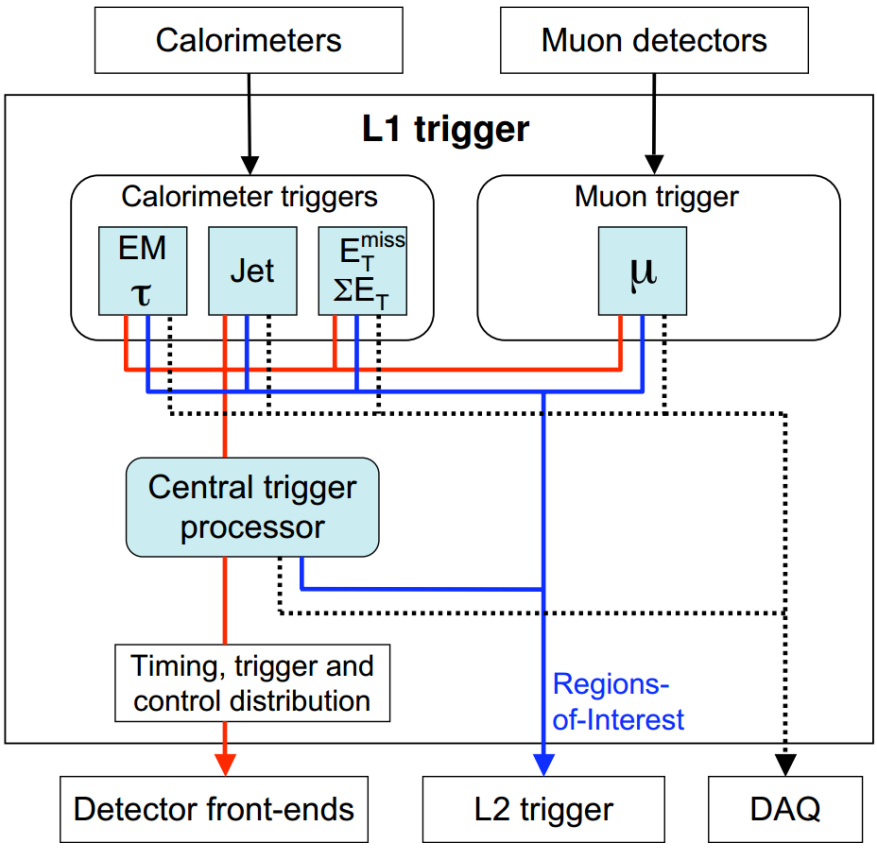

Figure 2.21 Block diagram of the L1 trigger. [12]

2.6.2 Level 2 trigger

The Level 2 Trigger (LV2) continues to select events after LV1 selection. An important piece of the strategy of the ATLAS trigger relies on the Region-of-Interest (RoI) mechanism for which the LV2 trigger makes use of information provided by the LV1 trigger in localized region of the calorimeter and muon sub-detectors. The information contained in the RoI typically include the position (η and ϕ) and the p_{T} of the candidate objects as well as energy sums. The LV2 trigger then deals with reduced volume of data, uses the ROI information on coordinates, energy and other signatures. Candidate objects selected by the LV1 can be muons with high p_{T}, electrons or photons, hadrons or taus, and jets. For all the events that are accepted by LV1, the RoI information is sent to the LV2 using a dedicated data path. It is important to note that all the data from all

the sub-detectors with full granularity is available for the LV2 algorithms if necessary. However, typically only a small fraction of the detector, centred around the RoI information selected by the LV1, is needed by the LV2 algorithms. The LV2 trigger is based on the software. The rate will be reduced to the level of 400 Hz.

2.6.3 Level 3 trigger and data acquisition

For events selected in the LV2, event building is performed. Each readout buffer contains fragments of many events for a small part of on sub-detector. The event builder collects all the fragments from one event into a single memory of a third level trigger (LV3) processor, or called event filter. LV3 is performed using farms of processors which will take the full event data into account. The complete selection criteria of the off-line analysis is used in a real-time environment.

Chapter 3 $W^+W^- \to \ell^+\nu_\ell\ell^-\bar{\nu}_\ell$ analysis

3.1 Physics overview

The precise measurement of W^+W^- cross section is an important di-boson analysis of the ATLAS experiment for several reasons. Firstly it tests our current understanding of electro-weak sector for the SM. Secondly it is an irreducible background for the $H \to WW$ analysis, therefore the study of this process is critical the Higgs studies. Thirdly, the $q\bar{q} \to W^+W^- \to \ell^+\nu_\ell\ell^-\bar{\nu}_\ell$ process ($l = e, \mu, \tau$, e.g, $q\bar{q} \to W^+W^- \to e^+\nu_e\mu^-\bar{\nu}_\mu$) can include Anomalous Tripple Gauge Boson Coupling (aTGC) vertices of WWZ and $WW\gamma$, so it provides a unique opportunity to study the physics beyond the SM.

The WW production includes contributions from quark-quark annihilation and gluon-gluon fusion. The leading-order Feynman diagrams for the dominant W^+W^- production mechanism at the LHC are shown in Figure 3.1 and are characterised by a quark-antiquark initial state, corresponding to $\sim$ 92% of the total WW contribution [29]. Gluon-gluon fusion is non-negligible. The $gg \to H \to WW$ process is considered as signal process, which corresponds to $\sim$ 4 % of the total WW contribution. We show the Feynman diagram of the gluon-gluon fusion mediated by the quark loop in the Figure 3.2 on the left. This process contributes $\sim$ 3% event rate of the W^+W^- production.

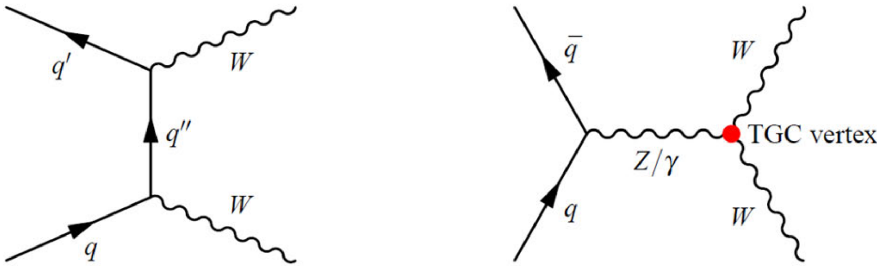

Figure 3.1 The Standard Model tree-level Feynman diagrams for W^+W^- production through the $q\bar{q}$ initial state. The s-channel diagram, on the right, contains the WWZ and $WW\gamma$ aTGC vertices. [30]

Because the WW process has much smaller cross section compared to the W+jets and multijet QCD processes, we only consider the final state with 2 leptons plus 2 neutrinos. The feature of the signal process is that we have 2 leptons with missing transverse energy. The important backgrounds include Z+jets, $t\bar{t}/Wt$, W+jets, and other di-bosons. The details will be discussed in the Section 3.5.

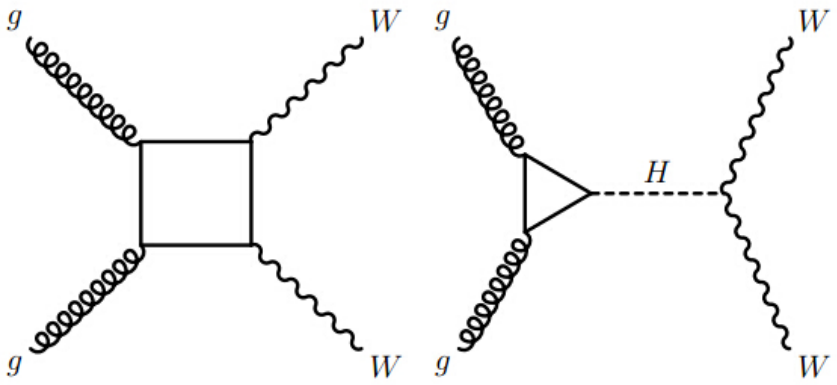

Figure 3.2 Standard Model Feynman diagrams for W^+W^- production through gluon-gluon fusion in hadron colliders. The first $NNLO$ contribution to W^+W^- shows the box diagram while the second one occurs via a Higgs boson. [30]

3.2 Dataset and MC samples

3.2.1 Dataset

This analysis uses the full 8 TeV dataset collected during the year 2012, corresponding to an integrate luminosity of 20.3 fb^{-1}. A total of 2.8% uncertainty is assigned for the corresponding integrated luminosity [10]. The Good Run List (GRL) is created from the data quality flags which selects good luminosity blocks from the data runs. It states the good data that can be used in the analysis.

3.2.2 Theoretical calculation for W^+W^- production cross section

The Next-to-Next-to-Leading Order (NNLO) cross section for on-shell W boson pair production has been presented in [31]. The MSTW2008 [32] PDF is used, where μ_R and μ_F are set dynamically as the invariant mass of the produced WW system $M_{WW}/2$. NNLO calculations for W^+W^- production in pp collisions at $\sqrt{s} = 8$ TeV is $59.1^{+1.2}_{-1.0}$ pb, and the uncertainty is evaluated by varying μ_F and μ_R independently by a factor of 0.5 or 2 except for the extreme cases like $\mu_R = 4\mu_F$ and $\mu_F = 4\mu_R$. The contribution from on-shell Higgs decays is excluded because of the requirement of on-shell W bosons.

Table 3.1 summarizes the predicted cross sections for various W^+W^- production processes. The partial NNLO cross section for total W^+W^- production includes the quark anti-quark annihilation at Next-to-Leading-Order (NLO) and non-resonant gluon-gluon fusion at Leading Order (LO). The full NNLO cross section incorporates the $q\bar{q}$ contribution at NNLO. The calculation of $q\bar{q} \to WW$ has already included the contribution of $gg \to WW$. In addition the $gg \to H \to WW$ contribution at NNLO is

included in both cases.

Process	σ [pb]	$\Delta\sigma^{Total}$ [pb]	Δ_σ^{Scale}	Δ_σ^{PDF}	$\Delta_\sigma^{Br.}$	Calculation
1) $q\bar{q} \to WW$	53.2	$^{+2.5}_{-2.2}$	$^{+2.3}_{-1.9}$	$^{+1.0}_{-1.1}$	-	NLO MCFM
2) $gg \to WW$	1.4	$^{+0.3}_{-0.2}$	$^{+0.3}_{-0.2}$	$^{+0.1}_{-0.1}$	-	LO MCFM
3) $q\bar{q} \to WW$	59.1	$^{+1.6}_{-1.7}$	$^{+1.2}_{-1.0}$	$^{+0.9}_{-0.9}$	-	NNLO [31]
4) $gg \to H \to WW$	4.1	± 0.5	$\pm$ 0.3	± 0.3	± 0.2	NNLO [33]
W^+W^- production (pNNLO)	58.7	$^{+3.0}_{-2.7}$	$^{+2.7}_{-2.3}$	$^{+1.3}_{-1.4}$	1)+2)+4)	
W^+W^- production (NNLO)	63.2	$^{+2.0}_{-1.8}$	$^{+1.6}_{-1.4}$	$^{+1.2}_{-1.2}$	3)+4)	

Table 3.1 The first row gives the predicted cross sections for the non resonant $q\bar{q} \to W^+W^-$ production with the uncertainty from scale, PDF and α_s variations shown in pb. The second and fourth rows show the theoretical production cross section for the non-resonant $gg \to WW$ and the resonant $gg \to H \to WW$ process with their respective error decomposition. The NNLO cross section and its uncertainties for $q\bar{q} \to W^+W^-$ production are given in the third row, the scale uncertainty comes from the NNLO paper while the PDF uncertainty is taken from the corresponding NLO calculation. The partial and full NNLO cross sections for W^+W^- production are shown in the fifth and sixth rows, the uncertainties of non-resonant and resonant (through Higgs decays) W^+W^- productions are combined linearly.

The full NNLO cross section is used as a reference and compared with the measured total cross section. The partial NNLO calculation corresponds to current MC precision and it is used in MC event normalisation, fiducial measurements and the extrapolation from fiducial region to total phase space.

3.2.3 Signal MC

The W^+W^- production from quark-quark annihilation process is modeled by the POWHEG [34, 35] Monte Carlo generator, which incorporates the NLO QCD matrix elements and is interfaced to parton showering using the Pythia [36] program. All W's are sequentially decayed to leptons. The parton density function (PDF) set CT10 [37] is used with POWHEG.

The W^+W^- production from gluon-gluon fusion process is modeled by the MC generator gg2ww [38] and PDF set CT10, interfaced to Herwig/Jimmy [39] for parton showering and multiple parton scattering.

To be consistent with the other ATLAS diboson analyses and also to make easier comparison with CMS results, the qq/gg signal normalisation is derived using MCFM [40] and CT10 PDFs. The comparison of the prediction with different PDF sets is given in Table 3.2. To assess the impact of α_S used in the PDF, we use CT10nlo_as_011N.LHgrid PDF sets where $N = 7, 8, 9$ to vary α_S by ± 0.001 from its default value of 0.118. This yields $^{+0.5}_{-0.3}$% uncertainty for the cross section. The PDF uncertainty is smaller, which is

	CT10	NNPDF	MSTW08	ATLAS epWZ
$q\bar{q} + gg$ xsec [fb]	637 ± 1	641 ± 1	649 ± 2	671 ± 1
deviation from CT10 [%]	0.0	0.6	1.9	5.3
gg contribution [%]	2.65	2.80	2.75	2.27
PDF uncertainty [fb]	$^{+12}_{-13}$	± 10	$^{+12}_{-9}$	$^{+9}_{-10}$
PDF uncertainty [%]	$^{+1.8}_{-2.0}$	± 1.5	$^{+1.9}_{-1.4}$	$^{+1.3}_{-1.4}$

Table 3.2 Cross section predictions by MCFM for $q\bar{q} + gg \to W^+W^- \to \ell^+\nu_\ell\ell^-\bar{\nu}_\ell$ using different PDF sets (cross section uncertainties given are statistical only). The CT10 PDF uncertainties have been divided by 1.645 to scale from 90% CL to 68% CL. [30]

$^{+1.8}_{-2.0}$%. The impact of μ_R and factorisation μ_F scales varied independently by a factor of 0.5 or 2 is shown in Table 3.3, yielding uncertainties of $^{+4.0}_{-3.5}$%. As default scale in MCFM, the dynamic scale of half the invariant mass of the final state system is used. Adding the uncertainties from scale, PDF and α_S in quadrature yields a total uncertainty

	0.5 * μ_R	1 * μ_R	2 * μ_R
0.5 * μ_F	3.25%	-0.39%	-3.48%
1 * μ_F	3.52%	0.00%	-2.79%
2 * μ_F	3.99%	0.31%	-2.42 %

Table 3.3 Dependence of the cross section predictions by MCFM for $q\bar{q} + gg \to W^+W^- \to \ell^+\nu_\ell\ell^-\bar{\nu}_\ell$ on the variation of the μ_R and μ_F. Using the maximum and minimum values to construct the uncertainty envelope yields a scale uncertainty of $+4.0\%$ and -3.5%. [30]

of $^{+4.4\%}_{-4.0\%}$. Dividing the MCFM prediction by $\mathrm{Br}(W \to \ell\nu)^2 = 0.108^2$ yields then the total cross section prediction 54.6 $^{+2.4}_{-2.2}$ pb.

The SM Higgs production via the gluon-gluon fusion process, $gg \to H \to WW$, is modelled with POWHEG interfaced to Pythia, using CT10 PDFs and assuming m_H = 125 GeV. This sample is normalised following the recommendations of the LHC Higgs Cross Section Working Group, with a cross section of 19.27 ± 2.9 pb and a $H \to WW$ branching ratio of 21.5 ± 0.9 % at m_H = 125 GeV. Adding the uncertainties in quadrature yields a $gg \to H \to WW$ cross section of 4.1 ± 0.5 pb.

For these signal samples, the AU2-CT10 underlying-event tune was used for Pythia, while Herwig was run with the AUET2-CT10 configuration [41].

Table A.1 lists all the W^+W^- MC signal samples used in this analysis and the corresponding cross sections, assigned as detailed above. The resulting total signal cross section is $58.7^{+3.0}_{-2.7}$ pb. The uncertainties of the the non-resonant-WW and Higgs cross section are added linearly.

3.2.4 MC modelling for backgrounds

For the signal W^+W^- process, the major backgrounds come from the production of W or Z bosons, which are together with jets (V+jets), and also the production of the top quark. For the Z+jets MC samples, in order to achieve a better modelling of lepton η distributions at pre-selection level, we reweight the CTEQ6L1 LO PDF to the CT10 NLO PDF.

For the top process, the samples include both $t\bar{t}$ and single top production. We use MC@NLO [42] to model $t\bar{t}$ and single top events with the exception of t-channel single top events which are modelled using AcerMC. The details are listed in the Table A.5.

For the V+jets background, we use Alpgen. The di-boson processes WZ, ZZ and $W\gamma$ are modelled with POWHEG, Alpgen and Sherpa respectively (Table A.6).

The production of a W boson and a massive virtual photon γ^* also has the di-lepton plus E_T^{miss} signature. This is because the photon will possibly convert to two oppositely charged leptons outside the detector material and in vacuum [43]. Because of the massive photon, the potential exists for a significant background yield even relative to the case of zero mass photons externally converting in the detector to e^+e^- pairs. Samples were generated with Sherpa, with an upper mass cutoff of 7 GeV to avoid overlap with the WZ samples. The details for the samples are shown in the Tables A.6. Whenever LO event generators are used, the cross-sections are corrected by using k-factors to NLO or NNLO (if available) calculations.

3.3 Object selection

In WW signal event, there are two leptons with opposite charges and no jets existed. So we need to choose carefully the lepton and jet candidates. The lepton candidates are required to be associated with the primary vertex. There are in general several vertex reconstructed in the event. We take the vertex with the largest $\sum p_T^2$ as the primary vertex.

3.3.1 Electron

The electron identification algorithm is crucial to identify electrons and reject the backgrounds typically originating from jets faking electrons with rejection factors up to 10^5. The standard algorithm starts with a cluster in the electromagnetic calorimeter, and matches to a track among all those reconstructed in the inner detector. Since the electrons are reconstructed together with contaminations, typically hadronic jets and photon conversions, we need to rely on the shower shape, impact parameter, isolation and other

discriminants to reduce the background. Additional identification requirements based on a multivariate technique are applied.

The longitudinal impact parameter, z_0, is required to be less than 0.4 mm. Furthermore, the electron candidates are required to have a transverse impact parameter significance (the transverse impact parameter, d_0, divided by its uncertainty) of less than 3.0.

The calorimeter isolation is corrected for lateral leakage of the electron shower and also for pile-up effects. $E_{\mathrm{T}}(i)^{corr}$ is the calorimeter isolation energy is computed as the sum of the transverse energies in the topological cluster (calibrated at the electromagnetic scale) within a cone of a radius around the cluster. The energy from the core of the cone in the electromagnetic calorimeter (5x7 cells around the object barycenter) is subtracted from the sum. Since a photon or electron will leak some of its energy outside of this central core, the leakage correction is performed. The pile-up conditions in 2012 required a different strategy because of the increase in calorimeter noise. The pile-up corrections are performed. We apply the correction based on the event-by-event ambient energy density (ED).

The track isolation is computed by summing the p_T of all inner detector tracks within a cone. This variable is quite insensitive to pile-up for electrons because of the impact parameter cuts which constrain the tracks to come from the same vertex associated to the electron. Electron and conversion tracks are also removed when selection tracks.

We apply an energy scale correction to MC samples. The correction is derived through the study of $W \to e\nu$ and $Z \to ee$ events. And the electron ID efficiency is determined from $Z \to ee$ data using the *tag-and-probe* method as described in the Section 2.5. The scale-factors for the isolation (Iso) and impact parameter (IP) requirements are measured in $Z \to ee$ events using a tag-and-probe technique as described in the in Ref. [22]. A detailed selection criteria is given in the Table 3.4.

3.3.2 Muon

The muons selected are STACO combined muons, which means the inner detector and muon spectrometer tracks are combined when reconstructing the muons. Like what we have done in the electron case, we have impact parameter and isolation requirements to reduce the background. The longitudinal impact parameter, z_0, is required to be within 1 mm for muons. Muon candidates are required to have a transverse impact parameter significance of less than 3.0. In order to ensure the quality of the muon track, the hits requirement is used in the inner detector. For calorimeter isolation, we study the total transverse energy deposited in the calorimeter cells in the cone around the muon,

Electron Selection	
Geometrical Acceptance:	$\lvert\eta\rvert < 2.47$, excluding the transition region $1.37 \leq \lvert\eta\rvert \leq 1.52$
Kinematic Acceptance:	$E_{\mathrm{T}} > 7$ GeV
Identification Criteria:	VeryTight likelihood
Calorimeter Isolation Requirement:	$p_{\mathrm{T}} < 15$ GeV: $\sum_{\Delta R<0.3} E_{\mathrm{T}}^{corr}(i)/E_{\mathrm{T}(e)} < 0.20$ $15 < p_{\mathrm{T}} < 20$ GeV: $\sum_{\Delta R<0.3} E_{\mathrm{T}}^{corr}(i)/E_{\mathrm{T}(e)} < 0.24$ $p_{\mathrm{T}} > 20$ GeV: $\sum_{\Delta R<0.3} E_{\mathrm{T}}^{corr}(i)/E_{\mathrm{T}(e)} < 0.28$
Track Isolation Requirement:	$p_{\mathrm{T}} < 15$ GeV: $\sum_{\Delta R<0.4} p_{\mathrm{T}}(i)/p_{\mathrm{T}}(el) < 0.06$ $15 < p_{\mathrm{T}} < 20$ GeV: $\sum_{\Delta R<0.3} p_{\mathrm{T}}(i)/p_{\mathrm{T}}(el) < 0.08$ $p_{\mathrm{T}} > 20$ GeV: $\sum_{\Delta R<0.3} p_{\mathrm{T}}(i)/p_{\mathrm{T}}(el) < 0.10$
Transverse Impact Parameter Requirement:	$\frac{d_0}{\sigma_{d_0}} < 3$
Longitudinal Impact Parameter Requirement:	$\lvert z_0 \times \sin(\theta)\rvert < 0.4\,mm$

Table 3.4 Electron definition used in this analysis.

excluding the muon itself. The calorimeter isolation energy is corrected for the muon energy loss. For track based isolation, we study the p_{T} sum extends over all charged particle tracks within the cone, excluding the track of the muon itself. Tracks must come from the primary and quality cuts applied.

Let nPixHits denote the number of pixel hits, nPixelDeadSensors the number of crossed dead pixel sensors, nPixHoles the number of pixel holes which are not dead but failing to record the hits. Let nTRThits denote the number of TRT hits on the muon track, nTRToutliers the number of TRT outliers (TRT comprises many layers of gaseous straw tube elements interleaved with transition radiation material) on the muon track. There are several hits requirement to ensure the quality of selected object. For example, the sum of the number of SCT hits and the number of the SCT dead sensors is required to be no less than 5, which is denoted as nSCTHits + nSCTDeadSensors ≥ 5. A detailed description is given in the Table 3.5.

3.3.3 Jet

In this analysis, jets are reconstructed from topological clusters using the anti-kT algorithm [25] [26] [44]. They are required to have p_{T} greater than 25 GeV and $\lvert\eta\rvert < 4.5$. The jet vertex fraction (JVF) of a pair of one jet and one vertex is defined as the total momentum sum of tracks contributing to the jet that are compatible with the respective vertex, divided by the total jet momentum. Since JVF relies on the reconstruction of track and vertex, it can only be sensibly defined in the central detector region. To reduce the pile-up contribution, candidate jets within ID acceptance ($\lvert\eta\rvert < 2.4$) are required to have more than half of the summed scalar p_{T} of their associated tracks coming from tracks originating from the primary vertex ($\lvert JVF\rvert > 0.5$). A detailed description for the jet selection is given in the Table 3.6.

Muon Selection	
Reconstructed combined staco muon	
Geometrical Acceptance:	$\lvert\eta\rvert < 2.47$
Kinematic Acceptance:	$p_{\mathrm{T}} > 7$ GeV
Inner Detector Requirements:	nPixHits + nPixelDeadSensors > 0 nSCTHits + nSCTDeadSensors ≥ 5 nPixHoles + nSCTHoles < 3 for $0.1 < \lvert\eta\rvert < 1.9$: (nTRTOutliers+nTRTHits)> 5 nTRTOutliers/(nTRTOutliers+nTRTHits)< 0.9
Calorimeter Isolation Requirement:	$p_{\mathrm{T}} < 15$ GeV: $\sum_{\Delta R<0.3} E_T(i)p_T(\mu) < 0.06$ $15 < p_{\mathrm{T}} < 20$ GeV: $\sum_{\Delta R<0.3} E_T^{corr}(i)/p_T(\mu) < 0.12$ $20 < p_{\mathrm{T}} < 25$ GeV: $\sum_{\Delta R<0.3} E_T^{corr}(i)/p_T(\mu) < 0.18$ $p_{\mathrm{T}} > 25$ GeV: $\sum_{\Delta R<0.3} E_T^{corr}(i)/p_T(\mu) < 0.30$
Track Isolation Requirement:	$p_{\mathrm{T}} < 15$ GeV: $\sum_{\Delta R<0.4} p_T(i)/p_T(\mu) < 0.06$ $15 < p_{\mathrm{T}} < 20$ GeV: $\sum_{\Delta R<0.3} p_T(i)/p_T(\mu) < 0.08$ $p_{\mathrm{T}} > 20$ GeV: $\sum_{\Delta R<0.3} p_T(i)/p_T(\mu) < 0.12$
Transverse Impact Parameter Requirement:	$\lvert\frac{d_0}{\sigma_{d_0}}\rvert < 3$
Longitudinal Impact Parameter Requirement:	$\lvert z_0 \times \sin\theta\rvert < 1mm$

Table 3.5 Muon definition used in this analysis.

Jet Selection	
anti-k_T algorithm Jet	
Geometrical Acceptance:	$\lvert\eta\rvert < 4.5$
Kinematic Acceptance:	$p_{\mathrm{T}} > 25$ GeV
Jet Vertex Fraction:	$\lvert JVF\rvert > 0.5$ for $p_{\mathrm{T}} < 50$ GeV and $\lvert\eta\rvert < 2.5$

Table 3.6 Jet definition used in this analysis.

3.3.4 Overlap removal

At the end of the object selection an overlap removal procedure is applied when two or more analysis objects are believed to represent the same particle. Four different types of object overlap removal are considered: e/e, μ/e, e/jet and μ/jet.

The summary of the removal criteria is given below:

– e/e removal

If two electron candidates overlap within a cone of $\Delta R = 0.1$, remove the electron candidates with lower p_T;

– μ/e removal

If one muon candidate and one electron candidate overlap within a cone of $\Delta R = 0.1$, remove the electron candidate;

– e/jet removal

If one jet candidate and one electron candidate overlap within a cone of $\Delta R = 0.3$, remove the jet candidate.

Among these overlap removals, the most important one is the e/jet overlap re-

moval. The high p_T electron candidate, which is associated with the calorimeter cluster, can also be reconstructed by the anti-k_T algorithm. For this reason, jet candidates inside a cone of $\Delta R < 0.3$ in the η-ϕ plane around the selected electron candidates are removed. Energy from other clusters of that jet candidate is not ignored and is considered in the calorimeter isolation criterion of the electron candidate.

The other three removal schemes are meant to deal with rare problems, and are more relevant in the case of loosened quality criteria and have little effect with the current selection. Duplicate electron candidates are not an issue any more and an overlap removal between the reconstruction algorithms are already included inside the reconstruction algorithms. This has been checked that in our selection there are no electron candidates overlapping within $\Delta R < 0.1$. In rare cases a muon candidate traversing the detector will fake an electron cluster, for example by emitting a bremsstrahlung photon. This can result in an electron object very close to the muon candidate. So if we find an electron candidate within the cone of $\Delta R < 0.1$ around a selected muon candidate, the electron candidate will be removed. Unlike electrons, muons are not likely to be reconstructed as jets. But muons can be originating from the heavy flavour jets, so the μ/jet overlap removal is applied. These are a frequent source of non-isolated muons. Although the rejection of such muons is the purpose of the muon isolation requirements residual contributions from heavy flavour jets are suppressed by removing muon candidates that overlap with a jet candidate inside a cone of $\Delta R < 0.3$. This procedure can also remove genuine, isolated muons that have final state radiation (FSR) photon conversions reconstructed as jets. Therefore, the μ/jet overlap removal negatively affects the efficiency of the muon identification.

3.4 Event selection

The analysis includes the three final states $e^+e^-E_{\mathrm{T}}^{\mathrm{miss}}$, $\mu^+\mu^-E_{\mathrm{T}}^{\mathrm{miss}}$ and $e^\pm\mu^\mp E_{\mathrm{T}}^{\mathrm{miss}}$. For all three channels, common event selection criteria are applied with the exception of the Z-veto cut which is used only for same flavour (ee and $\mu\mu$) channel. The cut values may be different between channels. The event selection cuts were optimised by maximising the signal significance $S/\sqrt{S+B}$ for W^+W^- detection.

This section presents the cuts used in the analysis, along with the cut-flows and event yields for both data and MC, which are also compared graphically at different selection stages.

3.4.1 W^+W^- event selection criteria

The pre-selection of $W^+W^- \to \ell^+\nu_\ell\ell^-\bar{\nu}_\ell$ candidate events follows the standard recommendation by data quality and performance groups and proceeds as follows:

1. **Data Quality**

   Good luminosity blocks (the time unit in which ATLAS data is recorded) are selected from the data runs.

2. **Object preselection**

   Events must contain physics objects relevant to the analysis. At this stage, we preselect the electrons, muons and jets. The details about the object selection criteria is already mentioned in the section 3.3.1, section 3.3.2, and section 3.3.3.

3. **Object Overlap Removal**

   Overlapping objects are removed as described in Section 3.3.4.

4. **Event Cleaning**

   There was a hot tile calorimeter cell that had not been masked in the reconstruction in some data taking periods. Events are removed if a jet points to that region. Events with LAr noise burst and data corruption are removed. A total of 0.2% data is removed because of this. Corrupted events caused by Tile are rejected, and tile corrupted events from one particular tile channel are removed for Periods G-J. What is more, the tile calorimeter has suffered from frequent module trips since data-taking at $\sqrt{s} = 7$ TeV. These trips are considered a tolerable data quality defect as the trip is accounted for during off-line reconstruction. However, in order to control the event quality in a better way, the relevant events are removed. BCH cleaning is performed since it is found that the correction which was used to correct for masked cells within the tile calorimeter was not able to properly handle entire dead modules. For high p_T jets, the effect is more obvious. It is important to kill events if a selected jet falling into masked regions; otherwise, the reconstructions for both jet and $E_{\mathrm{T}}^{\mathrm{miss}}$ will be affected. We follow the recommended procedure and adopt the medium criteria. Events are removed if there is at least one good jet.

   MET cleaning is done by looking for jets with $p_{\mathrm{T}} > 20$ GeV which do not overlap with a selected electron within ΔR of 0.3. These jets are tested to pass looser bad jets criteria. If any jet passes these criteria, the event is removed to avoid corresponding adverse effects on $E_{\mathrm{T}}^{\mathrm{miss}}$.

5. **Primary Vertex Selection**

   The vertex with largest $\sum p_T^2$ is recognized as the primary vertex. The primary vertex is required to be reconstructed with at least 3 good tracks. The previous analysis using 2011 data was reweighting MC events based on vertex multiplicity distributions, thus adjusting to the observed in-time pileup (number of interactions in a given bunch crossing). Out-of-time pileup (detector signals from adjacent bunch crossings are overlapping) plays an important role. We reweights

the average number of interactions per bunch crossing $< \mu >$ distribution with which the MC was generated to that observed in data. The reweighting leads to significant loss of MC statistics due to some pileup weights being zero.

6. **Trigger Selection**

   In order to get a better performance and also gain more statistics, this analysis uses di-lepton trigger in the same flavour channels and a logical "OR" of dilepton and single lepton triggers in the combined channel ($e\mu$). The details are in the Table 3.7. The electron trigger efficiency is measured as a function of electron η and p_{T} with respect to the off-line ID criteria. The muon trigger efficiency is measured in η and ϕ.

   For e24vhi_medium1 and e60_medium1, they refer to two electrons with a trigger threshold of 24 GeV and 60 GeV respectively. The letter 'i' means applying a cut on track isolation at Event Filter, $\frac{pTcone20}{pT(\mu)} < 0.12$, where $pTcone20$ is the p_{T} sum of ID tracks in cone $dR = 0.2$. And 'vh' means applying a cut on the hadronic core isolation at L1. Then 'medium' means the medium criteria on the electron likelihood ID. For mu24i_tight and mu36_tight, they refer to two muons with a trigger threshold of 24 GeV and 36 GeV respectively. Similarly, 'tight' means the tight criteria on the electron likelihood ID. The trigger items with lower thresholds have a lepton isolation criteria. The trigger items with higher thresholds for both electrons and muons are also considered. They are needed since the isolation criteria of the trigger items with lower thresholds tend to be strict for leptons with with p_{T} sufficiently far from the low p_{T} thresholds.

   For 2e12Tvh_loose1, it refers to 2 electrons with a trigger threshold of 12 GeV. The letter 'T' means the L1 seed is tighter than default. The letter 'i' means apply a cut on track isolation at Event Filter $\frac{pTcone20}{pT(e)} < 0.1$. 2e12Tvh_loose1_L2StarB is identical to 2e12Tvh_loose1, apart from a more efficient tracking at L2. The "EFFS" chain is to find multi-muons with full scanning at EF, once single muon trigger (L1 $\to$ L2 $\to$ EF) is confirmed. Here mu18_tight_mu8_EFFS is to find 18 GeV and 8 GeV muons with EF full scan after mu18_tight (L1_MU15 $\to$ L2_mu18_tight $\to$ EF_mu18_tight) is confirmed. For e12Tvh_medium1_mu8, it refers to an electron and a muon with a trigger threshold of 12 GeV and 8 GeV respectively.

   The typical efficiency for an 2e12Tvh_loose1 to trigger an electron with $p_{\mathrm{T}} > 25$ GeV is $> 98\%$ in the barrel and $> 95\%$ in the end-cap region. The single-electron triggers in contrast reach their plateau with comparable efficiencies at 60 GeV. Below that threshold the trigger exhibits a turn-on starting at 25 GeV with an efficiency of $> 90\%$ and $> 80\%$ in the barrel and end-cap at the plateau region

respectively.

For the $\mu\mu$ channel, the mu18_tight_mu8_EFFS trigger is used. The L1 seed is identical to mu24i_tight, i.e. the trigger is seeded by a single lepton trigger. The efficiency for the mu18_tight leg is 60-90% (80-95%) for barrel (end-cap), for mu8_EFFS it is $> 98\%$ ($> 95\%$) for the barrel (end-cap).

The combined $e\mu$ trigger e12Tvh_medium1_mu8 is only $\sim 80\%$ efficient for a di-lepton event). To gain more statistics, events are also selected with the single-lepton triggers mu24i_tight, mu36_tight, e24vhi_medium1 and e60_medium1. As a result $\sim 20\%$ of the events at preselection have passed the track-isolation cut. The combination of single- and di-lepton triggers has been chosen since it gives higher event yields for leading leptons of $25 < p_{\mathrm{T}} < 60$ GeV.

The trigger scale factors, which cover the trigger efficiency between data and MC, can be derived through the efficiency study of Z events. For an OR of several triggers, the scale factor is expressed as:

$$\mathrm{SF} = \frac{1 - \Pi_i(1 - \epsilon_i^{data})}{1 - \Pi_i(1 - \epsilon_i^{MC})} \tag{3.1}$$

where the product will go over leptons i in the event which pass the selection. The variables ϵ_i^{data}, ϵ_i^{MC} are the efficiencies for each lepton to pass the selection in the trigger system in data and MC, respectively.

7. **Dilepton Selection**
   An event is selected if it has exactly two isolated, oppositely charged leptons with $p_{\mathrm{T}} > 25/20$ GeV for leading/trailing leptons respectively according to the lepton selection which is described in Section 3.3.1 and Section 3.3.2. This requirement ensures that the considered lepton is on or close enough to the trigger plateau and enables the usage of the trigger scale factors. It also strongly reduces the W+jets and QCD backgrounds due to the p_{T} dependence of the muon fake rate. In order to suppress other diboson backgrounds, events are rejected if any additional leptons with $p_{\mathrm{T}} > 7$ GeV.

8. **Trigger matching**
   Both leptons have to be matched to the di-lepton trigger in the same flavour channels. This is to ensure the leptons which help to fire the trigger are truly the ones that are selected after nominal cuts. In the $e\mu$ channel, at least one of the leptons (with $p_{\mathrm{T}} > 25$ GeV) has to be matched to any of the single lepton triggers or both have to be matched to the di-lepton trigger.

After the preselection, the dominant contribution (>99%) to ee and $\mu\mu$ events comes from the inclusive $Z/\gamma* \to \ell^+\ell^-$ process. The W^+W^- signal only contributes

	$e\mu/\mu e$	ee	$\mu\mu$
single electron	e24vhi_medium1 e60_medium1	—	—
single muon	mu24i_tight mu36_tight	—	—
di-lepton	e12Tvh_medium1_mu8	2e12Tvh_loose1 2e12Tvh_loose1_L2StarB	mu18_tight_mu8_EFFS

Table 3.7 List of triggers used in the different channels. In the $e\mu$ channel any of the single-lepton triggers or the combined $e\mu$ trigger is required. In the same-flavour channels only a single di-lepton trigger is used.

$\sim$0.14% of the selected events. For the $e\mu$ final state, the W^+W^- signal contributes already 11.7%, where the major background contributions come from $t\bar{t}$/single-top (60.7%), $Z \to \tau\tau$ (22.6%) and QCD (W+jet and di-jets) (5%). Above decomposition numbers are based on MC studies.

The final W^+W^- event selection cuts are optimised for a better signal-over-background ratio. The details are listed below.

1. **Invariant mass cut**
   The invariant mass of the dilepton pair ($M_{\ell\ell}$) must be greater than 15 (10) GeV for $ee/\mu\mu$ ($e\mu$) events to further remove dijet events and the low mass spectrum not modelled by MC.

2. **Z-veto**
   $|M_{\ell_1\ell_2} - M_Z| > 15$ GeV for the ee and $\mu\mu$ channels to remove events from $Z \to \ell^+\ell^-$. M_Z represents the mass of the Z bosons $M_Z = 91.2$ GeV.

3. **Calorimeter MET**
   For calorimeter-based $E_{\mathrm{T}}^{\mathrm{miss}}$, four different cut variables are investigated: $E_{\mathrm{T}}^{\mathrm{miss}}$ (STVF), $E_{\mathrm{T,\,Rel}}^{\mathrm{miss}}$ (STVF), $E_{\mathrm{T}}^{\mathrm{miss}}$ (RefFinal), $E_{\mathrm{T,\,Rel}}^{\mathrm{miss}}$ (RefFinal). The details are in the appendix. $E_{\mathrm{T,\,Rel}}^{\mathrm{miss}}$ (RefFinal) is best modeled and it is preferred in the case of similar significance as others.

   For the calculation of the missing transverse energy, we use the four-vector sum of the transverse momentum of the neutrinos stemming from the W boson decays. In order to reduce the sensitivity due to possible mis-measured leptons or jets, this analysis uses a modified missing transverse energy. $E_{\mathrm{T,\,Rel}}^{\mathrm{miss}} > 45$ (15) GeV for the $ee/\mu\mu$ ($e\mu$) channels, respectively. The $E_{\mathrm{T,\,Rel}}^{\mathrm{miss}}$ variable is defined as [24]

$$E_{\mathrm{T,\,Rel}}^{\mathrm{miss}} = \begin{cases} E_{\mathrm{T}}^{\mathrm{miss}} \times \sin(\Delta\phi_{\ell,j}) & \text{if } \Delta\phi_{\ell,j} < \pi/2 \\ E_{\mathrm{T}}^{\mathrm{miss}} & \text{if } \Delta\phi_{\ell,j} \geq \pi/2, \end{cases} \tag{3.2}$$

   where $\Delta\phi_{\ell,j}$ is the difference in ϕ between the $E_{\mathrm{T}}^{\mathrm{miss}}$ and nearest lepton (e, μ) or jet. The use of this variable tends to reduce the sensitivity to mis-measured

leptons or jets, so that we can enhance the sensitivity to $E_{\mathrm{T}}^{\mathrm{miss}}$ from neutrinos. Hence $E_{\mathrm{T,\,Rel}}^{\mathrm{miss}}$ is the $E_{\mathrm{T}}^{\mathrm{miss}}$ transverse to the nearest lepton or jet if that object is in the same hemisphere and $E_{\mathrm{T}}^{\mathrm{miss}}$ itself otherwise. Figure 3.3 shows the $E_{\mathrm{T,\,Rel}}^{\mathrm{miss}}$ distributions for $ee,\ \mu\mu$ and $e\mu$ channels just before the $E_{\mathrm{T,\,Rel}}^{\mathrm{miss}}$ cut is applied.

4. **Track MET**

   The calorimeter based measurement of missing transverse energy suffers in high pile-up conditions from the large amount of energy deposited in the detector in each bunch crossing. This worsens the resolution of the measurement and the suppression of Z+jets background events. Therefore, track based missing transverse energy is used in combination with the calorimeter based measurement to discriminate against Z+jets background. It is defined as the negative vectorial sum of all tracks satisfying $p_{\mathrm{T}} > 500$ MeV, $|\eta| < 2.5$, $|d_0| < 1.5$ mm $|z_0 \sin\theta| < 1.5$ mm, $n_{\mathrm{Pix}} \geq 1$, $n_{\mathrm{SCT}} \geq 6$. The tracks from the signal leptons are included regardless of their quality; for signal electrons the track is replaced by the calorimeter based measurement of the transverse energy E_{T}, for signal muons the track is replaced by the track obtained using the full inner detector and spectrometer information.

   This calculation provides an alternative measurement to the Calorimeter MET $E_{\mathrm{T,\,Rel}}^{\mathrm{miss}}$ with uncorrelated systematic effects. The missing transverse momentum is based on information from the inner detector and therefore only includes charged particles within $|\eta| < 2.5$. It is more pile-up robust since it uses only tracks originating from the primary vertex. The systematic uncertainties of the measurement are evaluated independently from the calorimeter-based MET. Moreover, missing transverse momentum does not account for photons and neutral hadrons which limits the uncertainty sources.

   We require $p_{\mathrm{T}}^{\mathrm{miss}} > 45$ (20) GeV for $ee/\mu\mu$ ($e\mu$) channels to further suppress the Drell-Yan contribution. This variable is less sensitive to pile-up than $E_{\mathrm{T,\,Rel}}^{\mathrm{miss}}$. Figure 3.4 shows the $p_{\mathrm{T}}^{\mathrm{miss}}$ distributions for $ee,\ \mu\mu$ and $e\mu$ channels before the cut is applied. Figure 3.5 shows the $\Delta\phi(E_{\mathrm{T}}^{\mathrm{miss}}, p_{\mathrm{T}}^{\mathrm{miss}})$ before the missing transverse momentum cut and in the zero jet bin.

5. **Azimuthal angle of MET**

   Since in the Z events the missing transverse energy is usually fake, The azimuthal angle between $E_{\mathrm{T,\,Rel}}^{\mathrm{miss}}$ and $p_{\mathrm{T}}^{\mathrm{miss}}$ tends to be flat distributed. Unlike Z events, the WW events will have true missing transverse energy so that the $E_{\mathrm{T,\,Rel}}^{\mathrm{miss}}$ and $p_{\mathrm{T}}^{\mathrm{miss}}$ tend to go to the same direction. We require $|\Delta\phi(E_{\mathrm{T}}^{\mathrm{miss}}, p_{\mathrm{T}}^{\mathrm{miss}})| < 0.3$ (0.6) for $ee/\mu\mu$ ($e\mu$) channels. This variable is another powerful discriminant against Drell-Yan contamination. Figure 3.6 shows the distribution just before the final cut. The optical cut values are set by a grid scan of 2D significance plots which are shown

in the appendix.

6. **Jet-veto**

   Jet-veto is the final cut. We require the number of selected jets to be zero. Jet vertex fraction is only applied to jets with $E_T < 50$ GeV and $|\eta| < 2.4$. This cut removes very effectively inclusive top events with leptonic decay modes. Figure 3.7 shows the jet multiplicity distribution before the jet veto cut is applied.

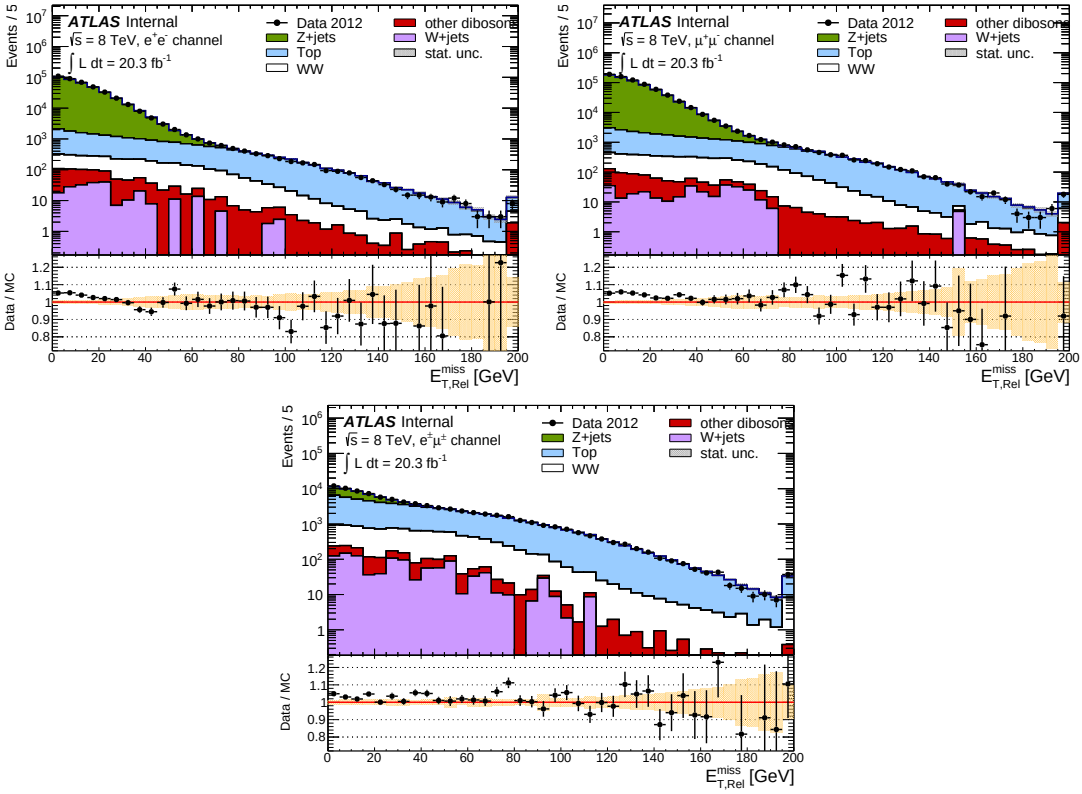

Figure 3.3 Relative missing transverse energy $E_{\mathrm{T,\,Rel}}^{\mathrm{miss}}$ distribution after Z veto for the ee (left) and $\mu\mu$ (middle) and $e\mu$ channels. Data are shown together with the processes predicted by Monte-Carlo and scaled to 20.3 fb^{-1}. Statistical uncertainties are shown as gray bands in the main plot or as orange bands on the ratio plot. [30]

Figures 3.8 and 3.9 shows kinematic distributions for W^+W^- candidate events after all selection cuts are applied. Figure 3.8 shows the transverse momenta p_{T} of the leading and trailing leptons as well as their azimuthal separation. Figure 3.9 shows several distributions of the di-lepton and the di-lepton+$E_{\mathrm{T}}^{\mathrm{miss}}$ system, i.e. the transverse momentum of dilepton $p_{\mathrm{T}}(\ell\ell)$, the transverse momentum of dilepton and $E_{\mathrm{T}}^{\mathrm{miss}}$ system $p_{\mathrm{T}}(E_{\mathrm{T}}^{\mathrm{miss}}\ell\ell)$ and the transverse mass of dilepton and $E_{\mathrm{T}}^{\mathrm{miss}}$ system $M_{\mathrm{T}}(E_{\mathrm{T}}^{\mathrm{miss}}\ell\ell)$. In these figures the points represent data and stacked histograms are from MC predictions for signal and background.

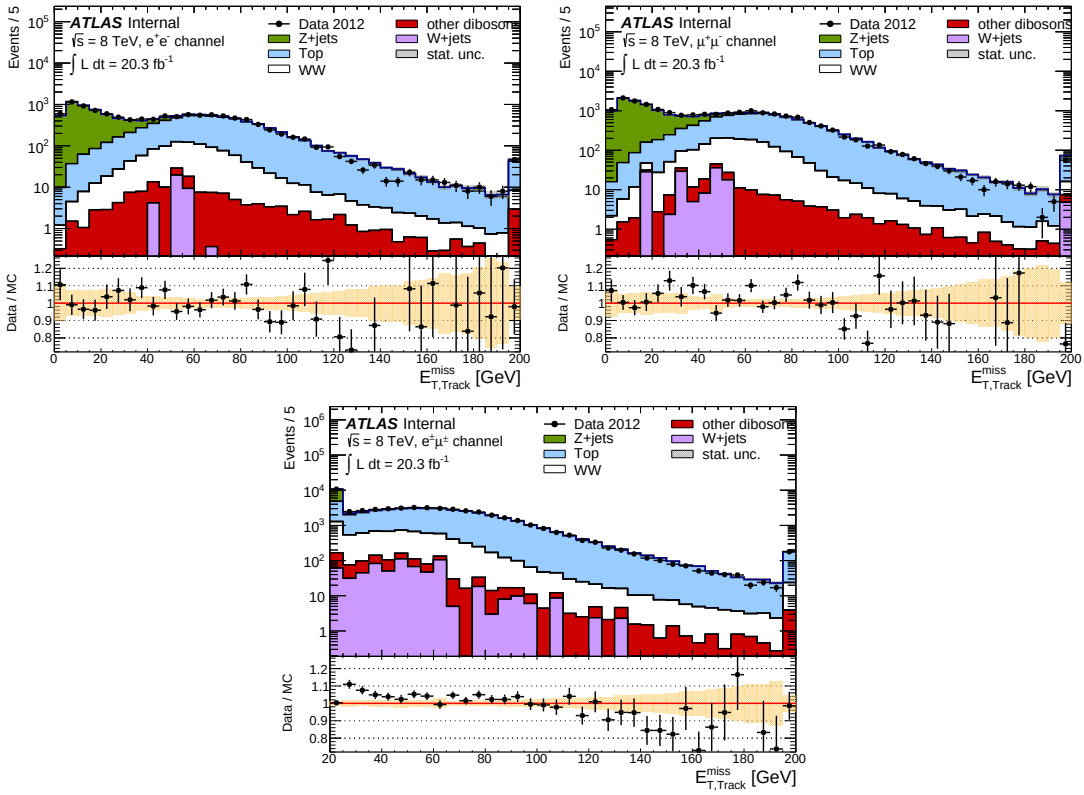

Figure 3.4 Missing transverse momentum $p_{\mathrm{T}}^{\mathrm{miss}}$ distribution after $E_{\mathrm{T,\,Rel}}^{\mathrm{miss}}$ cut for the ee (left) and $\mu\mu$ (middle) and $e\mu$ channels. Data are shown together with the processes predicted by Monte-Carlo and scaled to 20.3 fb^{-1}. Statistical uncertainties are shown as gray bands in the main plot or as orange bands on the ratio plot. [30]

Cuts	ee	$\mu\mu$	$e\mu$	Combined
2 leptons	6011503	10414698	167682	16593883
opposite-sign	5996645	10410426	157280	16564351
ℓ p_{T}, trigger-match	4945211	8406743	84698	13436652
BCHMedium Cleaning	4929115	8380532	83086	13392733
$M(\ell\ell) > 15/10$ GeV	4918726	8357583	83042	13359351
$\lvert M(\ell\ell) - M_Z \rvert > 15$ GeV	412853	721978	—	1217873
$E_{\mathrm{T,\,Rel}}^{\mathrm{miss}} > 45/15$ GeV	11594	19887	52142	83623
$p_{\mathrm{T}}^{\mathrm{miss}} > 45/20$ GeV	5762	9152	43718	58632
$\Delta\phi(E_{\mathrm{T}}^{\mathrm{miss}}, p_{\mathrm{T}}^{\mathrm{miss}}) < 0.3/0.6$	2613	4291	27591	34495
Jet Veto	594	975	5067	6636

Table 3.8 Event selection cut-flow for data collected in 2012 at 8 TeV for 20.3 fb^{-1} split in channels. For the $M(\ell\ell)$, $E_{\mathrm{T,\,Rel}}^{\mathrm{miss}}$, $p_{\mathrm{T}}^{\mathrm{miss}}$ and $\Delta\phi(E_{\mathrm{T}}^{\mathrm{miss}}, p_{\mathrm{T}}^{\mathrm{miss}})$ cuts, two cut values are presented in first column, with the first one for same flavor channel and the second one for $e\mu$ channel.

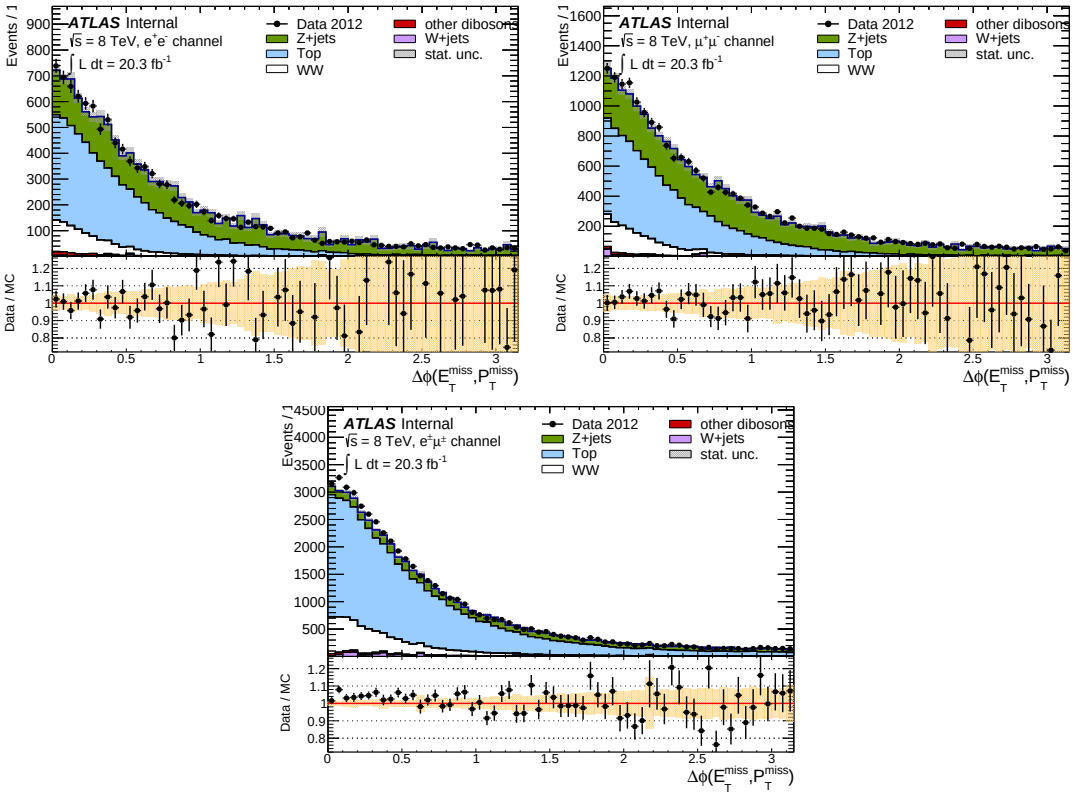

Figure 3.5 Azimuth angle between missing transverse energy and momentum $\Delta\phi(E_{\mathrm{T}}^{\mathrm{miss}}, p_{\mathrm{T}}^{\mathrm{miss}})$ distribution after $E_{\mathrm{T,\,Rel}}^{\mathrm{miss}}$ cut and in the zero jet bin. The channels follow from ee (left), $\mu\mu$ (middle) to $e\mu$ channel on the right. Data are shown together with the processes predicted by Monte-Carlo and scaled to 20.3 fb^{-1}. Statistical uncertainties are shown as gray bands in the main plot or as orange bands on the ratio plot. [30]

Final State	ee Channel	$\mu\mu$ Channel	$e\mu$ Channel	inclusive
Observed Events	594	975	5067	6636
Total MC prediction (S+B)	553.2± 13.0	903.9± 11.3	4427.9± 33.3	5884.9± 37.5
MC W^+W^- signal	349.6± 3.3	614.4± 4.5	3254.8± 10.3	4218.8± 11.7
Top	96.9± 4.8	131.4± 6.1	625.9± 12.5	854.2± 14.7
Z+jets	55.3± 6.3	106.0± 7.0	164.6± 15.4	326.0± 18.1
W+jets	21.6± 9.7	13.6± 4.3	225.3± 24.4	260.5± 26.6
Dibosons	27.3± 1.4	38.4± 1.3	149.7± 4.0	215.4± 4.4
Total Background	203.6± 12.6	289.5± 10.3	1173.1± 31.7	1666.1± 35.6

Table 3.9 Summary of observed data events and expected signal and background contributions as predicted by Monte-Carlo in the three channels and their combined results. Monte-Carlo yields are normalized to an integrated luminosity of 20.3 fb^{-1}. Only statistical uncertainties are shown.

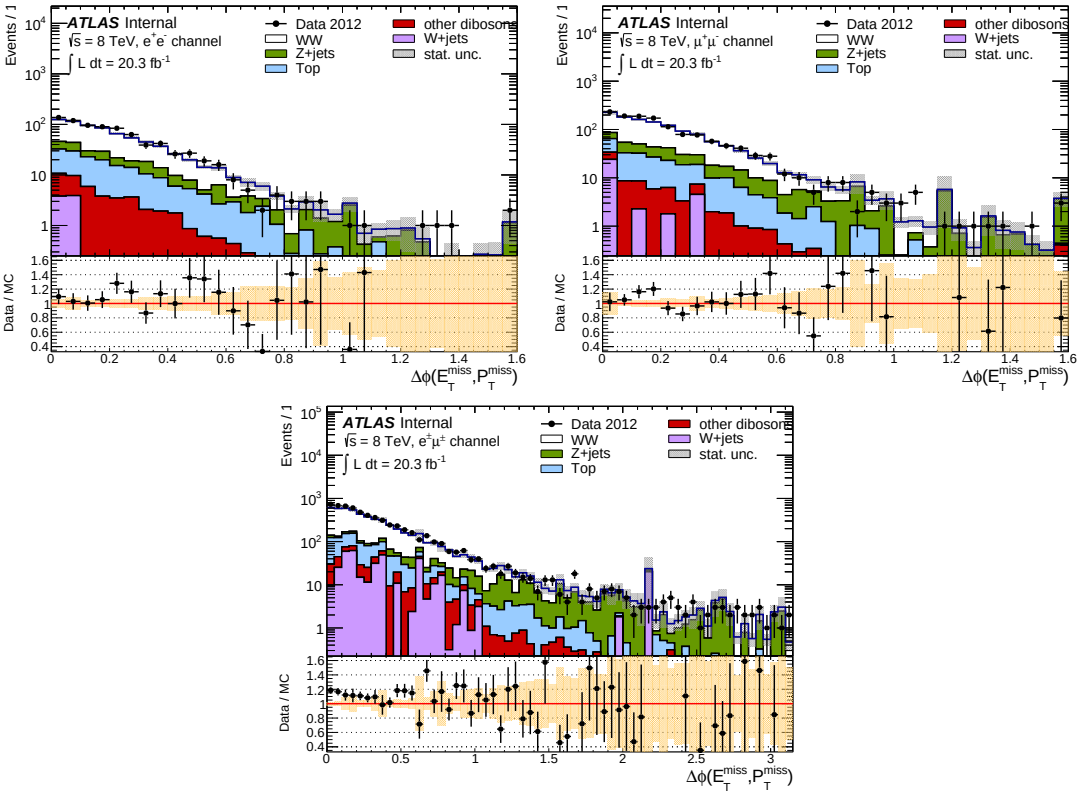

Figure 3.6 Azimuth angle between missing transverse energy and momentum $\Delta\phi(E_{\mathrm{T}}^{\mathrm{miss}}, p_{\mathrm{T}}^{\mathrm{miss}})$ distribution after $p_{\mathrm{T}}^{\mathrm{miss}}$ cut and in the zero jet bin. The channels follow from ee (left), $\mu\mu$ (middle) to $e\mu$ channel on the right. Data are shown together with the processes predicted by Monte-Carlo and scaled to 20.3 fb^{-1}. Statistical uncertainties are shown as gray bands in the main plot or as orange bands on the ratio plot. [30]

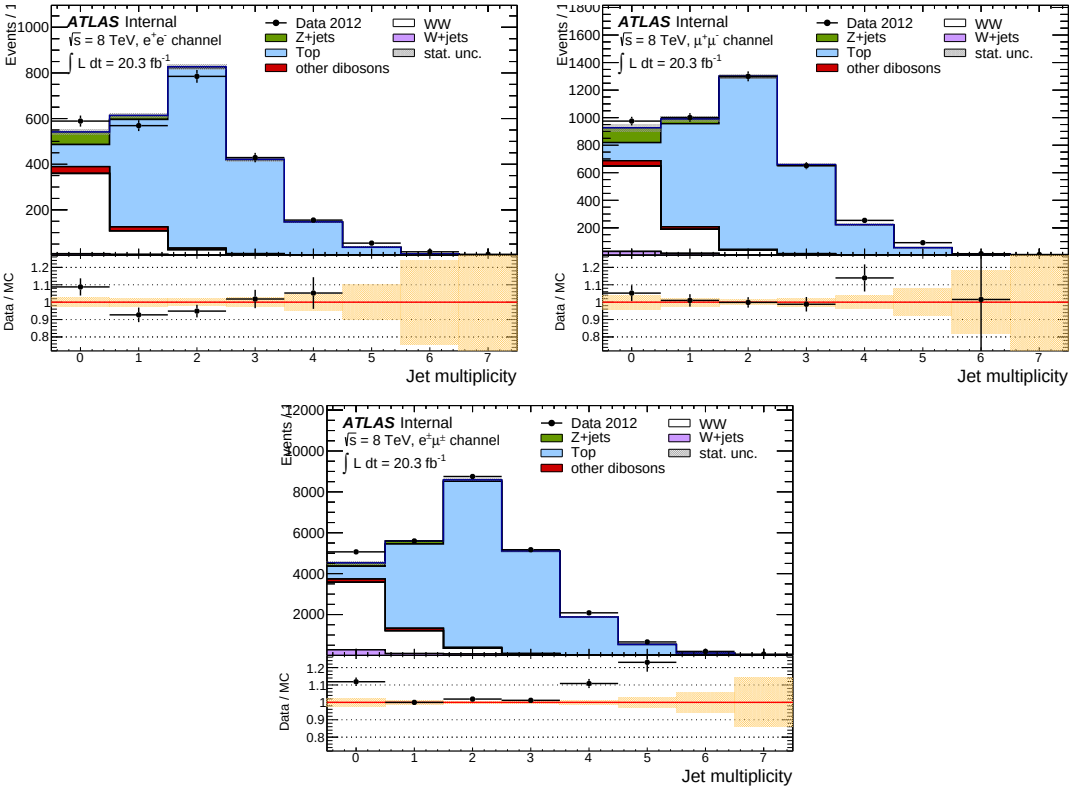

Figure 3.7 Jet multiplicity distribution before the jet veto. From left to right the ee and $\mu\mu$ and $e\mu$ channels are shown. Data are shown together with the processes predicted by Monte-Carlo and scaled to 20.3 fb^{-1}. Statistical uncertainties are shown as gray bands in the main plot or as orange bands on the ratio plot. [30]

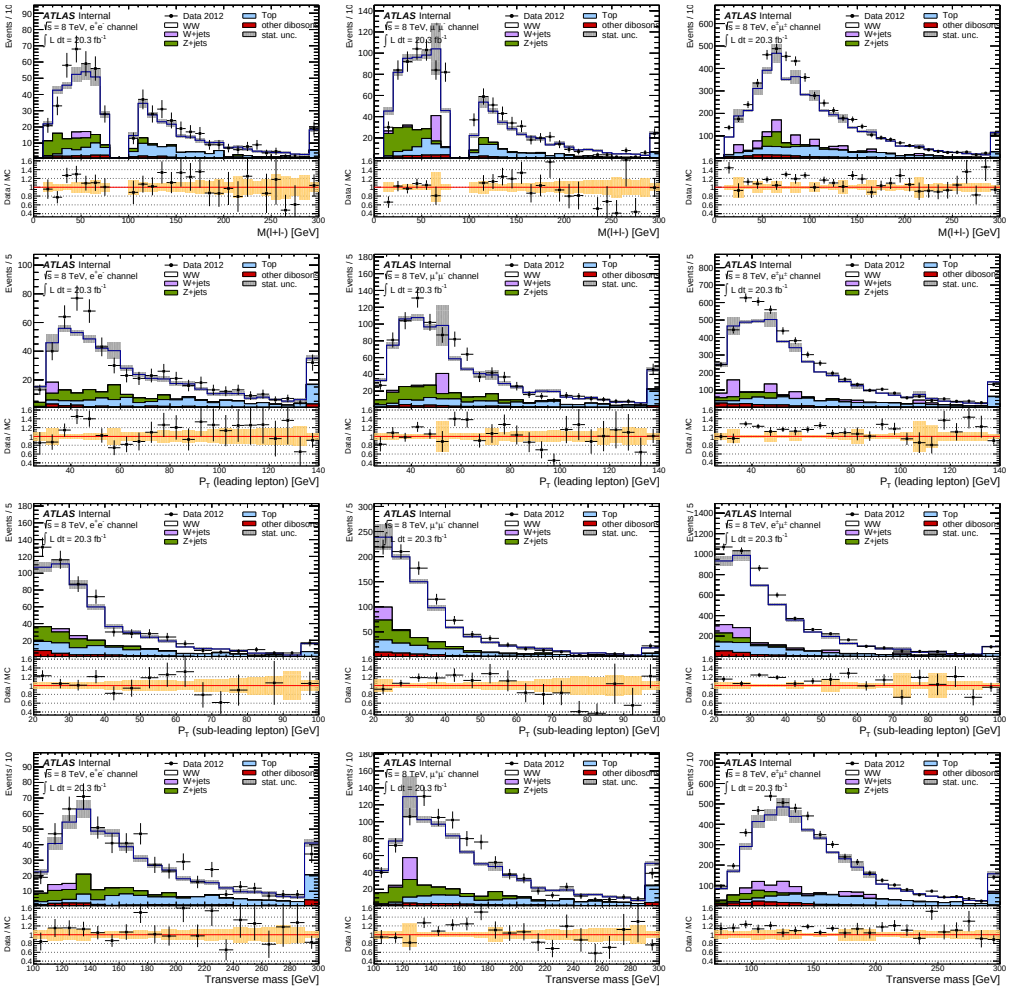

Figure 3.8 Distributions for WW candidate events after final selection for the ee (left), $\mu\mu$ (middle) and $e\mu$ channels (right). Data are shown together with the processes predicted by Monte-Carlo and scaled to 20.3 fb^{-1}. The top row shows invariant mass of the selected leptons, the second row the transverse momentum of the leading lepton p_{T}, the third row the transverse momentum p_{T} of the trailing lepton and the bottom row shows the transverse mass of the system. Statistical uncertainties are shown as gray bands in the main plot or as orange bands on the ratio plot. [30]

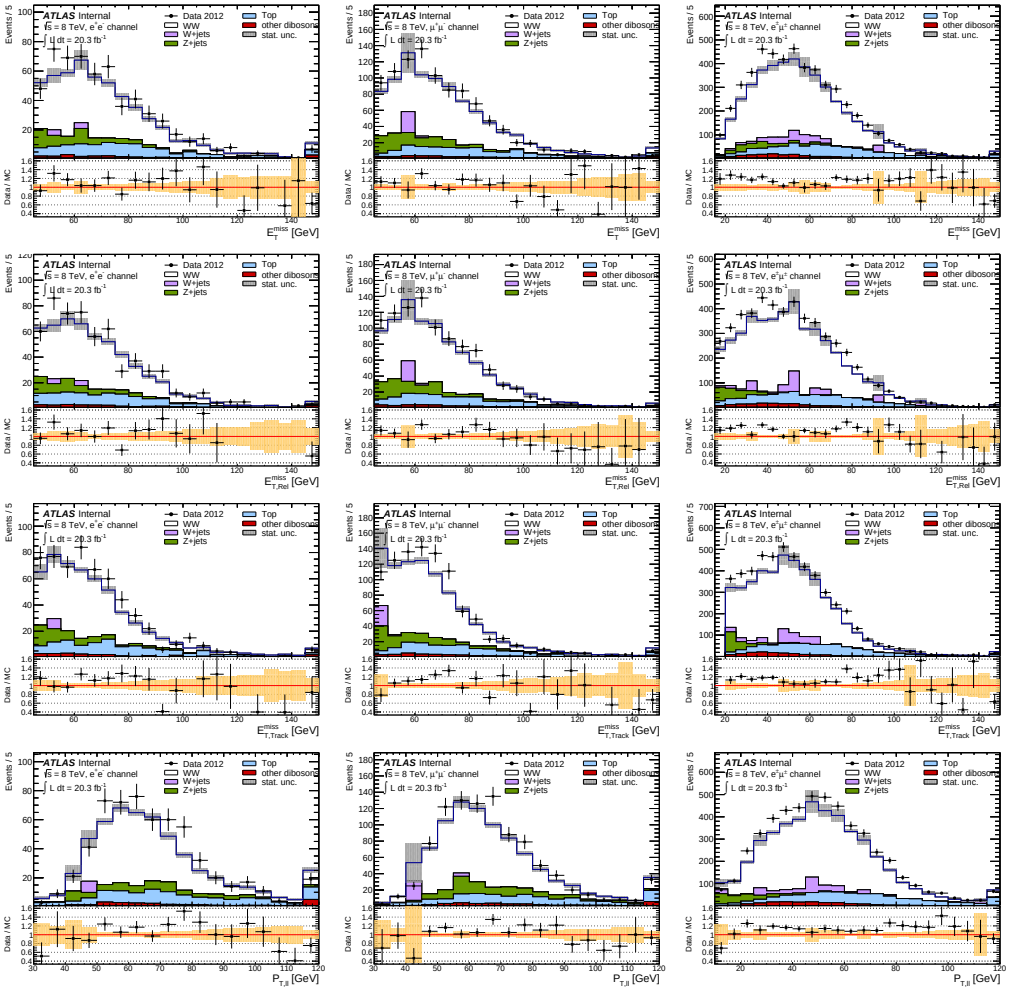

Figure 3.9 Distributions for WW candidate events after final selection for the ee (left), $\mu\mu$ (middle) and $e\mu$ channels (right). Data are shown together with the processes predicted by Monte-Carlo and scaled to 20.3 fb^{-1}. The top row shows the missing transverse energy $E_{\mathrm{T}}^{\mathrm{miss}}$, the second row the *relative* missing transverse momentum $E_{\mathrm{T,\,Rel}}^{\mathrm{miss}}$, the third row the missing transverse momentum $p_{\mathrm{T}}^{\mathrm{miss}}$ and the bottom row the transverse momentum of dilepton $p_{\mathrm{T}}\,(\ell\ell)$. Statistical uncertainties are shown as gray bands in the main plot or as orange bands on the ratio plot. [30]

3.5 Background estimation

In this analysis, the important background contributions are from Z+jets, top, W+jets, and di-boson.

- Z**+jets**
  with $E_{\mathrm{T}}^{\mathrm{miss}}$ due to mismeasurement.
- $t\bar{t}$ **and** Wt
  where no high energetic jets are detected.
- W**+jets**
  with a jet misidentified as a lepton.
- **Di-boson**
  $W + \gamma$ with the γ identified as an electron. $WZ/\gamma^* \to \ell\ell\ell\nu$ where one final state lepton is not detected. $ZZ \to \ell\ell\nu\nu$ where the dilepton invariant mass is not near the Z-mass. $ZZ \to \ell\ell\ell\ell$ where two leptons are not detected.
- **QCD**
  It is possible to get background from multijet QCD where both leptons and the missing energy are due to misidentification.

3.5.1 W+jets background

3.5.1.1 Matrix method

The baseline method, matrix method [45] is used to estimate the W+jets and QCD background. First we need to define the loose leptons. The loose selections are chosen to be:

- Loose electrons: satisfying selection criteria close to those of the full electron selection of the analysis, including the kinematic and basic quality requirements, and then only passing Medium operating point (instead of the VeryTight in the nominal analysis), no isolation and IP requirements are applied.
- Loose muons: satisfying the full muon ID used in the WW analysis except isolation and impact parameter requirements.

The tight criteria is the same with the nominal analysis. The relationship between the tight/loose leptons and real/fake leptons can be reflected in the Equation 3.3. The matrix element include the signal lepton efficiency and fake rate, which are needed for the estimating the W+jets/QCD yield. For our analysis there are two leptons in the final state, so this method can be expressed as the equation below.

$$\begin{pmatrix} N_{TT} \\ N_{TL} \\ N_{LT} \\ N_{LL} \end{pmatrix} = \begin{pmatrix} r_1 r_2 & r_1 f_2 & f_1 r_2 & f_1 f_2 \\ r_1(1-r_2) & r_1(1-f_2) & f_1(1-r_2) & f_1(1-f_2) \\ (1-r_1)r_2 & (1-r_1)f_2 & (1-f_1)r_2 & (1-f_1)f_2 \\ (1-r_1)(1-r_2) & (1-r_1)(1-f_2) & (1-f_1)(1-r_2) & (1-f_1)(1-f_2) \end{pmatrix} \times \begin{pmatrix} N_{RR} \\ N_{RF} \\ N_{FR} \\ N_{FF} \end{pmatrix} \tag{3.3}$$

with the following definitions:

- N_{TT} is the number of events which have exactly two tight leptons,
- N_{TL} and N_{LT} are the numbers of events which have one tight lepton and one loose one (which does not fulfil the tight criteria),
- N_{LL} is the number of events which have exactly two loose leptons (which do not fulfil the tight criteria),
- N_{RR} is the number of events which have exactly two real leptons,
- N_{RF} and N_{FR} are the number of events which have one real and one fake leptons,
- N_{FF} is the number of events which have exactly two fake leptons.
- The parameters in the matrix r_1, r_2 are the efficiencies for the loose real leptons to pass the tight criteria
- The parameters f_1, f_2 are the probabilities for loose fake-leptons to pass the tight criteria.

With the fake rates and lepton efficiency in the above equation, the contribution of W+jets and QCD can be interpreted as :

$$N_{W+\text{jets}} = N_{RF} \cdot r_1 f_2 + N_{FR} \cdot f_1 r_2 \tag{3.4}$$

$$N_{\text{QCD}} = N_{FF} \cdot f_1 f_2 \tag{3.5}$$

In practice, for each selected event we will calculate the matrix. The fake rates and lepton efficiency are dependent of η and p_{T}. And only one of the numbers N_{LL},N_{TL},N_{LT} and N_{TT} is non zero. So the main idea is to rightly get the fake rates and lepton efficiency. For the $e\mu$ channel we split it into 2 parts depending on whether the electron has larger p_{T} than muon. This can help us to better understand the behavior since more often the fake lepton will have relatively lower p_{T}. The crucial part of the matrix method, is how to determine the proper lepton efficiency and fake rate. By the equation above one can easily see the estimation is heavily dependent on them.

Because of the lack of a clean W+jets sample, the fake rate is estimated in a di-jet sample, which could provide us enough statistics. Di-jet events are selected by requiring exactly one jet in the detector, which is called the tag jet and is opposite to the fake-lepton candidate. And also we need dedicated selection criteria to reduce the contribution from genuine leptons:

- The same data quality as in nominal analysis.
- Lepton selection according to the loose criteria listed above.
- Z veto: events that have more than one loose lepton are rejected.
- W veto: events with a transverse mass $M_{\text{T}} > 40$ GeV or $E_{\text{T}}^{\text{miss}} > 25$ GeV are rejected.
- Exactly one jet in the event.

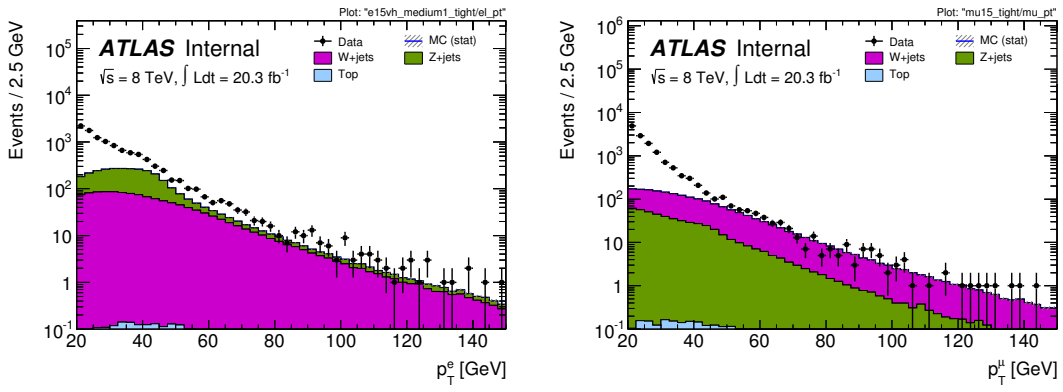

Figure 3.10 Measurement of fake-rates for electrons using EF_e15vh_medium1 (left) and for muons using EF_mu15 (right). Shown are the numerator plots, i.e. tight leptons. Contributions from genuine leptons are subtracted using Monte-Carlo. [30]

– Azimuthal angle between fake candidate and jet $\Delta\phi > 2$.

After these selections, the sample is highly contaminated by genuine leptons from $W \to \ell\nu$ and $Z \to \ell\ell$ decays, especially for the high transverse momentum. Contributions from genuine leptons are statistically subtracted using Monte-Carlo.

The resulting fake-rates for the different triggers are shown in Figure 3.11 as a function of transverse momentum. This is shown in Fig. 3.10. For the input to the matrix method the measurement is binned in seven or five bins in transverse momentum for electrons and muons respectively and two bins in pseudo-rapidity.

The signal lepton efficiency, as the other important element in the matrix, is derived by MC simulation and scaled by data-to-MC efficiency ratio. All the MC samples in the nominal analysis are used with all selection but $E^{miss}_{\mathrm{T,Rel}}$, p_T^{miss} and $\Delta\phi(E^{\mathrm{miss}}_{\mathrm{T}}, p^{\mathrm{miss}}_{\mathrm{T}})$ relaxed for higher statistics for Z+jets events. The efficiencies measured in MC are averaged according to the relative contribution of each component in the nominal selection. The Z+jets samples is studied to derive the correction factor which cover the efficiency difference between data and MC.

The main systematics is the sample dependence, which reflects the kinematic and flavor composition differences between the W+jets and the di-jet. We derive the fake rates from the di-jet samples and then use them in the W+jets control region where the analysis cuts are supplied. Many studies and cross-checks have been performed about this. We compare the fake rate from the di-jet MC with that from the W+jets MC where we apply the similar cuts in the analysis. In this way we can fully mimic the differences between two regions. The sample dependence is shown as a function of p_{T} in Figure 3.12. Flat uncertainties, 50%-60% for electron and 35%-60% for muon, are assigned.

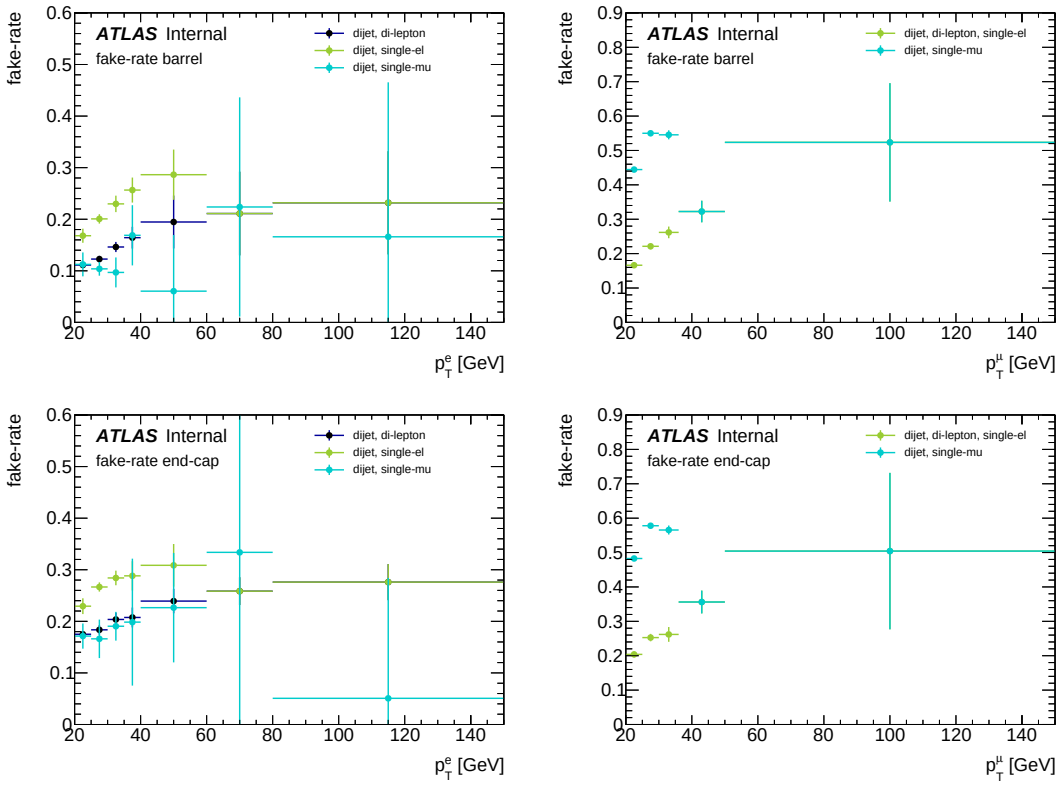

Figure 3.11 Fake-rates measured in data that serve as input to the matrix method for electrons (left) and muons (right). The fake-rates are measured with a set of supporting triggers. The labels indicate for which *analysis triggers* they are used. Shown are the barrel (top) and end-cap (bottom) regions with their systematic uncertainty (the sample dependence uncertainty is not included). [30]

Other systematic sources are also considered. The pile-up bias, which is the difference caused by different $< \mu >$ value, is estimated by dividing the sample into to tow parts with $< \mu >$ less than 20 and $< \mu >$ more than 20. The relative difference between these two parts are included in the final systematics.

The resulting W+jets data-driven estimate is shown in Table 3.10 with the statistical and systematic uncertainties from different sources. As we mentioned, the most important systematic source is the sample dependence.

3.5.1.2 Fake factor method

The matrix method is cross-checked by the so-called fake factor method. The lepton fake factor f_l, is defined for both electrons and muons. It is a ratio. The numerator is the event rate where the QCD jets can satisfy the lepton selection of the nominal analysis (good lepton). The denominator is the event rate where the QCD jets can satisfy "jet-rich lepton" identification requirements (bad lepton). This is shown in Equation 3.6.

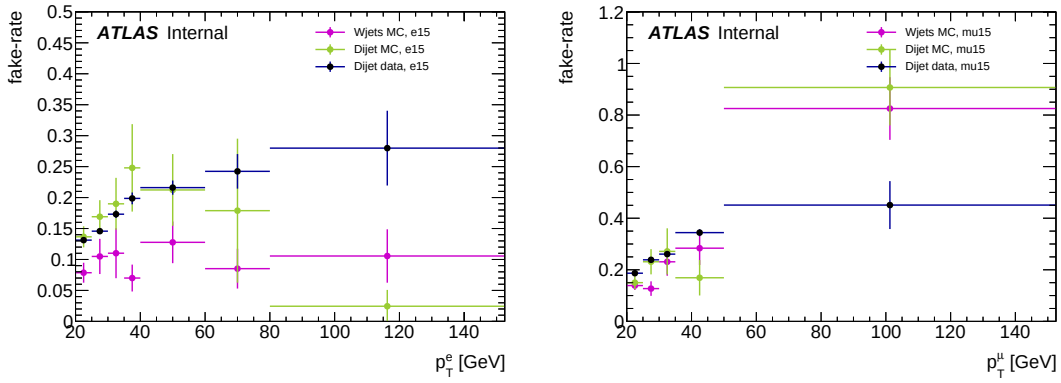

Figure 3.12 Fake-rates measured on a W+jets and di-jet MC samples for electrons (left) and muons (right) shown for two different triggers. The difference is assigned as a systematic uncertainty on the fake-rates measured on data. The integral over the full p_{T} range is used in order to average out statistical fluctuations. [30]

ee channel							
dd W+jets and QCD ($\pm$stat	$r\nearrow$	$r\searrow$	$f\nearrow$	$f\searrow$	$f_{\mathrm{sample}}\nearrow$	$f_{\mathrm{sample}}\searrow$)	W+jets MC prediction
13.93 ± 4.87	3.17	-3.28	3.36	-2.87	17.67	-7.07	21.55 ± 9.66
$e\mu$ channel							
dd W+jets and QCD ($\pm$stat	$r\nearrow$	$r\searrow$	$f\nearrow$	$f\searrow$	$f_{\mathrm{sample}}\nearrow$	$f_{\mathrm{sample}}\searrow$)	W+jets MC prediction
150.14 ± 11.76	17.87	-18.46	2.98	-27.87	73.74	-69.68	127.60 ± 17.44
$\mu\mu$ channel							
dd W+jets and QCD ($\pm$stat	$r\nearrow$	$r\searrow$	$f\nearrow$	$f\searrow$	$f_{\mathrm{sample}}\nearrow$	$f_{\mathrm{sample}}\searrow$)	W+jets MC prediction
6.07 ± 5.03	9.94	-10.29	-6.54	1.40	-3.37	-1.84	13.61 ± 4.30
μe channel							
dd W+jets and QCD ($\pm$stat	$r\nearrow$	$r\searrow$	$f\nearrow$	$f\searrow$	$f_{\mathrm{sample}}\nearrow$	$f_{\mathrm{sample}}\searrow$)	W+jets MC prediction
98.69 ± 9.73	19.41	-20.05	6.15	-12.52	68.95	-52.10	97.73 ± 17.02
$e\mu + \mu e$ channels							
dd W+jets and QCD ($\pm$stat	$r\nearrow$	$r\searrow$	$f\nearrow$	$f\searrow$	$f_{\mathrm{sample}}\nearrow$	$f_{\mathrm{sample}}\searrow$)	W+jets MC prediction
248.84 ± 15.26	37.28	-38.50	9.14	-40.39	142.69	-121.79	225.32 ± 24.37

ee channel				
dd QCD ($\pm$stat	$r\nearrow$	$r\searrow$	$f\nearrow$	$f\searrow$
0.20 ± 0.41	0.05	-0.04	0.35	-0.18
$e\mu$ channel				
dd QCD ($\pm$stat	$r\nearrow$	$r\searrow$	$f\nearrow$	$f\searrow$
13.89 ± 1.67	0.56	-0.52	19.19	-3.32
$\mu\mu$ channel				
dd QCD ($\pm$stat	$r\nearrow$	$r\searrow$	$f\nearrow$	$f\searrow$
1.87 ± 1.36	0.03	0.02	5.27	-1.31
μe channel				
dd QCD ($\pm$stat	$r\nearrow$	$r\searrow$	$f\nearrow$	$f\searrow$
8.31 ± 1.38	0.68	-0.63	3.23	-1.84
$e\mu + \mu e$ channels				
dd QCD ($\pm$stat	$r\nearrow$	$r\searrow$	$f\nearrow$	$f\searrow$
22.20 ± 2.17	1.24	-1.15	22.42	-5.16

Table 3.10 Data-driven W+jets estimate with its statistical and systematic uncertainties. The top part of the Table shows the combined W+jets + QCD estimate, the bottom part shows only the QCD part. The symbols $r\nearrow$ and $r\searrow$ indicate the up and down variations of the efficiencies, $f\nearrow$ and $f\searrow$ indicate the up and down variation of the fake-rates by the systematic uncertainties (without the sample dependence) and $f_{\mathrm{sample}}\nearrow$ and $f_{\mathrm{sample}}\searrow$) indicate the up and down variations of the fake-rates by the sample dependence uncertainty. [30]

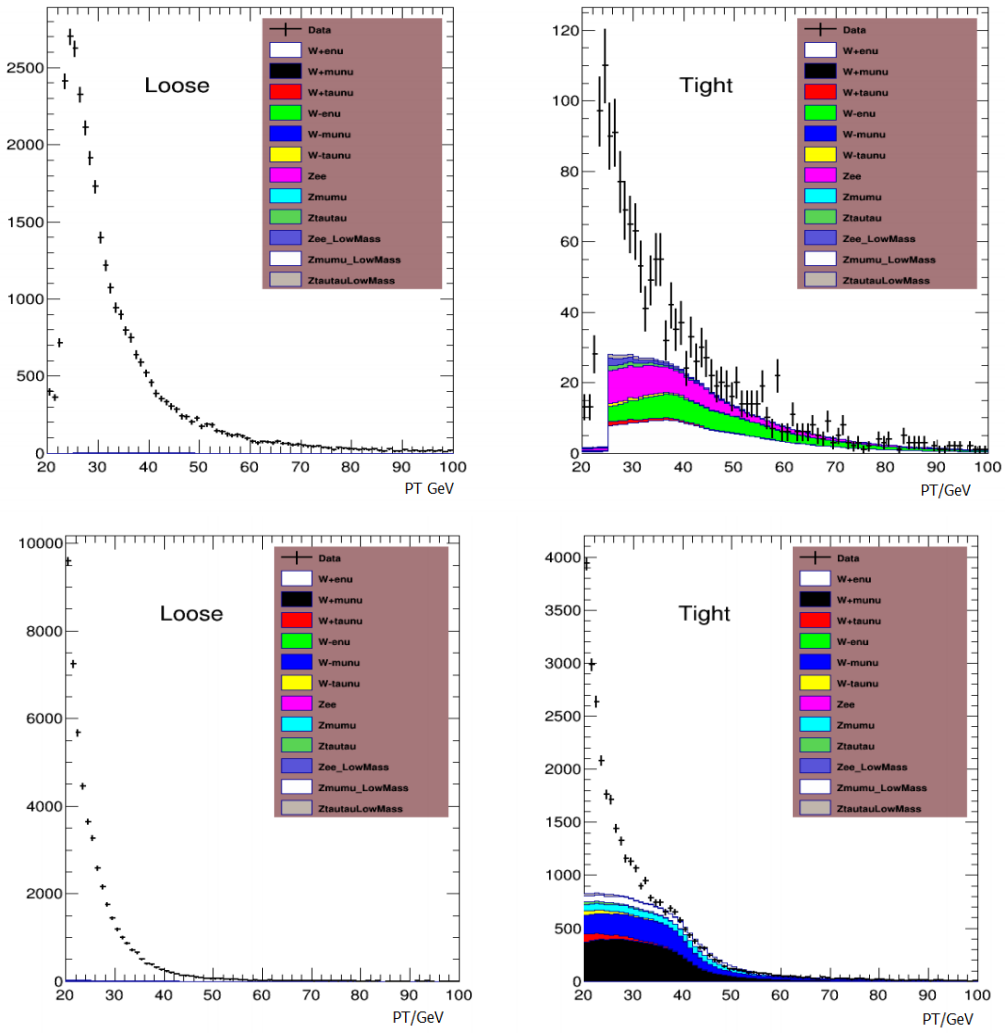

Figure 3.13 p_{T} distributions of tight and loose leptons for electron (top, EF_g20(24)_etcut) and muon (bottom, mu15). The distribution of data and MC (mainly from W and Z) are both shown.

The fake factor itself is measured in data from di-jet events.

$$\mathrm{f}_l = \frac{\mathrm{N}_{\text{identified lepton (good lepton)}}}{\mathrm{N}_{\text{jet-rich lepton (bad lepton)}}} \tag{3.6}$$

The W+jet background is calculated by scaling the number of events in the W+jet control region, $\mathrm{N}_{\text{one good + one bad}}$, using the fake factor derived above:

$$\mathrm{N}_{\text{one good + one fake}} = \mathrm{f}_l \times \mathrm{N}_{\text{one good + one bad}} \tag{3.7}$$

In the $e\mu$ channel the W+jet background prediction receives contributions from e (fake) plus μ and μ (fake) plus e as shown in Equation 3.8.

$$\mathrm{N}^{e\mu\text{-ch}}_{\text{one good + one fake}} = \mathrm{f}_e \times \mathrm{N}_{\text{one good } \mu \text{ + one bad e}} + \mathrm{f}_\mu \times \mathrm{N}_{\text{one good e + one bad } \mu} \tag{3.8}$$

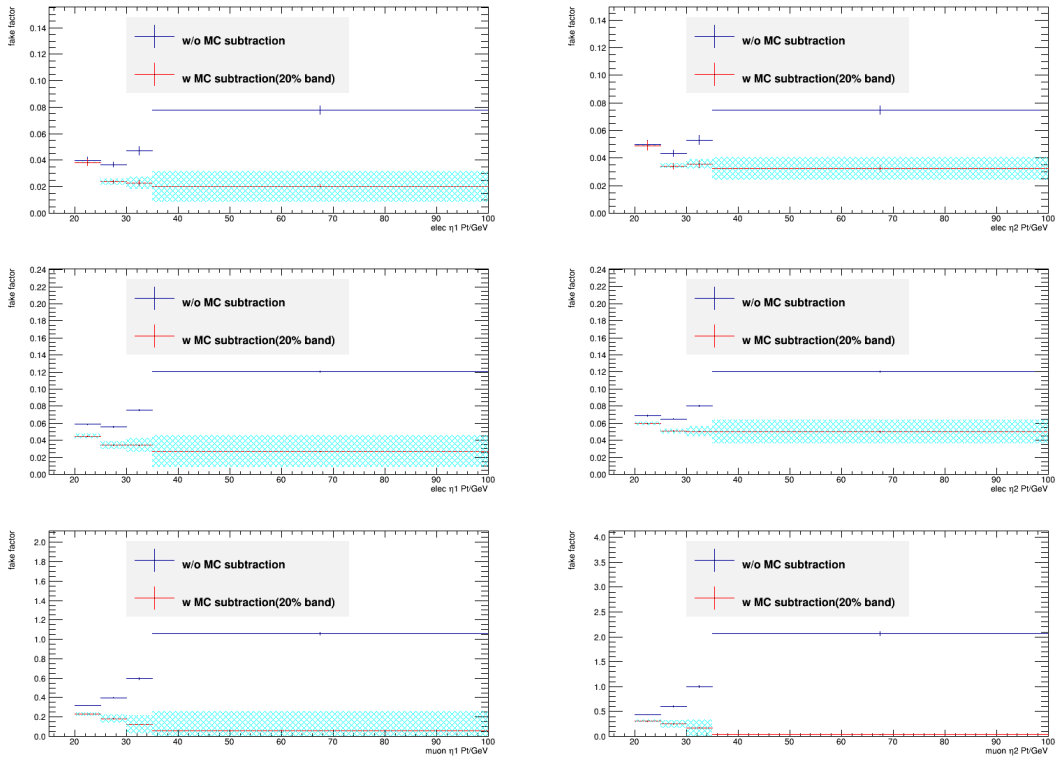

Figure 3.14 W+jets fake factor with and without MC subtraction. Top two plots are for electrons using photon trigger (g20_etcut, g24_etcut) and middle two plots are for electrons with supporting trigger(e22_vh_loose1) and bottom plots are for muons (mu15). Plots in the left are for $|\eta| < 1.5$ and plots in the right are for $|\eta| > 1.5$.

The "jet-rich" lepton definitions are given in Table 3.11. For "jet-rich" muons, the d_0 requirement is dropped, and the isolation requirements are loosened. For "jet-rich" (bad) electrons, only a minimal track requirement and none of the "VeryTight" quality requirements are imposed, so that the "jet-rich" electron must fail at least one of the "VeryTight" criteria or the isolation, since it is defined to be exclusive with the nominal analysis electron selection. Since the "jet-rich" muon definition can not be as loose as the "jet-rich" electron definition, the measured fake factor for muons is much higher than for electrons. However, the number of muons in the "jet-rich" control region will be correspondingly smaller.

Since we remove the good leptons in the denominator of fake factor, there are no overlap leptons between the denominator (bad lepton) and numerator (good lepton) of the fake factor. So the denominator and numerator have no correlations. If we do not remove the good lepton from the denominator, the fake factor definition will be changed and the definition of the denominator lepton in the W+jet control region will also change correspondingly. The final result is in principle not affected.

The measurement is performed in a grid of η and p_T bins. The η is divided into barrel and end-cap regions in order to explore the difference in these geometric regions.

The p_T is binned according to the statistical uncertainty in data leading to more bins in low p_T and one inclusive bin for the high p_T region.

"jet-rich" (bad) electron	"jet-rich" (bad) muon
the same p_{T} and η as identified electron	the same p_{T} and η as identified muon
Nhit(SCT + Pixel) ≥ 4	use ID track requirement of identified muon
$\lvert z_0 \times \sin\theta\rvert < 0.4$ mm	$\lvert z_0 \times \sin\theta\rvert < 1$ mm
$\lvert d_0/\sigma_{d_0}\rvert < 3$	d_0 cut removed
$\frac{\sum_{\Delta R<0.3} E_T^{corr}(i)}{p_T(\mu)} < 0.3$	$\frac{\sum_{\Delta R<0.3} E_T^{corr}(i)}{p_T(\mu)} < 0.3$
no track isolation requirement	no track isolation requirement
pass "Loose" and fail "Medium"	combined muon
remove identified (good) electrons	remove identified (good) muons

Table 3.11 Definitions of jet-rich electrons and muons for the fake factor measurements

The fake factor is derived using di-jet events after applying to following criteria:

- Trigger: In nominal analysis, for ee channel we are using di-lepton trigger while for the $e\mu$ we are using the di-lepton trigger and the single lepton trigger. So we have different trigger usded in fake factor study. For ee channel estimation, we are using e22_vh_loose1 while for $e\mu$ we will use fake factor from g20_etcut and g24_etcut. For muon, we use mu15.
- Missing E_T: Veto event if Missing $E_T > 30$ GeV.
- Z veto: Veto event if in the Z-mass window $|M_{\ell_1\ell_2} - M_Z| < 13$ GeV. The leptons used here are required to pass medium quality.
- EW subtraction: After the Z veto, the residual contribution from W,Z events are subtracted using the prediction from MC. The high contamination from W and Z is shown in Figure 3.13.
- Lepton-jet overlap: Keep tight electron and remove jet. Keep loose muon and remove jet. Keep jet and remove tight muon.
- Away-side jet requirement : The azimuthal angle between fake muon and good jet with $p_T > 25$ GeV must have $\Delta\phi > \pi/2$.

The following are considered as sources of systematic uncertainty.

- SM subtraction: The central value of the fake factor is affected by the EW subtraction. The theoretical cross sections of SM backgrounds which are used in the MC subtraction are varied by 20% to estimate the systematic uncertainty due to the background subtraction. This is shown in the Figure 3.14. The uncertainty is assigned for each p_T bin and η bin.
- Pile-up: It affects misidentification rates and can be present at different levels in the jet-enriched control region. In order to estimation this uncertainty, the data is separated into two sub-samples according to the number of primary vertices.

If the number of primary vertices is above 20, the event is recognized as high pile-up condition. If the number of primary vertices is below 20, the event is recognized as low pile-up condition. Results are shown in Figure 3.15. We use the difference between high and low pile-up to assign the uncertainty for each p_T bin and η bin.

- Trigger: The di-jet MC sample used to estimate the fake factor was varied with and without the trigger requirement. The results are shown in Figure 3.16. A p_T dependent systematic uncertainty is assigned.
- Sample dependence: Since we extract the fake factor from the jet-enriched sample and later apply it to the W+jet control region, a bias can be introduced by the differences in jet composition and kinematics between these two samples. This is a major systematic contribution in this analysis. For W+jets MC sample, we use truth information to get rid of the real leptons from W and study the remaining fake leptons without having to apply the W/Z veto requirement. For di-jet MC sample, we are using JF17 sample for electrons and JZ*W samples for muons. The JZ0W sample has large cross section and few loose or tight leptons, so we do not consider this sample. In order to take into account the different selection between fake factor control region and the W+jet control region, we also require the Missing E_T of W+jet samples to be larger than 30 GeV. We compare the fake factor in these two samples as shown in Figure 3.17. Finally, we derive an overall uncertainty 60% for electrons, 55% for muons.

The detailed uncertainty numbers for the 20 - 25 GeV bin is listed in Table 3.12. Similar as the systematic uncertainties in the matrix method, the fake factor suffers from large sample dependence uncertainties. When we estimate the sample dependence, we are trying to mimic the selections used in the nominal analysis when studying the W+jets control region. That means, for W+jets MC we are applying as many as possible the cuts used in the region of nominal analysis, where the fake factor are finally applied. But due to the statistical problem, we can not fully apply all the nominal cuts in the W+jets control region, and those cuts which are not applied will affect the p_{T} shape. This is an important reason why we do not use p_{T}-corrected fake factor but to put this sample dependence into systematics.

The W+jets control region is defined as events with 1 loose lepton and 1 tight lepton. First we require the event to be with only 1 tight lepton and more than 1 loose lepton. Then we remove loose leptons with lower transverse momentum. The leading and sub-leading lepton p_T spectra in the W+jets control region are shown in Figure 3.18 for electron-fake cases and Figure 3.19 for muon-fake cases. The W+jets MC simulation is not expected to model very well the value of fake factor in data, therefore

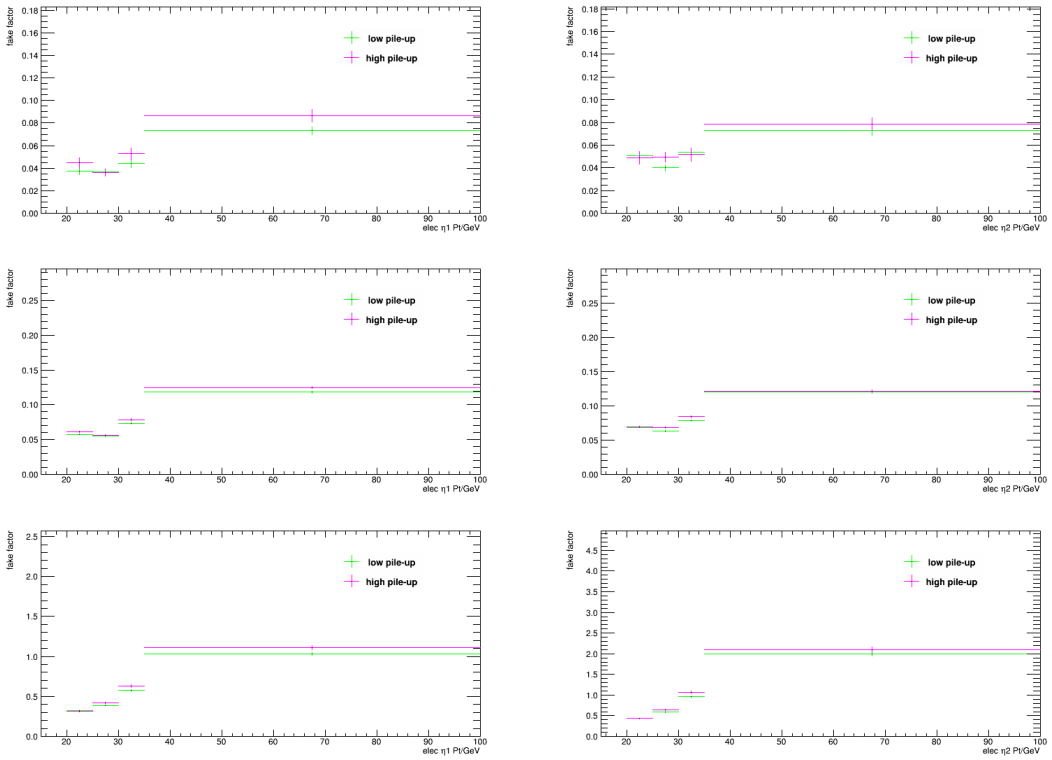

Figure 3.15 W+jets fake factor pile-up bias. Top two plots are for electrons using photon trigger and middle two plots are for electrons with supporting trigger and bottom plots are for muons. Plots in the left are for $|\eta| < 1.5$ and plots in the right are for $|\eta| > 1.5$.

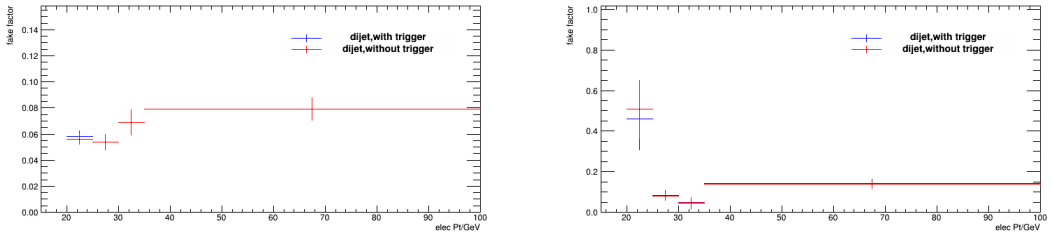

Figure 3.16 W+jets fake factor trigger bias. Left for photon trigger, and right for muon trigger.

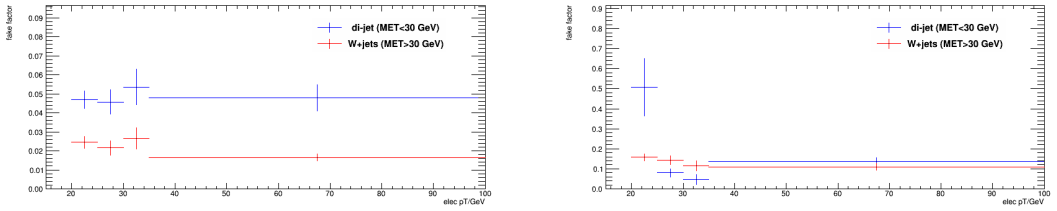

Figure 3.17 W+jets fake factor sample dependence. Left plot for electrons and right plot are for muons.

	Electron(photon trigger)	Electron (photon trigger)	Muon	Muon
Systematic source	$\|\eta\| < 1.5$	$\|\eta\| > 1.5$	$\|\eta\| < 1.5$	$\|\eta\| > 1.5$
EW-Contamination	0.7%	0.3%	7.7%	8.8%
Pile-up bias	16.7%	3.0%	2.7%	0.3%
Trigger bias	4.0%	4.0%	9.8%	9.8%
Sample dependence	60%	60%	55%	55%
Statistic uncertainty	6.4%	6.5%	0.9%	1.2%
Total uncertainty	62.8%	60.6%	56.5%	56.6%

Table 3.12 Summary of the fake factor uncertainties for 20-25 GeV bin. Total uncertainty is calculated by adding all uncertainties in quadrature.

we are not relying on MC to do this estimate.

The prediction includes the W+jet modeling from the fake factor procedure as well as non-W+jet contributions predicted from MC.

The W+jet background in the WW signal region obtained from the fake factor procedure is presented in Table 3.13 The total background is the sum of the W+jet estimation from data and the non-W+jet MC corrections. The total uncertainties are the quadratic sum of the uncertainties on the W+jet prediction from data and the MC corrections. The systematic uncertainties are due to the systematic uncertainty on the measured fake factor.

The Table 3.14 shows the comparison of estimation given by two methods. The results are in agreement.

	ee-ch	eμ-ch	$\mu\mu$-ch	Total
W+jet background (e-fakes)	$7.54 \pm 0.72 \pm 6.57$	$97.08 \pm 3.10 \pm 64.04$	-	$104.63 \pm 3.18 \pm 70.61$
W+jet background (μ-fakes)	-	$117.38 \pm 6.64 \pm 76.04$	$18.47 \pm 2.77 \pm 11.98$	$135.85 \pm 7.19 \pm 88.02$
Total W+jet background	$7.54 \pm 0.72 \pm 6.57$	$214.46 \pm 7.32 \pm 140.08$	$18.47 \pm 2.77 \pm 11.98$	$240.47 \pm 7.86 \pm 158.63$

Table 3.13 Summary of the W+jet background fake factor estimation with associated statistical and systematic uncertainties.

Method	ee channel	$\mu\mu$ channel	$e\mu$ channel
Matrix method	$13.9 \pm 4.9 \pm 14.2$	$6.1 \pm 5.0 \pm 11.5$	$248.8 \pm 15.3 \pm 138.7$
Fake factor method	$7.54 \pm 0.72 \pm 6.57$	$18.47 \pm 2.77 \pm 11.98$	$214.46 \pm 7.32 \pm 140.08$
MC prediction	21.6 ± 9.7	13.6 ± 4.3	225.3 ± 24.4

Table 3.14 Comparison of the W+jets background yields with two methods with associated statistical and systematic uncertainties.

3.5.2 Top background

The top decays are featured by the hadronic jet. The top events, which can mimic the signal WW process, can be from the a pair of top production ($t\bar{t} \to WbWb$) or from single top production ($tW \to WbW$).

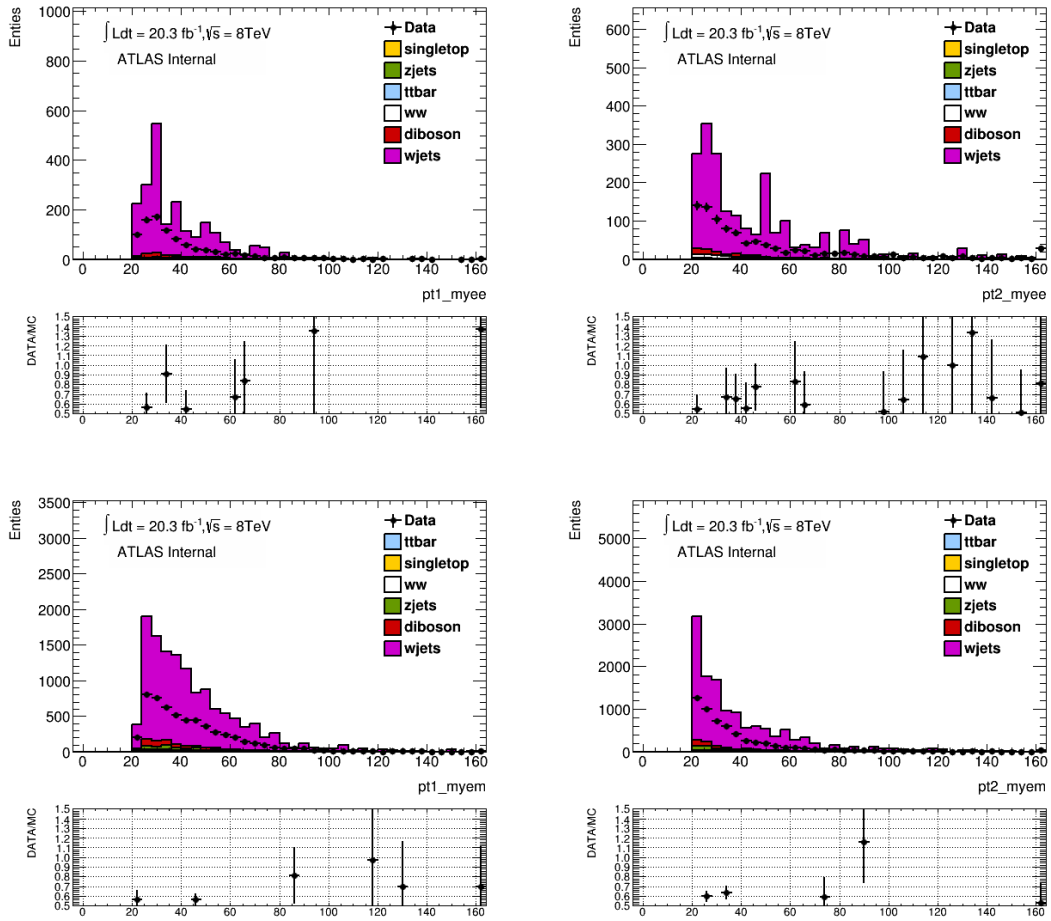

Figure 3.18 Leading and sub-leading lepton p_T for leptons in the signal region with one identified electron or muon and one jet-rich electron. All Monte Carlo samples including the W+jets simulation are shown, in the method itself the W+jets simulation is not used. And we have already multiplied fake factor in the plots. The top row shows the distributions for the ee channel, the lower row for the $e\mu$ channel. The W+jets simulation over-predicts the yield in this sideband, indicating that the probability of misidentifying a jet as electron-like is overestimated in simulation.

The top background contribution is estimated using a data driven method: the jet-veto survival probability (JVSP) method [46]. This method uses two control samples. The main idea is to derive the jet veto efficiency correction factor between data and MC in the first control sample and to derive the MC jet veto efficiency in the second sample.

The first control region selects events with di-lepton and one or more b-jets. The b-jet, which is regarded as the tagging jet, is required to pass the 85% MV1 b-tagging working point with the requirement of $E_T > 25$ GeV and $|\eta| < 2.5$. Probing jets, which are selected using the same p_{T} and η as in the nominal jet requirement of the analysis, are required to be in the opposite direction to the selected b-tagged jet ($\Delta R > 1$). The

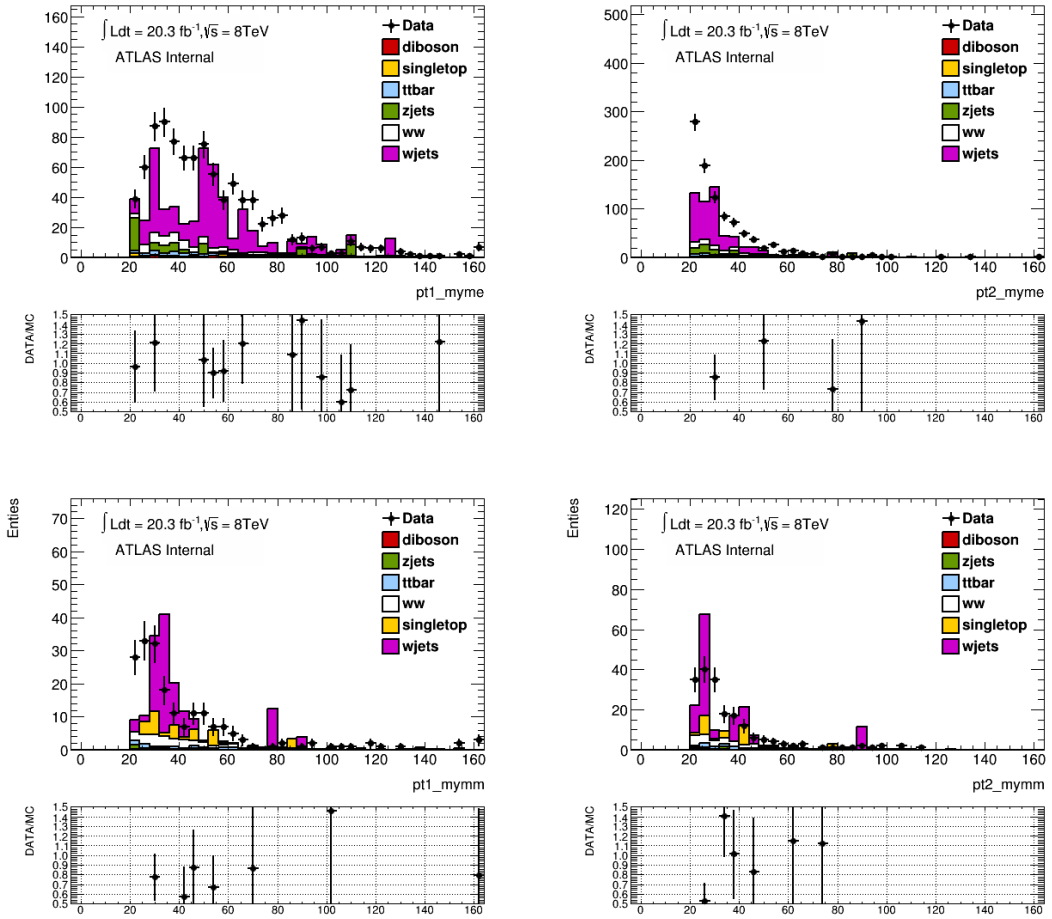

Figure 3.19 Leading and sub-leading lepton p_T for leptons in the signal region with one identified electron or muon and one jet-rich muon. All Monte Carlo samples including the W+jets simulation are shown, in the method itself the W+jets simulation is not used. And we have already multiplied fake factor in the plots. The top row shows the distributions for the $e\mu$ channel, the lower row for the $\mu\mu$ channel. The result indicates an underestimate of jet-rich muons in the W+jet simulation.

jet veto efficiency, $P_1^{\text{Btag,data}}$, is derived from the first control region.

$$P_1^{\text{Btag}} = \frac{N_{0j}^{\text{Btag}}}{N_{\text{all}}^{\text{Btag}}} \tag{3.9}$$

where N_{0j}^{Btag} is the number of events without probe jet founded. $N_{\text{all}}^{\text{Btag}}$ is the total number of events.

The second control region is required to pass all selection cuts except for the jet-veto. On top of this, we require the scalar sum of transverse energy of leptons and jets to be $H_t > 130$ GeV, which is to reduce contributions from WW signal in the control region. The cut efficiency is 95% for top events and 29% for WW events. The H_t cut efficiency is derived by counting the events before and after the H_t cut in the $t\bar{t}$ control region. The difference of the H_t cut efficiency between DATA and MC is within 1%,

which has been taken into account for the final systematics.

The definition of the two control regions are quite similar, which leads to the potential cancellation of systematic uncertainties. We use the second control region to get the jet-veto efficiency from MC. We make use of the first control region to derive the correction factor of the jet-veto efficiency between data and MC, which is dominated by top events using b-tagging technique.

Figures 3.20-3.22 show distributions in data compared to MC in the b-tagged control sample separately for ee, $\mu\mu$ and $e\mu$ channels. A $2b$-tagged control sample has been investigated and the integral has been compared to the $1b$-tagged control sample (see Figures 3.24 - 3.26). By further asking the additional b-tagging jet, this can check the stability of the b-tagging requirement.

The jet veto efficiency in the first control sample (Equation 3.9), can be derived from both data (subtract the non-top yields from the observed yields) and the MC (use top MC samples). The jet veto efficiency in the signal region for the data (P_2^{Data}) can be expressed as:

$$P_2^{\text{Data}} = \left(P_{1(\text{Btag})}^{\text{DATA}}\right)^2 \times \frac{P_2^{\text{MC}}}{\left(P_{1(\text{Btag})}^{\text{MC}}\right)^2}, \tag{3.10}$$

where P_2^{MC} and $P_{1(\text{Btag})}^{\text{MC}}$ are derived by MC. P_2^{MC} is estimated with the second control region, which uses all nominal selections but to use $H_(t)$ cut instead of the jet-veto.

$$P_2^{\text{MC}} = \frac{N_{\text{Top}}^{\text{MC}}(0j)}{N_{\text{Top}}^{\text{MC}}(all)} \tag{3.11}$$

The denominator is the total number of events in the top MC. The numerator is the event number after the requirement of 0 jet. The estimated number of top background events

Final State	ee Channel	$\mu\mu$ Channel	$e\mu$ Channel	combined
Observed Events	1966	3444	22134	27544
Top	1897.7 ± 18.1	3016.8 ± 23.4	20073.5 ± 59.6	24987.4 ± 66.5
WW	187.7 ± 3.2	341.8 ± 4.2	1847.2 ± 9.7	2376.1 ± 11.1
W+jets	2.67 ± 2.67	4.72 ± 4.72	118.0 ± 23.3	125.4 ± 23.9
Z+jets	10.1 ± 1.5	31.5 ± 8.4	73.8 ± 18.5	115.4 ± 20.4
Other diboson	18.6 ± 1.2	19.4 ± 0.9	99.7 ± 3.1	137.8 ± 3.4
Total non-top	219.1 ± 4.6	397.6 ± 10.6	2138.76 ± 31.5	2755.5 ± 33.6

Table 3.15 Summary of observed data events and MC expected top and non-top background contributions for the second control sample (full preselection except for jet veto cuts applied, with $H_t > 130$ GeV) in the three channels and their combined results. The uncertainties of the non-top processes include statistical uncertainties only.

in the signal region in data is

$$N_{\text{Top}}^{\text{Data}}(0j) = N_{\text{Top}}^{\text{Data}}(all) \times P_2^{\text{Data}} \tag{3.12}$$

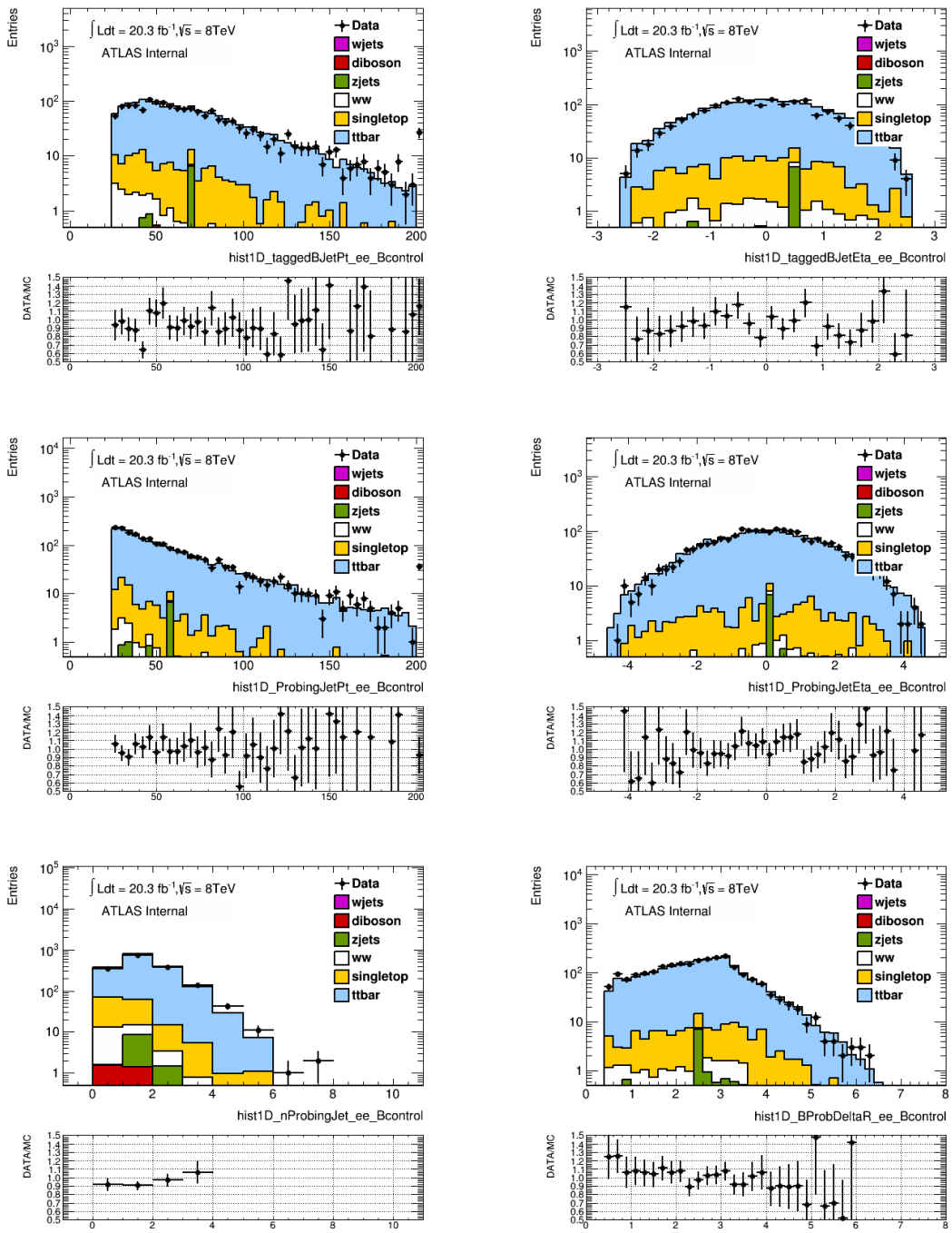

Figure 3.20 ee channel: Jet distributions in data compared to MC in the b-tagged control sample used to extract the jet veto efficiency for top backgrounds. The upper plots display the transverse momentum (left) and pseudo-rapidity (right) of the tagging b-jets. The middle plots are for the probing jet. The lower plots display the multiplicity of the probing jets (left) and the ΔR between tag and probing jet.

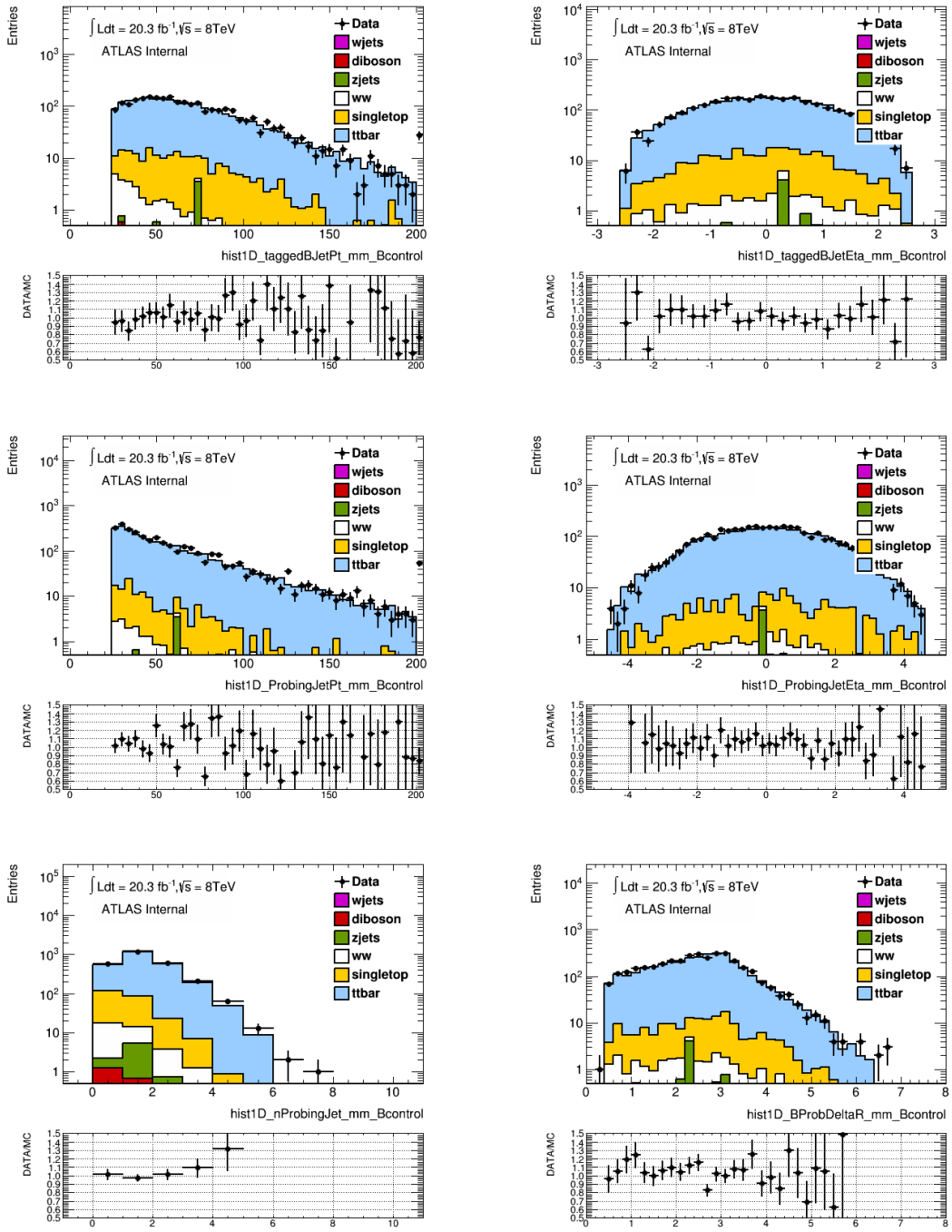

Figure 3.21 Same as Figure 3.20 for the $\mu\mu$ channel.

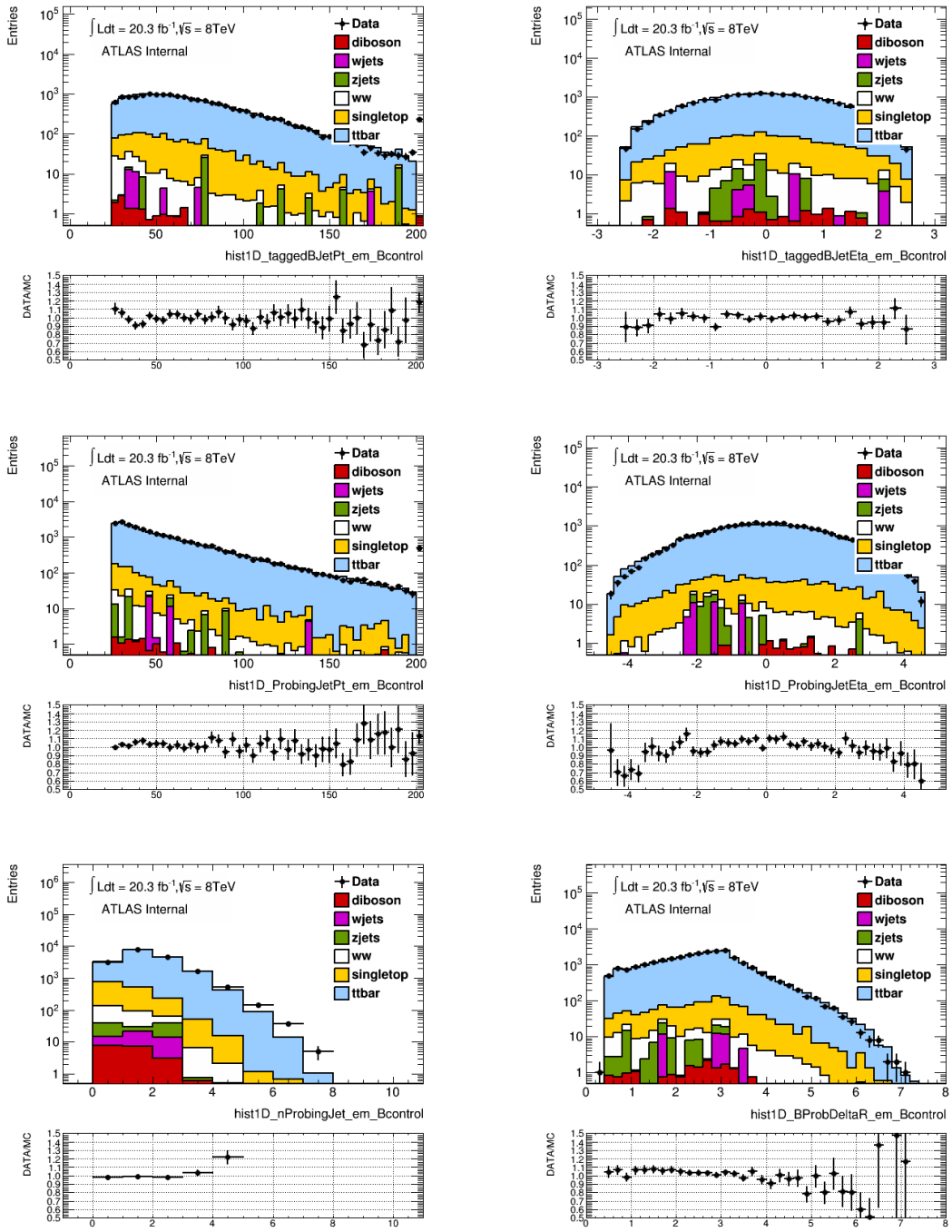

Figure 3.22 Same as Figure 3.20 for the $e\mu$ channel.

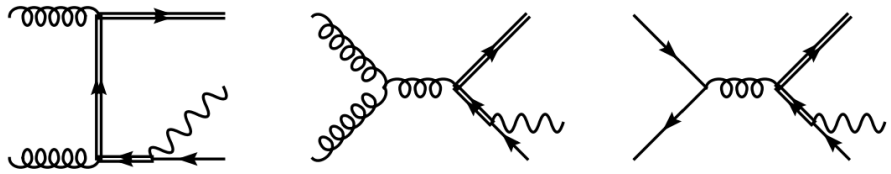

Figure 3.23 Diagrams that are doubly-resonant, in the sense that the intermediate $\bar{t}$ can be on-shell. The t-quark line is doubled.

where $N_{\text{Top}}^{\text{Data}}(all) = N_{\text{all}}^{\text{Data}} - N_{\text{all}}^{\text{non-top}}$ is the number of top background events observed in data in the second control sample after subtracting the non-top contribution. The non-top background contributions are shown in Table 3.15. Table 3.16 summarises the results of the top background extraction. The final number of top background events is estimated to be $836.6 \pm 12.3(\text{stat}) \pm 71.1(\text{syst})$,

The uncertainties of all these terms are shown explicitly in Table 3.16.

Channel	$P_{1(\text{Btag})}^{\text{MC}}$	$P_{1(\text{Btag})}^{\text{data}}$	P_2^{MC}	$P_2^{\text{MC}}/(P_{1(\text{Btag})}^{\text{MC}})^2$	$N_{\text{Top}}^{\text{Data}}(0j)$	$N_{\text{Top}}^{\text{MC}}(0j)$
ee	0.229 ± 0.004	0.231 ± 0.010	0.040 ± 0.002	0.762 ± 0.025	$91.8 \pm 7.3 \pm 7.9$	96.9 ± 4.8
$\mu\mu$	0.186 ± 0.004	0.185 ± 0.009	0.036 ± 0.002	0.937 ± 0.021	$127.2 \pm 9.4 \pm 10.9$	131.4 ± 6.1
$e\mu$	0.221 ± 0.001	0.217 ± 0.003	0.029 ± 0.001	0.593 ± 0.012	$608.6 \pm 17.5 \pm 52.3$	625.9 ± 12.5

Table 3.16 Summary of results for the jet veto efficiencies used for the prediction of the number of top background events and final data-driven top yield for each channel. The first is statistical and the second systematic in the last column.

The dominant systematics uncertainties are listed here. In many cases we will study the variation of the term $P_2^{\text{MC}}/(P_{1(\text{Btag})}^{\text{MC}})^2$, which contributes to the experimental and theoretical systematic uncertainties.

- **Experimental uncertainties**

  The JES and JER are varied up and down by 1 standard deviation, and we get a relative variation of 4.0% for JES and 1.8% for JER on $P_2^{\text{MC}}/(P_{1(\text{Btag})}^{\text{MC}})^2$. The corresponding average variations are $\pm 1.2\%$ and $\pm 3.9\%$. The relatively small systematic effect can be understood because of the cancellation in the ratio. This is expected because the two control regions have very similar definition. The uncertainties on the b-tagging are checked similarly with the relative variation of 3.5% on $P_2^{\text{MC}}/(P_{1(\text{Btag})}^{\text{MC}})^2$.

- **Non-top subtraction**

  The non-top MC background subtraction in the second control sample is another important source of systematics. In order to estimate its effect, we assign the uncertainty for each background (15% for WW, 50% for W+jets and Z+jets,

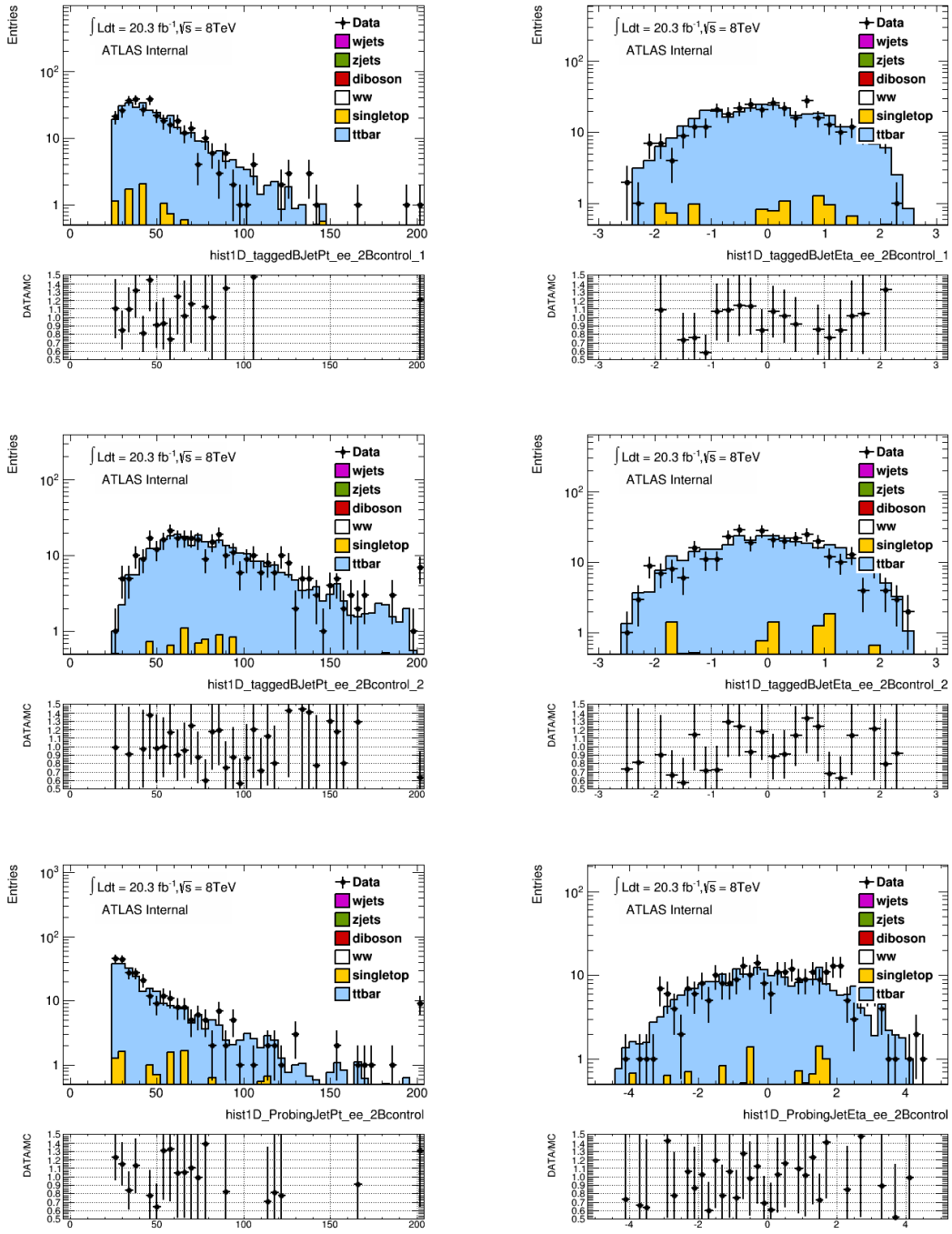

Figure 3.24 ee channel: Jet distributions in data compared to MC in the $2b$-tagged control sample used to extract the jet veto efficiency for top backgrounds. The upper plots display the transverse momentum (left) and pseudo-rapidity (right) of the 1st tagging b-jet. The middle plots are for the 2nd b-jet. The bottom plots are for the probing jet.

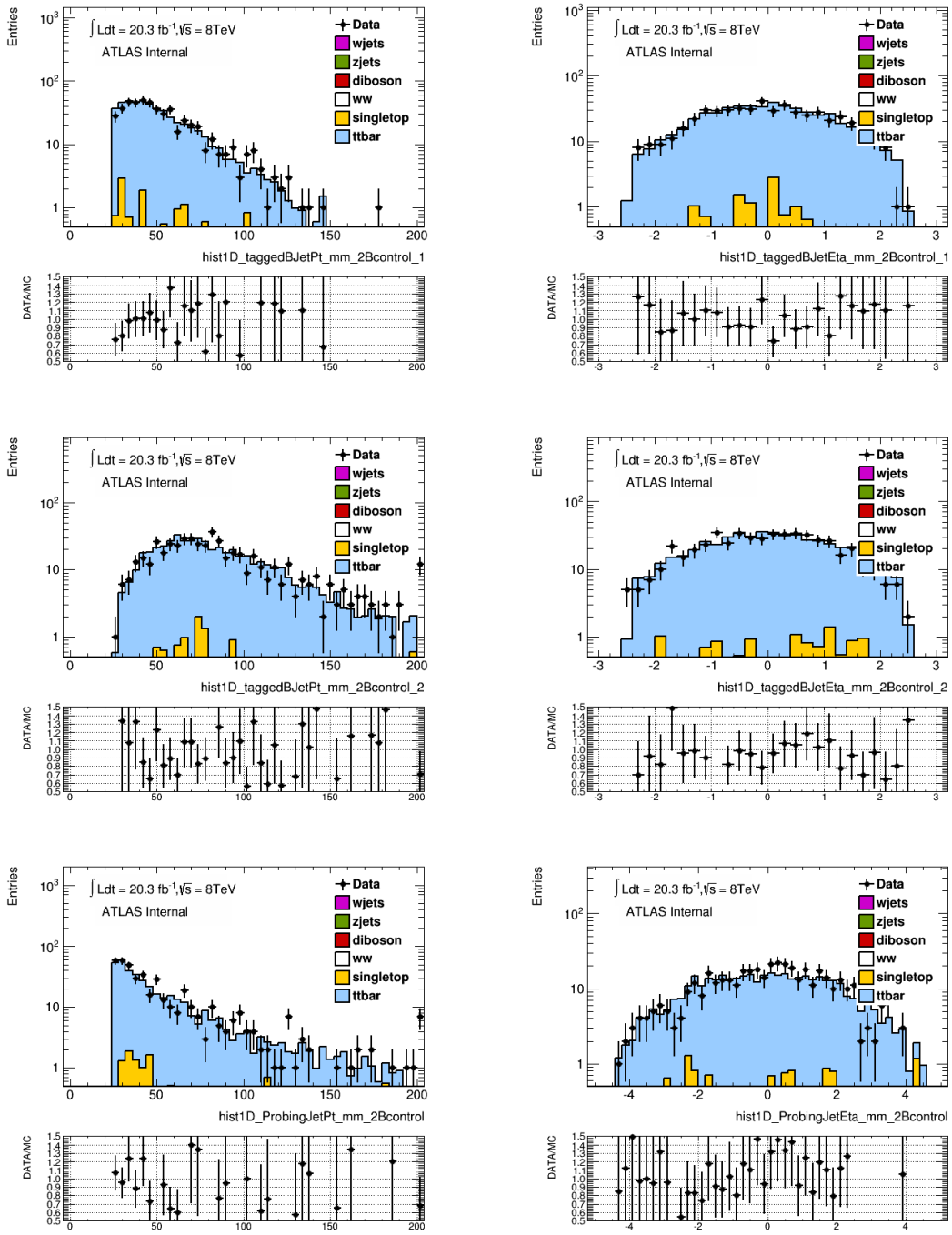

Figure 3.25 Same as Figure 3.24 for the $\mu\mu$ channel.

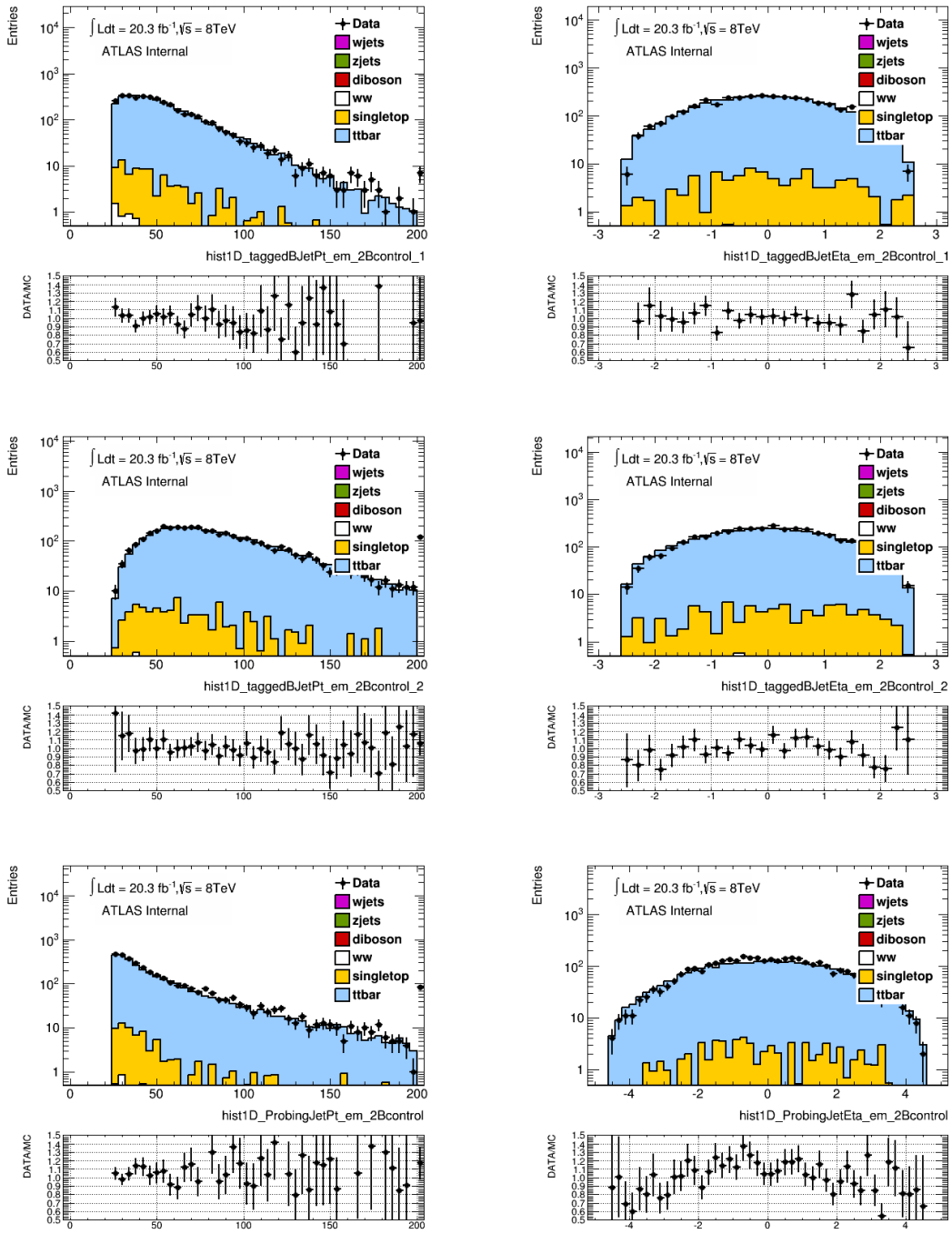

Figure 3.26 Same as Figure 3.24 for the $e\mu$ channel.

15% for diboson, all use MC) The uncertainty of the WW process corresponds to an enlarged uncertainty of 15% covering the difference between the measured cross section value and that of the NLO prediction. The relative error of $N_{\text{Non-top}}/N_{\text{data-Nontop}}$ is 2.1%.

– **Single top effect**

The single top cross-section is varied by 30% to estimate its effect. The difference is found to be 1.1%.

– **MC generator and parton shower/hadronisatoion**

The nominal sample has $MC@NLOJimmy$ for both single top and $t\bar{t}$. We also look at the $PowHegJimmy$ and $PowHegPythia$ samples calculate their values of $P_2^{\text{MC}}/(P_{1(\text{Btag})}^{\text{MC}})^2$. Then different value is compared. The difference between $MC@NLOJimmy$ and $PowHegJimmy$ is 5.1% while for $PowHegJimmy$ and $PowHegPythia$ it's 3.7%. The overall uncertainty is 6.3%, which is another dominant source of systematics. This result can be considered as a closure test using $PowHegJimmy$ and $PowHegPythia$ as test samples, since the difference between data-driven estimate and the correspoding MC prediction is proportional to $P_2^{\text{MC}}/(P_{1(\text{Btag})}^{\text{MC}})^2$.

– **Single top and $t\bar{t}$ interference**

The NLO Wt process shares the same final states as LO $t\bar{t}$. Beyond LO, some of the Feynman diagrams that contribute to Wt channel are shown in the Figure 3.23. These diagrams can be interpreted as the production of a $t\bar{t}$ pair at LO. In order to estimate the interference between these two processes, we search for the different ways of overlap removal and take their difference as the uncertainty. We present two definitions of the Wt channel, that are designed in such a way that, by comparing them, one can directly assess the impact of the interference with $t\bar{t}$ [47]. Firstly, it is the diagram removal. One simply removes all diagrams in the NLO Wt amplitudes that are doubly resonant (i.e. those diagrams shown in the Figure 3.23). Secondly, it is the diagram subtraction. One modifies the NLO Wt cross-section by implementing a subtraction term designed to cancel locally the $t\bar{t}$ cross-section. The dedicated MC@NLO samples for this study are produced by $H \to WW$ group. The relative difference between these two samples is 1.1%.

– **Renormalization and factorisation scale uncertainty**

We use the dedicated $MC@NLO$ samples produced by $H \to WW$ group. The μ_F and μ_R are varied independently by the factor 0.5 or 2, as we did many times in other places in this analysis where we estimate scale uncertainties. We compare their values with the nominal one and take the maximum variation 1.9%.

– **PDF uncertainly**
The nominal $MC@NLO$ top sample is generated with $CT10$, so we perform PDF reweighting to derive the relative variations of 52 sets. We compare their values with the nominal one and take the maximum variation 1.7% as the uncertainty.

– **Exponent effect**
The nominal exponent N=2 in the term $(P^{\text{MC}}_{\text{1(Btag)}})^2$ is chosen because of the assumption that there are 2 b-jets in the top events. This assumption is used when we derive the formula of this method. In order to test its effect, we also tried the variations N=1.5 or N=2.5 to conservatively have a look at the relative difference. It is within 1%.

– **Yield scaling effect**
We need to scale the yield concerning the H_t cut as we mentioned before, and we use MC cut efficiency as the scale factor. There is 1% uncertainty assigned for the difference between DATA and MC cut efficiency. And we checked the stability of the efficiency with the variation of experimental uncertainty sources. The experimental uncertainty related to the MC cut efficiency is 0.87%.

3.5.3 Di-boson

The estimate of other diboson background (WZ, ZZ,$W\gamma$ and $W\gamma^*$) is based on MC and normalised to the integrated luminosity 20.3 fb^{-1}. The WZ and ZZ MC samples are simulated using Powheg+Pythia. The Zγ is already included in the Z+jets data-driven estimation, which will be talked about later. The $W\gamma$ process is modelled with Alpgen+Jimmy. The $W\gamma^*$ process is simulated with Sherpa. It includes up to one additional parton in the matrix element, which is important to correctly describe high lepton p_T behavior. The k-factor is 0.979 $\pm$ 0.076 which is calculated with MCFM. Jet binned correction factors for $W\gamma^*$ are calculated with Sherpa with up to two additional partons on the matrix element. The production of $W\gamma^*$ with virtual photons is potentially included in the Powheg+Pythia samples of WZ events. To avoid the duplication, the WZ samples have a lower limit on the gauge boson mass of 7 GeV while the $W\gamma^*$ samples have an upper limit of 7 GeV.

The theoretical uncertainty for $W\gamma^*$ is found to be 18%, due to the scale uncertainties on k-factor and jet binned correction factors. For $W\gamma$ process, the uncertainty due to NLO cross section prediction and jet veto cut is estimated with MCFM, and found to be about 11%. The measured $W\gamma$ cross section with 2011 $\sqrt{s} = 7$ TeV data is reported to be 30% [48] higher than corresponding NLO prediction, and as a conservative approach, we consider this difference as an additional uncertainty and find the

final theoretical uncertainty on $W\gamma$ background to be 32%. The theoretical uncertainty for WZ background is about 8%, including the uncertainties due to NLO cross section prediction (5% [49]), higher order corrections (5% [50]), and jet veto cut (3%). As for ZZ background, the included theoretical uncertainties are quoted on NLO cross section prediction (4% [49]), NNLO corrections (12% [51]), and jet veto cut (3%), and the total uncertainty is about 13%. Please note, the theoretical jet-veto uncertainties for WZ and ZZ backgrounds are assumed to be similar to WW signal and a plain number of 3% is quoted.

The background yields and uncertainties for di-boson backgrounds are provided in Table 3.17.

Final State	$e^+e^-E_{\mathrm{T}}^{\mathrm{miss}}$	$\mu^+\mu^-E_{\mathrm{T}}^{\mathrm{miss}}$	$e^\pm\mu^\mp E_{\mathrm{T}}^{\mathrm{miss}}$	Combined
Diboson Background				
WZ	7.72 ± 0.68	19.35 ± 1.00	62.86 ± 1.75	89.92 ± 2.12
ZZ	10.61 ± 0.43	16.06 ± 0.54	2.76 ± 0.14	29.43 ± 0.70
Wgamma	3.67 ± 0.81	0.00 ± 0.00	41.08 ± 2.72	44.75 ± 2.84
Wgammastar	5.35 ± 0.83	2.96 ± 0.60	42.98 ± 2.31	51.28 ± 2.53
Total Background	27.34 ± 1.41	38.36 ± 1.28	149.68 ± 3.98	215.39 ± 4.41

Table 3.17 Other diboson background yields and their statistical uncertainties as determined from MC for 20.3 fb^{-1}.

3.5.4 Z+jets background

The Drell-Yan process $Z/\gamma^* \to l^+l^-$ may produce two high p_{T} leptons and has a large cross section. We adopt the simultaneous method for the Z+jets estimation. It is based on the profile likelihood approach, in which the numbers of signal and background events in the control regions are described by a Poisson probability density function.

Originally this method can provide signal and backgrounds (top, Z+jets) at the same time. The normalization of each component can act as the free parameter in which the uncertainties are treated as the nuisance parameters. In our analysis for Z+jets estimation, this method only uses a fit to constrain the Drell-Yan normalization. Although the method can also provide signal and top estimation, they are only treated as the cross checks.

For the W+jets and QCD, the input normalization and shape are from the data-driven estimation described in the Section 3.5.1. For top, the input input normalization and shape are from the JVSP method described in Section 3.5.2. Other contributions, including input template shapes of signal and Z+jets, are all from MC. The different sources of experimental and theoretical systematic uncertainties are included as nuisance parameters in the fit. The WW signal and Z+jets normalization factors are free

parameters. Only the Drell-Yan normalization is extracted from this fit and used further for the cross section determination.

In this estimation we define three control regions:

- **Signal Region**.
  The same selection as used in the WW analysis.
- **Drell-Yan Control Region**
  Different from signal region, we remove the $\Delta\phi(E_{\mathrm{T}}^{\mathrm{miss}}, p_{\mathrm{T}}^{\mathrm{miss}})$ cut. and the p_T^{miss} is inverted with a lower boundary 5 GeV.
- **Validation region**
  Different from signal region, the $E_{\mathrm{T}}^{\mathrm{miss}}$ and p_T^{miss} are inverted.

For Z+jets estimation, the profile likelihood fit is performed in both the control region and the signal region simultaneously. The fit is performed on the $\Delta\phi(E_{\mathrm{T}}^{\mathrm{miss}}, p_{\mathrm{T}}^{\mathrm{miss}})$ distribution in five bins with equal bin width. From the fit we can acquire the Z+jets normalization factor. An additional Drell-Yan enriched region (validation region), is used for cross check. The result of the fit is extrapolated to this validation region where a good data and MC agreement is observed.

The variations of the following systematic sources on the normalisation and the shape are taken into account in the signal and control regions. These include the experimental systematic uncertainties with respect to object selections (mainly for jets) and event selections (mainly for $E_{\mathrm{T}}^{\mathrm{miss}}$). In addition, the statistical uncertainty of the MC for each bin is treated as a systematic uncertainty with a gaussian constraint. What is more, the luminosity uncertainty 2.8% is added.

Depending on the process, the theoretical uncertainties is included. An uncertainty for the dependence on the generator, the parton shower and the initial and final state radiation is applied. Since the likelihood fit provides the total systematic uncertainties, the error decomposition in statistical and different systematic sources is obtained in the following way: First of all, as already described, the total error is obtained by letting all the nuisances and parameters of interest free. Secondly, the statistical uncertainty is obtained by fixing all the nuisance parameters to their fitted values and the parameters of interest free. The uncertainty returned by this fit corresponds to the statistical uncertainty. Finally, for the decomposition of the systematics, the nuisance parameters are fixed to their central values, the parameters of interest are let free and then in turn each nuisance gets fixed to the $+1\sigma$ and -1σ returned by the fit. The central value returned by each fit is then compared to the fit where all the nuisances fixed to their central values, to obtain an estimation of the contribution of each uncertainty source. Then, to estimate the QCD scale uncertainties, AlpgenPythia samples were generated by varying the μ_F and μ_R up and down by a factor of 0.5 or 2. The estimated accep-

tance difference is 3.5%. For the parton shower uncertainties, we perform two fits using samples with different parton shower and compare their final yields. The samples compared are AlpgenJimmy and AlpgenPythia and the observed difference is 8.5% which is then assigned as the uncertainty of parton shower . The PDF uncertainty is assessed in a similar way by performing two different fits with different PDF sets (CTEQ6 and CT10). The difference on the Drell-Yan yield is at the level of 1%.

After all, the main experimental uncertainties are related to the jet and missing transverse energy reconstruction. The main theoretical uncertainties are related to MC parton shower modelling.

A comparison of kinematic distributions before and after the fit in the control and signal region is shown in Figure 3.27. The normalization factor from the fit are given in the plot (denoted as μ_{best}). The simultaneous fit improves the agreement with data both by adjusting the normalisation of the samples and by adjusting the central values of the nuisance parameters.

The results of the simultaneous fit can also be used to extract the WW cross-section and as such serves as a cross-check of the default method. The cross-section is obtained from the fitted signal strength for WW. This results in total cross-sections of $\sigma^{\text{tot}}_{WW} = 75.0^{+10.4}_{-8.9}$ pb for the ee channel, $\sigma^{\text{tot}}_{WW} = 73.6^{+9.2}_{-8.0}$ pb for the $\mu\mu$ channel and $\sigma^{\text{tot}}_{WW} = 71.3^{+8.3}_{-7.1}$ pb for the $e\mu$ channel. The results are consistent with the results described in the Section 3.7.

3.5.5 Summary of the observed WW candidates and background expectations

The observed and expected event yields after applying all WW selection cuts are shown in Table 3.18.

Final State	$e^+e^-E_{\text{T}}^{\text{miss}}$	$\mu^+\mu^-E_{\text{T}}^{\text{miss}}$	$e^\pm\mu^\mp E_{\text{T}}^{\text{miss}}$
Observed Events	594	975	5067
Total expected events (S+B)	$507.3 \pm 9.4 \pm 73.4$	$817.2 \pm 11.6 \pm 105.1$	$4419.7 \pm 25.9 \pm 522.2$
MC WW signal	$346.3 \pm 3.3 \pm 33.4$	$612.5 \pm 4.5 \pm 59.9$	$3238.1 \pm 10.2 \pm 284.0$
Top(data-driven)	$91.8 \pm 7.3 \pm 7.9$	$127.2 \pm 9.4 \pm 10.9$	$608.6 \pm 17.5 \pm 52.3$
W+jets(data-driven)	$13.9 \pm 4.9 \pm 14.2$	$6.1 \pm 5.0 \pm 11.5$	$248.8 \pm 15.3 \pm 138.7$
Z+jets (data-driven)	$28.0 \pm 0.5 \pm 13.0$	$33.0 \pm 0.5 \pm 17.4$	$174.5 \pm 3.4 \pm 17.7$
Other dibosons (MC)	$27.3 \pm 1.4 \pm 4.9$	$38.4 \pm 1.3 \pm 5.4$	$149.7 \pm 4.0 \pm 29.5$
Total background	$161.0 \pm 8.8 \pm 40.0$	$204.7 \pm 10.7 \pm 45.2$	$1181.6 \pm 23.8 \pm 238.2$

Table 3.18 Summary of observed events and expected signal and background contributions in three dilepton channels. The first error is statistical, the second systematic. The systematic uncertainties for total background and total expectation are calculated assuming full correlation among processes.

Figures 3.28 and 3.29 provide the kinematic distributions after final selection with

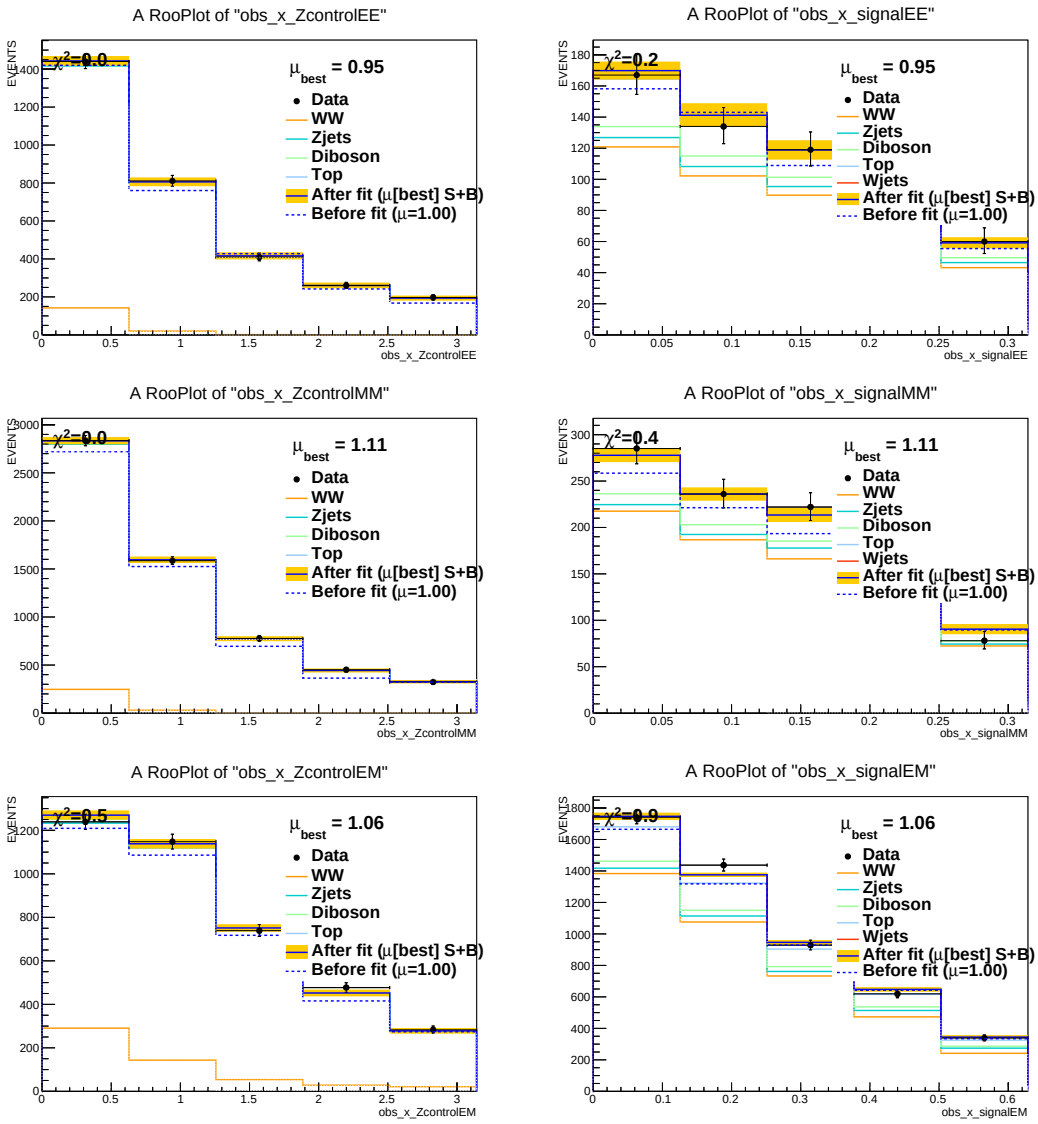

Figure 3.27 Comparison of $\Delta\phi(E_{\mathrm{T}}^{\mathrm{miss}}, p_{\mathrm{T}}^{\mathrm{miss}})$ used to fit the Z+jets and signal yield before and after the fit with data. The pre-fit distribution is shown in a dashed blue line where the signal yield was already scaled by a factor 1.15. The Z control region is shown on the left and the nominal selection (signal region) is shown on the right. From top to bottom the ee, $\mu\mu$ and $e\mu$ channels are shown. [30]

data and backgrounds estimated from baseline methods. Top, $W + jets$ and $Z + jets$ are estimated from data-driven methods, and other diboson backgrounds are estimated from MC.

3.6 Systematics

This section summarizes the systematic uncertainties on the WW signal acceptance. It mainly include the experimental uncertainties and theoretical uncertainties. One can define an overall correction factor C_{WW} for efficiencies, detector resolutions and geometric acceptance to the fiducial region under consideration: C_{WW} is the ratio of the MC signal event yield passing the analysis selection at reconstruction level to the MC event yield passing the fiducial selection at generator ("truth") level. The scale factor that allows to recover the total cross section from the fiducial one, the acceptance factor A_{WW}, defined as the ratio of the MC signal event yield passing the analysis selection at generator ("truth") level by the total number of generated signal MC events, encapsulates the extrapolation from the fiducial volume to the full phase space, and contains all the uncertainties related to the theoretical modelling used for the extrapolation. More details about A_{WW} and C_{WW} will be talked about in the Section 3.7.

Usually we consider experimental uncertainties and do conservative studies to determine theoretical uncertainties. Table 3.19 Shows the summary for all considered sources. We will talk about them in next few sections.

3.6.1 Experimental systematics

Experimental systematic uncertainties are handled independently considering different sources. The uncertainties due to the pile-up are estimated by varying the reweighting of the MC samples to reproduce the distributions of primary vertices in data. Trigger and reconstruction scale factors are applied to the MC simulation so that the simulation efficiencies match those measured in data. The trigger efficiencies for electrons and muons are varied in the simulation within the range of their uncertainties as determined from data. Lepton reconstruction and identification effects are also considered.

The uncertainty due to the lepton momentum scale and resolution is considered. Uncertainties related to the selection and measurement of jets affect the measurement primarily via the definition of jets which are selected for the jet-veto requirement, but also via $E_{\mathrm{T}}^{\mathrm{miss}}$ reconstruction. By varying each of these in the simulation within their corresponding uncertainties as determined from data, The impact on the cross-section measurements can be estimated. The main sources of uncertainty for jets are JES and JER.

Sources	$e^+e^-E_{\mathrm{T}}^{\mathrm{miss}}$	$\mu^+\mu^-E_{\mathrm{T}}^{\mathrm{miss}}$	$e^\pm\mu^\mp E_{\mathrm{T}}^{\mathrm{miss}}$	Combined
A_{WW} uncertainties				
PDF	0.94%	0.93%	0.81%	0.82%
Scale	0.2%	0.2%	0.2%	0.2%
$PS + GEN$	2.61%	2.67%	2.46%	2.50%
EWCorr	0.41%	0.43%	0.46%	0.45%
Jet-Veto	3.4%	3.4%	3.4%	3.4%
$\Delta A_{WW}/A_{WW}$	4.41%	4.45%	4.30%	4.33%
C_{WW} uncertainties				
Pileup	1.87%	1.97%	1.30%	1.44%
e Trigger Efficiency SF	2.52%	0%	0.30%	0.44%
m Trigger Efficiency SF	0%	2.84%	0.27%	0.62%
Muon MS Resolution	0%	0.05%	0.01%	0.01%
Muon ID Resolution	0%	1.53%	0.54%	0.63%
Muon Scale	0%	0.35%	0.10%	0.12%
Muon Efficiency SF	0%	0.77%	0.39%	0.41%
Muon Isolation SF	0%	1.13%	0.56%	0.60%
Electron Resolution	0.18%	0%	0.03%	0.02%
Electron Scale	1.40%	0%	0.37%	0.40%
Electron Efficiency SF	2.00%	0%	0.93%	0.88%
Electron Isolation SF	0.44%	0%	0.21%	0.20%
Jet Vertex Fraction	0.24%	0.21%	0.21%	0.21%
Jet Energy Resolution	1.25%	1.33%	1.32%	1.32%
Jet Energy Scale	3.56%	4.11%	3.85%	3.86%
Missing $E_{\mathrm{T,\,Rel}}^{\mathrm{miss}}$ Reso Soft Terms	0.31%	0.50%	0.29%	0.32%
Missing $E_{\mathrm{T,\,Rel}}^{\mathrm{miss}}$ Scale Soft Terms	1.91%	1.71%	1.07%	1.33%
Missing p_{T} Reso Soft Terms	0.16%	0.09%	0.11%	0.10%
Missing p_{T} Scale Soft Terms	0.36%	0.29%	0.22%	0.24%
Residual Theory	1.15%	1.01%	0.70%	0.61%
$\Delta C_{WW}/C_{WW}$	5.96%	6.26%	4.69%	4.85%
$A_{WW}C_{WW}$ uncertainties				
PDF	1.25%	0.98%	0.85%	0.90%
Scale	0.7%	0.7%	0.7%	0.7%
$PS + GEN$	3.01%	2.87%	2.52%	2.50%
EWCorr	0.34%	0.40%	0.47%	0.45%
Jet-Veto	3.4%	3.4%	3.4%	3.4%
$\Delta C_{WW}A_{WW}/C_{WW}A_{WW}$	7.55%	7.72%	6.40%	6.52%
Luminosity	2.8%	2.8%	2.8%	2.8%
$\sigma(WW)$ theoretic uncertainty	5.30%	5.30%	5.30%	5.30%
Full WW signal estimation uncertainty	9.64%	9.78%	8.77%	8.86%

Table 3.19 Uncertainty sources and associated relative uncertainties for WW signal acceptance estimations for ee, $e\mu$, $\mu\mu$ and all channels combined. The uncertainties for A_{WW}, C_{WW} and $A_{WW} \times C_{WW}$ are shown. The overall WW signal estimation uncertainties include A_{WW} C_{WW} uncertainties, luminosity and theoretical cross-section uncertainties. [30]

Considering the definition of $p_{\mathrm{T}}^{\mathrm{miss}}$, the uncertainties come from the momentum measurement of the selected leptons and the tracks not associated with the leptons (soft tracks). The lepton related uncertainty is simultaneously evaluated when propagating the lepton momentum scale and resolution systematics in the full selection. The uncertainty with respect to soft tracks is estimated from by $Z \to \mu\mu$ data events with no jets, as is described by JET/Etmiss group. It exploits the balance between the p_{T} of the hard interaction $p_{\mathrm{T}}^{\mathrm{lep}}$, which is for WW signal containing the leptons and the neutrinos with true $E_{\mathrm{T}}^{\mathrm{miss}}$, and the soft tracks $p_{\mathrm{T}}^{\mathrm{soft}}$. The $p_{\mathrm{T}}^{\mathrm{lep}}$ is defined as the magnitude of the vector sum ($\mathbf{p}_{\mathrm{T}}{}^{\mathrm{lep}}$) of the momenta of leptons or neutrinos. The $p_{\mathrm{T}}^{\mathrm{soft}}$ is defined as the magnitude of residual momentum vector ($\mathbf{p}_{\mathrm{T}}{}^{\mathrm{soft}}$) after subtracting $\mathbf{p}_{\mathrm{T}}{}^{\mathrm{lep}}$ from $\mathbf{p}_{\mathrm{T}}^{\mathrm{miss}}$. Furthermore, the $p_{\mathrm{T}}^{\mathrm{soft}}$ is decomposed along the transverse and longitudinal direction defined by $\mathbf{p}_{\mathrm{T}}{}^{\mathrm{lep}}$, yielding $p_{\mathrm{T}}^{\mathrm{soft,perp}}$ and $p_{\mathrm{T}}^{\mathrm{soft,para}}$, respectively. The scale uncertainty is derived based on $p_{\mathrm{T}}^{\mathrm{soft,para}}$ and the resolution uncertainties are estimated on both components by comparing with data. The similar decomposition is then conducted in the signal and other background MC events, and the scale and resolution uncertainties are propagated in order to estimate $p_{\mathrm{T}}^{\mathrm{miss}}$ uncertainty from soft tracks. The assumption is that, the systematic for each individual effect is independent. So the full systematic uncertainties can be estimated by varying the central value by $\pm 1\sigma$ when the analysis cuts are applied.

3.6.2 Theoretical systematics

This section describes the theoretical uncertainties that are considered in this analysis. The theoretical uncertainties on signal acceptance are taken into account in cross section extraction. The uncertainties on the signal shape and the fiducial cross section prediction are important in the aTGCs and unfolding studies.

3.6.2.1 Acceptance uncertainties

The precision of theoretical calculation and MC modelling can affect our signal selectoin efficiency. So it is quite important to evaluate the theoretical uncertainties which will be later taken into account in the cross section calculation. In the following we evaluate the acceptance uncertainties induced by the uncertainties of parton density functions (PDFs), choices of QCD renormalization and factorization scales, choices of NLO MC methods, comparison between different parton showers and the application of NLO electroweak correction. The jet-veto cut is at the final cut stage. It is very important, and the veto efficiency can contribute large theoretical uncertainty. This is because the jet veto cut introduces another scale at jet p_T threshold and large logarithmic terms can be introduced in the calculation. The pertubative uncertainty is usually evaluated by

varying QCD scales. However it is found that the usual scale variation cannot correctly account for the uncertainty of jet-veto efficiency. We have to use a dedicated method to derive the jet-veto uncertainty. It will be discussed later.

The uncertainties are presented for both fiducial acceptance A_{WW} and reconstruction correction C_{WW}. The uncertainties for $A_{WW} \times C_{WW}$ are also provided for reference. Since the fiducial volume is defined similarly as at the reconstruction level, the C_{WW} is expected to have small theoretical dependence. However, we still consider the C_{WW} uncertainties to address the residual theoretical dependence and also the uncertainty on the τ contribution which is only included in the numerator of C_{WW} calculation.

Table 3.20 gives the overview of the theoretical uncertainties on signal acceptance. These uncertainties are used in the cross-section extraction.

	A_{WW}				C_{WW}				$A_{WW} \times C_{WW}$			
	ee	$\mu\mu$	$e\mu$	incl.	ee	$\mu\mu$	$e\mu$	incl.	ee	$\mu\mu$	$e\mu$	incl.
PDF	0.94%	0.93%	0.81%	0.82%	0.34%	0.13%	0.10%	0.10%	1.25%	0.98%	0.85%	0.90%
Scale	0.2%	0.2%	0.2%	0.2%	0.6%	0.6%	0.6%	0.6%	0.7%	0.7%	0.7%	0.7%
$PS + GEN$	2.61%	2.67%	2.46%	2.50%	0.92%	0.80%	0.35%	0.00%	3.01%	2.87%	2.52%	2.50%
EWCorr	0.41%	0.43%	0.46%	0.45%	0.06%	0.04%	0.01%	0.00%	0.34%	0.40%	0.47%	0.45%
Jet-Veto	3.4%	3.4%	3.4%	3.4%					3.4%	3.4%	3.4%	3.4%
Total	4.41%	4.45%	4.30%	4.33%	1.15%	1.01%	0.70%	0.61%	4.77%	4.63%	4.40%	4.40%

Table 3.20 Fractional theoretical uncertainties on signal acceptance for WW signal events. [30]

3.6.3 PDF uncertainty

We follow the $PDF4LHC$ working group recommendation [52] and consider three common PDF sets: NNPDF2.3 [53], MSTW2008NLO [32] and CT10 [37]. As the first step of the calculation the internal PDF error bands are evaluated from each sets and following the recommendation we consider 100 sets for NNPDF, 40 sets for MSTW and 52 sets for CT10. The default signal MC events are used, and the LHAPDF package [54] is adopted to calculate the signal acceptance for the PDF sets other than default CT10 set in the MC samples.

The CT10 internal uncertainty is obtained by following a standard procedure

$$\sigma^+ = \sqrt{\sum_{i=0}^{N} [max(A_{i+} - A_0, A_{i-} - A_0, 0)]^2}/A_0 \tag{3.13}$$

$$\sigma^- = \sqrt{\sum_{i=0}^{N} [max(A_0 - A_{i+}, A_0 - A_{i-}, 0)]^2}/A_0 \tag{3.14}$$

where A_0, A_{i+} and A_{i-} are the WW acceptances evaluated at the central value of CT10, the one sigma up variation according to i-th (i goes from 1 to 52 for CT10) eigen error set

and the related down variation. The MSTW internal uncertainty is evaluated in a similar way. The NNPDF uncertainty is obtained by also studying the standard deviation of the acceptances calculated from all 100 error sets. These uncertainties are symmetrized by taking the largest deviations of the up and down variations.

The final PDF uncertainty is the calculated as the envelope of the three PDF error bands (CT10, MSTW, NNPDF). The results are summarized in Table 3.21.

PDF Uncert.	A_{WW}				C_{WW}				$A_{WW} \times C_{WW}$			
	ee	$\mu\mu$	$e\mu$	incl.	ee	$\mu\mu$	$e\mu$	incl.	ee	$\mu\mu$	$e\mu$	incl.
QQ												
CT10	0.45%	0.46%	0.49%	0.48%	0.20%	0.08%	0.07%	0.08%	0.56%	0.45%	0.52%	0.51%
MSTW	0.88%	0.87%	0.72%	0.76%	0.34%	0.12%	0.10%	0.11%	1.19%	0.94%	0.80%	0.85%
NNPDF	0.48%	0.58%	0.75%	0.68%	0.30%	0.08%	0.06%	0.07%	0.34%	0.54%	0.73%	0.67%
ATLAS-CT10	0.86%	0.61%	0.87%	0.83%	0.73%	0.14%	0.43%	0.41%	1.58%	0.75%	1.30%	1.24%
Final	0.88%	0.87%	0.75%	0.76%	0.34%	0.12%	0.10%	0.11%	1.19%	0.94%	0.80%	0.85%
GG												
CT10	1.06%	1.06%	1.06%	1.06%	0.28%	0.17%	0.03%	0.03%	1.30%	0.98%	1.04%	1.05%
MSTW	0.75%	0.77%	0.74%	0.75%	0.17%	0.11%	0.02%	0.01%	0.84%	0.68%	0.74%	0.74%
NNPDF	1.68%	1.69%	1.68%	1.68%	0.34%	0.19%	0.03%	0.03%	1.99%	1.55%	1.65%	1.66%
ATLAS-CT10	0.54%	0.66%	0.57%	0.58%	0.05%	0.09%	0.02%	0.02%	0.49%	0.75%	0.58%	0.60%
Final	1.68%	1.69%	1.68%	1.68%	0.34%	0.19%	0.03%	0.03%	1.99%	1.55%	1.65%	1.66%
Total	0.94%	0.93%	0.81%	0.82%	0.34%	0.13%	0.10%	0.10%	1.25%	0.98%	0.85%	0.90%

Table 3.21 Fractional PDF uncertainties on signal acceptance for WW signal events from $q\bar{q}$ initial state (QQ) on the top and from $gg \to (H) \to WW$ (GG) process at the bottom. The results from ATLAS-CT10 are only regarded as a reference and not used in the analysis. [30]

3.6.3.1 QCD scale uncertainty

The renormalization μ_R and factorization μ_F scales are varied independently by a factor of 0.5 or 2, with in total 9 sets of variations including the nominal one (M_{WW}). This is to study the impact on the acceptance. The full scale variations are explored for A_{WW} and the study is done at truth level by using privately generated MC $qq \to WW \to e\nu\mu\nu$ events, while the residual scale uncertainty on C_{WW} is checked using fast simulation samples which have only two scale variations: $\mu_R = \mu_F = 2\mu_0$ and $\mu_R = \mu_F = 0.5\mu_0$.

The scale uncertainty for $gg \to H \to WW$ signal is studied in a similar way in the $H \to WW$ paper [55] and the uncertainty on fiducial acceptance is found to be about 1.4%. As for the non-resonant $gg \to WW$ process, MCFM, a parton level generator, is used to calculate the fiducial acceptances with independent nine scale variations. Combining all variations, it gives the uncertainty of about 0.3%. The summary of scale uncertainties for WW signal acceptance is shown in Table 3.22.

Scale Uncert.	A_{WW}	C_{WW}	$A_{WW} \times C_{WW}$
QQ	0.2%	0.6%	0.7%
GGH	1.4%	0.6%	1.5%
GG	0.3%	0.6%	0.7%
Total	0.2%	0.6%	0.7%

Table 3.22 Fractional scale uncertainties on signal acceptance for WW signal events from $q\bar{q}$ initial state (QQ) on the top, $gg \to H \to WW$ (GGH) process in the middle, and non-resonant $gg \to WW$ (GG) process at the bottom. The total scale uncertainties for signal acceptance at the last row are combined from the individual processes assuming 100% correlation. [30]

3.6.3.2 Parton shower and Generator uncertainties

For $qq \to WW$ process, the parton shower uncertainty is evaluated by comparing the acceptances of PowHeg MC (showered with Pythia8 and Herwig/Jimmy). The generator uncertainty is evaluated by the difference between PowHeg and MC@NLO MC events (both showered with Herwig/Jimmy). For A_{WW} we generate private truth MC events to derive the uncertainties. For C_{WW} the residual uncertainties due to parton shower and generator are evaluated at once by comparing PowHeg+Pythia8 and MC@NLO+Herwig/Jimmy samples with full simulation. The parton shower and the generator uncertainties on A_{WW} are combined in quadrature, denoted as the $PS{+}GEN$ uncertainty.

The remaining gg initiated signal processes contribute a small portion of the total. The non-resonant $gg \to WW$ process is generated at LO precision and therefore can suffer from large uncertainties once the jet-veto is applied. For C_{WW}, unfortunately there are no available full simulation MC samples to study the $PS{+}GEN$ uncertainties, so we take the uncertainties from the above study done for $qq \to WW$, which is also applied for the $gg \to H \to WW$ case. For A_{WW}, the parton shower uncertainties for non-resonant $gg \to WW$ process is evaluated by comparing MCFM truth MC events showered with Pythia8 and Herwig/Jimmy. Then the A_{WW} generator uncertainty is derived by comparing MC sample (gg2WW+Herwig/Jimmy) and MCFM+Herwig/Jimmy at truth level. In the end the combined $PS + GEN$ uncertainty is the quadratic sum of the individual parton shower and generator uncertainties as in the $qq \to WW$ case.

The uncertainties for $gg \to H \to WW$ process are from the $H \to WW$ paper [55]. The detailed uncertainties are presented in the Table 3.23.

Finally the $PS + GEN$ uncertainties for $A_{WW} \times C_{WW}$ are calculated as the quadratic sum of those for A_{WW} and C_{WW}, and the total $PS + GEN$ uncertainties for WW signal acceptance are combined from each processes with the assumption of

full correlation.

PS+GEN Uncert.	A_{WW}				C_{WW}				$A_{WW} \times C_{WW}$			
	ee	$\mu\mu$	$e\mu$	incl.	ee	$\mu\mu$	$e\mu$	incl.	ee	$\mu\mu$	$e\mu$	incl.
QQ												
Parton Shower	0.30%	0.30%	0.30%	0.30%								
Generator	1.25%	1.25%	1.25%	1.25%								
Final	1.29%	1.29%	1.29%	1.29%	0.92%	0.80%	0.35%	0.00%	1.58%	1.51%	1.33%	1.29%
GG												
Parton Shower	27.87%	28.23%	26.96%	27.36%								
Generator	3.46%	6.07%	15.78%	12.10%								
Final	28.08%	28.88%	31.24%	29.92%	0.92%	0.80%	0.35%	0.00%	28.10%	28.89%	31.24%	29.92%
GGH												
Final	6.87%	6.87%	6.87%	6.87%	0.92%	0.80%	0.35%	0.00%	6.93%	6.92%	6.88%	6.87%
Total	2.61%	2.67%	2.46%	2.50%	0.92%	0.80%	0.35%	0.00%	3.01%	2.87%	2.52%	2.50%

Table 3.23 Fractional Parton Shower and Generator uncertainties on signal acceptance for WW signal events. [30]

3.6.3.3 Uncertainties due to NLO electroweak correction

The NLO electroweak (EW) contribution of $\mathcal{O}(\alpha^3_{EW})$ on di-boson production is described in [29, 56–58]. The corrections have been implemented in the MC sample, which gives an event-by-event EW k-factor (k_{EW}), calculated from the MC generator level kinematics of the initial state quarks. The calculation is only used when the bosons are on-shell. A systematic uncertainty is applied when at least one of the bosons are off-shell, which is defined when its mass satisfies $|M - M_W| > 25$ GeV. Events that are beyond the kinematically allowed regions ($\sqrt{s} > 2m_W$) of the calculation will be assigned $k_{EW} = 1$ without any systematic uncertainties.

The k_{EW} and its uncertainty δk_{EW} as a function of leading lepton p_{T} is given in Table 3.24.

p_{T} [GeV]	25-75	75-150	150-250	250-350	350-1000
k_{EW}	$< 1\%$	-4%	-10%	-16%	-24%
δk_{EW}	0.1%	0.4%	1.7%	4.0%	7.1%

Table 3.24 Size of electroweak correction and its systematic uncertainty as a function of leading lepton p_{T}. [30]

The electroweak k-factors have been applied to our nominal Powheg+Pythia $qq \to WW$ samples. The uncertainties are evaluated in nominal PowHeg+Pythia samples and presented in Table 3.25. Since the electroweak correction is only applicable for $qq \to WW$ events, this uncertainty is set to be zero for gg induced process.

After all, in our analysis the NLO electroweak correction is applied in the calculation of the selection efficiency for $qq \to WW$ events, while the cross section for this process is still taken from MCFM calculation in which the electroweak correction is

not applicable. The effect of the correction on signal yields is found to be less than one percent.

	A_{WW}				C_{WW}				$A_{WW} \times C_{WW}$			
$q\bar{q}$	ee	$\mu\mu$	$e\mu$	all	ee	$\mu\mu$	$e\mu$	all	ee	$\mu\mu$	$e\mu$	all
	0.44%	0.47%	0.49%	0.48%	0.07%	0.04%	0.01%	0.00%	0.37%	0.43%	0.50%	0.48%
Total	0.41%	0.43%	0.46%	0.45%	0.06%	0.04%	0.01%	0.00%	0.34%	0.40%	0.47%	0.45%

Table 3.25 Fractional electroweak correction uncertainties on signal acceptance for WW signal events from $q\bar{q}$ initial state on the top. The total uncertainties for signal acceptance at the last row are scaled by the fraction of yields of $q\bar{q}$ initial state over total signal prediction. [30]

3.6.3.4 Jet-Veto uncertainty

The pertubative uncertainty for jet-veto acceptance is discussed in this paragraph. It has been shown that accidental cancellations with log terms introduced by restricting QCD radiation can cause the scale uncertainty to be underestimated in a jet-binned analysis [59]. Stewart and Tackmann have provided an estimation of scale uncertainties in a jet veto acceptance. It is called S-T method, which assumes that the uncertainties in the inclusive jet-binned cross sections are uncorrelated, since the structure of these perturbative series are different. The uncertainty in the jet veto acceptance is expressed as:

$$\frac{\delta\epsilon}{\epsilon} = \left(\frac{1-\epsilon}{\epsilon}\right)\sqrt{\left(\frac{\delta\sigma_{\geq 0 \text{ jet}}}{\sigma_{\geq 0 \text{ jet}}}\right)^2 + \left(\frac{\delta\sigma_{\geq 1 \text{ jet}}}{\sigma_{\geq 1 \text{ jet}}}\right)^2} \tag{3.15}$$

where $\sigma_{\geq i \text{ jet}}$ is the fiducial cross section in jet bins, and the $\delta\sigma_{\geq i \text{ jet}}$ is the uncertainty of the fiducial cross section $\sigma_{\geq i \text{ jet}}$ due to scale variations.

The S-T method can be applied on currently available theoretical calculations, which include the pure NLO calculation using MCFM program, the NNLO prediction provided by the NNLO paper author [60]. To apply the S-T method on NNLO prediction, we need the cross section of $WW + 0$ jet and $WW + 1$ jet and their scale variations from NNLO prediction from the paper. In addition to the S-T method, one can also explore the high order pertubative uncertainty by comparing the jet-veto efficiencies calculated with different prescriptions [61]. It also provides a way of the pertubative uncertainty estimation for jet-veto efficiency, which gives the fractional maximum deviation 3.7%.

The S-T method can be applied on PowHeg signal MC samples. The final jet-veto uncertainty for $qq \to WW$ process is taken from the S-T approach applied on NNLO cross-sections, while we consider the uncertainty derived from the three jet-veto efficiencies (JVE) as a conservative cross check. With the numbers provided in above discussion the final uncertainty is found to be 2.9%.

We assign 11% as the jet-veto uncertainty for gg induced processes from $H \to WW$ paper [55]. The gg and qq processes are treated as fully correlated in order to combine the uncertainty, and finally we find that the jet-veto efficiency uncertainty for WW signal is about 3.4%, similar information is summarized in Table 3.27.

Scale Variations	$PowHeg$			NLO			NNLO		
	σ_{incl} [pb]	σ_{0j}	$\sigma_{\geq 1j}$	σ_{incl}	σ_{0j}	$\sigma_{\geq 1j}$	σ_{incl}	σ_{0j}	$\sigma_{\geq 1j}$
$\mu_R, \mu_F = 1, 1$	51.44	34.99	16.45	52.29	39.24	13.05	59.13	40.38	18.75
$\mu_R, \mu_F = 1, 2$	51.75	35.30	16.45	52.64	39.95	12.69	59.12	40.43	18.68
$\mu_R, \mu_F = 2, 2$	50.70	34.69	16.02	51.58	39.94	11.64	58.08	40.40	17.68
$\mu_R, \mu_F = 2, 1$	50.39	34.38	16.01	51.23	39.26	11.97	58.04	40.25	17.79
$\mu_R, \mu_F = 1, 0.5$	51.15	34.68	16.46	51.96	38.60	13.37	59.16	40.25	18.91
$\mu_R, \mu_F = 0.5, 0.5$	52.45	35.43	17.01	53.29	38.60	14.69	60.38	40.53	19.85
$\mu_R, \mu_F = 0.5, 1$	52.70	35.72	16.98	53.59	39.25	14.34	60.27	40.55	19.72
$\mu_R, \mu_F = 0.5, 2$	53.00	36.03	16.97	53.90	39.95	13.95			
$\mu_R, \mu_F = 2, 0.5$	50.07	34.06	16.00	50.86	38.60	12.26			
Frac. Scale Unc.	3.03%		3.40%	3.07%		12.58%	2.12%		5.88%
Jet-Veto eff.	68.02%			75.04%			67.49%		
S-T Unc.	2.14%			4.31%			2.90%		

Table 3.26 The inclusive and jet-binned cross sections with different scale variations for $qq \to WW$ process and the jet veto efficiencies calculated with default QCD scales as well as the corresponding fractional jet veto uncertainties evaluated with S-T method. The relevant numbers are derived from $PowHeg + Pythia8$ MC, MCFM (NLO) and NNLO calculations. The extreme scale variations are not available for NNLO calculation so these are left blank in the Table. The LO non-resonant gg contribution is included in the NNLO cross sections, while the cross sections from $PowHeg$ and NLO are derived for $qq \to WW$ only. [30]

Jet-Veto Uncert.	A_{WW}	C_{WW}	$A_{WW} \times C_{WW}$
QQ	2.9%	-	2.9%
GGH+GG	11%	-	11%
Total	3.4%	-	3.4%

Table 3.27 Fractional jet-veto uncertainties on signal acceptance for WW signal events from $q\bar{q}$ initial state (QQ) on the top, gg-induced (GGH+GG) processes in the middle. The total jet-veto uncertainties for signal acceptance at the last row are combined from the individual processes assuming 100% correlation. The theoretical jet-veto uncertainty on C_{WW} is neglected, and the uncertainties for A_{WW} and $A_{WW} \times C_{WW}$ are the same. [30]

3.7 Cross section

The formula used to determine the total cross-section is

$$\sigma_{WW} = \frac{N_{obs} - N_{bkg}}{\epsilon \mathcal{A} \mathcal{L}\, Br} \tag{3.16}$$

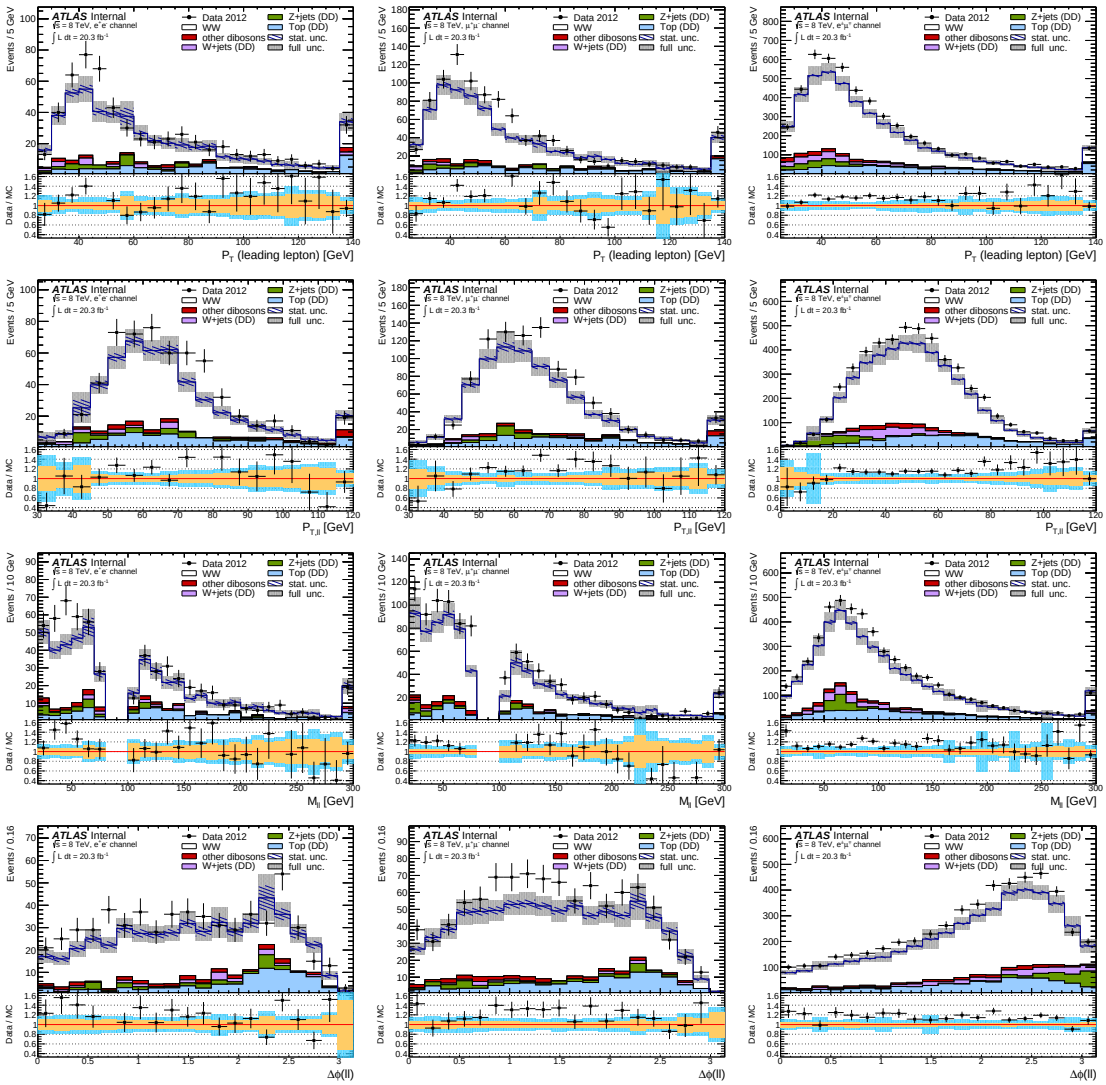

Figure 3.28 Distributions for WW candidates at final selection for combined ee, $\mu\mu$ and $e\mu$ channels: the left column shows the ee channel, the middle column the $\mu\mu$ channel and the right column the $e\mu$ channel. The first row shows the leading lepton p_{T}, the second row the transverse momentum of dilepton pair p_{T} $(\ell\ell)$, the third row shows the invariant mass of the dilepton pair $M(\ell\ell)$ distributions, and the fourth row shows the $\Delta\phi(\ell\ell)$ distributions. The points represent data and the stacked histograms describe the signal and backgrounds separately. Signal and "other dibosons" are modeled by MC, Z+jets is estimated by the simultaneous fit, top is estimated by JVSP method and the W+jets distribution has been obtained using the matrix method (indicated by the DD – data driven label). The uncertainty includes statistical uncertainties and systematics on the signal and backgrounds and is shown as grey bands in the main plot and in blue on the ratio plot. Statistical uncertainty itself is indicated by the line pattern in the main plot or the orange band in the ratio plot. The histograms are normalised by SM cross sections to 20.3 fb^{-1}.

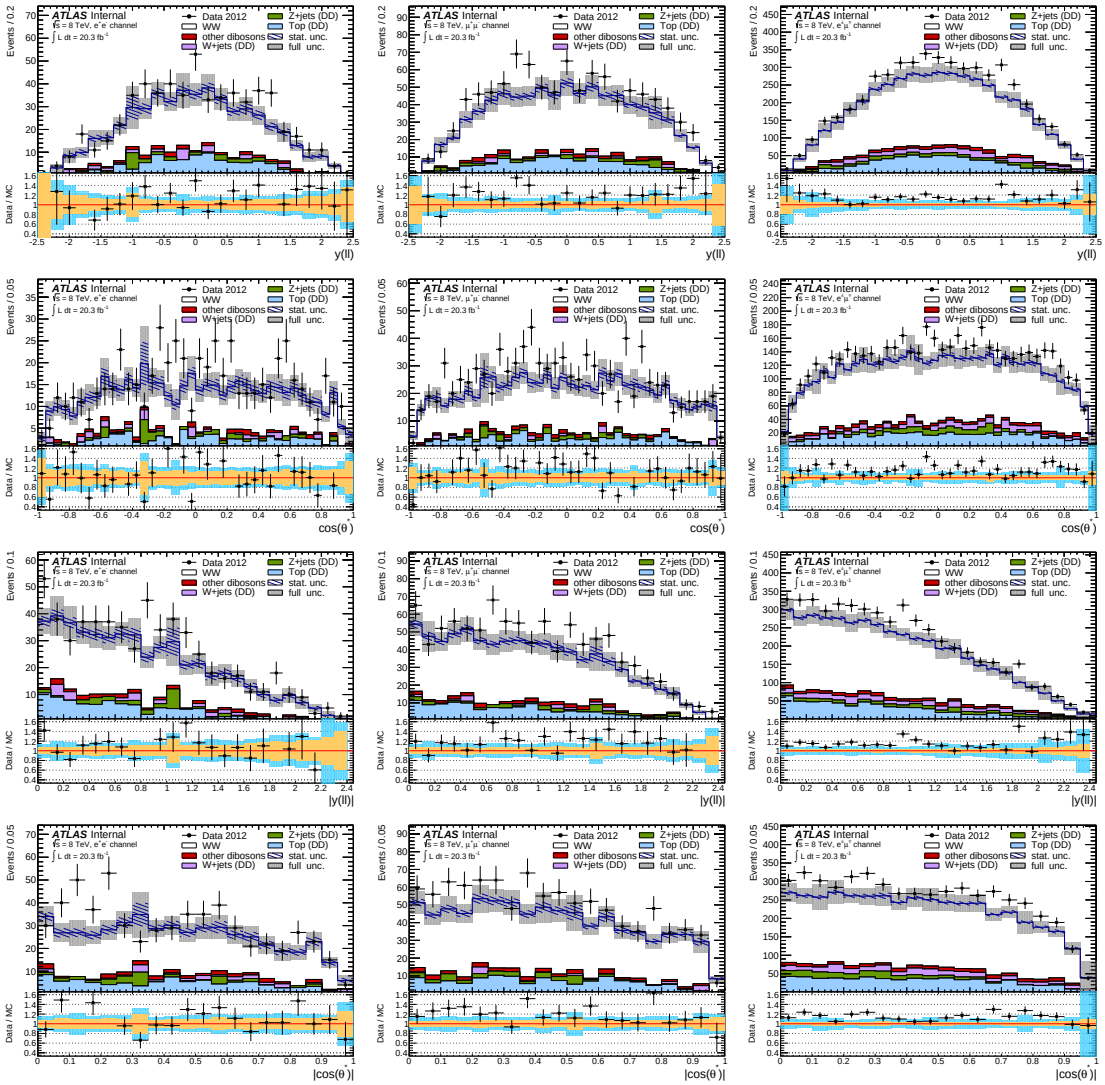

Figure 3.29 Distributions for WW candidates at final selection for combined ee, $\mu\mu$ and $e\mu$ channels: the left column shows the ee channel, the middle column the $\mu\mu$ channel and the right column the $e\mu$ channel. The first row shows $y(\ell\ell)$ distributions, the second row the $\cos(\theta^*)$ distributions, the third row show the $|\, y(\ell\ell)\,|$ distributions and the last row shows the $|\,\cos(\theta^*)\,|$ distributions. The points represent data and the stacked histograms describe the signal and backgrounds separately. Signal and "other dibosons" are modeled by MC, Z+jets is estimated by the simultaneous fit, top is estimated by JVSP method and the W+jets distribution has been obtained using the matrix method (indicated by the DD – data driven label). The uncertainty includes statistical uncertainties and systematics on the signal and backgrounds and is shown as grey bands in the main plot and in blue on the ratio plot. Statistical uncertainty itself is indicated by the line pattern in the main or the orange band in the ratio plot. The histograms are normalised by SM cross sections to 20.3 fb^{-1}.

where N_{obs} is the number of observed events, N_{bkg} is the number of expected background, $\epsilon\mathcal{A}$ is the acceptance times efficiency which are treated as one number, Br is the branching fraction of dileptonic WW decays and $\mathcal{L}$ is the integrated luminosity. In much of the text, the acceptance times efficiency is effectively reported as the expected number of reconstructed WW events in the 20.3fb^{-1} sample. Using the SM cross-sections reported in Table A.1, the full MC simulations and PDG branching fraction lead to a final acceptance times efficiency for $WW \to \ell\nu\ell\nu$ ($l = e,\ \mu$) of $\epsilon\mathcal{A} = 8.0\%$.

The total cross section defined above effectively extrapolates from the kinematic selection applied in the measurement, dictated by experimental considerations (detector, trigger acceptances), to the full phase space. Part of its uncertainty is therefore purely caused by the theoretical modelling of the WW signal. The fiducial cross section is also presented, which is within the phase space of the geometric and kinematic requirements of the measurement. A fiducial cross section allows for easier comparisons with other theoretical predictions, and constitutes a measurement which minimises theoretical uncertainties.

Replacing acceptance times efficiency $\epsilon\mathcal{A}$ by C_{WW} in the above cross section formula, one obtains the fiducial cross section:

$$\sigma^{fid}_{WW\to l\nu l\nu} = \frac{N_{obs} - N_{bkg}}{C \cdot \mathcal{L}}.$$

The fiducial region is defined by applying selection cuts at MC particle level as in the Table 3.28. The following relations among C_{WW}, A_{WW} and $\epsilon\mathcal{A}$ hold:

	$e\nu e\nu$ fiducial region	$\mu\nu\mu\nu$ fiducial region	$e\nu\mu\nu$ fiducial region
p_ℓ^T (leading/sub-leading)	$> 25(20)$ GeV	$> 25(20)$ GeV	$> 25(20)$ GeV
$\lvert\eta_\ell\rvert$	$1.37 < \lvert\eta\rvert, 1.52 < \lvert\eta\rvert < 2.47$	$\lvert\eta\rvert < 2.4$	$1.37 < \lvert\eta^e\rvert, 1.52 < \lvert\eta^e\rvert < 2.47$ and $\lvert\eta^\mu\rvert < 2.4$
$M_{\ell^+\ell^-}$	> 15 GeV	> 15 GeV	> 10 GeV
$\lvert M_Z - M_{\ell^+\ell^-}\rvert$	> 15 GeV	> 15 GeV	≥ 0 GeV
N_{jets} ($E_T > 25$ GeV, $\lvert\eta\rvert < 4.5$)	0	0	0
$E^{\text{miss}}_{\text{T, Rel}}$	$> 45GeV$	$> 45GeV$	$> 15GeV$
$p^{\text{miss}}_{\text{T}}$	$> 45GeV$	$> 45GeV$	$> 20GeV$

Table 3.28 Definitions of common fiducial region as well as of the fiducial regions for the different channels.

$$C_{WW} = \frac{N(reco - level\ analysis\ cuts)}{N(generator - level\ fiducial\ cuts)}, \tag{3.17}$$

$$A_{WW} = \frac{N(generator - level\ fiducial\ cuts)}{N(generated\ events)}, \tag{3.18}$$

$$\epsilon\mathcal{A} = A_{WW} \cdot C_{WW} = \frac{N(reco - level\ analysis\ cuts)}{N(generated\ events)}, \tag{3.19}$$

where the event counts are derived from a signal Monte-Carlo sample. A summary of A_{WW}, C_{WW} and $A_{WW} \times C_{WW}$ with their associated uncertainties is shown in Table 3.29.

	$e\nu e\nu$	$\mu\nu\mu\nu$	$e\nu\mu\nu$	Combined
A_{WW}	$0.0855 \pm 0.0003 \pm 0.0038$	$0.0930 \pm 0.0004 \pm 0.0041$	$0.2274 \pm 0.0004 \pm 0.0098$	$0.1583 \pm 0.0002 \pm 0.0069$
$\Delta A_{WW}/A_{WW}$	4.41%	4.45%	4.30%	4.33%
C_{WW}	$0.2913 \pm 0.0023 \pm 0.0174$	$0.4740 \pm 0.0025 \pm 0.0297$	$0.5124 \pm 0.0011 \pm 0.0240$	$0.4769 \pm 0.0010 \pm 0.0231$
$\Delta C_{WW}/C_{WW}$	5.96%	6.26%	4.69%	4.85%
$A_{WW} \times C_{WW}$	$0.0249 \pm 0.0002 \pm 0.0019$	$0.0441 \pm 0.0003 \pm 0.0034$	$0.1165 \pm 0.0003 \pm 0.0075$	$0.0755 \pm 0.0002 \pm 0.0049$
$\Delta(A_{WW} \times C_{WW})/(A_{WW} \times C_{WW})$	7.55%	7.72%	6.40%	6.52%

Table 3.29 The WW overall acceptance $A_{WW} \times C_{WW}$, fiducial phase space acceptance A_{WW} and correction factor C_{WW} and their uncertainties. [30]

A negative log-likelihood function can then be defined as follows

$$N_s^i(\sigma_{WW}^{tot}, \{x_k\}) = \sigma_{WW}^{tot} \times Br \times L \times A_{WW} \times C_{WW} \times (1 + \sum_{k=1}^{n} x_k S_k^i)$$

$$N_b^i(\{x_k\}) = N_b^i(1 + \sum_{k=1}^{n} x_k B_k^i).$$

$$-\ln L(\sigma, \{x_k\}) = \sum_{i=1}^{3} -\ln\left(\frac{e^{-(N_s^i(\sigma,\{x_k\})+N_b^i(\{x_k\}))} \times (N_s^i(\sigma,\{x_k\}) + N_b^i(\{x_k\}))^{N_{obs}^i}}{(N_{obs}^i)!}\right) + \sum_{k=1}^{n} \frac{x_k^2}{2}. \tag{3.20}$$

with the following definitions:

- Superscript i indicate the i-th channel.
- Subscript k indicate the k-th source of systemtics..
- S_k, B_k are the standard deviation amplitudes, representing the systematic uncertainties.
- N_s, N_b are the expected number of signal and background events.
- N_{obs} is the observed date events.
- $\{x_k\}$ is the nuisance systematic uncertainty. Typically assumed to be a normal distribution. $\{x_k\} \sim N(0,1)$. The last term takes care of the Gaussian constraints on the nuisance parameters.

A single random variable x_k is used over all channels in signal and background as the effect of each systematic source is 100% correlated across channels and between signal and background component. To calculate the cross section (fiducial or total) in a single channel i, the poisson probability is used for the channel i rather than the product over all channels.

The fiducial and total cross-section are shown in the Table 3.30 and 3.31.

In this analysis, a measurement of the WW production cross section in pp collisions at $\sqrt{s} = 8$ TeV is performed. The measured combined cross section is $71.0^{+1.1}_{-1.1}$(stat) $^{+5.7}_{-5.0}$(syst) $^{+2.1}_{-2.0}$(lumi) pb, to be compared with the NNLO prediction (full NNLO), which is $63.2^{+1.6}_{-1.4}$(scale)$\pm$1.2(PDF) pb.

The measured cross section is compared with the NNLO QCD calculation of the WW production process published in [31]. The central value of the WW NNLO QCD

Channel	Cross Section [fb]
ee	$73.3^{+4.2}_{-4.1}$(stat) $^{+6.5}_{-5.6}$(syst) $^{+2.2}_{-2.1}$(lumi)
$\mu\mu$	$80.1^{+3.3}_{-3.2}$(stat) $^{+6.4}_{-5.5}$(syst) $^{+2.4}_{-2.3}$(lumi)
$e\mu$	$373.8^{+6.9}_{-6.8}$(stat) $^{+25.0}_{-22.5}$(syst) $^{+11.2}_{-10.5}$(lumi)

Table 3.30 Measured fiducial cross sections for each channel.

Channel	Cross Section [pb]
ee	$73.5^{+4.2}_{-4.1}$(stat) $^{+7.5}_{-6.4}$(syst) $^{+2.3}_{-2.1}$(lumi)
$\mu\mu$	$73.9^{+3.0}_{-3.0}$(stat) $^{+7.1}_{-5.9}$(syst) $^{+2.2}_{-2.1}$(lumi)
$e\mu$	$70.5^{+1.3}_{-1.3}$(stat) $^{+5.8}_{-5.1}$(syst) $^{+2.1}_{-2.0}$(lumi)
combined	$71.0^{+1.1}_{-1.1}$(stat) $^{+5.7}_{-5.0}$(syst) $^{+2.1}_{-2.0}$(lumi)

Table 3.31 Measured total cross sections for each channel.

production proceess with renormalisation and factorisation scale set to $\mu_R = \mu_F = M_{WW}/2$ is 59.06. The scales are varied independently and the envelope is taken as scale uncertainties, amounting to +1.22 and -1.03 or +2.1% and -1.7% respectively. For the PDF uncertainty, the relative symmetrised uncertainty of the MSTW NLO PDF set at 68% confidence level is used, ± 0.93 or $\pm 1.6\%$. The NNLO QCD calculation contains the $gg \to WW$ process.

The resonant WW cross section via Higgs production is added linearly using the numbers from Ref. [33]. This is something different from CMS results since they treated it as backgrounds while we add it into the signal [62]. Central values and systematic uncertainties are added linearly to yield the SM NNLO prediction (full NNLO) for WW production of $63.2^{+1.6}_{-1.4}$(scale)± 1.2(PDF). It should be noted that, for fiducial cross-section our measurement is consistent with theoretic calculation [63] and also the

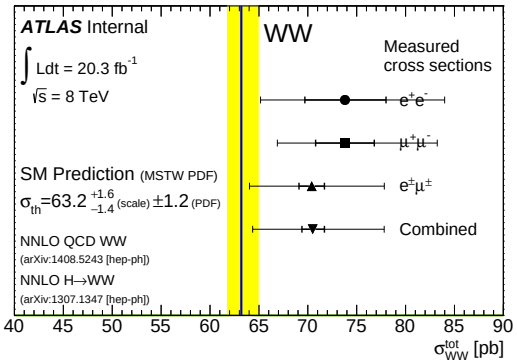

Figure 3.30 Overview plot: WW cross sections measured at $\sqrt{s} = 8$ TeV compared to the NNLO prediction [30]

total cross-section consistent with the theoretical NNLO prediction. The total cross-section measurement is also consistent with the latest CMS results considering we have different procedures for the analysis details. The 8 TeV data analysis is characterised large pile-up and hard modelling of $E_{\mathrm{T}}^{\mathrm{miss}}$, with less statistical uncertainty than that of 7 TeV [3] [4]. The jet-veto uncertainties, together with conservatively treated signal MC PS/Generator uncertainties are the main feature in the systematics evaluation. And we cannot forget the background uncertainties, although we have various methods and choose the one with the least uncertainty as our baseline. After all, we derive a precise measurement consistent with the SM prediction.

Figure 3.31 depicts the different WW cross sections measured by the CDF and D0 experiments at the Tevatron collider as well as the cross sections measured at the LHC collider by CMS and ATLAS at $\sqrt{s} = 7$ and 8 TeV as a function of the center-of-mass-energy. The measured value of the WW production cross section is compared to theoretical predictions based on NNLO QCD calculations. Below $\sqrt{s} = 8$ TeV only the non-resonant WW production cross section is shown, calculated with a scale choice of $\mu_F = \mu_R = M_{WW}/2$. In addition, previous measurements at the LHC by the ATLAS and CMS collaborations at $\sqrt{s}$ =7 and 8 TeV are shown as well as measurements at the proton-antiproton collider Tevatron. The CDF and D0 measurements are shown for a Tevatron collider energies of $\sqrt{s} = 1.96$ TeV. The measurements are compared to the WW production cross section as calculated in NNLO QCD. Above $\sqrt{s} = 7$ TeV, the resonant WW production via a Higgs boson with a mass of $m_H = 125$ GeV is added.

The results of the 8 TeV are published as a conference note [64]. Part of my work was used in the conference note. Main contributions are the event selection optimisation mainly for lepton p_{T} threshold and $E_{\mathrm{T}}^{\mathrm{miss}}$ selection, the fake factor method for W+jets and top background estimation with JVSP method. Currently for this analysis, since the conference results, the analysis is being finalized for a publication. Presented in this thesis is the final results that are currently reviewed for a publication.

3.8 The differential WW cross section measurement

The normalized differential W^+W^- cross section $\frac{1}{\sigma} \cdot \frac{d\sigma}{dX}$ is determined as a function of the leading lepton p_{T}, transverse momentum of dilepton pair $p_{\mathrm{T}}\,(\ell\ell)$, invariant mass of the dilepton pair $M(\ell\ell)$ and three angular distributions: $\Delta\phi(\ell\ell)$, $\mid y(\ell\ell) \mid$ and $\mid \cos(\theta^*) \mid$, where $\cos(\theta^*)$ is defined as:

$$\cos(\theta^*_{\ell\ell}) = \tanh\left(\frac{\Delta\eta_{\ell\ell}}{2}\right), \qquad \Delta\eta_{\ell\ell} = \eta_{\ell_1} - \eta_{\ell_2} \tag{3.21}$$

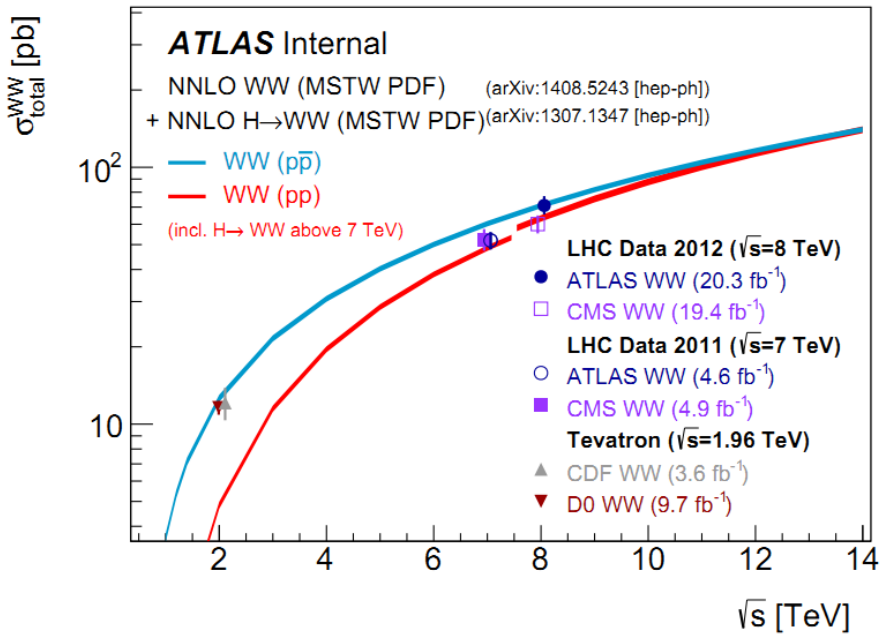

Figure 3.31 Overview over previous measurements as a function of centre-of-mass energy and comparison with NNLO prediction. [30]

The choice of binning is mostly limited by statistics:

$$p_T^{lead} = \{\ 25,\ 30,\ 35,\ 40,\ 50,\ 60,\ 70,\ 80,\ 100,\ 150,\ 500\ \}\ \text{GeV}$$
$$p_{\mathrm{T}}\,(\ell\ell) = \{\ 0,\ 25,\ 30,\ 35,\ 40,\ 50,\ 60,\ 70,\ 80,\ 500\ \}\ \text{GeV}$$
$$M(\ell\ell) = \{\ 10,\ 20,\ 30,\ 40,\ 50,\ 60,\ 70,\ 85,\ 100,\ 115,\ 135,\ 155,\ 175,\ 210,\ 650\ \}\ \text{GeV}$$
$$\Delta\phi(\ell\ell) = \{\ \pi/8,\ \pi/4,\ 3\pi/8,\ \pi/2,\ 5\pi/8,\ 3\pi/4,\ 7\pi/8,\ \pi\ \}$$
$$|\ y(\ell\ell)\ | = \{\ 0.0,\ 0.2,\ 0.4,\ 0.6,\ 0.8,\ 1.0,\ 1.2,\ 1.4,\ 1.6,\ 1.8,\ 2.0,\ 2.5\ \}$$
$$|\ \cos(\theta^*)\ | = \{\ 0.0,\ 0.1,\ 0.2,\ 0.3,\ 0.4,\ 0.5,\ 0.6,\ 0.7,\ 0.8,\ 1.\ \}$$

The cross section in each bin of each observable is determined from the event yields subtracting the backgrounds. In order to compare with predictions from event generators, we correct each distribution with event selection efficiencies and detector resolution effects, which is based on unfolding techniques using the iterative method as described by [65]. A response matrix is defined to connect the observable with and without detector effects. We divide the corrected number of events by the integrated luminosity and by the bin width, and obtain the differential cross section.

For each measured distribution, a response matrix is evaluated using W^+W^- events, generated by POWHEG, and with full detector simulation. The unfolding is performed using events considering only $e\mu$ final states. In order to minimize the model uncertainties due to unnecessary extrapolations of the measurement outside experimentally well-described phase space region, the normalized differential cross section is determined in

a visible phase space defined at the particle level by considering prompt leptons before final state radiation, with $p_{\mathrm{T}} > 20$ GeV and with $|\eta| < 2.5$. Events with one or more jets with $p_{\mathrm{T}} > 30$ GeV and $|\eta| < 4.7$ are rejected. The systematic uncertainties in each bin are derived from the variations of the nominal cross section, in the similar way as we described before, by redoing the procedure for every systematic variation. The difference with respect to the nominal value is taken as the systematic uncertainty for each bin and each measured observable. The possible correlations of the systematic uncertainties between bins are taken into account. Due to the normalisation, those systematic uncertainties that are correlated across all bins of the measurement, and therefore mainly affect the normalisation, cancel out at least partly. The errors also include the statistical error propagation through the unfolding method using the covariance matrix and the difference in the response matrix from MadGraph, POWHEG, and MC@NLO, the last one being almost negligible. The differential cross section is shown in the Figure 3.32. Reasonable agreement is observed between the measured differential distributions and the MC predictions.

3.9 Limits on anomalous gauge couplings

WW production in the dilepton with $E_{\mathrm{T}}^{\mathrm{miss}}$ final state may be sensitive to physics beyond the Standard Model. New physics introduces new production diagrams which can the alter total or differential production cross section. Examples of beyond the Standard Model physics include theories that involve new particles that decay into vector bosons [66] or decay into leptons with $E_{\mathrm{T}}^{\mathrm{miss}}$, sharing the same final state [67, 68].

3.9.1 Theoretical models

The operators of lowest dimension introduce anomalous triple gauge couplings. Any observable BSM physics effects can be described by a series of operators with mass dimension larger than four in addition to the dimension-four operators in the SM Lagrangian. In the effective field theory (EFT), the higher-dimensional operators are the low-energy description of interactions mediated by massive fields in the spectrum of an unknown BSM theory. If the mass scale of these fields is large compared to the experimentally accessible energies, only the first few terms in the series expansion are relevant. In the electro-weak sector of the SM, the first higher-dimension operators made solely from electro-weak vector fields and the Higgs doublet have mass dimension six. There are six different dimension-six operators that generate ATGC. Three of them are C and P conserving while the others are not. In this analysis, we will only consider models with with C and P conserving operators. BSM physics can be parameterized in

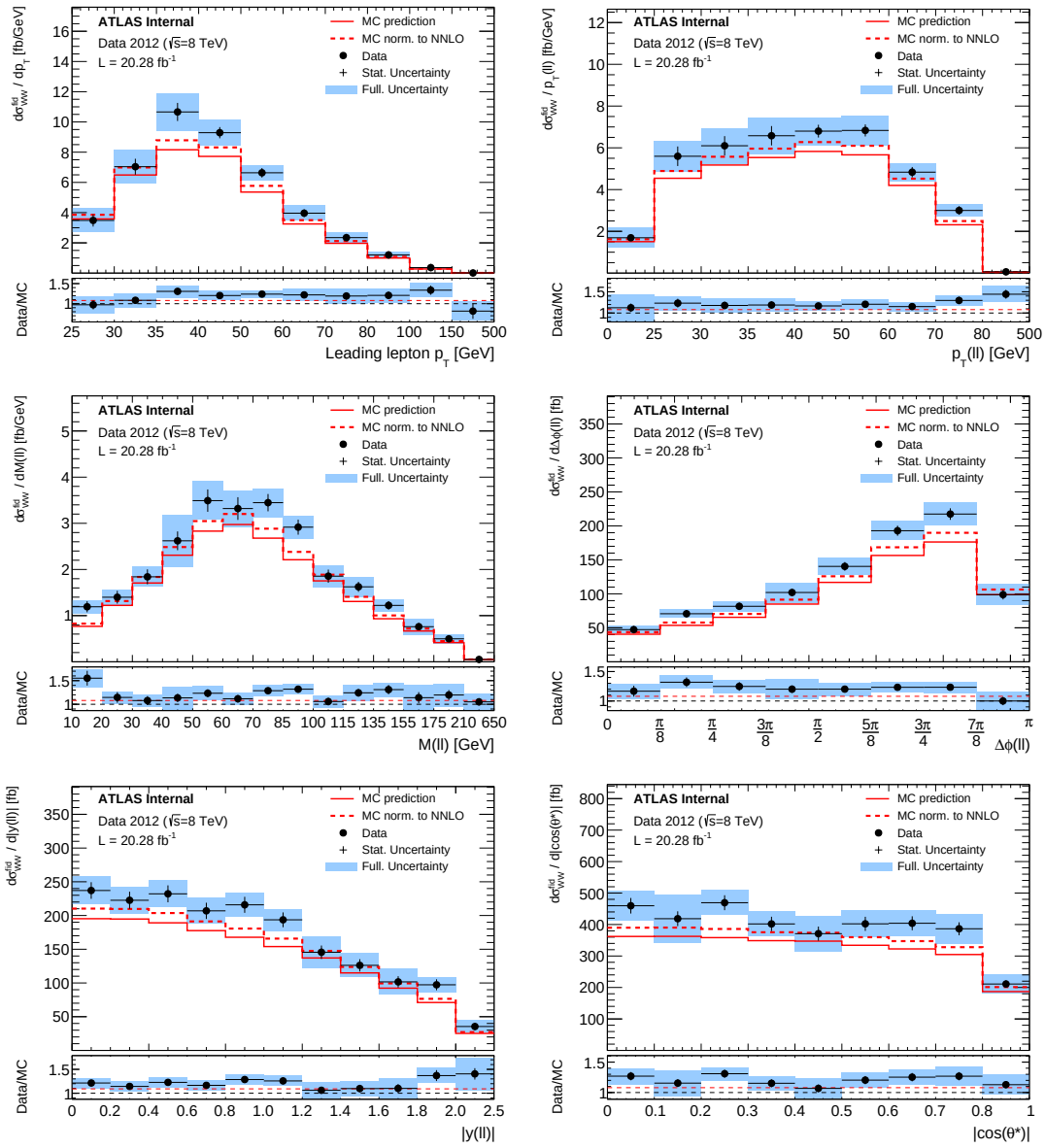

Figure 3.32 Unfolded unnormalized differential cross sections. [30]

terms of ATGC [69].

$$L = ig_{WWV}(g_1^V(W^+_{\mu\nu}W^{-\mu} - W^{+\mu}W^-_{\mu\nu})V^\nu + k^V W^+_\mu W^-_\nu V^{\mu\nu} + \frac{\lambda^V}{M_W^2}W^{\nu+}_\mu W^{-\rho}_\nu V^\mu_\rho) \tag{3.22}$$

where V = Z or γ; $W^\pm_{\mu\nu} = \partial_\mu W^\pm_\nu - \partial_\nu W^\pm_\mu$; $V_{\mu\nu} = \partial_\mu V_\nu - \partial_\nu V_\mu$. The overall coupling constants g_{WWV} are given by $g_{WW\gamma} = -e$ and $g_{WWZ} = -e\cot(\theta_W)$.

In the SM, three of these coupling parameters are $g_1^Z = 1$, $k^Z = 1$, and $k^\gamma = 1$ and the remaining parameters all equal to 0. Electro-magnetic gauge invariance requires

that $g_1^\gamma = 1$. These couplings can be taken as the deviations from the SM:

$$\Delta g_1^Z = 1 - g_1^Z \qquad \Delta k^Z = 1 - k^Z \qquad \Delta k^\gamma = 1 - k^\gamma \tag{3.23}$$

At high energies, the gauge boson self-interaction terms with anomalous couplings will violate unitarity. To avoid this, we introduce dipole form factors. One of the critiques against the framework of anomalous couplings is that these couplings are promoted from simple constants to arbitrary form factors [70].

$$\Delta g_1^V \to \frac{\Delta g_1^V}{\left(1 + \frac{\hat{s}}{\Lambda^2}\right)^2}, \qquad \Delta k^V \to \frac{\Delta k^V}{\left(1 + \frac{\hat{s}}{\Lambda^2}\right)^2}, \qquad \lambda^V \to \frac{\lambda^V}{\left(1 + \frac{\hat{s}}{\Lambda^2}\right)^2} \tag{3.24}$$

where $\hat{s}$ is the invariant mass of the vector boson pair and the form factor, Λ, is the mass scale at which new physics appears, typically taken to be in the TeV range.

We can add additional constraints to form different scenarios.

EFT Scenario An effective field theory approach removes these two complications. In the effective field theory approach [70], the effective Lagrangian is an expansion in operators which are $SU(2) \times U(1)$ gauge invariant and conserve charge and parity. The strength of the coupling between new physics and SM particles is parameterized by the dimensionless coefficients c_i.

$$\mathcal{L} = \mathcal{L}_{SM} + \sum_i \frac{c_i}{\Lambda^2}\mathcal{O}_i \tag{3.25}$$

There are three dimension six operators, $\mathcal{O}_i$, that lead to anomalous triple vector boson couplings.

$$\begin{aligned} \mathcal{O}_{WWW} &= \mathrm{Tr}[W_{\mu\nu}W^{\nu\rho}W_\rho^\mu] \\ \mathcal{O}_W &= (D_\mu\Phi)^\dagger W^{\mu\nu}(D_\nu\Phi) \\ \mathcal{O}_B &= (D_\mu\Phi)^\dagger B^{\mu\nu}(D_\nu\Phi) \end{aligned} \tag{3.26}$$

where Φ is the Higgs doublet field and

$$\begin{aligned} D_\mu &= \partial_\mu + \frac{i}{2}g\tau^I W_\mu^I + \frac{i}{2}g'B_\mu^I \\ W_{\mu\nu} &= \frac{i}{2}g\tau^I\left(\partial_\mu W_\nu^I - \partial_\nu W_\mu^I + g\epsilon_{IJK}W_\mu^J W_\nu^K\right) \\ B_{\mu\nu} &= \frac{i}{2}g'\left(\partial_\mu B_\nu - \partial_\nu B_\mu\right) \end{aligned} \tag{3.27}$$

The anomalous coupling constants can be calculated in terms of the constants in the effective field theory or vice versa.

$$\begin{aligned}
\Delta g_1^Z &= c_W \frac{m_Z^2}{2\Lambda^2} \\
\Delta k^Z &= [c_W - \tan^2\theta_W c_B]\frac{m_W^2}{2\Lambda^2} \\
\Delta k^\gamma &= (c_B + c_W)\frac{m_W^2}{2\Lambda^2} \\
\lambda^\gamma = \lambda^Z &= \frac{3m_W^2 g^2}{2\Lambda^2} c_{WWW} \qquad (3.28) \\
\frac{c_W}{\Lambda^2} &= \frac{2}{m_Z^2}\Delta g_1^Z \\
\frac{c_B}{\Lambda^2} &= \frac{2}{m_Z^2}(\Delta k^\gamma - \Delta k^Z) \\
\frac{c_{WWW}}{\Lambda^2} &= \frac{2}{3g^2 m_W^2}\lambda \qquad (3.29)
\end{aligned}$$

The free parameters of an effective field theory are $c_{WWW}/\Lambda^2, c_W/\Lambda^2, c_B/\Lambda^2$. Unlike the above, here we do not require arbitrary form factors to restore unitarity.

LEP Scenario the LEP constraint is defined by requiring:

$$\begin{aligned}
\Delta g_1^Z &= \Delta k^Z + \tan^2\theta_W \Delta k^\gamma \\
\lambda^\gamma &= \lambda^Z \qquad (3.30)
\end{aligned}$$

These restrictions, from $SU(2) \times U(1)$ gauge invariance, reduce the number of free anomalous coupling parameters to three. Equation 3.30 is referred to as the LEP constraints.

HISZ Scenario In addition to requiring $SU(2)\times U(1)$ gauge invariance, the choice of setting $c_W = c_B$ leads to what is called the Hagiwara-Ishihara-Szalapski-Zeppenfeld [71] (HISZ) constraint scenario.

$$\begin{aligned}
\Delta g_1^Z &= \frac{\Delta k^Z}{\cos^2\theta_W - \sin^2\theta_W} \\
\Delta k^\gamma &= 2\Delta k^Z \frac{\cos^2\theta_W}{\cos^2\theta_W - \sin^2\theta_W} \\
\lambda^\gamma &= \lambda^Z \qquad (3.31)
\end{aligned}$$

Equal Couplings Scenario Under the Equal Couplings scenario, it is assumed that the couplings for the WWZ and $WW\gamma$ vertex are equal. This leaves two independent parameters.

$$\begin{aligned} g_1^Z &= g_1^\gamma = 1 \\ \Delta k^\gamma &= \Delta k^Z \\ \lambda^\gamma &= \lambda^Z \end{aligned} \tag{3.32}$$

3.9.2 ATGC study and results

The reweighting method for MC@NLO is used to scale events generated with particular anomalous coupling parameters to another set of parameters. The number of signal events N_{sig} scales with the cross section and the amplitude $\mathcal{A}$ squared.

$$N_{sig} \propto \sigma \propto \mathcal{A}^2 \tag{3.33}$$

The amplitude can be written:

$$\mathcal{A} = \mathcal{A}_{SM} + \mu_1\mathcal{A}_{\mu_1} + \cdots + \mu_n\mathcal{A}_{\mu_n} \tag{3.34}$$

where μ_i are the n anomalous coupling parameters. Note that the first term is for Standard Model only, so here $\mu_0 = 1$. MC@NLO allows for up to six anomalous coupling parameters, $\boldsymbol{\mu} = \{1, \Delta g_1^Z, \Delta k^Z, \lambda^Z, \Delta g_1^\gamma, \Delta k^\gamma, \lambda^\gamma\}$. Additional constraints will lower the number of free parameters. Event weights are calculated by the generator:

$$\begin{aligned} w_{TOT} = w_0 &+ (\Delta g_1^Z)^2 w_1 + (\Delta k^Z)^2 w_2 + (\lambda^Z)^2 w_3 \\ &+ (\Delta g_1^\gamma)^2 w_4 + (\Delta k^\gamma)^2 w_5 + (\lambda^\gamma)^2 w_6 \\ &+ 2\Delta g_1^Z w_7 + \cdots + 2\lambda^\gamma w_{12} \\ &+ 2\Delta g_1^Z \Delta k^Z w_{13} + \cdots + 2\Delta k^\gamma \lambda^\gamma w_{27} \end{aligned} \tag{3.35}$$

The anomalous coupling event weights $a_i \equiv w_i/w_{TOT}$ are derived by MC, which can be used to calculate the event by event weight to a new set of aTGC parameters. The parameterisation after applying additional constraints the LEP, HISZ, Equal couplings, and EFT scenarios reduce the number of free parameters. Due to higher statistics, the MC@NLO sample generated with $\Delta g_1^Z = 0.6, \Delta k^Z = 0.2, \lambda^Z = 0.2$ is used to parameterize the aTGC modeling. A binned Poisson log-likelihood comparing the data and simulated event distributions is computed for the leading lepotn p_{T}. The expected number of events in each bin of the templates is interpolated using polynomial functions as a function of the coupling constants to create a continuous parametrization of the model. Log-likelihood function will include systematic uncertainties as nuisance parameters.

The final results are obtained using events in the $e\mu$ channel only with three bins in leading lepton p_{T} using the Feldman Cousins frequentist confidence intervals. Table 3.32 gives the 1-dimensional expected and observed 95% confidence level limits on anomalous coupling parameters (with no form factors applied) with the no scenario, LEP, HISZ, or Equal couplings scenario and also under the effective field theory scenario. Expected and observed limits with additional form factors are given in Table 3.34 and 3.35.

Figure 3.33 gives the leading lepton p_{T} distribution after reweighting to the best fit aTGC parameter values and those corresponding to the observed upper and lower 95% confidence interval bounds.

In addition to the above 1-dimensional limits, also 2-dimensional limits are calculated by fitting two anomalous coupling parameters and setting all others to zero. The 2-dimensional limits are calculated by fitting two anomalous coupling parameters and setting all others to zero. The 2D 95% confidence level contours under the LEP constraints and effective field theory framework are shown in Figure 3.34 and Figure 3.35 respectively. Compared to the previous limits published using data taken at 7 TeV, these new limits are better by a factor of almost four [3] [4], and also comparable with CMS 8 TeV results [62].

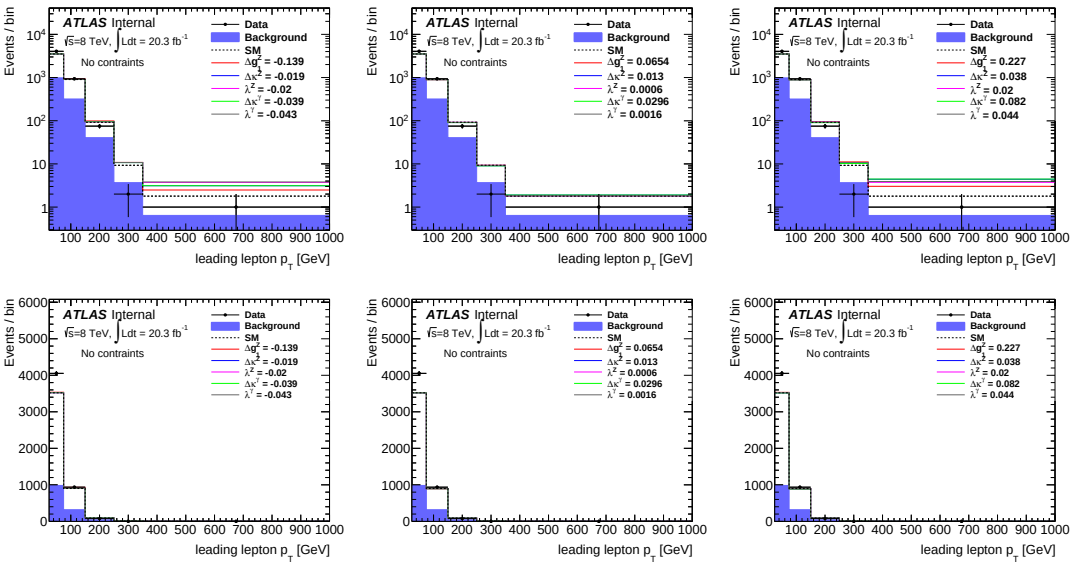

Figure 3.33 Leading lepton p_{T} distribution in the $e\mu$ channel for various aTGC parameters after reweighting to values corresponding to the lower 95% bound (left), the best fit value (middle), and upper bound (right). The values are obtained after fitting only for leading lepton $p_{\mathrm{T}} > 150$GeV. Nuisance parameters are not used in these plots. The plots on the top and bottom only differ by linear or log scale on the y-axis. [30]

Scenario	Parameter	Expected	Observed
No scenario	Δg_1^Z	[-0.498,0.524]	[-0.215,0.267]
	Δk^Z	[-0.053,0.059]	[-0.027,0.042]
	λ^Z	[-0.039,0.038]	[-0.024,0.024]
	Δk^γ	[-0.109,0.124]	[-0.054,0.092]
	λ^γ	[-0.081,0.082]	[-0.051,0.052]
LEP	Δg_1^Z	[-0.033,0.037]	[-0.016,0.027]
	Δk^Z	[-0.037,0.035]	[-0.025,0.020]
	λ^Z	[-0.031,0.031]	[-0.019,0.019]
HISZ	Δk^Z	[-0.026,0.030]	[-0.012,0.022]
	λ^Z	[-0.031,0.031]	[-0.019,0.019]
Equal Couplings	Δk^Z	[-0.041,0.048]	[-0.020,0.035]
	λ^Z	[-0.030,0.030]	[-0.019,0.019]
EFT	C_{WWW}/Λ^2	[-7.62,7.38]	[-4.61,4.60]
	C_B/Λ^2	[-35.8,38.4]	[-20.9,26.3]
	C_W/Λ^2	[-12.58,14.32]	[-5.87,10.54]

Table 3.32 95% confidence level expected and observed limits on anomalous coupling parameters assuming no scenario, LEP, HISZ, or Equal couplings scenarios, and Effective Field Theory (EFT) with leading lepton p_{T} bins of [150,250,350,1000] GeV in the $e\mu$ channel. The results are shown with $\Lambda = \infty$ for scenarios under the anomalous couplings framework. Electroweak corrections have been applied to the SM only term. [30]

Scenario	Parameter	Expected	Observed
No scenario	Δg_1^Z	[-0.519,0.563]	[-0.226,0.279]
	Δk^Z	[-0.057,0.064]	[-0.028,0.045]
	λ^Z	[-0.043,0.042]	[-0.026,0.025]
	Δk^γ	[-0.118,0.136]	[-0.057,0.099]
	λ^γ	[-0.088,0.089]	[-0.055,0.055]
LEP	Δg_1^Z	[-0.035,0.041]	[-0.017,0.029]
	Δk^Z	[-0.041,0.038]	[-0.027,0.021]
	λ^Z	[-0.033,0.033]	[-0.020,0.020]
HISZ	Δk^Z	[-0.028,0.033]	[-0.013,0.024]
	λ^Z	[-0.033,0.034]	[-0.020,0.020]
Equal Couplings	Δk^Z	[-0.045,0.052]	[-0.021,0.037]
	λ^Z	[-0.034,0.033]	[-0.020,0.020]

Table 3.33 95% confidence level expected and observed limits on anomalous coupling parameters assuming no scenario, LEP, HISZ, or Equal couplings scenarios with leading lepton p_{T} bins of [150,250,350,1000] GeV in the $e\mu$ channel. The results are shown with $\Lambda = 7$ TeV for scenarios under the anomalous couplings framework. Electroweak corrections have been applied to the SM only term. [30]

FF (TeV)	Δg_1^Z		Δk^Z		λ^Z		Δk^γ		λ^γ	
2	-0.728	0.836	-0.100	0.115	-0.076	0.076	-0.213	0.247	-0.158	0.159
3	-0.615	0.686	-0.074	0.085	-0.057	0.055	-0.156	0.182	-0.117	0.115
4	-0.561	0.617	-0.066	0.074	-0.049	0.048	-0.136	0.157	-0.101	0.102
5	-0.540	0.580	-0.061	0.069	-0.046	0.045	-0.126	0.147	-0.096	0.093
6	-0.535	0.575	-0.059	0.066	-0.044	0.043	-0.122	0.140	-0.091	0.089
7	-0.519	0.563	-0.057	0.064	-0.043	0.042	-0.118	0.136	-0.088	0.089
8	-0.515	0.541	-0.056	0.063	-0.042	0.041	-0.118	0.132	-0.084	0.084
10	-0.503	0.535	-0.055	0.061	-0.041	0.041	-0.113	0.131	-0.084	0.084
100	-0.498	0.524	-0.053	0.059	-0.039	0.038	-0.109	0.124	-0.081	0.082

Table 3.34 95% confidence level expected limits on anomalous coupling parameters with no constraints with leading lepton p_{T} bins of [150,250,350,1000] GeV in the $e\mu$ channel with for different form factors (FF). The form factors are given in the first column in units of TeV. Here, $\Lambda = 100$TeV is sufficiently high that it can be considered as $\Lambda = \infty$ or not applying a form factor. Electroweak corrections have been applied to the SM only term. [30]

FF(TeV)	Δg_1^Z		Δk^Z		λ^Z		Δk^γ		λ^γ	
2	-0.298	0.390	-0.042	0.070	-0.038	0.039	-0.083	0.157	-0.083	0.085
3	-0.247	0.328	-0.034	0.056	-0.031	0.031	-0.068	0.121	-0.066	0.065
4	-0.237	0.295	-0.031	0.050	-0.028	0.028	-0.063	0.110	-0.060	0.061
5	-0.232	0.285	-0.029	0.048	-0.027	0.027	-0.059	0.105	-0.057	0.058
6	-0.228	0.283	-0.028	0.046	-0.026	0.026	-0.058	0.101	-0.055	0.056
7	-0.226	0.279	-0.028	0.045	-0.026	0.025	-0.057	0.099	-0.055	0.055
8	-0.219	0.276	-0.027	0.044	-0.025	0.025	-0.056	0.098	-0.054	0.054
10	-0.215	0.274	-0.027	0.044	-0.025	0.025	-0.056	0.094	-0.052	0.054
100	-0.215	0.267	-0.027	0.042	-0.024	0.024	-0.054	0.092	-0.051	0.052

Table 3.35 95% confidence level observed limits on anomalous coupling parameters with no constraints with leading lepton p_{T} bins of [150,250,350,1000] GeV in the $e\mu$ channel with for different form factors (FF). The form factors are given in the first column in units of TeV. Here, $\Lambda = 100$TeV is sufficiently high that it can be considered as $\Lambda = \infty$ or not applying a form factor. Electroweak corrections have been applied to the SM only term. [30]

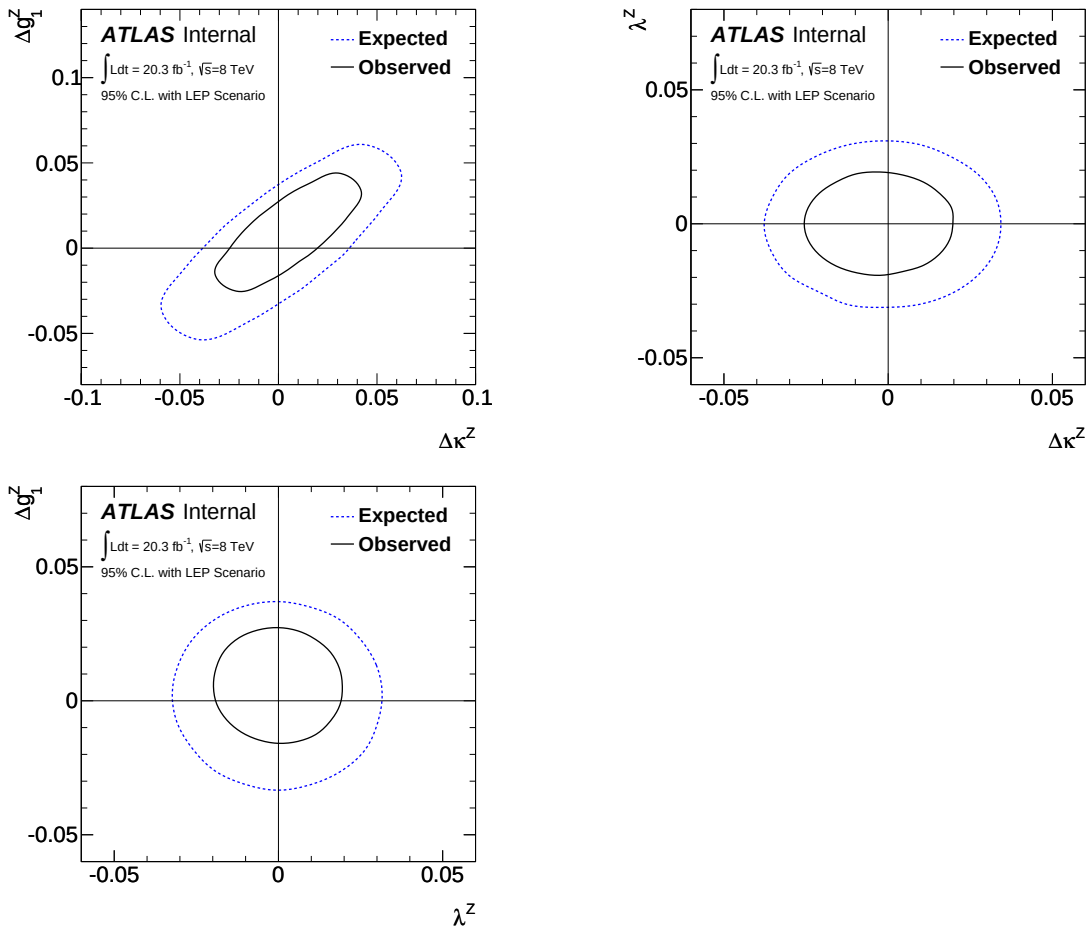

Figure 3.34 2-dimensional 95% confidence level contours assuming the LEP constraint scenario. Except for the two anomalous coupling parameters under study, all others are set to zero. [30]

3.10 Conclusions

The WW production cross section in pp collisions at $\sqrt{s} = 8$ TeV is measured using 20.3 fb^{-1} of data collected by the ATLAS detector during 2012. The measurement is conducted using three WW leptonic decay channels. A total of 6636 candidates are selected with an estimated background of 1600 events. The measured WW production cross section $\sigma(pp \to W^+W^-)$ is $71.0^{+1.1}_{-1.1}$(stat) $^{+5.7}_{-5.0}$(syst) $^{+2.1}_{-2.0}$(lumi) pb, to be compared with the Standard Model NNLO prediction with MSTW PDF set $63.2^{+2.0}_{-1.8}$ pb and found to be consistant with WW cross section measured. With large amount of data taken at 2012, the statistical uncertainty is less than 7 TeV analysis. For 8 TeV main uncertainties come from the jet selection (mainly from experimental and jet-veto cut) and the background uncertainties.

We reported also results on the normalized differential cross section as a function of lepton kinematics. Reasonable agreement is observed between the measured differential distributions and the MC predictions. The transverse momentum of the leading lepton

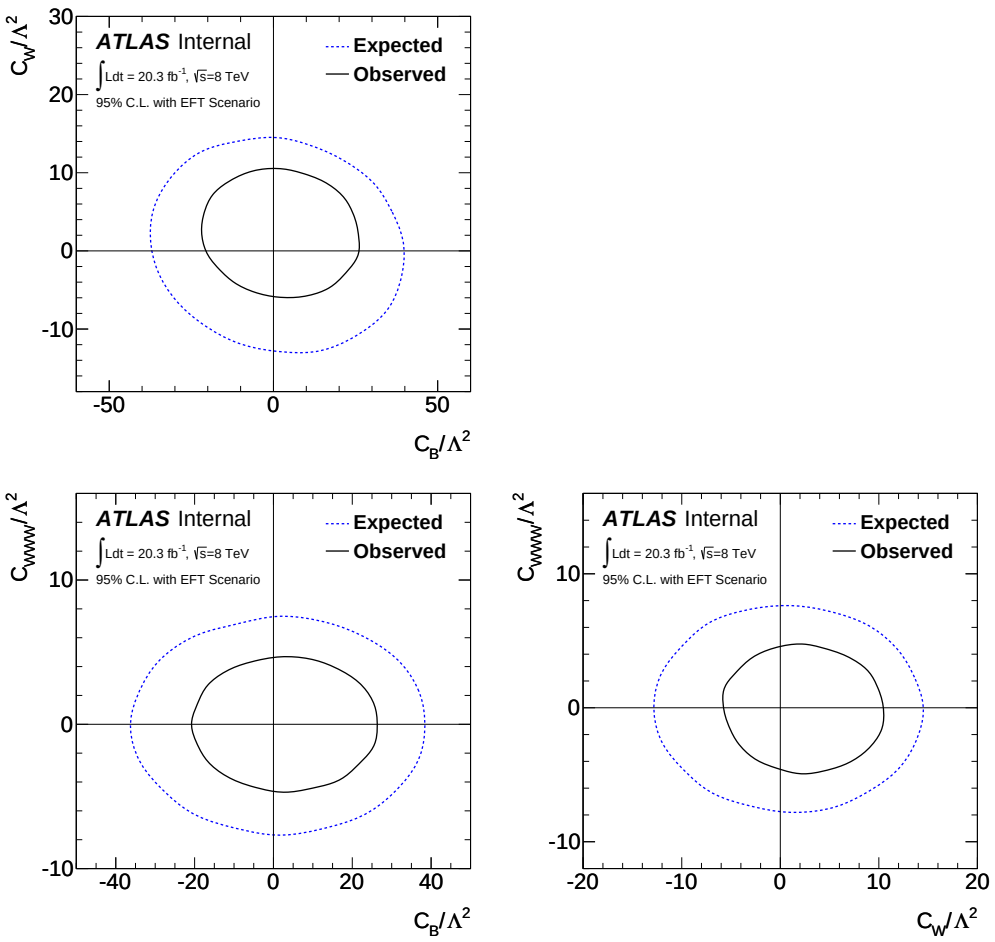

Figure 3.35 2-dimensional 95% confidence level contours for the coupling parameters under the effective field theory framework. Except for the two effective field theory couplings under study, the third is set to zero. [30]

p_{T} is the distribution most sensitive to anomalous triple gauge couplings and is used to set limits on aTGC coupling parameters. No evidence for anomalous WWZ and $WW\gamma$ triple gauge-boson couplings is found, and limits on their coupling parameters are set. The limits are better by a factor of almost four compared to the limits previously published by the ATLAS collaboration, and also comparable with CMS 8 TeV result.

Bibliography

[1] Particle Data Group Collaboration, K. A. Olive et al., *Review of Particle Physics*, Chin. Phys. **C38** (2014) 090001.

[2] ATLAS Collaboration, G. Aad et al., *Measurement of the W^+W^- Cross Section in $\sqrt{s} = 7$ TeV pp Collisions with ATLAS*, Phys. Rev. Lett. **107** (2011) 041802.

[3] ATLAS Collaboration, G. Aad et al., *Measurement of the WW cross section in $\sqrt{s} = 7$ TeV pp collisions with the ATLAS detector and limits on anomalous gauge couplings*, Phys. Lett. **B712** (2013) 289–308, arXiv:1203.6232 [hep-ex].

[4] ATLAS Collaboration, G. Aad et al., *Measurement of W^+W^- production in pp collisions at $\sqrt{s}$=7 TeV with the ATLAS detector and limits on anomalous WWZ and $WW\gamma$ couplings*, Phys. Rev. **D87** (2013) no. 11, 112001, arXiv:1210.2979 [hep-ex].

[5] CDF Collaboration, T. Aaltonen et al., *Measurement of the W^+W^- Production Cross Section and Search for Anomalous $WW\gamma$ and WWZ Couplings in $p\bar{p}$ Collisions at $\sqrt{s} = 1.96$ TeV*, Phys. Rev. Lett. **104** (2010) 201801, arXiv:0912.4500 [hep-ex].

[6] D0 Collaboration, V. M. Abazov et al., *Measurement of the WW production cross section with dilepton final states in $p\bar{p}$ collisions at $\sqrt{s}$ = 1.96 TeV and limits on anomalous trilinear gauge couplings*, Phys. Rev. Lett. **103** (2009) 191801, arXiv:0904.0673 [hep-ex].

[7] http://www.hep.ph.ic.ac.uk/~wstirlin/plots/plots.html.

[8] H. Burkhardt and P. Grafstrom, *Absolute Luminosity from Machine Parameters*, Tech. Rep. LHC-PROJECT-Report-1019, 2007.

[9] S. van der Meer, *Calibration of the effective beam height in the ISR*, Tech. Rep. CERN-ISR-PO-68-31, CERN, Geneva, 1968.

[10] ATLAS Collaboration, G. Aad et al., *Improved luminosity determination in pp collisions at $\sqrt{s}$ = 7 TeV using the ATLAS detector at the LHC*, Eur. Phys. J. **C73** (2013) no. 8, 2518, arXiv:1302.4393 [hep-ex].

[11] ATLAS Collaboration, G. Aad et al., *Measurement of the muon reconstruction performance of the ATLAS detector using 2011 and 2012 LHC proton−proton collision data*, Eur. Phys. J. **C74** (2014) no. 11, 3130, arXiv:1407.3935 [hep-ex].

[12] G.Aad et al., *The ATLAS Experiment at the CERN Large Hadron Collider*, tech. rep., JINST3 (2008) S08003.

[13] ATLAS Collaboration, *Performance of the ATLAS Inner Detector Track and Vertex Reconstruction in the High Pile-Up LHC Environment*, Tech. Rep. ATLAS-CONF-2012-042, CERN, Geneva, Mar, 2012.

[14] A. Rosenfeld and J. L. Pfaltz, *Sequential Operations in Digital Picture Processing*, J. ACM **13** (1966) no. 4, 471–494.

[15] ATLAS Collaboration, G. Aad et al., *A neural network clustering algorithm for the ATLAS silicon pixel detector*, JINST **9** (2014) P09009, arXiv:1406.7690 [hep-ex].

[16] ATLAS TRT Collaboration, V. A. Mitsou, *The ATLAS transition radiation tracker*, in , pp. 497–501. 2003. arXiv:hep-ex/0311058 [hep-ex].

[17] ATLAS Electromagnetic Barrel Calorimeter Collaboration, M. Aharrouche et al., *Energy linearity and resolution of the ATLAS electromagnetic barrel calorimeter in an electron test-beam*, Nucl. Instrum. Meth. **A568** (2006) 601–623, arXiv:physics/0608012 [physics].

[18] ATLAS Collaboration, *ATLAS liquid-argon calorimeter: Technical Design Report*. Technical Design Report ATLAS, CERN-LHCC-96-041. CERN, Geneva, 1996.

[19] ATLAS Collaboration, G. Aad et al., *Electron and photon energy calibration with the ATLAS detector using LHC Run 1 data*, Eur. Phys. J. **C74** (2014) no. 10, 3071, arXiv:1407.5063 [hep-ex].

[20] TMVA Core Developer Team Collaboration, J. Therhaag, *TMVA: Toolkit for multivariate data analysis*, AIP Conf. Proc. **1504** (2009) 1013–1016.

[21] https://twiki.cern.ch/twiki/bin/view/AtlasPublic/TileCaloPublicResults.

[22] ATLAS Collaboration, *Electron efficiency measurements with the ATLAS detector using the 2012 LHC proton-proton collision data*, Tech. Rep. ATLAS-CONF-2014-032, CERN, Geneva, Jun, 2014.

[23] ATLAS Collaboration, *Pile-up Suppression in Missing Transverse Momentum Reconstruction in the ATLAS Experiment in Proton-Proton Collisions at $\sqrt{s}$ = 8 TeV*, Tech. Rep. ATLAS-CONF-2014-019, CERN, Geneva, May, 2014.

[24] ATLAS Collaboration, *Performance of Missing Transverse Momentum Reconstruction in ATLAS studied in Proton-Proton Collisions recorded in 2012 at 8 TeV*, Tech. Rep. ATLAS-CONF-2013-082, CERN, Geneva, Aug, 2013.

[25] M. Cacciari and G. P. Salam, *Dispelling the N^3 myth for the k_t jet-finder*, Phys. Lett. **B641** (2006) 57–61, arXiv:hep-ph/0512210 [hep-ph].

[26] M. Cacciari, G. P. Salam, and G. Soyez, *The anti-kt jet clustering algorithm*, JHEP **04** (2008) 063, arXiv:0802.1189 [hep-ph].

[27] M. Cacciari and G. P. Salam, *Pileup subtraction using jet areas*, Phys. Lett. **B659** (2008) 119–126, arXiv:0707.1378 [hep-ph].

[28] ATLAS Collaboration, *Pile-up subtraction and suppression for jets in ATLAS*, Tech. Rep. ATLAS-CONF-2013-083, CERN, Geneva, Aug, 2013.

[29] A. Bierweiler, T. Kasprzik, J. H. Kühn, and S. Uccirati, *Electroweak corrections to W-boson pair production at the LHC*, JHEP **1211** (2012) 093, arXiv:1208.3147 [hep-ph].

[30] ATLAS Collaboration, *Measurement of the WW Production Cross Section in Proton-Proton Collisions at $\sqrt{s} = 8$ TeV with the ATLAS Detector*, Tech. Rep. ATL-COM-PHYS-2013-1450, CERN, Geneva, Oct, 2013.

[31] T. Gehrmann, M. Grazzini, S. Kallweit, P. Maierhfer, A. von Manteuffel, et al., *W^+W^- production at hadron colliders in NNLO QCD*, arXiv:1408.5243 [hep-ph].

[32] A. Martin, W. Stirling, R. Thorne, and G. Watt, *Parton distributions for the LHC*, Eur.Phys.J. **C63** (2009) 189–285, arXiv:0901.0002 [hep-ph].

[33] LHC Higgs Cross Section Working Group Collaboration, S. Heinemeyer et al., *Handbook of LHC Higgs Cross Sections: 3. Higgs Properties*, arXiv:1307.1347 [hep-ph].

[34] P. Nason, *A New method for combining NLO QCD with shower Monte Carlo algorithms*, JHEP **0411** (2004) 040, arXiv:hep-ph/0409146 [hep-ph].

[35] S. Frixione, P. Nason, and C. Oleari, *Matching NLO QCD computations with Parton Shower simulations: the POWHEG method*, JHEP **0711** (2007) 070, arXiv:0709.2092 [hep-ph].

[36] T. Sjostrand et al., *High-energy physics event generation with PYTHIA 6.1*, Comput. Phys. Commun. **135** (2001) 238–259, arXiv:hep-ph/0010017.

[37] H.-L. Lai, M. Guzzi, J. Huston, Z. Li, P. M. Nadolsky, et al., *New parton distributions for collider physics*, Phys.Rev. **D82** (2010) 074024, arXiv:1007.2241 [hep-ph].

[38] T. Binoth, M. Ciccolini, N. Kauer, and M. Kramer, *Gluon-induced W-boson pair production at the LHC*, JHEP **12** (2006) 046, arXiv:hep-ph/0611170.

[39] G. Corcella et al., *HERWIG 6.5: an event generator for Hadron Emission Reactions With Interfering Gluons (including supersymmetric processes)*, JHEP **0101** (2001) 010, arXiv:hep-ph/0011363.

[40] QCD Tools Working Group Collaboration, R. K. Ellis et al., *Report of the QCD Tools Working Group*, in , pp. 1–46. 1999. arXiv:hep-ph/0011122 [hep-ph]. [,1(1999)].

[41] ATLAS Collaboration, *Summary of ATLAS Pythia 8 tunes*, **ATL-PHYS-PUB-2012-003** (2012) .

[42] S. Frixione and B. R. Webber, *Matching NLO QCD computations and parton shower simulations*, JHEP **06** (2002) 029, arXiv:hep-ph/0204244 [hep-ph].

[43] R. C. Gray, C. Kilic, M. Park, S. Somalwar, and S. Thomas, *Backgrounds To Higgs Boson Searches from $W\gamma^* -> l\nu l(l)$ Asymmetric Internal Conversion*, arXiv:1110.1368 [hep-ph].

[44] ATLAS Collaboration, G. Aad et al., *Jet energy measurement with the ATLAS detector in proton-proton collisions at $\sqrt{s} = 7$ TeV*, Eur. Phys. J. **C73** (2013) no. 3, 2304, arXiv:1112.6426 [hep-ex].

[45] ATLAS Collaboration, G. Aad et al., *Measurement of the $W \to \ell\nu$ and $Z/\gamma^* \to \ell\ell$ production cross sections in proton-proton collisions at $\sqrt{s} = 7$ TeV with the ATLAS detector*, JHEP **12** (2010) 060, arXiv:1010.2130 [hep-ex].

[46] B. Mellado, X. Ruan, and Z. Zhang, *Extraction of Top Backgrounds in the Higgs Boson Search with the $H \to WW^\star \to \ell\ell + E_{\mathrm{T}}^{\mathrm{miss}}$ Decay with a Full Jet Veto at the LHC*, Phys. Rev. **D84** (2011) 096005, arXiv:1101.1383 [hep-ph].

[47] S. Frixione, E. Laenen, P. Motylinski, B. R. Webber, and C. D. White, *Single-top hadroproduction in association with a W boson*, JHEP **07** (2008) 029, arXiv:0805.3067 [hep-ph].

[48] ATLAS Collaboration, *Measurements of $W\gamma$ and $Z\gamma$ production in pp collisions at $\sqrt{s}$=7 TeV with the ATLAS detector at the LHC*, Phys.Rev. **D87** (2013) no. 11, 112003, arXiv:1302.1283 [hep-ex].

[49] J. M. Campbell, R. K. Ellis, and C. Williams, *Vector boson pair production at the LHC*, JHEP **1107** (2011) 018, arXiv:1105.0020 [hep-ph].

[50] F. Campanario and S. Sapeta, *WZ production beyond NLO for high-pT observables*, Phys.Lett. **B718** (2012) 100–104, arXiv:1209.4595 [hep-ph].

[51] F. Cascioli, T. Gehrmann, M. Grazzini, S. Kallweit, P. Maierhöfer, et al., *ZZ production at hadron colliders in NNLO QCD*, arXiv:1405.2219 [hep-ph].

[52] M. Botje et al., *The PDF4LHC Working Group Interim Recommendations*, arXiv:1101.0538 [hep-ph].

[53] R. D. Ball, L. Del Debbio, S. Forte, A. Guffanti, J. I. Latorre, et al., *A first unbiased global NLO determination of parton distributions and their uncertainties*, Nucl.Phys. **B838** (2010) 136–206, arXiv:1002.4407 [hep-ph].

[54] M. Whalley, D. Bourilkov, and R. Group, *The Les Houches accord PDFs (LHAPDF) and LHAGLUE*, arXiv:hep-ph/0508110 [hep-ph].

[55] ATLAS Collaboration, G. Aad et al., *Observation and measurement of Higgs boson decays to WW^* with the ATLAS detector*, Phys. Rev. **D92** (2015) no. 1, 012006, arXiv:1412.2641 [hep-ex].

[56] M. Billoni, S. Dittmaier, B. Jager, and C. Speckner, *Next-to-leading-order electroweak corrections to $pp \to WW \to 4$ leptons in double-pole approximation at the LHC*, PoS **RADCOR2013** (2014) 018, arXiv:1311.5491 [hep-ph].

[57] J. Baglio, L. D. Ninh, and M. M. Weber, *Massive gauge boson pair production at the LHC: a next-to-leading order story*, Phys.Rev. **D88** (2013) 113005, arXiv:1307.4331.

[58] A. Bierweiler, T. Kasprzik, and J. H. Kuhn, *Vector-boson pair production at the LHC to $\mathcal{O}(\alpha^3)$ accuracy*, JHEP **1312** (2013) 071, arXiv:1305.5402 [hep-ph].

[59] C. F. Berger, C. Marcantonini, I. W. Stewart, F. J. Tackmann, and W. J. Waalewijn, *Higgs Production with a Central Jet Veto at NNLL+NNLO*, JHEP **04** (2011) 092, arXiv:1012.4480 [hep-ph].

[60] T. Gehrmann, M. Grazzini, S. Kallweit, P. Maierhofer, A. von Manteuffel, S. Pozzorini, D. Rathlev, and L. Tancredi, *W^+W^- Production at Hadron Colliders in Next to Next to Leading Order QCD*, Phys. Rev. Lett. **113** (2014) no. 21, 212001, arXiv:1408.5243 [hep-ph].

[61] S. Dittmaier, S. Dittmaier, C. Mariotti, G. Passarino, R. Tanaka, et al., *Handbook of LHC Higgs Cross Sections: 2. Differential Distributions*, arXiv:1201.3084 [hep-ph].

[62] CMS Collaboration, V. Khachatryan et al., *Measurement of the W^+W^- cross section in pp collisions at $\sqrt{s} = 8$ TeV and limits on anomalous gauge couplings*, arXiv:1507.03268 [hep-ex].

[63] P. F. Monni and G. Zanderighi, *On the excess in the inclusive $W^+W^- \to l^+l^-\nu\bar{\nu}$ cross section*, JHEP **05** (2015) 013, arXiv:1410.4745 [hep-ph].

[64] *Measurement of the W^+W^- production cross section in proton-proton collisions at $\sqrt{s} = 8$ TeV with the ATLAS detector*, Tech. Rep. ATLAS-CONF-2014-033, CERN, Geneva, Jul, 2014.

[65] G. D'Agostini, *Improved iterative Bayesian unfolding*, ArXiv e-prints (2010) , arXiv:1010.0632 [physics.data-an].

[66] D. Curtin, P. Jaiswal, and P. Meade, *Charginos Hiding In Plain Sight*, Phys.Rev. **D87** (2013) no. 3, 031701, arXiv:1206.6888 [hep-ph].

[67] B. Feigl, H. Rzehak, and D. Zeppenfeld, *New Physics Backgrounds to the $H \to WW$ Search at the LHC?*, Phys.Lett. **B717** (2012) 390–395, arXiv:1205.3468 [hep-ph].

[68] K. Rolbiecki and K. Sakurai, *Light stops emerging in WW cross section measurements?*, JHEP **1309** (2013) 004, arXiv:1303.5696 [hep-ph].

[69] K. Hagiwara, R. D. Peccei, D. Zeppenfeld, and K. Hikasa, *Probing the Weak Boson Sector in e+ e- —> W+ W-*, Nucl. Phys. **B282** (1987) 253.

[70] C. Degrande, N. Greiner, W. Kilian, O. Mattelaer, H. Mebane, T. Stelzer, S. Willenbrock, and C. Zhang, *Effective Field Theory: A Modern Approach to Anomalous Couplings*, Annals Phys. **335** (2013) 21–32, arXiv:1205.4231 [hep-ph].

[71] K. Hagiwara, S. Ishihara, R. Szalapski, and D. Zeppenfeld, *Low energy effects of new interactions in the electroweak boson sector*, Phys. Rev. D **48** (1993) 2182–2203.

Appendix A Appendix

A.1 MC samples

Process	cross-section [pb]	ϵ_{filter}	N_{MC}	Generator
$q\bar{q}' \to W^+W^- \to e^+\nu e^-\nu$	0.62	1.0	299700	Powheg
$q\bar{q}' \to W^+W^- \to \mu^+\nu\mu^-\nu$	0.62	1.0	300000	Powheg
$q\bar{q}' \to W^+W^- \to e^+\nu\mu^-\nu$	0.62	1.0	299999	Powheg
$q\bar{q}' \to W^+W^- \to \mu^+\nu e^-\nu$	0.62	1.0	300000	Powheg
$q\bar{q}' \to W^+W^- \to e^+\nu\tau^-\nu$	0.62	1.0	299996	Powheg
$q\bar{q}' \to W^+W^- \to \mu^+\nu\tau^-\nu$	0.62	1.0	299999	Powheg
$q\bar{q}' \to W^+W^- \to \tau^+\nu\mu^-\nu$	0.62	1.0	300000	Powheg
$q\bar{q}' \to W^+W^- \to \tau^+\nu e^-\nu$	0.62	1.0	299999	Powheg
$q\bar{q}' \to W^+W^- \to \tau^+\nu\tau^-\nu$	0.62	1.0	299999	Powheg
$gg \to W^+W^- \to e^+\nu e^-\nu$	0.017	1.0	30000	gg2ww
$gg \to W^+W^- \to \mu^+\nu\mu^-\nu$	0.017	1.0	30000	gg2ww
$gg \to W^+W^- \to e^+\nu\mu^-\nu$	0.017	1.0	30000	gg2ww
$gg \to W^+W^- \to \mu^+\nu e^-\nu$	0.017	1.0	30000	gg2ww
$gg \to W^+W^- \to e^+\nu\tau^-\nu$	0.017	1.0	30000	gg2ww
$gg \to W^+W^- \to \mu^+\nu\tau^-\nu$	0.017	1.0	30000	gg2ww
$gg \to W^+W^- \to \tau^+\nu\mu^-\nu$	0.017	1.0	30000	gg2ww
$gg \to W^+W^- \to \tau^+\nu e^-\nu$	0.017	1.0	30000	gg2ww
$gg \to W^+W^- \to \tau^+\nu\tau^-\nu$	0.017	1.0	30000	gg2ww
$gg \to H \to W^+W^- \to \ell\nu\ell\nu$	0.440563	0.49105	500000	Powheg

Table A.1 The WW signal production processes, cross-sections and numbers of fully simulated MC events. The MC simulation 'filter' is an event selection at the generator level. The last sample has a filter which requires two leptons, each with $p_{\text{T}} > 5$ GeV and $|\eta|$<5.0, and requires at least one lepton with $p_{\text{T}} > 15$ GeV. The corresponding filter efficiencies are given in the Table. We also indicate the MC generators used to produce the MC events.

A.2 2D significance plots for missing transverse energy

For the missing transverse energy, a grid scan is performed to determine the cut value. The stability of cut values is shown in the 2D significance plots.

A.3 Double ration study for missing transverse energy

Except for the signal and background ratio and the correlation, the agreement between data and MC is another important feature which we take into account for event selection optimization. This consideration is particularly useful when we are rejecting DY events, whose data-driven estimation partially relies on MC. The data and MC

Process	cross-section	k-factor	ϵ_{filter}	N_{MC}	Generator
ZeeNp0($M > 60$ GeV)	718.89	1.18	1	6619984	Alpgen
ZeeNp1($M > 60$ GeV)	175.6	1.18	1	1329498	Alpgen
ZeeNp2($M > 60$ GeV)	58.849	1.18	1	404998	Alpgen
ZeeNp3($M > 60$ GeV)	15.56	1.18	1	109999	Alpgen
ZeeNp4($M > 60$ GeV)	3.9322	1.18	1	30000	Alpgen
ZeeNp5($M > 60$ GeV)	1.1994	1.18	1	10000	Alpgen
ZmumuNp0($M > 60$ GeV)	718.91	1.18	1	6608490	Alpgen
ZmumuNp1($M > 60$ GeV)	175.81	1.18	1	1334697	Alpgen
ZmumuNp2($M > 60$ GeV)	58.805	1.18	1	404995	Alpgen
ZmumuNp3($M > 60$ GeV)	15.589	1.18	1	110000	Alpgen
ZmumuNp4($M > 60$ GeV)	3.9072	1.18	1	30000	Alpgen
ZmumuNp5($M > 60$ GeV)	1.1933	1.18	1	10000	Alpgen
ZtautauNp0($M > 60$ GeV)	718.85	1.18	1	6615490	Alpgen
ZtautauNp1($M > 60$ GeV)	175.83	1.18	1	1334998	Alpgen
ZtautauNp2($M > 60$ GeV)	58.63	1.18	1	405000	Alpgen
ZtautauNp3($M > 60$ GeV)	15.508	1.18	1	108999	Alpgen
ZtautauNp4($M > 60$ GeV)	3.9526	1.18	1	30000	Alpgen
ZtautauNp5($M > 60$ GeV)	1.1805	1.18	1	10000	Alpgen
ZeeNp0($10 < M < 60$ GeV)	3477.9	1.19	0.01045	6994180	Alpgen
ZeeNp1($10 < M < 60$ GeV)	108.72	1.19	0.20383	4497280	Alpgen
ZeeNp2($10 < M < 60$ GeV)	52.837	1.19	0.13841	1468393	Alpgen
ZeeNp3($10 < M < 60$ GeV)	11.291	1.19	0.20806	438397	Alpgen
ZeeNp4($10 < M < 60$ GeV)	2.5852	1.19	0.25262	108930	Alpgen
ZeeNp5($10 < M < 60$ GeV)	0.6937	1.19	1.0	112180	Alpgen
ZmumuNp0($10 < M < 60$ GeV)	3477.7	1.19	0.01086	6984686	Alpgen
ZmumuNp1($10 < M < 60$ GeV)	108.74	1.19	0.21096	4491587	Alpgen
ZmumuNp2($10 < M < 60$ GeV)	52.814	1.19	0.14253	1503397	Alpgen
ZmumuNp3($10 < M < 60$ GeV)	11.299	1.19	0.21385	439699	Alpgen
ZmumuNp4($10 < M < 60$ GeV)	2.5793	1.19	0.25869	108890	Alpgen
ZmumuNp5($10 < M < 60$ GeV)	0.69373	1.19	0.69373	115000	Alpgen
ZtautauNp0($10 < M < 60$ GeV)	3477.9	1.19	0.00002	27969	Alpgen
ZtautauNp1($10 < M < 60$ GeV)	108.71	1.19	0.00136	30000	Alpgen
ZtautauNp2($10 < M < 60$ GeV)	52.827	1.19	0.00174	27610	Alpgen
ZtautauNp3($10 < M < 60$ GeV)	11.311	1.19	0.00387	29600	Alpgen
ZtautauNp4($10 < M < 60$ GeV)	2.592	1.19	1.0	365497	Alpgen
ZtautauNp5($10 < M < 60$ GeV)	0.6929	1.19	1.0	114420	Alpgen

Table A.2 MC samples/processes used to model Z+jets background. The corresponding cross-sections (pb), generator names, generator level filter efficiencies and total numbers of events are shown in this Table. NpX (X=0..5) in the process name refers to the number of additional partons in the final state. The samples with filter efficiency not equal to 1 have the filter that requires two leptons in an event. The filter requires two leptons, each with $p_{\text{T}} > 7$ GeV and $|\eta|$<3.0. The k-factors are calculated according to the NNLO inclusive W/Z production cross-sections, and the inclusive k-factors are assigned for each NpX samples.

Process	cross-section [pb]	k-factor	ϵ_{filter}	N_{MC}	Generator
WenuNp0	8037.1	1.19	1	3459894	Alpgen
WenuNp1	1579.2	1.19	1	2499491	Alpgen
WenuNp2	477.2	1.19	1	3769487	Alpgen
WenuNp3	133.93	1.19	1	1009997	Alpgen
WenuNp4	35.622	1.19	1	249999	Alpgen
WenuNp5	10.533	1.19	1	70000	Alpgen
WmunuNp0	8040	1.19	1	3469692	Alpgen
WmunuNp1	1580.3	1.19	1	2499694	Alpgen
WmunuNp2	477.5	1.19	1	3769886	Alpgen
WmunuNp3	133.94	1.19	1	1006698	Alpgen
WmunuNp4	35.636	1.19	1	254999	Alpgen
WmunuNp5	10.571	1.19	1	69900	Alpgen
WtaunuNp0	8035.8	1.19	1	3419992	Alpgen
WtaunuNp1	1579.8	1.19	1	2499793	Alpgen
WtaunuNp2	477.55	1.19	1	3765989	Alpgen
WtaunuNp3	133.79	1.19	1	1009998	Alpgen
WtaunuNp4	35.583	1.19	1	249998	Alpgen
WtaunuNp5	10.54	1.19	1	65000	Alpgen

Table A.3 MC samples/processes used to model W+jets background. The corresponding cross-sections, generator names, generator level filter efficiencies and total numbers of events are shown in this Table. NpX (X=0..5) in the process name refers to the number of additional partons in the final state. The k-factors are calculated according to the NNLO inclusive W/Z production cross-sections, and the inclusive k-factors are assigned for each NpX samples.

agreement is especially important for ee and $\mu\mu$ channels. The double ration is defined to describe the modeling:

$$\frac{N^{ee}_{data}}{N^{ee}_{MC}} \Big/ \frac{N^{\mu\mu}_{data}}{N^{\mu\mu}_{MC}} \quad \text{or} \quad \frac{N^{ee}_{data}}{N^{\mu\mu}_{data}} \Big/ \frac{N^{ee}_{MC}}{N^{\mu\mu}_{MC}}, \tag{A.1}$$

The Figure A.3- A.7 show double-ratios for different distributions and cut-efficiencies in the Z control region, requiring zero jets.

Process	cross-section [pb]	k-factor	ϵ_{filter}	N_{MC}	Generator
WcNp0	807.89	1.19	1	6499580	Alpgen
WcNp1	267.61	1.19	1	2069796	Alpgen
WcNp2	69.823	1.19	1	519998	Alpgen
WcNp3	20.547	1.19	1	110000	Alpgen
WcNp4	4.3069	1.19	1	19900	Alpgen
WbbNp0	55.682	1.19	1	474997	Alpgen
WbbNp1	45.243	1.19	1	359500	Alpgen
WbbNp2	23.246	1.19	1	174898	Alpgen
WbbNp3	11.144	1.19	1	50000	Alpgen
WccNp0	150.19	1.19	1	1274900	Alpgen
WccNp1	132.68	1.19	1	1049994	Alpgen
WccNp2	71.807	1.19	1	524900	Alpgen
WccNp3	30.264	1.19	1	169500	Alpgen

Table A.4 MC samples/processes used to model W+jets with heavy quark flavor (b and c) backgrounds. The corresponding cross-sections, generator names, generator level filter efficiencies and total numbers of events are shown in this Table. NpX (X=0..5) in the process name refers to the number of additional partons in the final state. The k-factors are calculated according to the NNLO inclusive W/Z production cross-sections, and the inclusive k-factors are assigned for each NpX samples.

Process	cross-section [pb]	k-factor	ϵ_{filter}	N_{MC}	Generator
ttbar	21.806	1.2177	1	9977338	MC@NLO
Wt	20.67	1.082	1	1999194	MC@NLO
tchan->e	9.48	1	1	299899	AcerMC
tchan->mu	9.48	1	1	300000	AcerMC
tchan->tau	9.48	1	1	293499	AcerMC
schan->e	0.606	1	1	199899	MC@NLO
schan->mu	0.606	1	1	199899	MC@NLO
schan->tau	0.606	1	1	199799	MC@NLO

Table A.5 MC samples/processes used to model top backgrounds ($t\bar{t}$ and single top). The corresponding cross-sections, generator names, generator level filter efficiencies and total numbers of events are shown in the Table.

Process	cross-section[pb]	k-factor	ϵ_{filter}	N_{MC}	Generator
$W^+Z \to e^+\nu e^+e^-$	1.407	1	0.29456	190000	Powheg
$W^+Z \to e^+\nu\mu^+\mu^-$	0.9328	1	0.35211	190000	Powheg
$W^+Z \to e^+\nu\tau^+\tau^-$	0.1746	1	0.16682	76000	Powheg
$W^+Z \to \mu^+\nu e^+e^-$	1.399	1	0.29351	189999	Powheg
$W^+Z \to \mu^+\nu\mu^+\mu^-$	0.9537	1	0.35132	190000	Powheg
$W^+Z \to \mu^+\nu\tau^+\tau^-$	0.1746	1	0.16863	76000	Powheg
$W^+Z \to \tau^+\nu e^+e^-$	1.399	1	0.14289	75400	Powheg
$W^+Z \to \tau^+\nu\mu^+\mu^-$	0.9382	1	0.18256	76000	Powheg
$W^+Z \to \tau^+\nu\tau^+\tau^-$	0.1719	1	0.058517	19000	Powheg
$W^-Z \to e^-\nu e^+e^-$	0.9795	1	0.29694	189899	Powheg
$W^-Z \to e^-\nu\mu^+\mu^-$	0.639	1	0.35302	190000	Powheg
$W^-Z \to e^-\nu\tau^+\tau^-$	0.1125	1	0.15969	76000	Powheg
$W^-Z \to \mu^-\nu e^+e^-$	0.9359	1	0.29766	76000	Powheg
$W^-Z \to \mu^-\nu\mu^+\mu^-$	0.6488	1	0.35414	190000	Powheg
$W^-Z \to \mu^-\nu\tau^+\tau^-$	0.1125	1	0.16023	190000	Powheg
$W^-Z \to \tau^-\nu e^+e^-$	0.9359	1	0.14803	76000	Powheg
$W^-Z \to \tau^-\nu\mu^+\mu^-$	0.638	1	0.18657	76000	Powheg
$W^-Z \to \tau^-\nu\tau^+\tau^-$	0.1107	1	0.056651	19000	Powheg
$ZZ \to 4e$	0.0735	1.0	0.90765	1099997	Powheg
$ZZ \to 2e2\mu$	0.1708	1.0	0.82724	1599696	Powheg
$ZZ \to 2e2\tau$	0.1708	1.0	0.58278	599899	Powheg
$ZZ \to 4\mu$	0.0735	1.0	0.91241	1099798	Powheg
$ZZ \to 2\mu2\tau$	0.1708	1.0	0.58725	600000	Powheg
$ZZ \to 4\tau$	0.0735	1.0	0.10604	300000	Powheg
$ZZ \to 2e2\nu$	0.168	1.0	1.0	299400	Powheg
$ZZ \to 2\mu2\nu$	0.168	1.0	1.0	300000	Powheg
$ZZ \to 2\tau2\nu$	0.168	1.0	1.0	299999	Powheg
$W\gamma$Np0	229.88	1.15	0.31372	14296258	Alpgen
$W\gamma$Np1	59.518	1.15	0.44871	5393984	Alpgen
$W\gamma$Np2	21.39	1.15	0.54461	2899389	Alpgen
$W\gamma$Np3	7.1203	1.15	0.62974	859697	Alpgen
$W\gamma$Np4	2.1224	1.15	1.0	364999	Alpgen
$W\gamma$Np5	0.46612	1.15	1.0	60000	Alpgen
$W\gamma* \to \ell\nu ee$	10.17487	1.0	1.0	2008998	Sherpa
$W\gamma* \to \ell\nu\mu\mu$	2.53518	1.0	1.0	504996	Sherpa
$W\gamma* \to \ell\nu\tau\tau$	0.22830	1.0	1.0	50000	Sherpa

Table A.6 MC samples/processes used to model the diboson backgrounds WZ, ZZ, $W\gamma$, and $W\gamma*$. The corresponding cross-sections, generator names, generator level filter efficiencies and total numbers of events are shown in the Table. The samples with filter efficiency not equal to 1 have lepton filter. The WZ sample has a filter which requires two leptons, each with $p_{\text{T}} > 5$ GeV and $|\eta|$<2.7. The ZZ sample has a filter which requires two leptons, each with $p_{\text{T}} > 5$ GeV and $|\eta|$<10.0. The $W\gamma$ sample has a filter which requires two leptons, each with $p_{\text{T}} > 8$ GeV and $|\eta|$<3.0. NpX (X=0..3) in the process name refers to the number of additional partons in the final state. For the last three samples, $M_{\gamma*} < 7$ GeV.

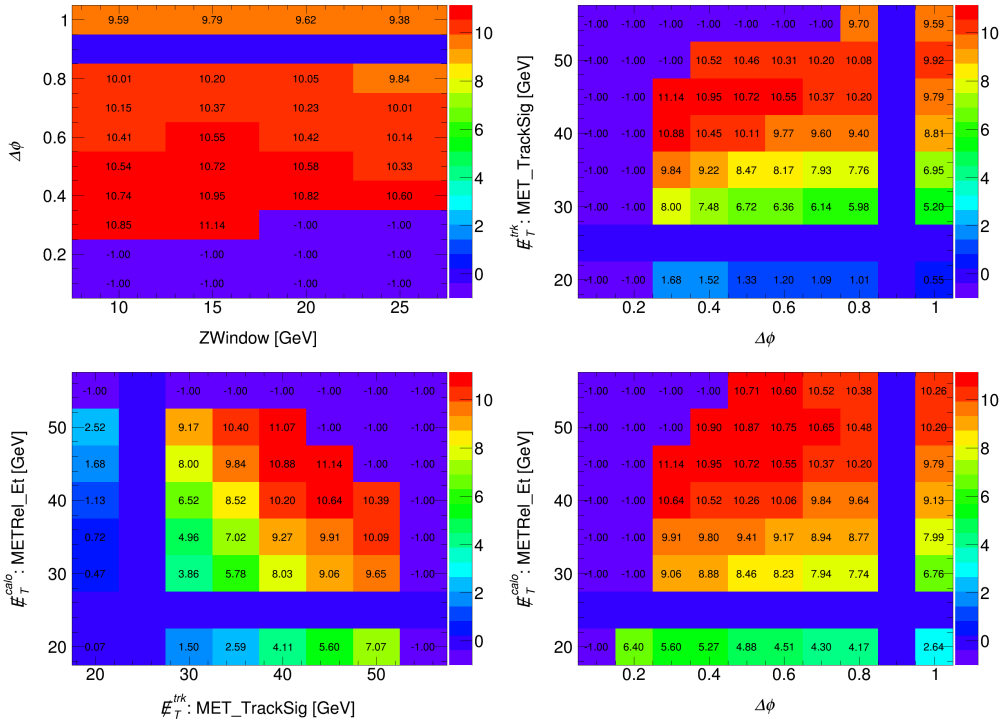

Figure A.1 The 2D significance plots in same flavor channel for optimization study performed on cut variable pairs. While one cut variable pair is plotted, other cuts are set to be nominal. Top left shows $\Delta\phi(p_{\mathrm{T}}^{\mathrm{miss}}, E_{\mathrm{T}}^{\mathrm{miss}})$ and Z veto cuts, top right shows $p_{\mathrm{T}}^{\mathrm{miss}}$ and $\Delta\phi(p_{\mathrm{T}}^{\mathrm{miss}}, E_{\mathrm{T}}^{\mathrm{miss}})$, bottom left shows $p_{\mathrm{T}}^{\mathrm{miss}}$ and $E_{\mathrm{T,\,Rel}}^{\mathrm{miss}}$ and bottom right shows $E_{\mathrm{T,\,Rel}}^{\mathrm{miss}}$ and $\Delta\phi(p_{\mathrm{T}}^{\mathrm{miss}}, E_{\mathrm{T}}^{\mathrm{miss}})$.

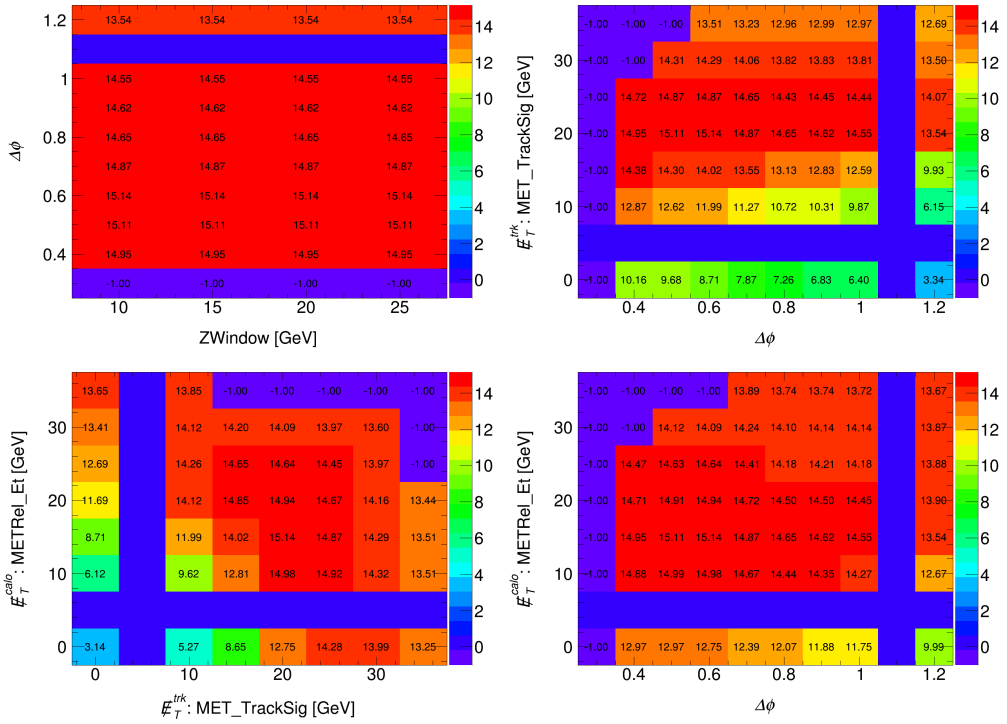

Figure A.2 The 2D significance plots in $e\mu$ flavor channel for optimization study performed on cut variable pairs. While one cut variable pair is plotted, other cuts are set to be nominal. Top left shows $\Delta\phi(p_{\mathrm{T}}^{\mathrm{miss}}, E_{\mathrm{T}}^{\mathrm{miss}})$ and Z veto cuts, top right shows $p_{\mathrm{T}}^{\mathrm{miss}}$ and $\Delta\phi(p_{\mathrm{T}}^{\mathrm{miss}}, E_{\mathrm{T}}^{\mathrm{miss}})$, bottom left shows $p_{\mathrm{T}}^{\mathrm{miss}}$ and $E_{\mathrm{T,\,Rel}}^{\mathrm{miss}}$ and bottom right shows $E_{\mathrm{T,\,Rel}}^{\mathrm{miss}}$ and $\Delta\phi(p_{\mathrm{T}}^{\mathrm{miss}}, E_{\mathrm{T}}^{\mathrm{miss}})$.

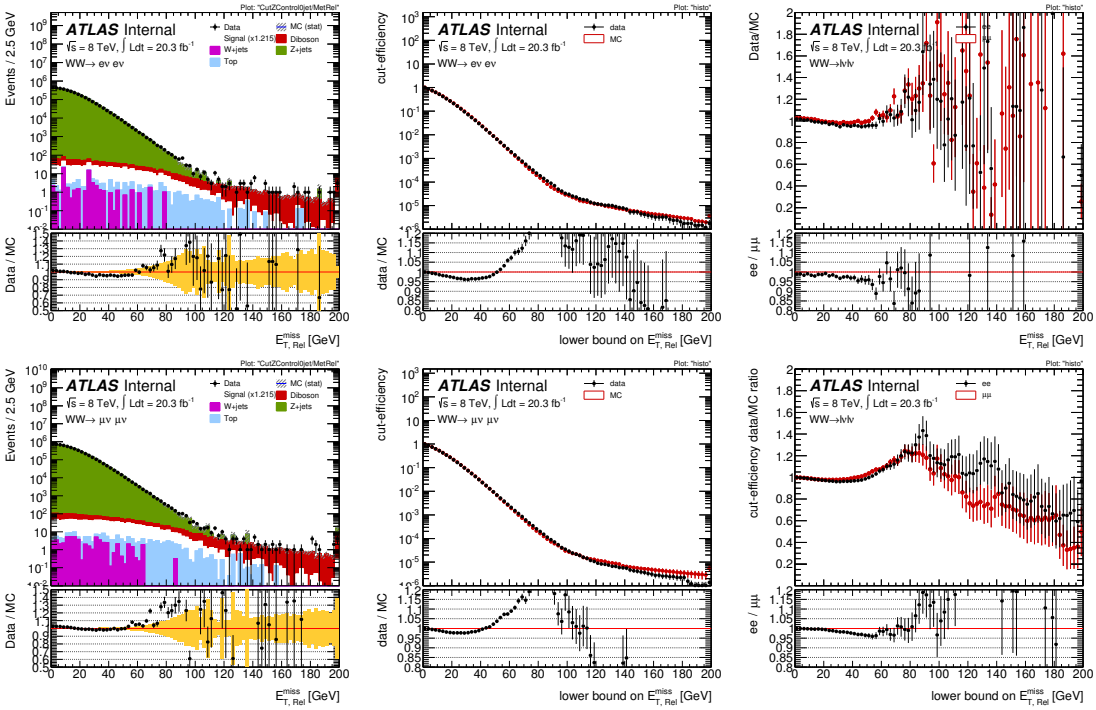

Figure A.3 Comparison of $E_{\mathrm{T,\,Rel}}^{\mathrm{miss}}$ (RefFinal) in the two same-flavour channels. The two plots on the left show a data/MC comparison for the ee (top) and $\mu\mu$ channels. The middle plots show the cut-efficiencies on data and MC, again for ee (top) and $\mu\mu$ channels. The right hand side plots show the ratios of the data/MC distribution (top) and the ratios of the cut-efficiencies (bottom). The double-ratios Eq. A.1 correspond to the lower part of the left hand side figures.

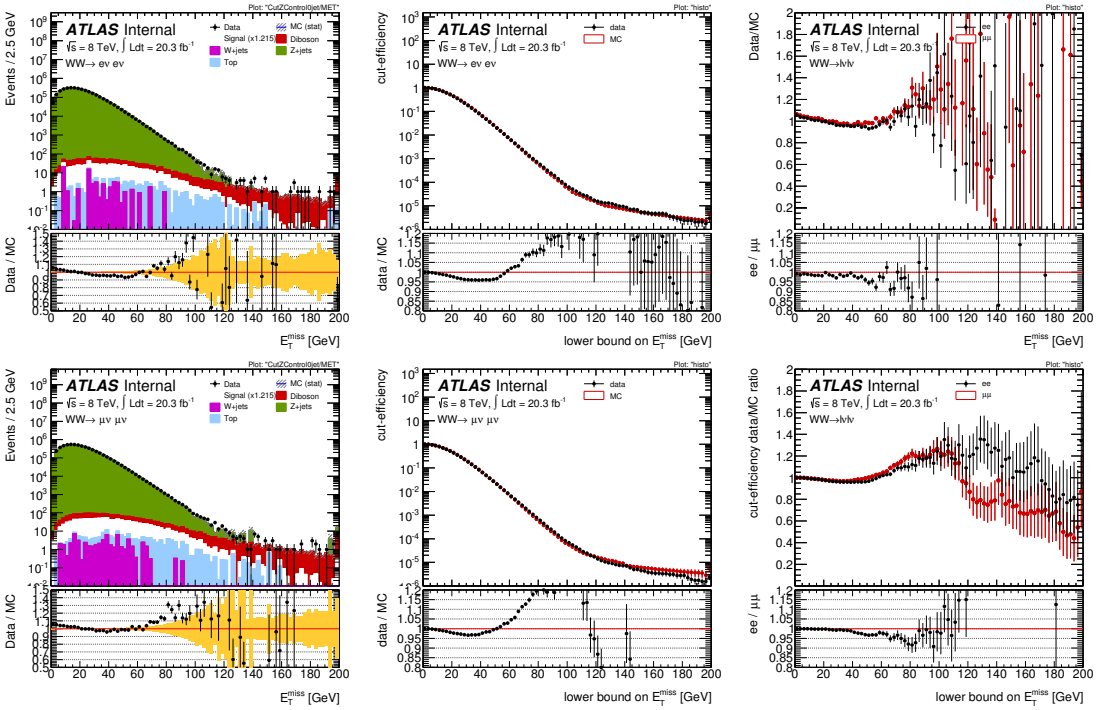

Figure A.4 Same as Figure A.3 for $E_{\mathrm{T}}^{\mathrm{miss}}$ (RefFinal)

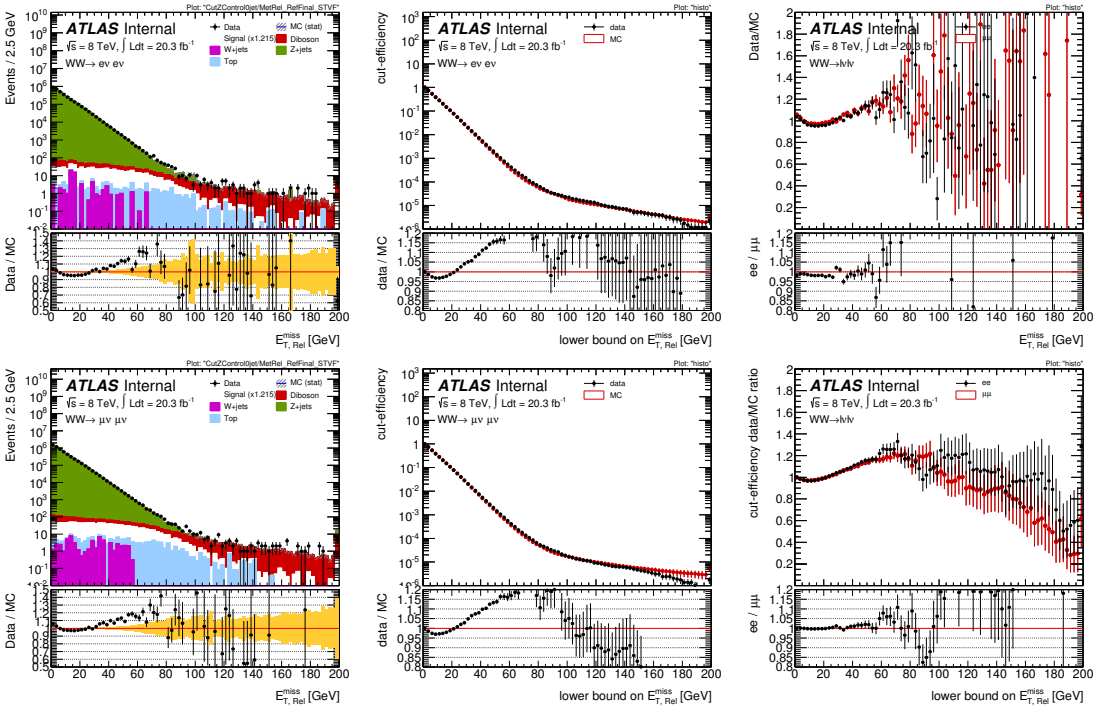

Figure A.5 Same as Figure A.3 for $E_{\mathrm{T,\ Rel}}^{\mathrm{miss}}$ (STVF)

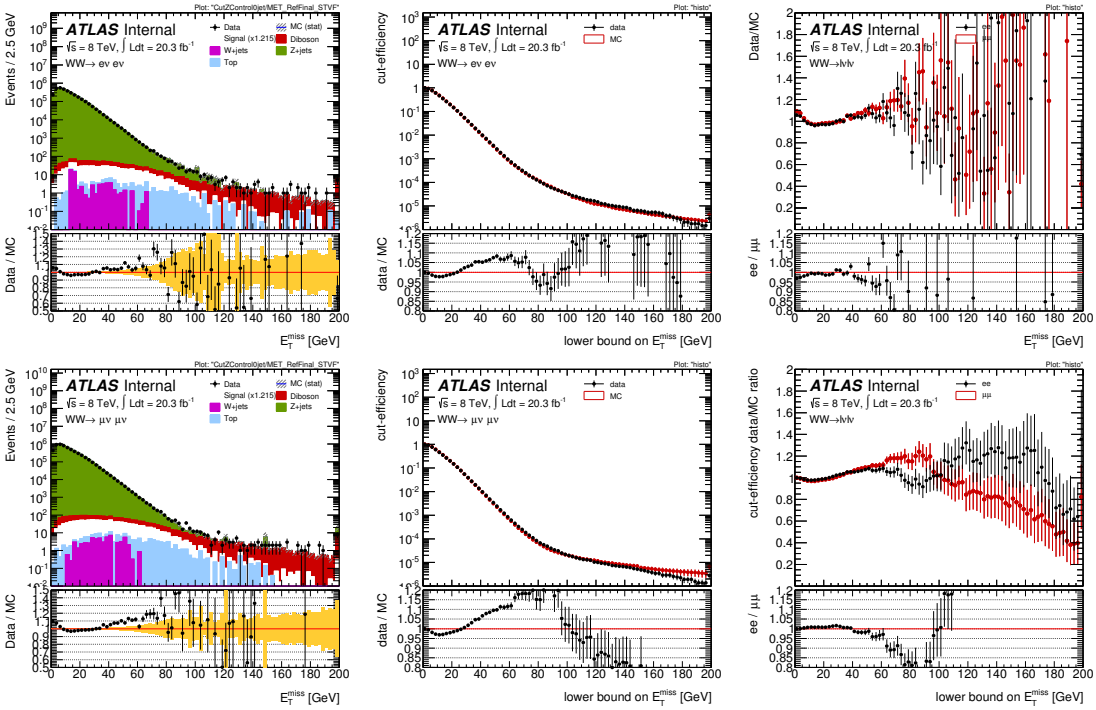

Figure A.6 Same as Figure A.3 for $E_{\mathrm{T}}^{\mathrm{miss}}$ (STVF).

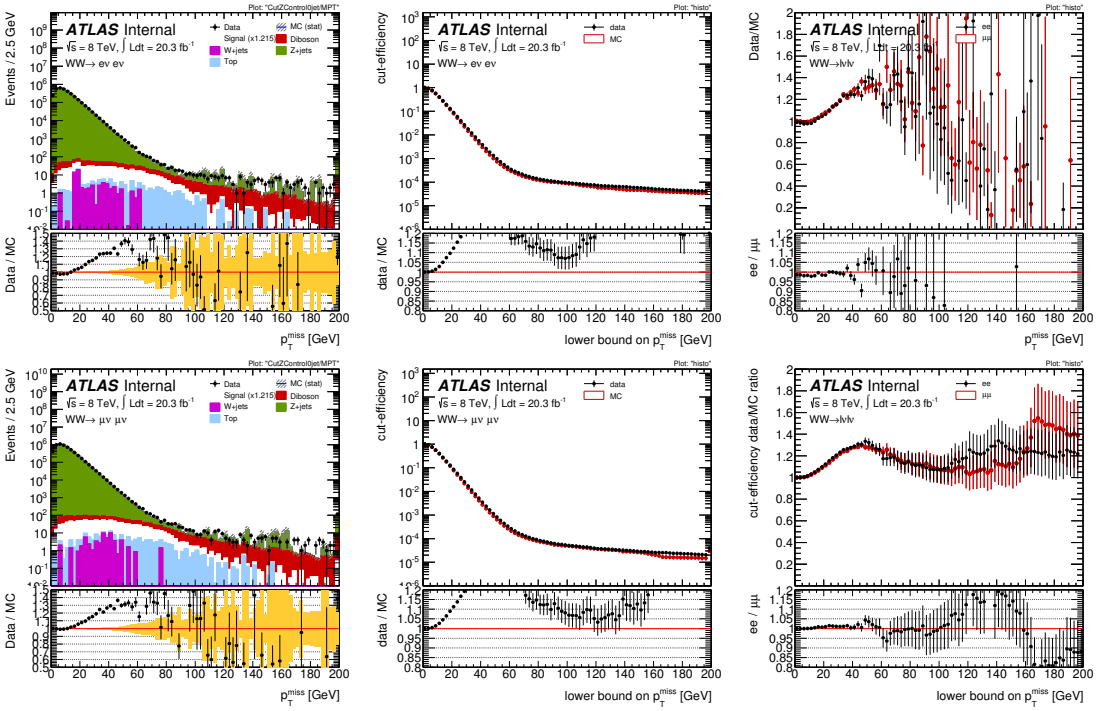

Figure A.7 Same as Figure A.3 for track-based MET $p_{\mathrm{T}}^{\mathrm{miss}}$.

List of Tables

List of Figures

Thanks

I would like to sincerely give thanks to those who offered help during my PhD career and about this thesis.

I'm particularly grateful to my supervisors Emmanuel Monnier and Yanwen Liu who offer me precious opportunities involving in the $ATLAS$ experiment. It was four years ago, yanwen took the decision to join in the WW analysis for the ATLAS experiment. At that time, Shu Li and Emmanuel were making progress in WW analysis at CPPM. I spent two years in France, joined in the fruitful CPPM team, in particular so many different aspects within the ATLAS experiment. Both Emmanuel and Yanwen supported my work and gave me lots of suggestions and comments, not only for the brainstorms of the research but also the positive altitude for the every-day life. I could still recall the time we would sit in the coffee area discussing the way to joining into the analysis. I could recall the time Emmanuel talked with me the life for researchers, and the time Yanwen energetically summoned people to climb the mountains during the weekends, and even more for interesting stories. They played an very important role during my PhD life. I have to say they are very excellent supervisors and it is lucky to have both of them guiding me.

I will remember the days in CPPM, especially for the nice atmosphere. Shu Li was involved in the previous WW analysis, so he is an expert. He helped with me a lot, and I would like to thank him a lot. I would also like to thank people sharing the office with me. Daniele Madaffari is very nice and optimistic for life. We had a lot of nice time together. Otilica Ducu discussed with me about the studies since our topics are more or less similar. CPPM also has a big group working on B-taggning. From Kazuya Mochizuki I could know the latest news about their progress for b-tagging. Alessandro Mord¨¤ is very friendly and patient for explaining things. There are more people who helped me a lot and I will not list all of the names. Thank you for all the people at CPPM.

I would also thank the collegues working on the WW analysis. All of them are willing to help and discuss issues. The convener, Kristin Lohwasser, Yusheng Wu and Dimitra Tsionou make the team function well. Kristin is experienced in how to handle things properly and truly leading a good way. Yusheng helped a lot with the problems I came to and he is quite willing to go through the problems with me. And I also thank the analysers, especially Philip Sommer and Jiri Hejbal, for their help with all the cross checks.

I spent in total 7 years in USTC. I have a very special feeling to this campus. During

my PhD life, I've learned a lot from professors and students. Professor Zhengguo Zhao is devoted in the way of training students to be ready for the international communication, and he always has new ideas about that. Professor Jianbei Liu is very professional in ATLAS experiment and can sort out practical information for the analysis. Professor Haiping Peng devotes to his work and works late at the office, and he is quite serious for his work. Kun Liu always shows his optimistic opinion in front of us, and takes his responsibility for all of the challenges. Lailin Xu is a reliable college and he works very hard to solve the problems. Bing Li was kindly sharing room with me when I was in Gevena. Minghui Liu is an experienced researcher and always ready to help us solve the questions. I will not list more people, and i just want to thank all those people, especially who was, is, and will be to help others.

I want to thank my old friends. Wei Sun was working on LHCb and we had comfortable time both in USTC and Geneva. I also want to give my thanks to Longke Li, who has been working on Belle experiment. He is a nice guy orgnizing many activities for USTC students. We had a nice time. And I also want to mention those friends who are not working on LHC, or even not working on physics. I would remember the time we had been through.

Last but not least, I would like to thank my family. They have done what they can do to support me during the last few years.

Thanks to all of you. The memory will last forever.

ABSTRACT

The Standard Model (SM), actual fundamental theory for particle physics, provides a description of the elementary particles and the fundamental interactions: the electromagnetic, weak and strong forces. Extensively tested by many world-wide experiments. Questions still remains to be answered for the completeness of this theory. New experiments have been designed and built to create and explore particle interactions at a new high energy scale. The data from those experiments will offer us a chance to test deeper our understanding of the SM and to search for physics beyond the SM. At the European Organization for Nuclear Research (CERN), physicists and engineers from all over the world are searching to understand the fundamental laws of the universe. It is at CERN that the world's largest and most sophisticated experimental instruments have been built, to accelerate particles at the energy of 3.5-4 TeV with the Large Hadron Collider (LHC) and collide them at the center of detectors. In this way physicists may be able to find hint on how particles interact, and further on the laws of nature.

A Toroidal LHC ApparatuS (ATLAS), one of the four main detectors at LHC, aims at a wide range of physics studies, including the precision measurement of the SM processes, the search for the Higgs bosons and hint of new physics. The CMS experiment is aiming at a similar program.

In ATLAS, di-boson production is one of the most important electro-weak processes. Among the massive vector boson pair production processes, W^+W^- production has a larger cross section compared to the WZ and ZZ ones. The electro-weak sector of the SM, as well as the strong interactions, can be tested through the precision measurements of the W^+W^- production cross section. A measurement of the $W + W-$ production cross section in 8 TeV center of mass proton-proton collisions is presented here from data collected with the ATLAS detector at the LHC for a total integrated luminosity of 20.3 fb^{-1}.

The W^+W^- events are selected with 3 final states: ee, $e\mu$, and $\mu\mu$. In order to suppress the background contamination, mainly from the Drell-Yan and $t\bar{t}$ processes, a cut on missing transverse energy is applied and events with hadronic jets satisfying appropriate selection criteria are rejected. The major backgrounds, mainly including W +jets, top and Z+jets, are estimated by data driven technique. These background estimations are cross-checked by independent methods. The measured cross section is $71.0^{+1.1}_{-1.1}$(stat)$^{+5.7}_{-5.0}$(syst)$^{+2.1}_{-2.0}$(lumi) pb, which is consistent with SM Next-to-Next-Leading-Order prediction of $63.2^{+2.0}_{-1.8}$ pb.

The normalized differential W^+W^- cross section $\frac{1}{\sigma}\frac{d\sigma}{dX}$ is determined as a function of six kinematic variables. The unfolded distributions for these variables are given. The possible deviation from the SM can be parameterized with operators of higher order dimensions. The operators of lowest dimension introduce anomalous triple gauge couplings (ATGC). The distribution of the leading lepton p_{T} is used to constrain the anomalous coupling constants. Therefore, the measurement of the coupling constants provides an indirect search for new physics at mass scales not accessible at the LHC. In our study, no evidence for anomalous WWZ and $WW\gamma$ triple gauge-boson couplings is found, and limits on their coupling parameters are set. The limits are better by a factor of almost four compared to the limits previously published by the ATLAS collaboration.

Keywords: ATLAS detector, W^+W^- production, Cross Section, Differential measurement, Anomalous Gauge Couplings

RÉSUMÉ

Le Modéle Standard (MS), actuelle théorie fondamentale de la physique des particules, fournit une description des particules élmentaires et de plusieurs interactions fondamentales : les forces électromagnétique, forte et faible. Cette théorie a été testée par de nombreuses expériences mais des questions demeurent, témoignant de la nécessité de disposer d'une théorie plus complète. De nouvelles expériences ont t conçues pour étudier les interactions entre particules à une nouvelle échelle d'énergie. Les données obtenues offrent la possibilit de tester plus profondément le Modèle Standard, ainsi que de chercher des signes de physique au-delà du MS.

Au Centre Européen pour la Recherche Nucléaire (CERN), des scientifiques du monde entier cherchent à comprendre les lois fondamentales régissant l'Univers. Pour cela, les instruments expérimentaux les plus imposants et les plus sophistiqués ont été construits, accélérant des faisceaux de particules à une énergie de 3.5-4 TeV, grâce au LHC (Large Hadron Collider), pour les faire entrer en collision au centre des détecteurs et obtenir des indications quant à la manière dont les particules interagissent et ainsi appréhender les lois fondamentales de la nature.

L'expérience ATLAS (A Toroidal Lhc ApparatuS), un des quatre principaux détecteurs installés auprès du LHC, couvre un large spectre de mesures physiques, incluant des mesures de précision du MS, la recherche du boson de Higgs, ou de trace de nouvelle physique. L'expérience CMS a un programme similaire.

La production de paires de bosons est l'un des processus électrofaibles les plus intéressants à étudier. Parmi les différents modes de production de paires de bosons vecteurs massifs, la section efficace $pp \rightarrow W^+W^-$ est la plus importante, comparée aux processus WZ ou ZZ. Le secteur électrofaible du MS, ainsi que les interactions fortes, peuvent être testés par la mesure précise de la section efficace de production W^+W^-. Ce document présente une mesure de cette section efficace à partir de collisions proton-proton, à une énergie au centre de masse de 8 TeV, et correspondant à une luminosité totale intégrée de 20.3 fb^{-1}.

Les événements W^+W^- sont sélectionnés à partir de trois états finaux : ee, $e\mu$, and $\mu\mu$. Afin de réduire le bruit de fond, constitué principalement de processus Drell-Yan ou de paires $t\bar{t}$, une coupure est appliquée sur l'énergie transverse manquante, et les événements contenant des jets hadroniques satisfaisant certains critères de sélection sont rejetés. Les principaux bruits de fonds résiduels, essentiellement des processus W+jets, top, Z+jets, sont estimés à l'aide de modéles établis à partir des données observées (méthodes data driven). Ces méthodes d'estimation sont validées en les comparants àd'autres méthodes indépendantes. La section efficace mesurée est $71.0^{+1.1}_{-1.1}$(stat)$^{+5.7}_{-5.0}$(syst)$^{+2.1}_{-2.0}$(lumi) pb, en accord avec la prédiction NNLO du MS de $63.2^{+2.0}_{-1.8}$ pb.

Les sections efficaces différentielles normalisées $\frac{1}{\sigma}\frac{d\sigma}{dX}$ sont obtenues pour six différentes variables cinématiques. Les distributions de ces variables, déconvoluées de l'efficacité de reconstruction du détecteur, sont présentées. Les éventuelles déviations de la section efficace mesurée par rapport à la prédiction du MS peuvent être paramétéres par des opérateurs de dimensions supérieures. Les opérateurs de dimension la plus basse induisent des couplages tribosons de jauge anomaux (ATGC). La distribution p_{T} du lepton dominant est utilisée pour contraindre ces couplages anomaux. Ainsi, les mesures des constantes de couplage permettent une recherche indirecte de physique au-delà du MS, à une échelle de masse non accessible au LHC. L'étude présentée ici ne met pas en évidence de tels couplages anomaux WWZ ou $WW\gamma$, et donne des limites supérieures sur la magnitude de ces couplages. Les limites sont améliorées d'un facteur quatre par rapport aux limites préalablement publiées par la collaboration ATLAS.

Mots-clés : détecteur ATLAS, production W^+W^-, section efficace, couplage anomal